Title
Salt Concentration Gradients in Block Copolymer Electrolytes

Author
Galluzzo, Michael

Publication Date
2021

Peer reviewed|Thesis/dissertation

Salt Concentration Gradients in Block Copolymer Electrolytes

By
Michael D. Galluzzo

A dissertation submitted in partial satisfaction of the

requirements for the degree of

Doctor of Philosophy

in

Chemical Engineering

in the

Graduate Division

of the

University of California, Berkeley

Committee in charge:
Professor Nitash P. Balsara, Chair
Professor Bryan D. McCloskey
Professor Gerbrand Ceder

Summer 2021

Salt Concentration Gradients in Block Copolymer Electrolytes

Abstract

Salt Concentration Gradients in Block Copolymer Electrolytes

By

Michael D. Galluzzo
Doctor of Philosophy in Chemical Engineering
University of California, Berkeley
Professor Nitash P. Balsara, Chair

Rechargeable batteries are ubiquitous in our daily lives thanks to advancements in technology and low manufacturing costs for large scale production of lithium-ion batteries. State of the art, commercially available batteries are comprised of a graphite anode and liquid electrolyte. There is considerable interest in developing next-generation lithium batteries based on a lithium metal anode and solid-state electrolyte. While several commercial ventures have indicated that there is demand for such a product and significant capital to back them, lithium metal batteries have not been widely implemented due to high cost and poor cyclability compared to lithium-ion technology. We are motivated to study solid electrolytes which are compatible with lithium metal anodes. The majority of this thesis is focused on a nanostructured block copolymer electrolyte with phase-separated mechanically rigid and ion conducting domains: polystyrene-block-poly(ethylene oxide) (SEO) with lithium bis(trifluoromethanesulfonyl)imide salt (LiTFSI). Polystyrene (PS) provides mechanical rigidity which aides stable lithium deposition during battery charging and poly(ethylene oxide) (PEO) solvates the lithium salt and conducts ions between the electrodes. A variety of morphologies are accessible by tuning the volume fraction of one phase and the chain length. The viability of SEO/LiTFSI electrolytes in lithium metal batteries has been well established in the literature. However, there are many open questions about the mechanisms by which SEO facilitates the transportation of lithium ions between electrodes. Our goal is to shed light on the phenomena which govern the performance of block copolymer electrolytes via rigorous characterization of their ion transport properties and transient structure. The primary tools used in our analysis are electrochemical techniques involving a potentiostat to study the rate of ion transport under different conditions and small angle X-ray scattering (SAXS) to characterize block copolymer structure at equilibrium and while ions flow through the electrolyte.

Unlike simple electronic conductors (*e.g.,* a copper wire) which have only one charge carrier (electrons), a battery electrolyte has two charge carriers (cations and anions). When implementing an electrolyte into a lithium-ion or lithium metal battery, the electrodes are designed such that only lithium cations can cross the electrode/electrolyte interface. The unavoidable consequence is that passing ionic current through the electrolyte (*i.e.*, charging or discharging the battery) results in accumulation of ions near one electrode and depletion of ions near the other. In other words, a salt concentration gradient develops along the axis perpendicular to the planar electrodes. Under galvanostatic conditions (constant current), thermodynamics requires that a

larger driving force (over potential) be required to maintain the same current as the salt concentration gradient evolves. Under potentiostatic conditions (constant voltage), thermodynamics requires that a smaller current density be passed through the electrolyte as the salt concentration gradient evolves. Consequently, the nature of the salt concentration gradients which develop during battery operation are closely tied to material performance. In this dissertation, we characterize salt concentration gradients in symmetric cells composed of two lithium electrodes sandwiched around a polymer electrolyte.

After introducing lithium-based batteries, polymer electrolytes, and SAXS in Chapter 1, we develop a framework for quantifying electrolyte performance in the presence of small salt concentration gradients. Measurement of the ionic conductivity, κ, by ac impedance spectroscopy characterizes ion transport in the absent of concentration gradients. In the presence of concentration gradients, electrolyte performance is quantified by the product of κ and the current fraction, ρ_+. The current fraction is the ratio of the steady state current, i_{ss}, to the initial current, i_0, in a potentiostatic experiment. We rank order a list of electrolytes reported on in the literature based on $\kappa\rho_+$ and find that there is a tradeoff between total ionic conductivity and selective cation transport. In Chapter 3, we explore the relationship between ρ_+ and the cation transference number, t_+, to show how the two parameters dictate ion transport at early and long times when an electrolyte of initially uniform salt concentration is subjected to ionic current. Negative transference numbers have been reported in the literature, however the result has not been definitively proven. Our analysis leads us to propose a cell based on anion exchange membranes which could be used to conclusively prove the result.

In Chapter 4, we return our attention to SEO/LiTFSI block copolymer electrolytes and extend our discussion of electrochemical characterization beyond Chapter 2. By measuring κ, ρ_+, the salt diffusion coefficient, D, and the equilibrium potential of concentration cells, U, we fully characterize ion transport in a series of SEO/LiTFSI electrolytes with various morphologies and chain lengths to solve for the transference number with respect to the solvent velocity, t_+^0. We obtain negative values of t_+^0 over a wide range of salt concentrations and morphologies. Universal relationships are uncovered for ρ_+ and $\frac{dU}{d\ln m}$ which apply for any PEO/LiTFSI or SEO/LiTFSI electrolyte. The result allows us to predict salt concentration gradients for any SEO/LiTFSI electrolyte by simply measuring κ as a function of salt concentration.

An important consideration when studying any electrochemical system is the interactions which take place at the electrode/electrolyte interface. For PEO-containing electrolytes in contact with a lithium electrode, we found that lithium metal is sparingly soluble in PEO. The primary evidence is obtained from nuclear magnetic resonance spectroscopy (NMR), which is discussed in Chapter 5. We show that this phenomenon is detectable by phase transitions in a low molecular weight SEO/LiTFSI electrolyte. We take this result into account when studying the phase behavior of SEO/LiTFSI electrolytes in lithium symmetric cells in the Chapters 6 and 7.

In Chapter 6 and 7, we describe simultaneous polarization and SAXS experiments on SEO/LiTFSI electrolytes to study the transient structure in the presence of ionic current and salt concentration gradients. Our methodology allows us to study the nanostructure of the electrolyte as a function of time and distance from an electrode during polarization. In Chapter 6, we focus

on a low molecular weight (3.1 kg mol^{-1}) SEO/LiTFSI electrolyte which has accessible phase transitions over a wide salt concentration window. Under dc polarization, the initially lamellar morphology transforms into a disordered morphology near the negative electrode where salt concentration is lower, and pockets of the gyroid morphology form near the positive electrode where salt concentration is higher. The emergence of the gyroid phase is unexpected as it is only thermodynamically favored at significantly higher salt concentrations than should be accessible based on the initial salt concentration. We hypothesize the presence of the gyroid morphology is indicative of localized salt dense pockets which form at bottlenecks in the block copolymer structure. In Chapter 7, we study a higher molecular weight (39 kg mol^{-1}) SEO/LiTFSI electrolyte which exhibits a lamellar morphology at all salt concentrations studied. The domain spacing, d, increases with salt concentration, and we study the change in d as a function of position in the cell. By measuring d at several current densities, we show that the spatial gradient in domain spacing aligns with model predictions at low to moderate current densities based on the measurements made in Chapter 4. The behavior at large current densities indicates that the rearrangement of the structure may limit the maximum sustainable current density which can be passed through the electrolyte. In our sample which consists of a distribution of lamellar grain orientations, we find those with PS/PEO interfaces aligned perpendicular to the current are distorted more than those with interfaces aligned parallel to the current. While grains with interfaces oriented perpendicular to the current do not provide pathways for current to pass between the electrodes, we show that the distortion of the structure is critical for facilitating the formation of a salt concentration gradient.

In this dissertation, we discuss the physics that are responsible for the development of a salt concentration gradient when current flows through an electrolyte. Careful characterization of transport parameters provides microscopic insight into the mechanisms of ion transport and the magnitude of salt concentration gradients. Structural characterization of block copolymer electrolytes subjected to ionic current provides fresh insight into the mechanisms which limit the rate of ion transport between the electrodes. Our characterization of the dynamic relationship between salt concentration gradients, ion transport, and nanostructure in block copolymer electrolytes provides guiding principles for the design of novel electrolyte materials aimed at enabling the lithium metal anode.

Table of Contents

List of Figures

List of Tables

This thesis is dedicated to my mother,

Donna Galluzzo,

and written in loving memory of my father,

Tony Galluzzo Jr.

Thank you both, for everything.

Acknowledgements

The research presented in this dissertation culminates a satisfying journey through a chemical engineering PhD curriculum. I have benefited from many interactions with many individuals, and I am grateful to have spent my time as a graduate student surrounded by talented people. I cannot adequately thank them all in a few short paragraphs (but I will try).

First, I would like to thank my advisor and mentor, Nitash Balsara. When I joined the lab, I was given the freedom to guide the path of my own research, an experience which was both challenging and highly rewarding. Along the way, I learned a lot from Nitash and his excitement for my results encouraged me to push forward. He is driven to obtain fundamental understanding of the phenomena he studies, and that philosophy carries forward to his students. I admire his leadership. I am thankful for his dedication to my education and for allowing me to be a part of the group culture he fosters.

When I joined the lab, I was both impressed and intimated by the caliber of the students and postdocs in the group. However, the senior students in the lab were extremely approachable and I owe them a lot for helping me learn and grow as an independent researcher. Many of the students who I only overlapped with for a short amount of time continued to engage me well after they left the lab. Jacob Thelen's excitement for my research was encouraging at a time when I was just getting started and learning the ropes. Kevin Wujcik, Mahati Chintapalli, and Chaeyoung Shin were all extremely welcoming and I am glad to have gotten to know them. Their confidence, knowledge, and excitement for science set an example of how a senior student should carry themselves in the lab. Alex Wang was an excellent communicator and I enjoyed learning from him. Adri Rojas went out of her way to get to know me, and I admired her confidence. I appreciate that they both put work aside at a busy time in their PhDs to socialize with the lab, setting an example for the rest of us. Doug Greer navigated a challenging research project with grace. I am grateful for his friendship and the advice he has given me throughout my graduate career.

I have always felt that the postdocs in the Balsara Lab are unique. Collectively, they are experts in their field with ambition, and yet they have fostered a sense of camaraderie in the group as opposed to competition. Dr. Mahesh Bhatt helped me get set up in lab and set an example of how to be a leader. Dr. Irune Villaluenga is a brilliant synthetic chemist and always fun to be around in lab. Dr. Kim Mongcopa had the difficult task of educating us all on neutron scattering, but I will most remember her quips and contagious laughter, and that her husband appreciates a good sauce. Professor Hee Jeung Oh was a leader in the lab and was calming force when the occasional monomer jar cracked or glove box fuse blew. Outside the lab, she has great potential as a marathon runner, and I look forward to settling a score with her in a series that we are currently tied 1 to 1. Dr. Youngwoo Choo was a great addition to our group, and I miss our scientific discussions. He is incredibly hard working and a great collaborator. Dr. Louise Frenck has been a great friend to me, and I am as appreciative of her happy hour planning as I am of her expertise in all things batteries. I was fortunate that when I began doing NMR experiments, Dr. David Halat joined the lab and immediately taught me a lot about NMR and helped me with my project. I have enjoyed both getting to know him and talking shop. Dr. Saheli Chakraborty has been a great resource for me in the lab for all things chemistry. She impressively juggles several projects and I

have always appreciated the way she carries herself in the group: I have never seen her get down when things do not go as planned, and I am impressed at what she accomplishes when they do. Dr. Xiaopeng Xu joined the lab at a difficult time but has shown impressive results, I am excited to see what he will show next. Dr. Jaeyong Lee just joined the group, but from my few interactions with him, I am confident he will be a great addition to the group's scientific and social culture.

Danielle Pesko, Rita Wang, and Ksenia Timachova gave me an example of what to work towards. Danielle spearheaded research that has guided many current and future projects, including my own. She was meticulous and confident in lab, and I appreciated her dedication to department and lab social events. Ksenia left a legacy by making NMR techniques a staple in the lab's research program. Beyond that, she has been a great friend to me, and I have enjoyed our hiking and skiing adventures. I hope I lived up to her expectations as ski trip organizer. Rita tackled a project combining electrochemical measurements and synchrotron radiation, a challenge that I can fully appreciate now. She was always full of positive energy in lab, and it was a pleasure to work with her.

The students who graduated a year before me were a cast of characters, and I am incredibly grateful for my relationship with Whitney Loo, Deep Shah, and Jackie Maslyn. Some of my favorite moments in grad school were spent debating and deriving equations at the white board with each of them. As a second year when I joined, Whitney already displayed incredible depth in her knowledge of polymer thermodynamics, and it set the bar for what I needed to do to keep up. At the same time, she was a great resource, teaching me polymer synthesis and X-ray scattering. She helped me get my first X-ray scattering experiments started which would become the foundation of much of my PhD research. It was a pleasure to work with somebody so knowledgeable and always willing to help. I am excited to see what she accomplishes in her academic career. Deep Shah was a great coworker for numerous reasons. He was just as willing to talk about the theory of ion transport as he was to talk about career paths, negotiating, and networking. I benefited greatly from all sorts of conversations with Deep and he was an integral part of our lab culture. We often argued over equations in the most productive way possible, and I missed that greatly when he graduated. Jackie Maslyn is perhaps the most diligent researcher I have ever met. Early on, she taught me the importance of deriving and understanding every equation that is used in a particular calculation, a lesson that stuck with me through graduate school. Despite having terabytes of tomography data to analyze, she always found time to work through equations with me, and I greatly enjoyed collaborating with her. I appreciated finding the best value on wine while editing textbook chapters, and that she shared her passion for softball and ab workouts with me. Jackie, Deep and I shared several painful yet rewarding experiences together, most notably writing a review article and biweekly Insanity workouts. To say the least, Whitney, Deep, and Jackie were great lab mates and friends to me throughout grad school.

I am very glad to have grown as a researcher alongside Gumi Sethi. We navigated the lab together and she was a great friend to share ideas with and vent about the more stressful parts of graduate school. She is an impressive researcher and carries herself with a confidence that I admire. I have learned a lot from her research, and I am excited to see what she accomplishes next. Kevin Gao and Lorena Grundy are two highly intelligent individuals that I have enjoyed working with. Kevin has spurred a new research direction in our group with polymer blends, and I admire his

willingness to improve on the methodologies in the literature instead of accepting them as best practice. I will miss our workouts together but am lucky to have him as a friend. Collaborating with Lorena over the last year has been one of the highlights of my education, and I look forward to seeing what she will do with her projects in her last year in the lab. Beyond our work together, she has produced fascinating results in her NMR studies that I have enjoyed learning about. I am grateful for her friendship and leadership in the lab. The younger students are certainly in good hands with Kevin and Lorena as the senior students.

Alec Ho, Zach Hoffman, and Neel Shah have taken very different research paths and have made it clear that the future of the lab is in good hands. I am impressed by Alec's approach to research by tackling new analysis and spearheading the study of lithiation of graphite electrodes using X-ray tomography. Zach has proven to be a diligent researcher and I have been lucky to work with him. I am excited to see where he takes the Raman project, and glad that it is being left in good hands. Neel has grown a lot as a researcher over the last two years, and I am impressed with his knowledge of polymer thermodynamics. Morgan Seidler and Darby Hickson are making impressive progress on their projects during a difficult time. They have already stepped up as leaders in the group, and I am sure they will continue to accomplish a lot. Karim Aruta and Vivaan Patel, the newest students, are already well on their way to great accomplishments. The lab has a strong future.

Outside of the Balsara Lab, I have benefited from several collaborations. I am grateful to have worked with Maddie Gordon and Jeff Urban and have learned a lot about Raman spectroscopy from them. I was hesitant at first to tackle a new technique, XPCS, in my final year of graduate school, but it has been highly rewarding thanks to great collaborators: Chris Tacaks, Hans-Georg Steinrück, Chuntian Cao, and Mike Toney. Chris has taught me a lot about X-ray scattering and it has greatly benefited my project. I have had many stimulating conversations with Hans, and he has taught me a lot. I will miss their lighthearted conversation and synchrotron-related humor. My research has been enabled by superb beamline scientists: Chenhui Zhu, Eric Schaible, Suresh Narayanan, Eric Dufresne, and Anthony Fong.

My research would not have been possible without the skilled machining of Doug Scudder and Clint Jessel. I thoroughly enjoyed my trips to the machine shop and many conversations with Doug. I wish him the best in his upcoming retirement. Joseph Nolan and Carlet Altamirano have provided amazing support throughout my time in Berkeley, and I have enjoyed getting to know them both. I was fortunate to work with several talented undergraduate students: Andrew Wang, Amber Walton, and Michael Rivas Valadez. The have taught me more than they likely know and are well on their way to impressive careers in academia and industry.

I would like to thank my qualifying exam committee: Prof. Bryan McCloskey, Prof. Jeff Long, Prof. Kranthi Mandadapu, and Prof. Gerd Ceder. The provided a rigorous exam experience which gave me fresh motivation to tackle my research questions with care. I am grateful that Bryan and Gerd have served on this thesis committee. Bryan, in particular, has provided helpful feedback throughout my graduate school education.

Grad school can be stressful at times, but it helps when you have great friends to work through it together. The most lasting memories of grad school will be from the many social events and impromptu evenings spent at our favorite bars around Berkeley. I would like to thank my

housemates throughout grad school, Darwin Yang, Ari Fischer, Eric McShane, and David Gardner, for all the good times and making the painful parts less painful. My graduate school experience would have been far less enjoyable without them and the many other friends I have made in my time here. Finally, Dylan Clark, Cam Doe, and Eli Brown are like brothers to me, and we have been through a lot together over the last ten years. I hope they are proud of what I have accomplished in graduate school; it would have been a much greater challenge without their support.

Lastly, and most importantly, I must thank my family for supporting me in this pursuit. Anthony, Matt, and Kim have served as role models to me my whole life. They are now starting or have their own families, and I am thankful for the endless joy that brings me. Dom is my first call when I need help or advice, and he is my best friend. He has made it easier to live 3,000 miles from home. I am so very proud of the strong and capable women that Gianna and Olivia have become, doing so much growing up over the last five years. I somehow feel closer to them now, despite the distance. All of my siblings continue to make me a proud brother. Auntie, thank you for being the rock we all hang on to.

I have written this thesis in memory of my father, Tony. He taught me the meaning of hard work and not to cut corners. He put family before all else and worked hard to give seven kids a start in life that I am proud to say we have all taken advantage of. He was the strongest man I have ever met, and I am lucky if I have inherited a fraction of that strength.

This thesis is dedicated to my mother, Donna, who deserves more credit for this work than she is probably willing to accept. Her strength and dedication to our family has served me well throughout my life. I would not be here without her encouragement to pursue my craziest dreams, even when it takes me far from home. Thank you, Ma.

FUNDING ACKNOWLEDGEMENT

This work was supported by the Assistant Secretary for Energy Efficiency and Renewable Energy, Vehicle Technologies Office, under the Advanced Battery Materials Research (BMR) Program, of the U.S. Department of Energy under Contract No. DE-AC02-05CH11231. Additional funding support was provided by the Joint Center for Energy Storage Research (JCESR), an Energy Innovation Hub funded by the U.S. Department of Energy, Office of Science, Basic Energy Sciences. Some of this research was completed at the Stanford Synchrotron Radiation Light Source, a user facility at SLAC National Accelerator Laboratory, was supported by the U.S. Department of Energy, Office of Science, Office of Basic Energy Sciences under Contract No. DE-AC02-76SF00515. Additional work used beamline 7.3.3 of the Advanced Light Source, which is a DOE Office of Science User Facility under contract no. DE-AC02-05CH11231. Work at the Molecular Foundry was supported by the Office of Science, Office of Basic Energy Sciences, of the U.S. Department of Energy under Contract No. DE-AC02-05CH11231.

1. Introduction

1.1 Motivation

The demand for reliable energy storage has grown over the last few decades for several reasons: increasing dependence on portable electronics, a shift towards intermittent renewable energy sources such as wind and solar, the emerging dominance of electric vehicles, and interest in alternative mobility options such as electric bikes, scooters, and skateboards. Batteries have emerged as a key enabler for many of these technologies, and batteries themselves are a popular area for research and development. While other energy storage systems such as pumped hydro, compressed air storage, fly wheels, and fuel cells are competitive technologies for many applications, recent investments in large scale manufacturing of lithium-ion batteries have indicated that rechargeable batteries will be a relevant technology for the foreseeable future.[1]

A battery converts chemical potential energy into electrical energy by forcing the electrons involved in the chemical conversion through an electrical circuit. There are three main components to a battery: the anode, cathode, and electrolyte. The chemical mechanism that allows a battery to charge and discharge varies between battery chemistries. Broadly speaking, during battery discharge oxidation occurs at the anode, sending electrons around an external circuit. The electrons are consumed at the same rate at the cathode, where reduction occurs. The electrolyte facilities the passage of ionic current from the anode to the cathode, while being electrically insulating. Charging occurs by the opposite process: oxidation occurs at the cathode, and ionic current is passed from the cathode to the anode where reduction occurs. From a technical standpoint, the term ‘anode’ and ‘cathode’ describe the electrode where oxidation and reduction occur, respectively. For rechargeable batteries, it is common to define the anode and cathode based on the discharge processes and use the designation for both charge and discharge. Batteries which are designed to be discharged once and then discarded are known as primary batteries. Batteries which can be charged and discharged multiple times are known as secondary batteries. The purpose of this thesis is to characterize the mechanisms of ion transport through electrolytes designed for next-generation secondary batteries.

1.2 Lithium-ion Batteries

A typical lithium-ion battery is shown schematically in Fig. 1.1a. Graphite anode particles are separated from transition metal oxide cathode particles by a polypropylene separator. The separator serves to physically separate the electrodes and prevent a short circuit.[2] All three components are wetted by an electrolyte which facilitates the transportation of ions between the electrodes. Commercial lithium-ion batteries are based on a lithium salt (*e.g.*, lithium hexafluorophosphate, $LiPF_6$) dissolved in a mixture of ethylene carbonate (EC) and dimethyl carbonate (DMC). A variety of transition metal oxide cathode materials may be used.[3] Lithium cobalt oxide (LCO) serves as one example, which produces a cell with a nominal voltage of 3.6 V when paired with a graphite anode.[4] Both graphite and LCO operate through a lithium intercalation mechanism. Lithium-ion batteries have achieved huge commercial success due to the high-power

density relative to other battery technologies (a lead acid battery, for example, operates at a nominal voltage of 2 V) and development of cells which can achieve thousands of cycles with minimal decay in performance.[5]

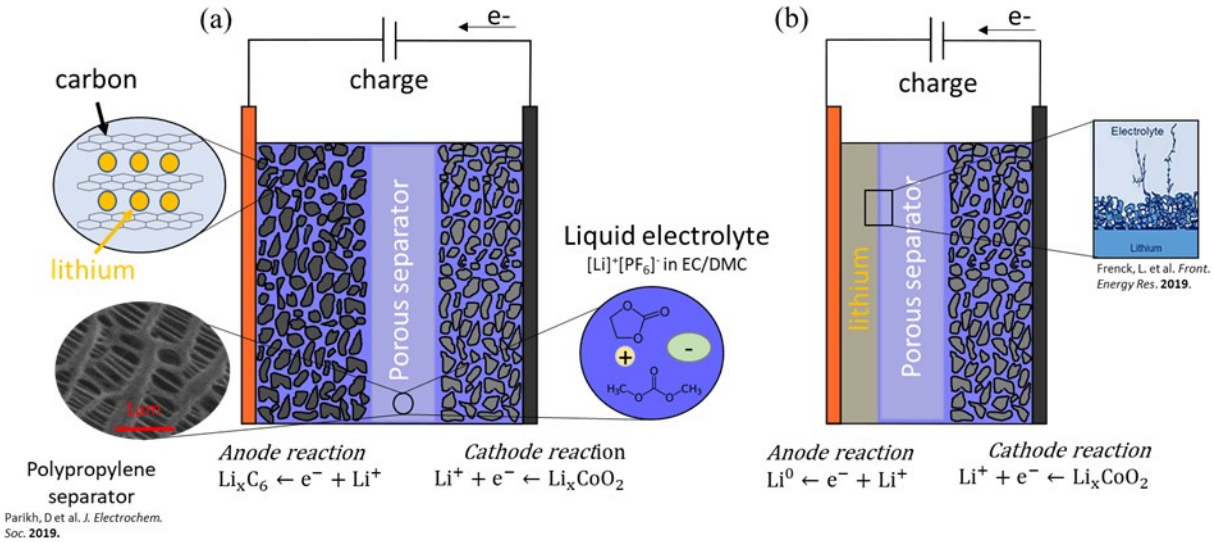

Figure 1.1. Schematic of a lithium-ion and lithium metal battery. (a) A lithium-ion battery which comprises a graphite anode, lithium cobalt oxide (LCO) cathode, polypropylene separator, and liquid electrolyte. SEM image of the polypropylene separator was taken from ref [6]. A cartoon image of lithium intercalated into graphite is shown. (b) A lithium metal battery which comprises lithium metal plated on a copper current collector with the remaining components identical to the lithium-ion battery. In this configuration, lithium deposition during charging is typically unstable, resulting in the formation of dendrites which can result in a short circuit of the battery. A cartoon representation of the dendritic structure which are typical of lithium metal deposited through a liquid electrolyte was taken from ref [7]. The electrode reactions for the charging process are shown below each electrode in (a) and (b). We use the convention of defining the "anode" and "cathode" based on the discharge reactions at each electrode.

1.3 Lithium Metal Batteries

A graphite anode requires six carbon atoms to intercalate one lithium ion, as shown in Fig. 1.1a. A more energy dense solution is to plate lithium metal directly onto a copper current collector, thus eliminating the need for a carbon-based anode.[8] The lithium metal anode has a theoretical specific capacity of 3.86 Ah g^{-1} compared to 0.372 Ah g^{-1} for graphite[9,10]. A schematic of a lithium metal battery is shown in Fig. 1.1b where the graphite anode in Fig. 1.1a is replaced with a lithium metal anode. The main limitation of this approach is that unstable lithium deposition results in the formation of branched structures, called dendrites, which can grow during charging and short circuit the cell, resulting in catastrophic failure.[7,9] Overcoming this limitation has been an intense research focus over the last two decades.

Several strategies have been employed in attempt to enable commercial success of the lithium metal battery, including liquid electrolyte additives,[11] interfacial engineering,[12] and implementing rigid solid electrolytes.[13] For the latter, there are generally two classes of materials which have been studied: polymer and ceramic electrolytes. In theoretical study, Monroe and

Newman showed in 2005 that using an electrolyte with a shear modulus twice that of lithium metal would mechanically suppress the formation of lithium dendrites during charging.[14] Ceramic electrolytes meet this condition yet still suffer from dendritic failure due to other mechanisms involving propagation of lithium metal through defects.[15,16] For polymer electrolytes, this conclusion poses a significant challenge: in general, polymer materials become less conductive as they become more rigid. We are thus motivated to study polymer electrolytes which overcome this barrier.

1.4 Polymer Electrolytes

In 1973, Fenton, Parker, and Wright demonstrated that alkali metal salts were soluble in poly(ethylene oxide) (PEO).[17] Since then, there has been significant interest in studying polymer/salt mixtures as electrolytes for secondary batteries. The ability of PEO to solvate lithium salts derives from the formation of helical complexes where six ether oxygens stabilize the alkali cation.[18] Of particular interest for lithium-ion batteries, lithium salts are highly soluble in PEO, and the resulting electrolytes have ionic conductivities on the order of 10^{-3} S cm^{-1} at temperatures above the crystalline melting temperature of the polymer (~60 °C).[19] The development of polymer electrolytes which exceed this ionic conductivity is a worthy research goal, however it has proven a difficult task. In addition to the goal of enabling the lithium metal anode, polymer electrolytes are typically far less flammable than their volatile organic liquid counterparts, and offer improved safety over the current state of the art. For applications such as electric vehicles that require large numbers of lithium-ion cells, complicated thermal management systems are required to avoid thermal runaway and catastrophic failure. Implementation of non-flammable polymer electrolytes may significantly reduce the need for such auxiliary systems which further improves the practical energy density of the system.

Unfortunately, PEO is a liquid at practical operating temperatures with shear modulus far below the threshold proposed by Monroe and Newman.[20] One strategy to overcome this is to use PEO-containing block copolymers. Block copolymers are a class of materials which combine two or more chemically distinct polymers through one or more chemical bond.[21] Due to enthalpic and entropic interactions, ordered nanostructures form by which the mechanical and ion conducting properties are decoupled.[22] The nature of these microstructures has been well studied in the literature for a variety of systems.[23–29] Polystyrene-block-polyethylene oxide (SEO) is a system of interest for battery applications where the polystyrene (PS) block provides mechanical stability while PEO serves as the ion conducting block. The most common salt used in PEO-based electrolytes is lithium bis(trifluoromethanesulfonyl)imide (LiTFSI). The chemical structure of SEO and LiTFSI are provided in Fig. 1.2a. It has been demonstrated that SEO/LiTFSI electrolytes can operate in a secondary battery configuration and offers resistance to dendrite growth.[30–32] A schematic of an SEO-based rechargeable battery is presented in Fig. 1.2b. SEO/LiTFSI electrolytes can form a variety of structures (including spherical, cylindrical, and co-continuous), however the lamellar morphology is most commonly studied, and arguably the best-suited for battery applications.[33] Figure 1.2b illustrates a block copolymer electrolyte comprising randomly oriented grains of the lamellar morphology. The domains are characterized by the conducting phase volume fraction, ϕ_c, and the distance between the center of two lamellae of the same

component, *i.e.*, the domain spacing, d. The commercial success of such a battery configuration relies on: 1) stable deposition of lithium through the block copolymer electrolyte membrane, 2) repeated cycling of the cell with minimal loss in capacity (thousands of cycles), 3) facile manufacturing, 4) compatibility with high voltage cathodes, and 5) ability to sustain fast charge and discharge rates.

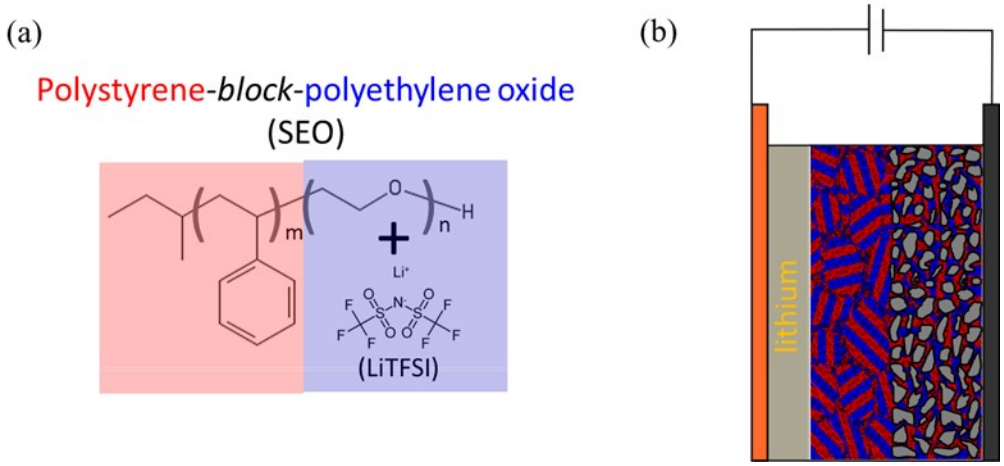

Figure 1.2. Chemical structure of polystyrene-block-polyethylene oxide (SEO) and a schematic of a lithium metal battery with a block copolymer electrolyte. (a) Chemical structure of SEO and lithium bis(trifluoromethanesulfonyl)imide (LiTFSI). Throughout this dissertation, red domains are indicative of a polystyrene (PS) phase and blue domains are indicative of the conducting poly(ethylene oxide)/LiTFSI phase. (b) Schematic of a lithium metal battery based on an SEO electrolyte. Several grains are drawn (not to scale) to highlight the point that block copolymer electrolytes are typically comprised of many randomly oriented grains.

Block copolymer electrolytes are formed by dissolving the block copolymer and salt in solvent, and then removing the solvent either by freeze-drying or evaporation. The processing conditions and thermal history is strongly correlated to the size of the grains depicted in Fig. 1.2b.[34] When the membrane is formed, the salt uniformly fills the PEO domains. (On the length scale of a single lamella, salt may be distributed differently near the center of the domain versus near the interfaces.)[35,36] Both the grain size and d depend on the salt concentration of the electrolyte, as discussed in ref [37] and Chapters 6 and 7. In Chapters 2 and 3, we discuss the formation of salt concentration gradients which develop along the axis perpendicular to the electrodes during battery operation. To briefly summarize, the magnitude of the salt concentration gradient increases with increasing current density. In a liquid electrolyte, the solvent molecules can rearrange easily to accommodate the salt concentration gradient. Prior to this work, few publications have addressed how this process occurs in solid electrolytes.[38] Our goal is understand the mechanisms by which block copolymer electrolytes facilitate the passage of ionic current at high current densities by studying their electrochemical and structural properties.

1.5 Small Angle X-ray Scattering

X-ray scattering techniques characterize the structure of a sample by analyzing diffraction patterns in reciprocal space. When a sample is irradiated with an X-ray beam, some of the photons interact with the electrons in the sample and are scattered. Two-dimensional (2D) detectors are used to measure the intensity of the scattered photons. Contrast arises from differences in electron density, and the length scale which is probed depends on the values of the scattering vector, q, which are accessible based on the experiment geometry. q is related to wavelength of the incident X-ray beam, λ, and the scattering angle, θ, by:

$$q = \frac{4\pi}{\lambda} sin\frac{\theta}{2}. \tag{1.1}$$

Thus, the length scales probed in a scattering experiment depend on the wavelength of the incident X-ray beam and the scattering angles which can be resolved by the detector. The later depends on the detector pixel size and the distance between the sample and the detector. Small angle X-ray scattering (SAXS) accesses small scattering angles by leveraging relatively large sample-to-detector distances, typically on the order of 3 m and probes length scales of 2-100 nm in the sample. A schematic of a typical SAXS experiment is presented in Fig. 1.3a. A sample is irradiated with a monochromatic X-ray beam (λ = 1.24 Å or 1.03 Å were used in this work). The majority of the beam is transmitted through the sample and blocked by a beam stop to avoid damaging the detector. The intensity of scattered X-rays is measured by the detector at an angle, θ, relative to the incident beam. The scattering pattern is then analyzed to extract real-space information from the reciprocal-space data. A thorough discussion of X-ray scattering experiments, techniques, and data analysis can be found in Chapter 2 of the thesis by Jacob Thelen, so we direct the reader to that and other references for more details.[39–41]

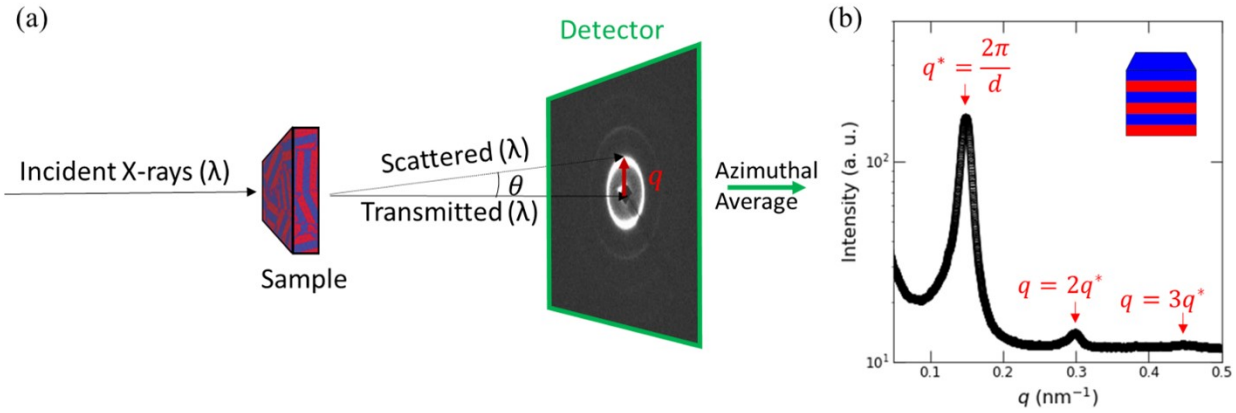

Figure 1.3. Schematic of a small angle X-ray scattering (SAXS) experiment and data reduction. (a) A block copolymer electrolyte comprising randomly oriented lamellar grains is irradiated with a monochromatic X-ray beam. The transmitted beam is block by a beam stop, and the scattered X-ray intensity is measured by a 2D detector. The scattering vector, q, is drawn from the beam center to the location of the primary scattering peak. Increasing brightness on the detector represents increased scattered intensity. (b) Azimuthal averaging of the data results in a 1D intensity versus q plot. A primary scattering peak at $q = q^*$ with reflections at $q = 2q^*$ and $3q^*$ is a signature of the lamellar morphology.

The scattering pattern shown in Fig. 1.1a resulted from a SAXS experiment carried out on lamellar block copolymer sample with a distribution of grain orientations. The result is a ring of scattered intensity. The 2D scattering pattern can then be azimuthally averaged to obtain the scattered intensity versus q, $I(q)$. Analysis of distinct sectors of the detector can be performed to deconvolute information from grains with different orientations in the sample, as discussed in Chapter 7. In Fig. 1.1b, we present a 360° azimuthal average of the 2D scattering pattern. The location of the primary scattering peak, q^*, is related to the domain spacing of the lamellar sample by Brag's law:

$$q^* = \frac{2\pi}{d} \tag{1.2}$$

Higher order peaks in the $I(q)$ data at $q = 2q^*$ and $q = 3q^*$ are characteristic of the lamellar morphology. SAXS provides a tool to characterize the structure of block copolymer electrolytes on the relevant length scale for phase separation. In this dissertation, we use SAXS to probe the morphology of block copolymer electrolytes under inert conditions and during dc polarization experiments.

1.6 Outline of this Dissertation

In Chapter 1, we have motivated the study of block copolymer electrolytes to enable high energy density lithium metal batteries. Our goal is to understand how the nanostructure of a block copolymer electrolyte is related to the electrochemical performance and how the nanostructure evolves in the presence of salt concentration gradients which arise when ionic current passes through the membrane. In Chapter 2, we describe a methodology for evaluating the performance of electrolytes for lithium (or sodium) batteries based on polarization experiments in symmetric cells with two lithium (or sodium) electrodes. We compile data from the literature and show that there is a tradeoff between high ionic conductivity and selectivity of cation transport (characterized by the current fraction, ρ_+). In Chapter 3, we discuss the formation salt concentration gradients when ionic current passes through an electrolyte and how the cation transference number, current fraction, and concentration gradients are interrelated. Our discussion motivates the study of lithium-ion battery electrolytes using cation-blocking electrodes. Next, we dive into the electrochemical characterization of SEO/LiTFSI electrolytes as a function of their morphology in Chapter 4. These measurements serve as the foundation for predicting the spatial dependence of salt concentration as a function of applied current density. Before exploring the structure of block copolymer electrolytes during polarization, we highlight an important phenomenon that is relevant for PEO-containing electrolytes in Chapter 5: dissolution of lithium metal from the electrodes. We show that when PEO is contact with lithium metal at elevated temperatures, lithium species dissolve from the electrode into the bulk of the electrolyte using nuclear magnetic resonance spectroscopy (NMR), electrochemical techniques, and SAXS. Signatures of this process are readily observed in lithium symmetric cells containing an SEO/LiTFSI electrolyte. In Chapters 6 and 7, we use SAXS to study the structure of SEO/LiTFSI electrolytes in the presence of ionic current with temporal and spatial resolution. In Chapter 6, we study a low molecular weight SEO/LiTFSI electrolyte which exhibits phase transitions due to the presence of salt concentration

gradients. Our results indicate the formation of "concentration hotspots" where salt builds up into dense pockets. In Chapter 7, we use a more practical SEO/LiTFSI electrolyte with a longer chain length in similar experiments. Using Newman's concentrated solution theory[42], we use the data presented in Chapter 4 to predict the salt concentration gradients and compare the results to experiment, using d as a proxy for salt concentration. We show that the distortion of the lamellae depends on their orientation relative to the current direction and that the rearrangement of the block copolymer limits the maximum sustainable current which can be passed through the electrolyte. Chapter 8 provides a summary of the work and outlook for future experiments.

This work should appeal to anyone interested in implementing solid electrolytes into next generation batteries. The formation of salt concentration gradients during battery operation is ubiquitous, and the designers of novel electrolyte materials should consider how the material will respond in their presence.

1.7 Nomenclature

Table 1.1 List of symbols and abbreviations

Symbol	Meaning
$\boldsymbol{d}$	domain spacing (nm)
DMC	dimethyl carbonate
EC	ethylene carbonate
LCO	lithium cobalt oxide
$LiPF_6$	lithium hexafluorophosphate
LiTFSI	lithium bis(trifluoromethanesulfonyl)imide
PEO	poly(ethylene oxide)
PS	polystyrene
$\boldsymbol{q}$	scattering vector (nm^{-1})
SEO	polystyrene-block-polyethylene oxide
SAXS	small angle X-ray scattering

Table 1.2 List of symbols (Greek)

Symbol	Meaning
$\boldsymbol{\theta}$	scattering angle
$\boldsymbol{\lambda}$	X-ray wavelength (Å)
$\boldsymbol{\rho_+}$	current fraction

2. Ohm's Law for Ion Conduction in Lithium and Beyond-Lithium Battery Electrolytes*

ABSTRACT

The viability of next generation lithium and beyond-lithium battery technologies hinges on the development of electrolytes with improved performance. Comparing electrolytes is not straightforward, as multiple electrochemical parameters affect the performance of an electrolyte. Additional complications arise due to the formation of concentration gradients in response to dc potentials. We propose a modified version of Ohm's law to analyze current through binary electrolytes driven by a small dc potential. We show that the proportionality constant in Ohm's law is given by the product of the ionic conductivity, κ, and the ratio of currents in the presence (i_{ss}) and absence (i_{Ω}) of concentration gradients, ρ_+. The importance of ρ_+ was recognized by J. Evans, C.A. Vincent, and P.G. Bruce [*Polymer* 28, 2324 (1987)]. The product $\kappa\rho_+$ is used to rank order a collection of electrolytes. Ideally, both κ and ρ_+ should be maximized, but we observe a trade-off between these two parameters, resulting in an upper bound. This trade-off is analogous to the famous Robeson upper bound for permeability and selectivity in gas separation membranes. Designing polymer electrolytes that overcome this trade-off is a worthwhile but ambitious goal.

2.1 Introduction

In a battery, the passage of ionic current between the cathode and anode is enabled by the electrolyte. The dependence of the current on the potential drop between the electrodes is at the core of battery design and engineering.[42,43] The kind of device that can be powered by a battery is limited by the maximum current that can be passed safely through the electrolyte.

The starting point for understanding the relationship between potential drop and current is Ohm's law. For a simple conductor with one charge carrier, such as a copper wire (Fig. 2.1a), the current density, *i*, is proportional to the potential drop per unit length, $\Delta V/L$, and Ohm's law can be written as:

$$i = \sigma \frac{\Delta V}{L}, \tag{2.1}$$

where σ is the electronic conductivity of the material. All materials are electrically neutral and have at least two charge carriers; the one charge carrier approximation is valid because the compensating copper cations are essentially immobile. Current density versus $\Delta V/L$ for copper is presented in Fig. 2.1b, where the slope, m, is given by 5.8×10^5 S cm^{-1}.[44] In this case, $m = \sigma$. For a copper wire, carrier concentration gradients do not develop as the copper cations are stationary and charge neutrality is maintained.

* Adapted (with permission) from Galluzzo, M. D.; Maslyn, J. A.; Shah, D. B.; Balsara, N. P. Ohm's Law for Ion Conduction in Lithium and Beyond-Lithium Battery Electrolytes. *J. Chem. Phys.* **2019**. *151* (2), 020901.

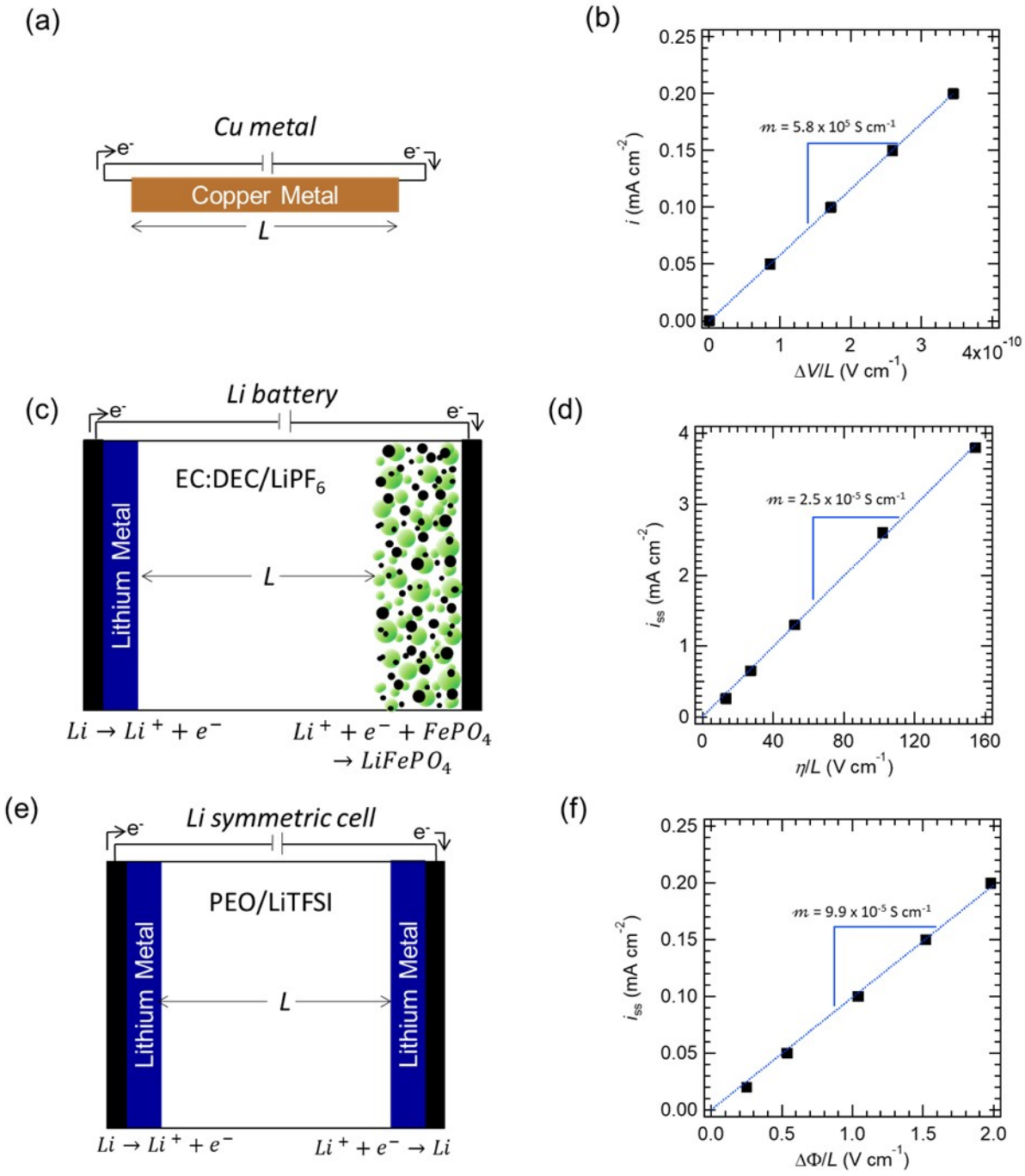

Figure 2.1. Empirical relationship between current density and normalized potential drop across three types of cells. a) Schematic of a piece of copper metal, which is an electronic conductor. b) Current density, i, as a function of normalized voltage drop, $\Delta V/L$, for the copper metal depicted in Fig 2.1a. Adapted from Ref. [44]. c) Schematic of a battery with a lithium metal anode, a lithium iron phosphate cathode, and an EC:DEC/LiPF6 electrolyte. d) Steady-state current density, i_{ss}, as a function of normalized overpotential, η/L, for the battery depicted in Fig. 2.1c. Adapted from Ref.[45]. e) Schematic of a lithium symmetric cell containing a PEO/LiTFSI electrolyte. f) Steady-state current density, i_{ss}, as a function of normalized voltage drop over the electrolyte, $\Delta\Phi/L$, in the cell depicted in Fig. 2.1e. Adapted from Ref.[46]. The difference between values of m obtained in electronic and ionic conductors is ten orders of magnitude.

An example of a rechargeable battery is shown schematically in Fig. 2.1c. It consists of a lithium metal anode and a lithium iron phosphate, $LiFePO_4$, cathode separated by an EC:DEC/$LiPF_6$ electrolyte in a porous separator. During discharge, the passage of ionic current through the electrolyte from the anode to the cathode is driven by an overpotential, η, which is the equilibrium potential of the cell minus the operating voltage, $U^0 - V$.[42] When an overpotential is present, concentration gradients develop across the electrolyte because both cations (in this case, Li^+) and anions (PF_6^-) are mobile in the system. Under a constant overpotential, this would result in a time-dependent current density until the concentration gradient reaches steady-state. Only Li^+ ions are transported across electrode/electrolyte interfaces; this also affects the nature of the gradients. In Fig. 2.1d, we plot the steady-state current density, i_{ss}, as a function of the overpotential per unit length, η/L, for the cell depicted in Fig. 2.1c.[45] It appears that the relationship between i_{ss} and η/L is approximately linear, similar to the copper wire. However, the slope, $\mathcal{m}$ = 2.5 ×10^{-5} S cm^{-1}, is not equal to the conductivity of the electrolyte. It reflects numerous processes that include charge transfer between the electrodes and the electrolyte, diffusion of lithium in the cathode, and diffusion and migration of ions in the electrolyte. Thus, the relationship between i_{ss} and η/L in Fig. 2.1d, although it appears linear, is not a manifestation of Ohm's law.

In Fig. 2.1e, a schematic for a symmetric cell consisting of an electrolyte sandwiched between two identical non-blocking electrodes is presented. In this perspective, we focus on symmetric cells comprising either lithium or sodium foil electrodes and electrolytes containing a lithium or sodium salt, respectively. This cell, popularized by pioneering work of Evans, Vincent, and Bruce, and others,[47–49] is similar to that shown in Fig. 2.1c with one crucial difference: $U^0 = 0\ V$. This cell enables a fair comparison of the ion transport properties of different electrolytes: the symmetry of the cell allows electrode effects to be deconvoluted from the properties of the electrolyte. In Fig. 2.1f, we plot i_{ss} as a function of the potential drop across the electrolyte, $\Delta\Phi/L$, for a cell with lithium foil electrodes and an electrolyte comprising poly(ethylene oxide) (PEO) and bis(trifluoromethylsulfonyl)amine lithium salt (LiTFSI).[46] Here, the slope $\mathcal{m}$ = 9.9 × 10^{-5} S cm^{-1} is not equal to the ionic conductivity of the electrolyte. However, unlike in a full battery, $\mathcal{m}$ is related to the properties of the electrolyte alone. In our effort to design high performance electrolytes, it is the slope in Fig. 2.1f which we wish to maximize. Many publications, however, disregard this. It is fairly common, these days, to invent a new electrolyte, measure the ionic conductivity, and declare victory if it is greater than that of a baseline electrolyte.

The purpose of this perspective is to analyze symmetric cell data obtained from different electrolytes. Evans, Bruce, and Vincent[47,49] and Watanabe et al.,[50] modeled symmetric cells containing dilute and ideal electrolytic solutions. In later studies, Newman and coworkers[42,51] considered symmetric cells containing concentrated electrolytic solutions and developed the relationships between $\mathcal{m}$ and intrinsic transport and thermodynamic properties of the electrolyte. This perspective is focused on small applied potentials wherein the concentration dependence of the relevant electrolyte properties can be neglected. Based on the work in Refs.[46–52], we develop a framework for measuring the Ohm's law coefficient which allows us to produce a rank ordered list of electrolytes based on their ability to maximize the flux of lithium or sodium cations. We conclude by discussing the limitations of our approach as, ultimately, the rank ordering of electrolytes needs to be reassessed in the presence of significant concentration gradients for practical devices.

2.2 Theory

Electrolytes of interest comprise a salt $(M^{z+})_{\nu_+}(X^{z-})_{\nu_-}$ dissolved in a matrix. Characterization of ion transport typically begins with measurement of the ionic conductivity, κ, by ac impedance spectroscopy. A powerful feature of ac impedance spectroscopy is that κ is measured without introducing significant concentration gradients. When a dc potential, $\Delta\Phi$, is applied across an electrolyte of dimension L in a symmetric cell (Fig. 2.1e), there are, by definition, no concentration gradients at the first instant of polarization ($t = 0^+$). The initial current density, i_0, at $t = 0^+$ is given by:

$$i_0 = \kappa \frac{\Delta\Phi}{L}. \tag{2.2}$$

With time, i.e. at $t > 0$, salt concentration gradients develop in the cell and eventually the gradient becomes time-invariant. The measured current density decreases with time as these concentration gradients develop and reaches a steady value at long times. We refer to the current obtained at long times as i_{ss}. In the limit of small applied potentials, an expression for i_{ss} can be derived based on concentrated solution theory,[51,53]

$$i_{ss} = \frac{\kappa}{1 + Ne} \frac{\Delta\Phi}{L}, \tag{2.3}$$

$$Ne = a \frac{\kappa RT(1 - t_+^0)^2}{F^2 Dc} \left(1 + \frac{d\ ln\, \gamma_\pm}{d\ ln\, m}\right), \tag{2.4}$$

where R is the gas constant, T is the temperature, F is Faraday constant, D is the restricted diffusion coefficient of the salt, c is the salt concentration, t_+^0 is the transference number of the cation with respect to the velocity of the solvent, $\gamma_\pm$ is the mean molal activity coefficient of the electrolyte, and m is the salt molality. The parameter a is related to the stoichiometry of the salt:

$$a = \frac{\nu}{(\nu_+ z_+)^2}, \tag{2.5}$$

where ν is the total number of cations and anions to which the salt dissociates, ν_+ is the total number of cations to which the salt dissociates, and z_+ is the charge number of the cation. (For a binary salt, $a = 2$.) Equations 2.3 and 2.4 are based on Newman's concentrated solution theory wherein electrolytes are characterized by three transport parameters, κ, D, and t_+^0, and a thermodynamic factor, $T_{\mathrm{f}} = 1 + \frac{\mathrm{d}\ln\gamma_\pm}{\mathrm{d}\ln m}$. This theory builds on the work of Onsager[54] who recognized that ion transport in binary electrolytes is governed by three Stefan-Maxwell diffusion coefficients, $\mathcal{D}_{0-}$, $\mathcal{D}_{0+}$, and $\mathcal{D}_{+-}$. Relationships between κ, D, and t_+^0, and the Stefan-Maxwell diffusion coefficients are given in Refs [51,55].

While all four parameters (κ, D, t_+^0, and T_{f}) dictate the time-dependent current at a given applied potential, explicit knowledge of all these parameters is not required to determine i_{ss} or Ne. In fact, Ne can be determined in a single experiment by measuring i_0 and i_{ss} at constant dc polarization, $\Delta\Phi$, over the electrolyte:

$$\frac{i_{ss}}{i_0} = \frac{1}{1 + Ne}. \tag{2.6}$$

Bruce and Vincent pioneered the measurement of i_{ss}/i_0.[47,49]

Equations 2.6 and 2.4 can be recast as:

$$\frac{i_{ss}}{i_0} = \frac{\beta + t_+^0}{\beta + 1} \tag{2.7}$$

where

$$\beta = \nu_- \frac{\mathcal{D}_{0+}}{\mathcal{D}_{+-}} \frac{c}{c_0} \tag{2.8}$$

and c_0 is the solvent concentration. Equations 2.7 and 2.8 were first derived by Balsara and Newman.[51] Only in the limit $c \to 0$, $\beta \to 0$ does

$$\frac{i_{ss}}{i_0} = t_+^0, \tag{2.9}$$

a result presented by Bruce and Vincent.[9] Determining the range of concentration over which β is small enough such that Eq. 2.9 is valid requires knowledge of the Stefan-Maxwell diffusion coefficients. For dilute 0.01 M aqueous potassium chloride (Fig. 14.1 of Ref.[42]), $\mathcal{D}_{+-}$= 1.1 x 10^{-7} cm^2 s^{-1}, $\mathcal{D}_{0+}$ = 1.9 x 10^{-5} cm^2 s^{-1}, c_0 = 56 mol L^{-1}, β = 0.031 and Eq. 2.9 is a good approximation. However, most practical electrolytes are not dilute. For a 1 M aqueous potassium chloride solution, $\mathcal{D}_{+-}$= 1.9 x 10^{-6} cm^2 s^{-1}, $\mathcal{D}_{0+}$= 2.0 x 10^{-5}, c_0= 53.6 mol L^{-1}, and β= 0.20. For 2.6 M PEO/LiTFSI (Fig. 3 and 4 of Ref. [55]), $\mathcal{D}_{+-}$= 4.0 x 10^{-9} cm^2 s^{-1}, $\mathcal{D}_{0+}$ = 1.1 x 10^{-8} cm^2 s^{-1}, c_0 = 16 mol L^{-1}, and β = 0.44. Equation 2.9 is not a good approximation for either 1M KCl or 2.6 M PEO/LiTFSI.

We thus define the current ratio, ρ_+, which can be rewritten on the basis of Eq. 2.6 as

$$\rho_+ = \frac{i_{ss}}{i_0} = \frac{1}{1 + Ne}. \tag{2.10}$$

The current ratio is an intrinsic property of an electrolyte, irrespective of whether it is dilute or concentrated. The transference number, t_+^0, is defined as the fraction of current carried by the cation in a solution of uniform salt concentration and is only approximated by ρ_+ when β is small. For this reason, we prefer to use ρ_+ to refer to the current ratio, $\frac{i_{ss}}{i_0}$, rather than using t_+^0 or "the transference number" as is commonly done in the literature. This point was alluded to by Bruce and Gray in 1995, who referred to this current ratio as "the limiting current fraction".[56]

The discussion thus far ignores the resistance of the electrode/electrolyte interface. In practice, when a dc voltage, ΔV, is supplied to a symmetric cell, the potential drop across the electrolyte, $\Delta\Phi$, will be reduced by an amount equal to the product of the interfacial resistance and the current. Assuming other sources of ohmic loss are negligible,

$$\Delta\Phi = \Delta V - iR_i A \tag{2.11}$$

where R_i is the interfacial impedance that is readily measured by ac impedance spectroscopy, A is the electrochemically active surface area of the electrode, and i is the current density through the symmetric cell. We can combine Eq. 2.2, 2.3, 2.10 and 2.11 to obtain a useful expression:

$$\rho_{+,0} = \frac{i_{ss}}{i_0} \frac{\left(\Delta V - i_0 R_{i,0} A\right)}{\left(\Delta V - i_{ss} R_{i,ss} A\right)} \tag{2.12}$$

where i_ss and i_0 refer to steady-state and initial current density through a symmetric cell as in Eq. 2.11. The importance of corrections for interfacial resistance was recognized by Evans, Bruce and

Vincent[47] and Watanabe et al.[50] We use the term $\rho_{+,0}$ in Eq. 2.12 to clarify that this current ratio is based on a measured value of i_0, which we discuss next.

In order to apply Eq. 2.10-2.12, the value of i_0 must be measured. A practical approach is to take the first data point measured after the potential is applied. However, this method is inherently problematic because the current is a strong function of time in the first instant of polarization. An example of such a measurement is shown in Fig. 2.2. A small potential, ΔV = 8.9 mV, was applied across a lithium symmetric cell (A = 0.079 cm^2 and L = 0.050 cm) containing a 35 kg mol^{-1} PEO/LiTFSI electrolyte with salt concentration r = 0.010, where r is defined as the molar ratio of lithium ions to ethylene oxide moieties. A sampling rate of 1 ms^{-1} was used for the first few seconds. Figure 2.2 presents the current response over the entire time window (400 min) required to reach steady-state and the inset highlights the first 10 ms. Over the first 10 ms, the current is approximately constant with time. Thus, we have confidence that the current density we measure, i_0 = 0.051 mA cm^{-2}, truly captures the initial current.

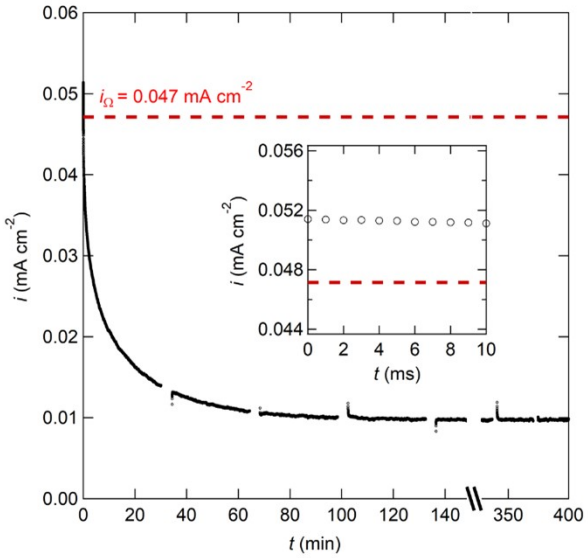

Figure 2.2. Example measurement of the current fraction, ρ_+, in a PEO/LiTFSI electrolyte. A plot of current density versus time in a lithium symmetric cell containing a PEO/LiTFSI electrolyte with r = 0.010 after applying a potential of ΔV = 8.9 mV across the L = 0.050 cm electrolyte. The current response over the entire time window (400 min) required to reach a steady-state is presented as a function of time. (The breaks in the curve are due to ac impedance measurements.) The inset highlights the first 10 ms, when the current is approximately constant with time. The dashed red line represents the value of i_Ω= 0.047 mA cm^{-2} calculated from Eq. 14. The high sampling frequency at early times provides confidence that the measured initial current density is accurate. In this case, the first measurement of current density (i_0 =0.051 mA cm^{-2}) is in reasonable agreement with i_Ω.

An alternative that has been proposed[47,57–60] is to calculate i_0 by combining Eq. 2.2 and 2.11. In this case,

$$i_0 = \kappa \frac{(\Delta V - i_0 R_i A)}{L}. \tag{2.13}$$

We can rearrange Eq. 2.13 to solve for i_0. We refer to this calculated current density as i_Ω because it is a statement of Ohm's law (Eq. 2.1):

$$i_{\Omega} = \frac{\Delta V}{L/\kappa + R_i A}. \quad (2.14)$$

For the electrolyte and cell used in Fig. 2.2, κ = 0.33 mS cm^{-1} and R_i = 495 Ω, yielding i_{Ω} = 0.047 mA cm^{-2} (shown as a red dashed line in Fig. 2.2). We see reasonable agreement between i_0 and i_{Ω} from this experiment. The advantage of using i_{Ω} instead of i_0 is that it is based on parameters that are easily measured (ΔV, L, R_i, κ, and A). Further rationale for this is discussed in Section 2.4. For the purposes of this paper, we define ρ_+ as:

$$\rho_+ = \frac{i_{ss}}{i_{\Omega}} \frac{\left(\Delta V - i_{\Omega} R_{i,0} A\right)}{\left(\Delta V - i_{ss} R_{i,ss} A\right)}. \quad (2.15)$$

Eq. 2.15 differs from Eq. 2.12 only in the use of i_{Ω} for i_0. In the discussion below, electrolytes are characterized by two transport properties, κ and ρ_+. We use Eq. 2.15 to calculate ρ_+.

2.3 Data

To select the systems used in this perspective, we studied the 472 papers which cited Evans, Vincent, and Bruce's 1987 paper titled "Electrochemical measurement of transference numbers in polymer electrolytes"[47] since 2010. Only a small fraction of these papers reported all parameters necessary for our analysis. These parameters are listed in Table 2.1.

Table 2.1. List of parameters related to the Evans, Vincent, and Bruce measurement of i_{ss}/i_0 gathered for the electrolyte systems described in this study. We also list their symbols and descriptions.

Parameter	Symbol	Description
ionic conductivity, blocking	κ_b	ionic conductivity of the electrolyte measured by ac impedance using blocking electrodes (e.g. stainless steel)
ionic conductivity, non-blocking	κ_{nb}	ionic conductivity measured by ac impedance using non-blocking electrodes (e.g. lithium metal)
applied voltage	ΔV	constant voltage applied by the potentiostat in order to elicit a steady-state current density
current density, initial	i_0	initial current density measured after polarization at ΔV
current density, steady-state	i_{ss}	current density measured at steady-state in response to ΔV
interfacial resistance, initial	$R_{i,0}$	interfacial resistance measured by ac impedance spectroscopy just before ΔV is applied
interfacial resistance, steady-state	$R_{i,ss}$	interfacial resistance measured by ac impedance spectroscopy after the steady-state current is reached
bulk resistance	R_b	bulk resistance measured in the cell during the steady-state current experiment

cell thickness	L	distance between electrodes; electrolyte thickness
interfacial area	A	nominal electrode area in contact with the electrolyte

The four categories of electrolytes covered in this study are pictured in Fig. 2.3: homopolymer electrolytes containing a lithium salt and no solvent (HPE), gel polymer electrolytes containing a crosslinked polymer mixed with a solvent and a lithium salt (GPE), polymer electrolytes containing a sodium salt (NaPE), and multicomponent polymer electrolytes containing a polymer mixed with a salt and at least one additional component (MCPE). The additional component in the MCPEs may be another polymer (blended or covalently bonded), an ionic liquid, or a ceramic particle. All of the electrolytes were designed to transport lithium ions except for those placed in the sodium electrolyte category. A long-form description of each electrolyte, its category, and its reference is provided in Table 2.2.

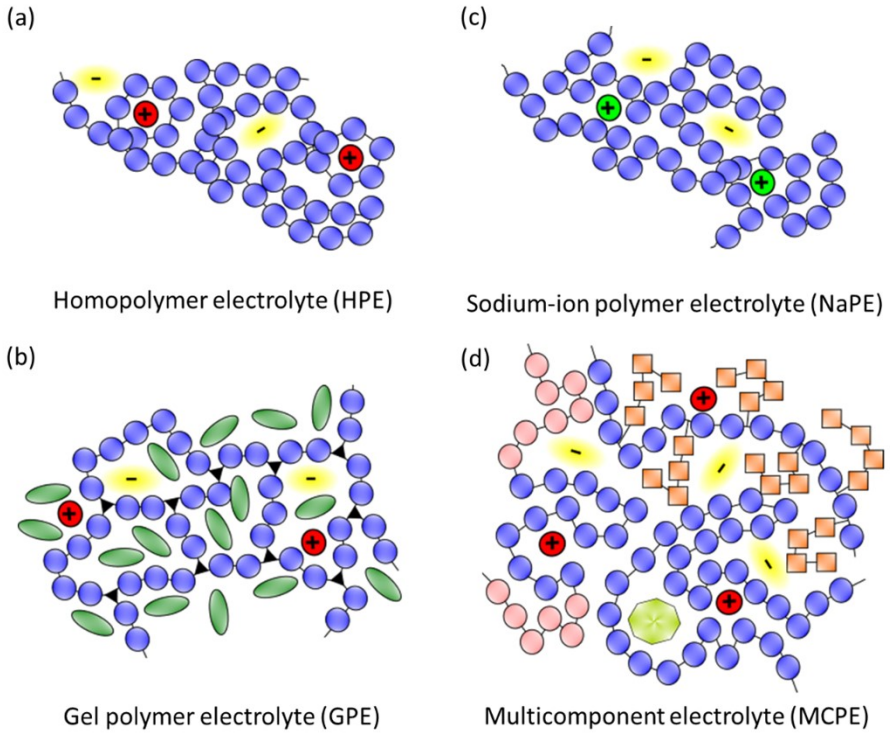

Figure 2.3. Schematics of the four categories of electrolytes analyzed in this chapter. (a) Simple homopolymer electrolytes containing a lithium salt (HPE). Blue spheres represent monomer beads on a polymer chain, red spheres indicate lithium cations, and yellow ovals represent the negative counterion. (b) Gel or crosslinked polymer electrolytes (GPE). Black triangles represent crosslinks in a polymer network and green ovals represent solvent molecules. (c) Polymer electrolytes containing a sodium salt (NaPE). Green spheres represent sodium cations. (d) Multicomponent polymer electrolytes (MCPE). The schematic depicts several types of MCPEs. Pink spheres represent a second monomer type on a copolymer chain, orange cubes represent ionic liquid side chains grafted to a polymer chain, and the green octagon represents a nanoparticle dispersed in the polymer.

Table 2.2. Long-form descriptions of the electrolyte systems analyzed in this chapter and their categories: HPE – homopolymer electrolyte, GPE – gel polymer electrolyte, MCPE – multicomponent polymer electrolyte, NaPE – sodium ion polymer electrolyte.

Electrolyte description	Category	Ref
polyethylene oxide with bis(trifluoromethylsulfonyl)amine lithium salt (PEO/LiTFSI) with 0.017 moles of LiTFSI per mole of ether oxygen ($r = 0.017$)	HPE	[60]
PEO/LiTFSI with $r = 0.08$	HPE	[58]
poly(diethylene oxid-alt-oxymethylene) with LiTFSI (P(2EO-MO)/LiTFSI) with 0.04 moles of LiTFSI per mole of oxygen ($r = 0.04$)	HPE	[61]
P(2EO-MO)/LiTFSI with $r = 0.08$	HPE	[61]
P(2EO-MO)/LiTFSI with $r = 0.14$	HPE	[61]
perfluoroether containing 8 carbon atoms with dimethyl carbonate end groups and bis(fluorosulfonyl)imide lithium salt (C8-DMC/LiFSI) with 5.84 wt% LiFSI	HPE	[62]
C8-DMC/LiFSI with 19.9 wt% LiFSI	HPE	[62]
perfluoropolyether with hydroxyl end groups containing 10 fluoro-ether oxygens ($PFPE_{D10}$-Diol) and 9.1 wt% LiTFSI	HPE	[63]
perfluoropolyether with dimethyl carbonate end groups containing 10 fluoro-ether oxygens ($PFPE_{D10}$-DMC) and 9.1 wt% LiTFSI	HPE	[63]
PEO/LiTFSI gel mixed with tetraethylene glycol dimethyl ether (TEGDME)	GPE	[64]
80 wt% methoxy-PEO-methacrylate and 20 wt% hexadecal-PEO-methacrylate copolymerized into a matrix (PMH20) with $LiClO_4$ salt	GPE	[65]
crosslinked PEO plasticized by TEGDME with LiTFSI	GPE	[66]
PEO/LiTFSI blended with poly[(trifluoromethyl)sulfonyl acrylamide] (PA-LiTFSI)	MCPE	[67]
$Li_7La_3Zr_2O_{12}$ (LLZO) dispersed in poly(vinylidene fluoride-hexa-fluoropropylene) (PVDF-HFP)	MCPE	[68]
polyhedral oligomeric silsesquioxane (POSS) grafted with ionic liquid (IL) side chains doped with LiTFSI	MCPE	[69]
perfluoropolyether with 2 ethylene oxide units on each end terminated with dimethyl carbonate end groups containing 10 fluoro-ether oxygens ($PFPE_{E10}$-DMC) and 9.1 wt% LiTFSI	MCPE	[63]
corn starch crosslinked with γ-(2,3-Epoxypropoxy)propyltrimethoxy-silane with LiTFSI	MCPE	[70]
PEO blended with sodium carboxyl methyl cellulose (Na-CMC) with sodium perchlorate ($NaClO_4$)	NaPE	[71]

organic ionic plastic crystals consisting of triisobutylmethylphosphonium bis(fluorosulfonyl)imide with added bis(fluorosulfonyl)imide sodium salt (NaFSI)	NaPE	[72]

For each electrolyte in Table 2.2, we calculated ρ_+ using Eq. 2.15 and the values of the parameters we obtained from the publication. For some references, all parameters were listed explicitly. In others, we needed to estimate the parameters from raw data such as Nyquist impedance spectra or current versus time plots. In three cases, the parameters needed were supplied in a personal communication from the authors.[58,61,72] Finally, if our calculated value for $\rho_{+,0}$ differed substantially from the reported value (usually referred to by others as t_+), the reference was not included in this study. Only 13 out of the 472 papers satisfied all of the constraints. The most common reason a paper was excluded from our analysis was not reporting L and A. Unfortunately, we could not find any papers which characterized single ion conductors that met all our requirements.

2.4 Characterization of Electrolyte Performance

In most papers, the reported current ratio is based on the measured value of i_0. One criterion for including papers in this study was that all parameters needed to calculate i_Ω from Eq. 2.14 were reported. We were thus able to calculate ρ_+ using Eq. 2.15 and compare it with the reported value, $\rho_{+,0}$, obtained using Eq. 2.12. Figure 2.4 is a plot of ρ_+ versus $\rho_{+,0}$ for the 19 electrolytes listed in Table 2.2. For references that report only ρ_+, we plot $\rho_+ = \rho_{+,0}$: these are represented by filled in symbols. Points which lie on the dashed line in Fig. 2.4 indicate that the measured value of i_0 was consistent with the calculated value of i_Ω. A significant number of data points in Fig. 2.4 fall well below the dashed line. A likely reason for this is the use of a sampling rate that is too slow to capture i_0 accurately. Because the current density falls rapidly at early times (see Fig. 2.2), use of a less frequent sampling rate will result in a lower value of i_0 and thus an inflated value of $\rho_{+,0}$.

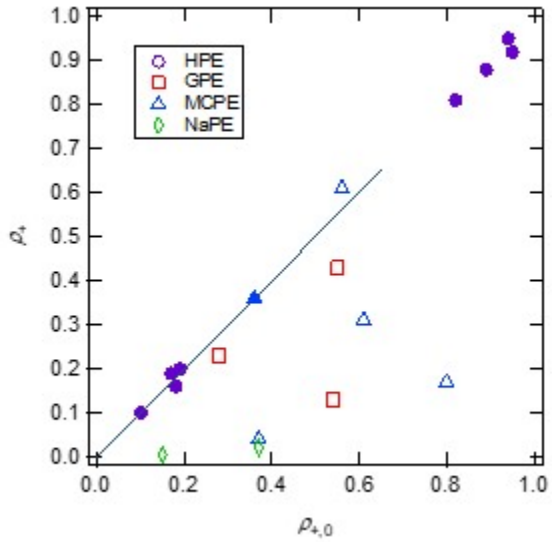

Figure 2.4. Comparison of ρ_+ calculated using different values for the initial current for the electrolytes in Table 2.2. On the vertical axis, ρ_+ is calculated using the initial current from Ohm's law,

i_Ω, as defined in Eq. 15. On the horizontal axis, $\rho_{+,0}$ is calculated using the measured initial current density, i_0, as defined in Eq. 12. The dashed line indicates the case where $i_\Omega = i_0$. For references that report only ρ_+, we plot $\rho_+ = \rho_{+,0}$: these are represented by filled in symbols.

While using i_Ω to calculate ρ_+ has been proposed by some,[47,57–63] the literature is dominated by reports of $\rho_{+,0}$ based on measured values of i_0. Our analysis suggests that ρ_+ is a more robust method for determining the current ratio of an electrolyte. For consistency, all calculations will utilize i_Ω beyond this point.

In principle, the conductivity of an electrolyte measured by ac impedance spectroscopy is a material property that should not depend on the electrodes used in the experiment. Either non-blocking electrodes (lithium or sodium metal), or blocking electrodes (stainless steel, aluminum, etc.) can be used when conducting ac impedance spectroscopy. Conductivities measured using non-blocking or blocking electrodes are denoted κ_{nb} and κ_{b}, respectively. Fig. 2.5 presents κ_{nb}versus κ_{b} for the electrolytes in Table 2.2. For many electrolytes, κ_{nb} is significantly lower than κ_{b}. A few electrolytes show the opposite trend. It is not immediately clear whether κ_{nb} or κ_{b} should be used to quantify the performance of an electrolyte. To answer this question, we rearrange Eq. 2.3 and 2.10 to obtain:

$$\kappa\rho_+ = \frac{i_{ss}}{\Delta\Phi/L}. \tag{2.16}$$

This is a statement of Ohm's law for an electrolyte at steady-state under small polarization, where $\kappa\rho_+$ can be defined as the effective conductivity of the electrolyte at steady-state. In Fig. 2.6a we plot $\kappa_{\mathrm{b}}\rho_+$ versus $\frac{i_{\mathrm{ss}}}{\Delta\Phi/\mathrm{L}}$, while in Fig. 2.6b we plot $\kappa_{\mathrm{nb}}\rho_+$ versus $\frac{i_{ss}}{\Delta\Phi/\mathrm{L}}$. The data in Fig. 2.6b are consistent with Eq. 2.16 while the data in Fig. 2.6a are not. Fig. 2.6 shows that only κ_{nb} can be used to accurately describe the experimental steady-state current. This is because ρ_+ and κ_{nb} are both measured in symmetric cells with non-blocking electrodes. For consistency, as we compare the ρ_+ of electrolytes, we must also use κ_{nb} when evaluating the performance of an electrolyte. Future studies aimed at characterizing new electrolytes should report both κ_{b} and κ_{nb}. For cases where κ_{b} and κ_{nb} differ substantially, attempts should be made to understand the root cause as it may be an indication of electrolyte degradation or inconsistencies in cell fabrication. For ether-based polymer electrolytes, it may be an indication of physical dissolution (i.e. non-electrochemical) of lithium or sodium metal from the electrodes (see Chapter 5).

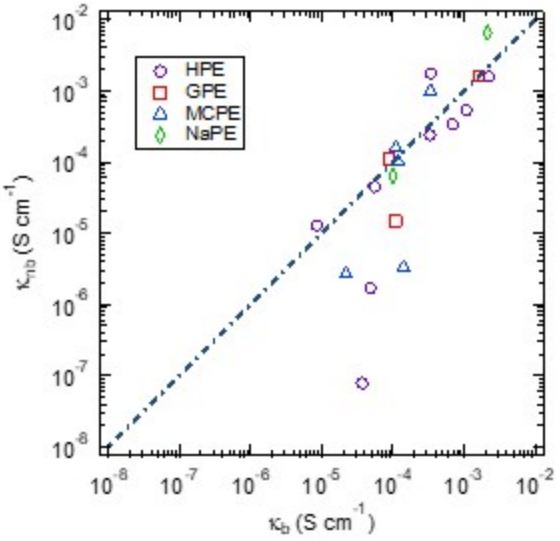

Figure 2.5. Ionic conductivity measured with non-blocking electrodes, κ_{nb}, versus ionic conductivity measured with blocking electrodes, κ_b. The dashed line represents the case where $\kappa_b = \kappa_{nb}$: principally, these two values should be the same.

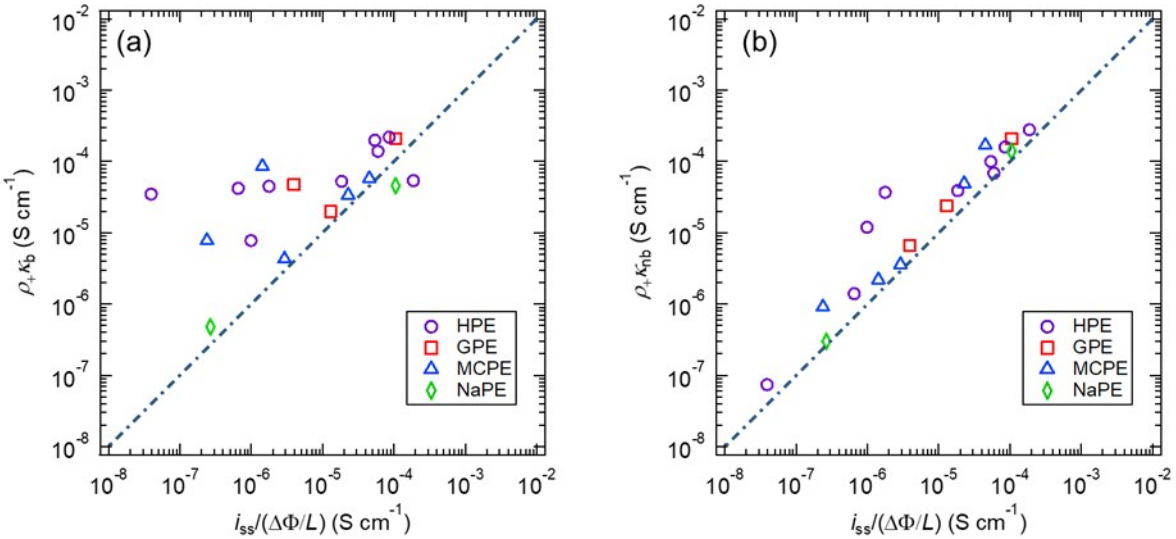

Figure 2.6. The effective conductivity, $\kappa\rho_+$, versus the measured steady-state current normalized by the voltage drop per unit length, $\frac{i_{ss}}{\Delta\Phi/L}$. (a) Plot with $\kappa = \kappa_b$, the conductivity measured with blocking electrodes and (b) Plot with $\kappa = \kappa_{nb}$, the conductivity measured with non-blocking electrodes. The dashed line represents Eq. 2.16, a statement of Ohm's law for electrolytes under dc polarization at steady-state. Only $\kappa_{nb}\rho_+$ data are reasonably consistent with Ohm's law. Rank ordering of electrolytes is thus based on $\kappa_{nb}\rho_+$.

2.5 Trade-off Between Conductivity and Selective Cation Transport

In an electrolyte, both cations and anions are mobile, but our main interest is to maximize the flux of the working cation. This is similar to a gas separation process wherein a membrane is used to concentrate a desired species.[73,74] In this process, a pressure gradient is used to drive transport

through the membrane, which is designed such that one species is more permeable. Selective transport in this system is characterized by two parameters: (1) the permeability of species i, P_i, relates the molar flux and driving force ($\Delta P/L$), where ΔP is the pressure drop across a membrane of thickness L, and (2) the selectivity of species i, α_{ij}, which is defined as P_i/P_j where j refers to the other species being transported. Ideally, one would like to maximize both P_i and α_{ij}. The difficulty of realizing this ideal was noted by Robeson, who showed that membranes with high permeability typically had low selectivity while membranes with high selectivity had low permeability.[75] When data from a large number of membranes were compiled on a plot of selectivity versus permeability, a clear upper bound was evident. Robeson presented a straight line on a log-log plot of selectivity versus permeability such that all compiled data lay below this line. This is referred to as the Robeson upper bound for gas separation.

We present a similar analysis for ion transport in polymer electrolytes under a small dc potential. Selective transport in this system is characterized by two parameters: (1) the conductivity, κ, relates the total current, with contributions from both ions, and driving force ($\Delta\Phi/L$), and (2) the current ratio, ρ_+, which is a measure of selectivity for cation transport. Ideally, one would like to maximize κ and ρ_+.[76–78] In Fig. 2.7, we plot ρ_+ versus κ_{nb} for the electrolytes in Table 2.2. The line in Fig. 2.7 is analogous to the Robeson upper bound. The upper bound is defined empirically by $\rho_+ = -0.64 - 0.34 \log \kappa_{nb}$, where κ_{nb} is in S cm^{-1} and ρ_+ is bounded between 0 and 1.

The best electrolyte would be one that supports the highest steady-state current density for a given applied potential, i.e. maximizing the slope in Fig. 2.1f, $m = \kappa_{nb}\rho_+$. Since both parameters have been calculated, we can rank order the electrolytes of interest. This is done in Table 2.3, where the third column gives the product $\kappa_{nb}\rho_+$. For completeness, we also give values of κ_b, κ_{nb}, Ne, ρ_+, and t_+^0 (when known). The top six electrolytes are identified by their rank in Fig. 2.7. Interestingly, ρ_+ is less than or equal to 0.2 for all six. In other words, the best electrolytes to date rely on high ionic conductivity rather than selective transport of cations, and efforts to achieve a value of ρ_+ closer to 1 have come at the cost of a disproportionate reduction in ionic conductivity. Considerable research has focused on surpassing the Robeson upper bound because there is no physical reason that a membrane cannot surpass it. The same is true for polymer electrolytes: future research aimed at surpassing the upper bound presented in Fig. 2.7 seems warranted.

While our analysis focuses on the bulk properties of the electrolyte, we recognize the importance of the electrolyte/electrode interface. Both interfacial resistance and the stability of the electrolyte/electrode interface contribute to the efficacy of an electrolyte in a battery. Our approach accounts for interfacial resistance (Eq. 2.11-2.15). The rank ordering of electrolytes is, however, based on bulk properties alone.

Table 2.3. Rank ordered list of electrolytes included in this study, in order of largest to smallest $\kappa_{nb}\rho_+$. The top-ranked electrolyte is the most efficacious. Rank, electrolyte description, effective conductivity at steady-state ($\kappa_{nb}\rho_+$), blocking electrode conductivity (κ_b), non-blocking electrode conductivity (κ_{nb}), Newman number (Ne), current ratio (ρ_+), transference number t_+^0 (when known), category, and reference are presented for each electrolyte. All calculated parameters are taken from the reference by methods described in Section 2.3.

Rank	Electrolyte (Ref)	$\kappa_{nb}\rho_+$ [mS/cm]	κ_b [mS/cm]	κ_{nb} [mS/cm]	Ne	ρ_+	t_+^0	Category
1	PEO/LiTFSI with r = 0.017 [60]	0.28	0.34	1.8	5.4	0.16		HPE

2	PEO/LiTFSI gel mixed with TEGDME [64]	0.21	1.6	1.6	6.8	0.13		GPE
3	Crosslinked cornstarch with LiTFSI [70]	0.17	0.34	1.0	4.9	0.17		MCPE
4	PEO/LiTFSI with r = 0.08 [58]	0.16	2.2	1.58	9.07	0.10	0.43	HPE
5	Organic ionic plastic crystals with NaFSI [72]	0.14	2.1	6.6	45	2.2×10^{-2}		NaPE
6	P(2EO-MO)/LiTFSI with *r* = 0.08 [61]	0.10	1.1	0.54	4.3	0.19		HPE
7	P(2EO-MO)/LiTFSI with *r* = 0.04 [61]	6.9×10^{-2}	0.69	0.34	3.9	0.20		HPE
8	LLZO dispersed in PVDF-HFP [68]	4.9×10^{-2}	0.11	0.16	2.3	0.31		MCPE
9	P(2EO-MO)/LiTFSI with *r* = 0.14 [61]	3.9×10^{-2}	0.33	0.24	5.2	0.16		HPE
10	C8-DMC with 19.9 wt% LiFSI [62,79]	3.7×10^{-2}	5.5×10^{-2}	4.5×10^{-2}	0.23	0.81	-0.07	HPE
11	PMH20/$LiClO_4$ [65]	2.4×10^{-2}	8.9×10^{-2}	0.11	3.4	0.23		GPE
12	C8-DMC with 5.84 wt% LiFSI [62,79]	1.2×10^{-2}	8.5×10^{-3}	1.3×10^{-2}	9.0×10^{-2}	0.92	-0.97	HPE
13	Crosslinked PEO/LiTFSI with TEGDME [66]	6.7E-03	0.110	1.5×10^{-2}	1.3	0.43		GPE
14	POSS with IL side chains and LiTFSI [68]	3.6×10^{-3}	0.120	0.10	27	4.0×10^{-2}		MCPE
15	PEO/LiTFSI blended with PA-LiTFSI [67]	2.2×10^{-3}	0.141	3.3×10^{-3}	0.64	0.61		MCPE
16	$PFPE_{D10}$-DMC with 9.1 wt% LiTFSI [63]	1.4×10^{-3}	4.8×10^{-2}	1.7×10^{-3}	0.14	0.88		MCPE
17	$PFPE_{E10}$-DMC with 9.1 wt% LiTFSI [63]	9.1×10^{-4}	2.2×10^{-2}	2.7×10^{-3}	1.8	0.36		MCPE
18	PEO/Na-CMC blend with $NaClO_4$ [71]	3.0×10^{-4}	0.10	6.5×10^{-2}	210	4.8×10^{-3}		NaPE
19	$PFPE_{D10}$-Diol with 9.1 wt% LiTFSI [63]	7.4×10^{-5}	3.70×10^{-2}	7.9×10^{-5}	5.0×10^{-2}	0.95		MCPE

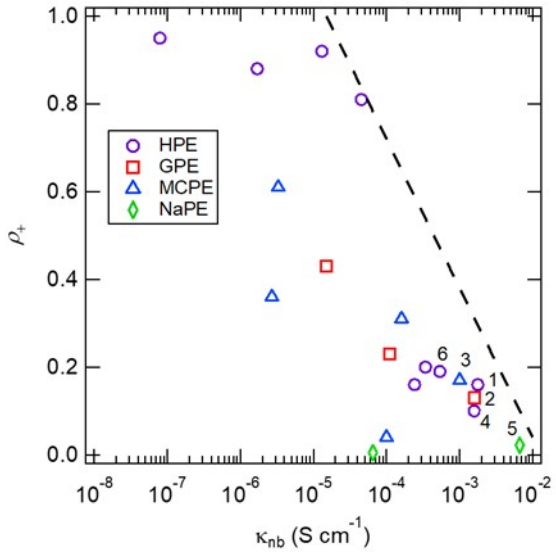

Figure 2.7. Plot of ρ_+ versus κ_{nb} for the electrolytes in Table 2.2. The dashed line is analogous to the Robeson upper bound in gas separation membranes, here defined by $\rho_+ = -0.64 - 0.34 \log \kappa_{nb}$, where κ_{nb} is in S cm^{-1} and ρ_+ is bounded between 0 and 1. The six electrolytes with the highest $\kappa_{nb}\rho_+$ in Table 2.3 are identified by their rank.

2.6 Discussion

The relationship between ρ_+ and transport properties of concentrated electrolytes is quantified by Eq. 2.4-2.7. In Table 2.3, there are some electrolytes for which Ne is small (i.e., Ne $\leq$ 0.1), and others for which Ne is large (i.e., Ne $\geq$10). In the limit of small Ne, $\frac{1}{1+\mathrm{Ne}} \approx 1 - \mathrm{Ne}$ and Eq. 2.3 reduces to

$$i_{ss} = \kappa(1 - Ne)\frac{\Delta\Phi}{L}, \tag{2.17}$$

which implies that the effective conductivity of the electrolyte at steady-state is marginally reduced from that at $t = 0^+$ by a factor equal to $(1 - \mathrm{Ne})$. When Ne is large, $1 + \mathrm{Ne} \approx \mathrm{Ne}$ and Eq. 2.3 can be combined with Eq. 2.4 and written as

$$i_{ss} = \frac{F^2 Dc}{aRT(1 - t_+^0)^2 T_f}\frac{\Delta\Phi}{L}. \tag{2.18}$$

The surprising conclusion from Eq. 2.18 is that there is a class of ion conductors for which the relationship between i_{ss} and $\Delta\Phi/L$ is independent of conductivity.

Maximizing ρ_+ is equivalent to minimizing Ne. It is clear from Eq. 2.4 that Ne may be reduced by either reducing κ, reducing $(1\text{-}t_+^0)^2$, reducing T_f, or increasing D. Ultimately, we desire small values of Ne and large values of κ: thus, reducing Ne by reducing κ is not desirable. On the other hand, reducing $(1\text{-}t_+^0)^2$, reducing T_f, or increasing D are desirable routes to increasing ρ_+. There are very few publications where t_+^0, T_f, and D are measured (see also Chapter 4).[43,55,57,79,80] Table 2.3 presents values of t_+^0 in cases where it has been reported. Note that there is little correspondence between ρ_+ and t_+^0.[58] The relationship between ρ_+ and t_+^0 is discussed in further detail in Chapter 3.

Our discussion has been limited to electrolytes under small applied dc potentials. Whether polarizations are large or small, the salt concentration gradients in the cell affect the current-voltage relationship. At large potential gradients obtained in practical batteries (Fig. 2.1c,d), the concentration dependence of κ, D, t_+^0, and T_f, can no longer be ignored, and rank ordering electrolytes would require numerical calculations described in Refs. [46,76].

2.7 Conclusions

Ion transport through a binary battery electrolyte is governed by four concentration dependent parameters: κ, D, t_+^0, and T_f. Under large applied potentials typical of many battery applications, explicit knowledge of these four parameters and their concentration dependence is required to predict the relationship between i and $\Delta\Phi/L$. The problem is simplified for small applied potentials wherein two parameters govern the relationship between i and $\Delta\Phi/L$: κ and ρ_+. Data obtained from symmetric cells with non-blocking electrodes can be used to determine ρ_+ using Eq. 2.14 and 2.15. In principle, κ can be determined using either blocking (κ_b) or non-blocking electrodes (κ_{nb}). Our study of the literature revealed a surprising discrepancy between these two measurements reported in a significant number of publications (see Table 2.3). When a discrepancy was found, κ_{nb} was often significantly lower than κ_b, although a few electrolytes show the opposite trend. While the analysis reported here is based on κ_{nb}, it is likely that practical electrolytes are those wherein the two conductivities are within experimental error, i.e., those that are unaffected by contact with the alkali metal of interest. Our analysis is restricted to publications wherein both κ_{nb} and ρ_+ were rigorously measured. Ideally, both κ_{nb} and ρ_+ should be maximized. However, there appears to be a trade-off between these two parameters, resulting in an upper bound ($\rho_+ = -0.64 - 0.34 \log \kappa_{nb}$, where κ_{nb} is in S cm^{-1}) that is analogous to one exposed by Robeson for the relationship between permeability and selectivity in gas separation membranes. Designing polymer electrolytes to surpass this upper bound may enable next-generation lithium and sodium batteries. In the limit of small applied potentials, the proportionality factor between i and $\Delta\Phi/L$ for binary electrolytes at steady-state is the product $\kappa_{nb}\rho_+$. This relationship is analogous to Ohm's law for electronic conductors. When comparing electrolyte performance, the preferred electrolyte is the one for which $\kappa_{nb}\rho_+$ is maximized. We use this principle to rank order electrolytes. We hope this perspective will serve as a guide for quantifying the efficacy of future electrolyte designs.

2.8 Acknowledgement

This work was supported by the Joint Center for Energy Storage Research (JCESR), an Energy Innovation Hub funded by the U.S. Department of Energy (DOE), Office of Science, Basic Energy Sciences (BES), under Contract No. DEAC02-06CH11357. JAM was supported by a National Science Foundation Graduate Research Fellowship (DGE 2752814). We are grateful to Dr. Danielle Pesko for supplying portions of the data used in this perspective.

2.9 Nomenclature

Table 2.4 List of symbols and abbreviations

Symbol	Meaning
$\boldsymbol{A}$	electrode area (cm^2)

a	salt stoichiometric coefficient
c	salt concentration (mol cm^{-3})
c_0	solvent concentration (mol cm^{-3})
D	restricted diffusion coefficient of the salt (cm^2 s^{-1})
$\mathcal{D}_{0+}$	Stefan-Maxwell diffusion coefficient describing the interactions between the solvent and cation (cm^2 s^{-1})
$\mathcal{D}_{0-}$	Stefan-Maxwell diffusion coefficient describing the interactions between the solvent and anion (cm^2 s^{-1})
$\mathcal{D}_{+-}$	Stefan-Maxwell diffusion coefficient describing the interactions between the cation and anion (cm^2 s^{-1})
F	Faraday constant (96485 C mol^{-1})
i	current density (mA cm^{-2})
i_0	initial current density measured after polarization at ΔV (mA cm^{-2})
i_{ss}	current density measured at steady-state in response to ΔV (mA cm^{-2})
i_Ω	initial current density calculated using Ohm's law at $t = 0^+$, see equation 14 (mA cm^{-2})
L	electrolyte or membrane thickness (cm)
m	slope
m	salt molality (mol kg^{-1})
M	general cation
Ne	Newman number
P_i	permeability of species *i* (mol m^{-1} s^{-1} Pa^{-1})
R	universal gas constant (8.314 J mol^{-1} K^{-1})
r	molar ratio of lithium cations to oxygens in the electrolyte
R_b	bulk resistance of the electrolyte measured by ac impedance spectroscopy (Ω)
R_i	interfacial resistance between electrolyte and non-blocking electrode (Ω)
$R_{i,0}$	interfacial resistance measured by ac impedance spectroscopy just before ΔV is applied (Ω)
$R_{i,ss}$	interfacial resistance measured by ac impedance spectroscopy after the steady-state current is reached (Ω)
T	temperature (K)
T_f	thermodynamic factor
t	time (s)
t_+^0	transference number of the cation with respect to the velocity of the solvent
U^0	battery open circuit potential (V)
V	battery operating voltage (V)
X	general anion
z_+	charge number of cation
z_-	charge number of anion

Table 2.5 List of symbols (Greek)

Symbol	Meaning
$\alpha_{i,j}$	selectivity of species *i* compared to species *j*
β	dimensionless parameter defined by Eq. 8

$\boldsymbol{\gamma_{\pm}}$	mean molal activity coefficient of the electrolyte
$\boldsymbol{\Delta\Phi}$	dc potential drop across an electrolyte, excluding ohmic drop across interfaces (V)
$\boldsymbol{\Delta P}$	pressure drop across a membrane (Pa)
$\boldsymbol{\Delta V}$	dc potential drop across a symmetric cell (V)
$\boldsymbol{\eta}$	overpotential (V)
$\boldsymbol{\kappa}$	ionic conductivity (S cm^{-1})
$\boldsymbol{\kappa_{b}}$	ionic conductivity measured using blocking electrodes (S cm^{-1})
$\boldsymbol{\kappa_{nb}}$	ionic conductivity measured using non-blocking electrodes (S cm^{-1})
$\boldsymbol{\nu}$	total number of ions to which the salt dissociates
$\boldsymbol{\nu_{+}}$	number of cations in the dissociated salt
$\boldsymbol{\nu_{-}}$	number of anions in the dissociated salt
$\boldsymbol{\rho_{+}}$	current ratio obtained using i_{Ω}
$\boldsymbol{\rho_{+,0}}$	current ration obtained using i_0
$\boldsymbol{\sigma}$	electronic conductivity (S cm^{-1})

3. Relationship Between the Transference Number, Current Fraction, and Salt Concentration Gradients

ABSTRACT

Electrolyte performance can be quantified by measuring the product of the ionic conductivity, κ, and the current fraction, ρ_+. While this is a good starting point for rank ordering electrolytes based on their performance, these measurements alone provide minimal insight into the microscopic interactions which govern ion transport. Additional information can be gained by measuring the cation transference number with respect to the solvent velocity, t_+^0. In the limit of dilute electrolytes, $\rho_+ = t_+^0$. For most electrolytes, this is a poor approximation. t_+^0 describes the contribution of the cation and anion fluxes to the current density in the first instant of polarization in a cell of uniform concentration. ρ_+ is the ratio of the current obtained at steady state in a constant polarization experiment to the initial current. Thermodynamics bounds ρ_+ between zero and one while t_+^0 is unbounded by thermodynamics. We describe the formation of salt concentration gradients during a constant polarization experiment and show that there are fundamental differences which arise when $t_+^0 > 1$, $t_+^0 = 1$, $0 < t_+^0 < 1$ and $t_+^0 < 0$. ρ_+ is a function of t_+^0 and we describe their relationship when all other transport parameters are fixed. Importantly, there are two values of t_+^0 which can result in one value of ρ_+ for all cases except when $\rho_+ = 1$ (in this case, $t_+^0 = 1$). The true value of t_+^0 can be determined by measuring the sign of the concentration gradient. We further propose that measuring the current fraction in cells with cation blocking electrodes would be more informative for typical polymer electrolytes than using anion blocking electrodes (*e.g.*, lithium metal), however the materials to do so have not been fully developed to date. We propose a practical cell based on anion exchange membranes which block cations while conducting anions to prove the existence of negative transference numbers in PEO/LiTFSI electrolytes.

3.1 Introduction

In Chapter 2, we analyzed the performance of a series of electrolytes reported on in the literature based on their conductivity, κ, and the current fraction, ρ_+. The product of these two quantities, $\kappa\rho_+$, is a useful measuring stick for evaluating the efficacy of an electrolyte: $\kappa\rho_+$ is the proportionality constant between the potential drop across the electrolyte, $\Delta\Phi$, and the current density at steady state, i_{ss}. From a practical standpoint, measurement of κ and ρ_+ is a good starting point to predict the performance of an electrolyte in a battery. However, there is limited fundamental insight that can be gained from measuring these properties alone. Using Newman's concentrated solution theory as our framework[42], ion transport is governed by $\frac{1}{2}n(n-1)$ independent transport parameters where n is the number of species in the system. In this thesis, we are primarily interested in studying nanostructured block copolymer electrolytes where one

phase conducts ions and the other is ionically insulating but provides mechanical rigidity. For such a system, there are n = 4 component which thus requires six independent parameters to fully characterize the system. In Chapter 4, we assume that we can neglect the insulating phase of the block copolymer (polystyrene, in our case), and treat the system as a three-component system. In Chapter 7, we revisit this assumption and find that it is valid, at least a low to moderate current densities.

The basis of concentrated solution theory is the Stefan-Maxwell diffusion equations, originally derived from the kinetic theory of gases. The gradient in electrochemical potential of species i, $\nabla\mu_i$, is related to the species velocities, $\boldsymbol{v_i}$, by:

$$c_i \nabla \mu_i = RT \sum_j \frac{c_i c_j}{c_T \mathcal{D}_{ij}} (\boldsymbol{v}_j - \boldsymbol{v_i}), \tag{3.1}$$

where c_i is the concentration of species i, R is the gas constant, T is the temperature, and $\mathcal{D}_{ij}$ is a Stefan-Maxwell diffusion coefficient. For a binary electrolyte (n = 3) comprising cations (denoted i = +), anions (i = -), and solvent (i = 0), there are three independent transport parameters: $\mathcal{D}_{+0}$, $\mathcal{D}_{-0}$, and $\mathcal{D}_{+-}$. It is expected, and has been shown experimentally, that these parameters vary with salt concentration.[55] If all $\mathcal{D}_{ij}$'s are known as a function of salt concentration, the theory can be used to predict salt concentration and potential gradients as a function of time and position in a cell under polarization with no adjustable parameters. Experimentally, $\mathcal{D}_{ij}$'s cannot be measured directly, however they can be recast into measurable quantities.[42,51] Ion transport can be fully characterized by the measurement of ionic conductivity, κ, current fraction, ρ_+, salt diffusion coefficient, D, and a thermodynamic quantity related to the change in equilibrium potential of a lithium/electrolyte interface (U) as a function of salt concentration, $\frac{dU}{d\ln m}$ (where m is the salt molality). By measuring this set of transport parameters as a function of salt concentration, we can gain considerable insight into the mechanisms which dictate bulk transport behavior compared to simply measuring the κ and ρ_+.

In this chapter, we are particularly interested in the cation transference number, t_+, and how it relates to microscopic interactions of the molecules which comprise an electrolyte. t_+ is defined as the fraction of current carried by the cation in an electrolyte of uniform concentration. This definition is stated mathematically by Eqn. 1.26 of ref [42]:

$$t_+ = \frac{z_+ F \boldsymbol{N}_+}{\boldsymbol{i}} \tag{3.2}$$

where z_i is the charge number of species i (for LiTFSI which dissociates into Li^+ and $TFSI^-$, z_+ = 1 and z_-= -1), F is Faraday's constant (96485 C mol^{-1}), $\boldsymbol{N}_i$ is the flux of species i, and $\boldsymbol{i}$ is the current density. The current density is defined by:

$$\boldsymbol{i} = \sum_i z_i F \boldsymbol{N}_i \tag{3.3}$$

The anion transference number is defined in the same way as t_+, replacing all '+' with '-' in Eqn. 3.2. It follows from Eqn. 3.2 and 3.3 that the anion transference number, t_-, is related to t_+ by:

$$t_- = 1 - t_+ \tag{3.3}$$

Next, we consider how the transference number relates to the formation of salt concentration gradients when a dc potential is applied across an electrolyte in a cell with anion blocking electrodes (e.g. lithium metal).

3.2 Salt concentration gradients in an electrolyte under polarization

The physical importance of t_+ is demonstrated in Fig. 2.1. Each cell in Fig. 2.1 shows a schematic of a lithium metal anode (left), intercalation cathode (right), and electrolyte (center). The electrolyte consists of a solvent matrix (blue) and salt where yellow circles represent lithium atoms and green circles represent $TFSI^-$ anions. In the electrolyte, lithium has a charge of +1, which is denoted by a '+'. In the cathode, lithium is electrically neutral, so no charge is drawn. When a potential is applied across the cell, cations are driven in the direction of the electric field (shown by a black arrow), and anions are driven in the opposite direction. Figure 2.1a shows the first instant of polarization and the electrolyte is initially spatially uniform in salt concentration. If we choose an arbitrary reference plane, we can count the number of cations and anions which travel through the plane and use this to calculate the current density and t_+. For the purposes of this exercise, we state that each ion drawn represents 0.001 mol of ions, the reference plane has an area of 1 m^2, we count the ions which pass through the plane over the span of 1 s, and the positive x-axis points in the direction of the electric field, from right to left. In this schematic, one cation travels through the plane to the left, so N_+ = 0.001 mol s^{-1} m^{-2}. Two anions travel through the plane to the right, so N_- = -0.002 mol s^{-1} m^{-2}. It follows from Eqn. 3.3 that the current density at time t = 0 is given by i_0 = 3*96485 C s^{-1} m^{-2} = 28.9 mA cm^{-2} where the subscript '0' denotes t = 0. From Eqn. 3.2, it follows that $t_+ = \frac{1}{3}$.

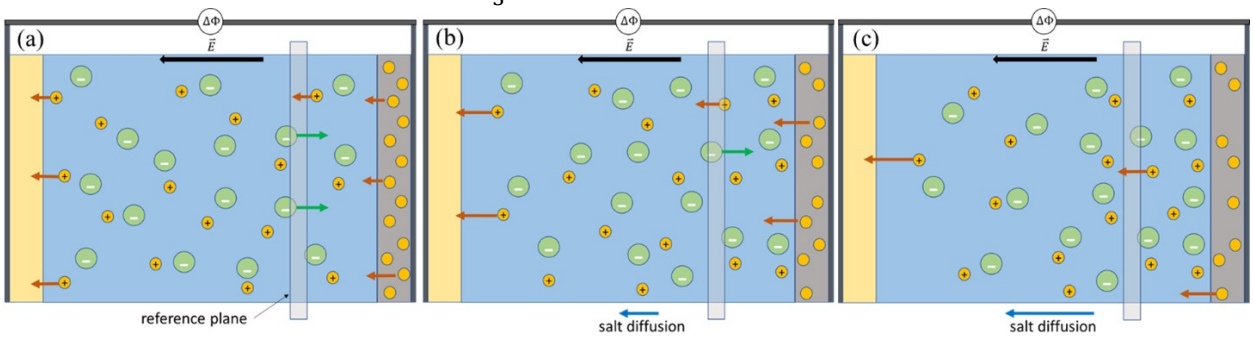

Figure 3.1. Development of salt concentration gradients in a battery electrolyte with $0 < t_+ < 1$. A constant potential, ΔΦ, is applied across the cell, resulting in an electric field pointing from left to right. Yellow circles represent cations and green circles represent anions in solution. (a) Initial moment of polarization. A reference plane is drawn which is used to "count" the ions as they pass and determine the anion and cation contributions to the current density. (b) At later times, a salt concentration gradient begins to form because anions cannot react at the electrodes. There is a diffusive component of the ion fluxes from left to right, which is indicated by the blue arrow. (c) At steady state, the flux of anions to the right due to migration is matched by the diffusive flux down the concentration gradient to the left and the net flux of the anion is zero, and only cations carry current through the reference plane.

The above discussion is based on the first instant of polarization. As polarization continues, salt concentration gradients develop across the cell because the anion cannot react at the electrode

and the solvent remains electrically neutral on length scales larger than a few cubic nanometers, *i.e.*, the number of cations and anions in a region of the cell must be equal. We show this intermediate time in Fig. 3.1b. Migration drives the anions to the right, so there is a buildup of anions near the right electrode and a depletion near the left electrode. Electroneutrality dictates that the anion and cation concentrations must be matched at each position in the cell, so the result is a salt concentration gradient. Note that the total number of ions in the electrolyte phase in Fig. 3.1a, 3.1b, and 3.1c remain constant. The formation of a salt concentration gradients results in a concentration overpotential which increases the total resistance across the electrolyte with time. Thus, with the applied potential remaining constant, i decreases monotonically with time, and $i_1 < i_0$, where the subscript '1' denotes a later time. Because the cell is no longer uniform in salt concentration, Eqn. 3.2 is no longer valid. As the salt concentration gradient develops, diffusion down the salt concentration gradient begins to contribute to the transportation of ions in the system. Both cations and anions will have a component of their flux in the direction from right to left in Fig. 3.1, *i.e.*, down the concentration gradient, represented by the arrow below Fig. 3.1b. At long times, the migratory flux of the anion in the direction opposite the electric field will be matched by the diffusional flux in the direction of the electric field. When this occurs, the concentration gradient becomes independent of time, as shown in Fig. 3c where the net flux of the anion is equal to zero and the current density reaches a steady-state value, i_{ss}, where $i_{ss} < i_1 < i_0$. The current fraction, ρ_+, is given by the ratio i_{ss}/i_0, as defined in Eqn. 2.10.

Thermodynamics places bounds on the value of i_{ss} in a constant polarization experiment: i_{ss} cannot be greater than i_0 and it cannot be less than zero. The system loses entropy in the formation of a salt concentration gradient as more constraints are placed on where the ions can be located. This is a non-spontaneous process and requires work. If the potential applied across the cell (*i.e.,* the work being done on the system) is fixed, the second law of thermodynamics requires that the formation of a salt concentration gradient must be compensated by a reduction in work done by the electrical current (*i.e.*, the current must decrease). A current less than zero would suggest that the Coulombic force acting on an ion in one direction results in momentum in the opposite direction: this forbidden by the first law of thermodynamics. Therefore, ρ_+ is bounded between 0 and 1.

Under certain circumstances (extremely dilute solutions of uncorrelated ions – see Chapter 2), ρ_+ and t_+ are equivalent, as discussed in the context of Eqn. 2.7 through 2.9. In most cases, t_+ and ρ_+ are not equivalent. Importantly, thermodynamics places no bounds on the value of t_+. In this section and the previous chapter, we have introduced the current fraction and the cation transference number while discussing them in the context of an electrolyte under polarization. The purpose of the remainder of this chapter is to discuss the relationship between ρ_+, t_+, and salt concentration gradients. We will consider the implications of t_+ values which are outside of the bounds of 0 and 1.

3.3 Relationship between the transference number and the current fraction

Measurement of the transference number requires us to specify a reference frame, which we have so far neglected to discuss. In Fig. 3.1, our reference plane was stationary relative to the electrodes, which is perhaps the most obvious reference frame to choose. If we could simply count

the ions which move through a stationary reference plane, as we did in our discussion of Fig. 3a, we could easily determine the transference number from a constant polarization experiment. This has not been done in practice. Mathematically, the task of recapitulating the transference number into measurable quantities is more straightforward if we choose a reference frame which moves with the solvent velocity. The cation transference number with respect to the solvent velocity, t_+^0, is related to the Stefan Maxwell diffusion coefficients by:[42]

$$t_+^0 = \frac{z_+ \mathcal{D}_{+0}}{z_+ \mathcal{D}_{+0} - z_- \mathcal{D}_{-0}}. \tag{3.5}$$

Beginning with Eqn. 3.1, we can derive an expression for t_+^0 in terms of measurable quantities for a monovalent salt:

$$t_+^0 = 1 \pm \sqrt{\frac{F^2 Dc}{2\kappa RT}\left(\frac{1}{\rho_+} - 1\right)\Big/\left(\frac{d\, ln\, \gamma \pm}{d\, ln\, m} + 1\right)} \tag{3.6}$$

where $\gamma_\pm$ is the mean molal activity coefficient of the salt. The denominator under the square root in Eqn. 3.6 is often referred to as the "thermodynamic factor (T_f)", and is related to the transport properties by:

$$T_f = \left(\frac{d\, ln\, \gamma \pm}{d\, ln\, m} + 1\right) = -\frac{F}{2RT(1 - t_+^0)}\left(\frac{dU}{d\, ln\, m}\right) \tag{3.7}$$

A complete derivation of Eqn. 3.5 and 3.6, based on refs [42,51], is presented in Appendix 10.1. Equations 3.6 and 3.7 provide a mathematical relationship between t_+^0 and ρ_+, however κ, D, and $\frac{dU}{d \ln m}$ are also independent parameters.

In practice, it is extremely difficult to design electrolytes while independently tuning t_+^0, κ, D and T_f, which makes deconvoluting their relationships to ρ_+ exceedingly difficult. For our purposes, we will leverage the luxury of working with mathematical equations where we can easily hold some parameters constant while varying others, with the goal of better understanding the relationship between t_+^0 and ρ_+. In Figure 3.2, we plot ρ_+ as a function of t_+^0 in the range -2 < t_+< 4 while holding κ, D, T_f and c constant. For the transport parameters we hold constant, we choose their values corresponding to a PEO/LiTFSI electrolyte above the entanglement threshold with a molar ratio of lithium ions to ethylene oxide moieties, r, equal to 0.08 (c = 1.59 x 10^{-3} mol cm^{-3}). This corresponds to κ = 1.60 x 10^{-3} S cm^{-1}, D = 8.76 x 10^{-8} cm^2 s^{-1}, and T_f = 3 based on ref [81].

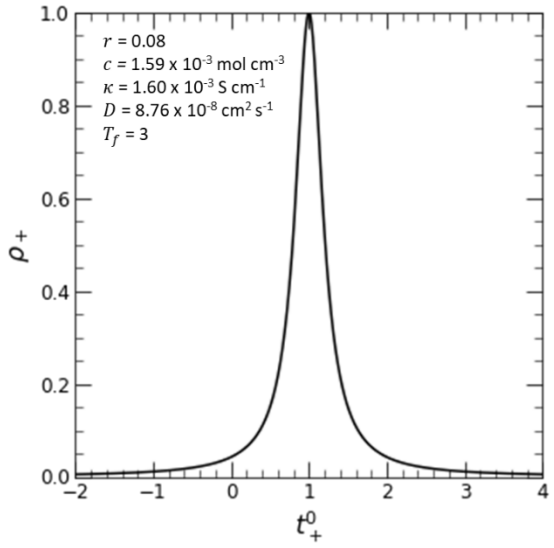

Figure 3.2. Relationship between the current fraction, ρ_+, and transference number, t_+^0, with all other properties fixed, based on measurement in a symmetric cell with anion blocking electrodes. ρ_+ is bounded between zero and one, and for any value of ρ_+ there are two possible values for t_+^0 except $\rho_+ = 1$.

Equation 3.5 is derived for ρ_+ measured in a symmetric cell with anion-blocking electrodes (*e.g.*, lithium metal for electrolytes with a lithium salt or sodium metal for electrolytes with a sodium salt). Based on Eqn. 3.5, we are guaranteed that $\rho_+ = 1$ if $t_+^0 = 1$. When all other parameters are fixed, as in Fig. 3.2, ρ_+ is symmetric about $t_+^0 = 1$. The non-monotonic dependence of ρ_+ on t_+^0 has an important implication: when measuring the current fraction, $\rho_+ = i_{ss}/i_0$, there are two possible values of t_+^0 which yield the same result for all $\rho_+ \neq 1$ (as indicated by the +/- symbol in Eqn. 3.6). For example, if $\rho_+ = 0.10$, the possible values of t_+^0 are 0.37 or 1.63 based on Fig. 3.2. In Fig. 3.1, we discussed a scenario where $0 < t_+^0 < 1$. In Fig. 3.3, we consider the other possibilities and how to distinguish between the two possible values of t_+^0.

A cation transference number of unity implies that the flux of the anion is equal to zero at the first instant of polarization. This is shown schematically in the top cell shown in Fig. 3.3a. Initially, all the current is carried by the cation through the reference plane, unlike the situation in Fig. 3.1 where $t_+^0 = \frac{1}{3}$. Because the cations can react at the electrodes, no concentration gradients develop. Therefore, the salt concentration is independent of both time and position in the cell: this is depicted qualitatively in the plots of c versus position below each schematic in Fig. 3.3a. As a result, the resistance across the electrolyte remains constant throughout the polarization experiment and i is independent of time, as shown in the lower plot in Fig. 3.3a.

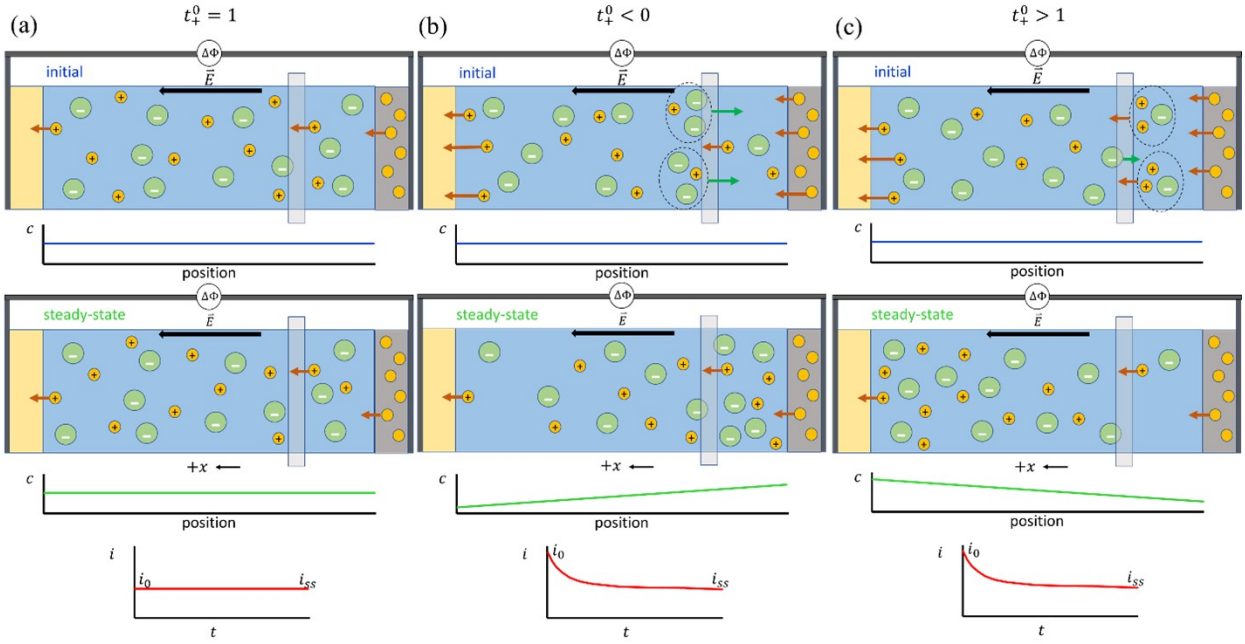

Figure 3.3. Development of salt concentration gradients in electrolytes with different values of t_+^0. In each figure, the top schematic represents the first instant of polarization and the lower schematic represents the steady state condition. Below each schematic, the salt concentration, c, is plotted versus positon in the cell. Initially, the salt concentration is uniform in all three cases. At the bottom of each figure, the current density, i, as a function of time, t, is plotted. The current density at $t = 0$, i_0, and at steady state, i_{ss}, are marked. (a) For $t_+^0 = 1$, concentration gradients do not develop, and the current density is independent of time. (b) For $t_+^0 < 0$, clusters of two anions (identified with dashed circles) drag a cation through the reference plane and the net flux of cations is in the direction opposite the electric field initially. At steady state, a concentration gradient forms with higher c near the positive (right) electrode and lower c near the negative (left) electrode. (c) For $t_+^0 > 1$, clusters of two cations (identified with dashed circles) drag an anion through the reference plane and the net flux of anions is in the direction of the electric field initially. At steady state, a concentration gradient forms in the opposite direction as part (b). In both (b) and (c), the formation of a salt concentration gradient results in a current density which decays with time until reaching a steady state value.

We next consider the case where $t_+^0 < 0$. Based on Eqn. 3.1, a negative cation transference number implies that at the first instant of polarization, the net flux of cations is negative, i.e., the net velocity of cations is initially in the direction opposite the electric field. There have been several examples of negative cation transference numbers reported in the literature based on both experimental and computational results.[43,55,58,79,82–84] It is hypothesized that this is the result of negatively charged clusters of anions and cations which are highly mobile (relative to free cations). This is shown schematically in the top cell in Fig. 3.3b. A dashed circle is drawn around a cluster of two anions and one cation. If the motion of these species is highly correlated, the negatively charged cluster will migrate towards the positive electrode, dragging two anions and one cation through the reference plane to the right. If the number of cations in negatively charged clusters passing through the reference plane to the right outnumber the number of free cations passing through the plane to the left (as shown in Fig. 3.3b), the result is a negative net flux of cations and therefore a negative t_+^0. We conclude from this argument that migration drives cations opposite

the electric field initially. As polarization continues, salt accumulates near the positive electrode and a salt concentration gradient begins to form. As a result, salt will begin to diffuse down the salt concentration gradient from right to left. Eventually, the diffusive flux of cations to the left will outweigh the migratory flux of cations to the right, and the net flux of cations will become positive. Steady state is reached when the diffusive flux of anions to the left matches the migratory flux of anions to the right, identically to Fig. 3.1c and shown schematically in the bottom cell of Fig. 3.3b. The qualitative plot of c versus position at steady state shows an increasing salt concentration from left to right in the cell. So, when measuring the current fraction with anion-blocking electrodes, there is no defining feature marking the change from a positive to negative cation transference number.

There is, however, a definitive signature for $t_+^0 > 1$ compared to $t_+^0 < 1$. Based on Eqn. 3.3, $t_+^0 > 1$ implies $t_-^0 < 0$. Therefore, at the first instant of polarization, the net flux of anions is positive, *i.e.*, the net velocity of anions is initially in the same direction as the electric field, which is unexpected for a negatively charged species. In a similar fashion, we hypothesize that this could occur due to the presence of positively charged clusters of ions which are highly mobile (relative to free anions). This is shown schematically in the top cell of Fig. 3.3c. A dashed circle is drawn around a cluster of two cations and one anion. If the motion of these species is highly correlated, the positively charged cluster will migrate towards the negative electrode, dragging two cations and one anion through the reference plane to the left. If the number of anions in positively charged clusters passing through the reference plane to the left outnumber the number of free anions passing through the plane to the right (as shown in Fig. 3.3c), the result is a positive net flux of anions and therefore a negative t_-^0 and $t_+^0>1$. We conclude from this argument that migration drives anions in the direction of the electric field initially. In this case, as polarization continues, salt accumulates near the negative electrode and therefore salt begins to diffuse down the salt concentration gradient from left to right (opposite to the case of $t_+^0 < 1$). The condition for steady state is the same as before when $t_+^0 < 1$: steady state is achieved when the migratory flux of anions is matched by the diffusive flux. The difference is that the signs have flipped: migration drives anions to the left and diffusion to the right when $t_+^0 > 1$. This is shown schematically in the bottom cell of Fig. 3.3c. The qualitative plot of c versus position at steady state shows a decreasing salt concentration from left to right in the cell.

Through the schematics in Fig. 3.3 we have shown that the defining feature of t_+^0 greater, less than, or equal to one is the direction of the concentration gradient: for $t_+^0 > 1$, $\frac{dc}{dx} > 0$, for $t_+^0 < 1$, $\frac{dc}{dx} < 0$, and for $t_+^0 = 1$, $\frac{dc}{dx} = 0$. (Recall that we defined the x-axis to be perpendicular to the electrodes and pointing in the direction of the electric field, as shown in Fig. 3.3.) We next consider how the sign of the concentration gradient impacts the current density at steady state. For a monovalent salt, the current density in one dimension is given by:[51]

$$i = -\kappa \frac{d\Phi}{dx} + \left[-\frac{\kappa}{F}(-1 + t_+^0) \frac{d\mu_e}{dx} \right] \tag{3.8}$$

where $\frac{d\Phi}{dx}$ is the potential gradient and $\frac{d\mu_e}{dx}$ is the electrochemical potential gradient of the electrolyte. For the purpose of this discussion, we do not need to directly relate $\frac{d\mu_e}{dx}$ and $\frac{dc}{dx}$ but it is

sufficient to say that they will always have the same sign. We use Eqn. 3.8 to describe an experiment where the electric field (and thus $\frac{d\Phi}{dx}$) are held constant. Based on the direction of the electric field relative to the x-axis, the first term on the left side of Eqn. 3.8 is positive. Initially, there are no concentration gradients so the initial current is given by: $i_0 = -\kappa \frac{d\Phi}{dx}$. The second term on the right side of Eqn. 3.8 will always be negative: if $t_+^0 > 1$ (which implies $\frac{d\mu_e}{dx} > 0$), then $\left[-\frac{\kappa}{F}(-1 + t_+^0)\frac{d\mu_e}{dx}\right] < 0$, and if $t_+^0 < 1$ (which implies $\frac{d\mu_e}{dx} < 0$), then $\left[-\frac{\kappa}{F}(-1 + t_+^0)\frac{d\mu_e}{dx}\right] < 0$. We conclude from the above analysis that, regardless of the direction of the salt concentration gradient, the steady state current will always be less than the initial current, as shown in the bottom plots of Fig. 3.3b and 3.3c. This is consistent with the plot of ρ_+ versus t_+^0 in Fig. 3.2 and our discussion of how thermodynamics bounds ρ_+ between zero and one. An important conclusion is that it is undesirable to design an electrolyte with $t_+^0 > 1$. For a fixed κ, the product $\kappa\rho_+$ is maximized when $t_+^0 = 1$. Our analysis has shown that there is a way to differentiate between the two possible values of t_+^0 for a given ρ_+. One must simply measure the sign of the salt concentration gradient. This may be done using a spectroscopic technique such as X-ray absorption spectroscopy (XAS)[85] or Raman microscopy[86,87] (see also Chapter 7) .

3.4 Negative transference numbers

Use of symmetric cells with anion-blocking electrodes to characterize electrolytes for lithium ion (or sodium-ion) batteries is ubiquitous. Our conclusion in the last section was that measurement of the sign of the salt concentration gradient that develops during a constant polarization experiment in a lithium (or sodium) symmetric cell can distinguish between t_+^0 greater than one ($\frac{dc}{dx} > 0$), less than one ($\frac{dc}{dx} < 0$) , or equal to one ($\frac{dc}{dx} = 0$). It turns out that this is not a particularly useful conclusion. A few studies have experimentally measured the salt concentration gradient which has indicated that $t_+^0 < 1$ (including Chapter 7 of this thesis)[85–87], and computational work has suggested that negatively charged ion clusters are more prevalent than positively charged ones in PEO/LiTFSI electrolyte.[88] In my opinion, there is no evidence to suggest that a sodium- or lithium-ion electrolyte with $t_+^0 > 1$ has ever been created, although there is no physical reason why they cannot exist. There is, however, ample evidence to suggest that sodium- or lithium-ion electrolytes with $t_+^0 < 0$ have been created and are perhaps commonplace. For polymer electrolytes with a lithium or sodium salt, reports of t_+^0 typically lie between -0.6 and 0.4.[58,81] These measurements come with large error bars, and many believe that negative transference numbers have not been definitively proven.

It is easy to cast doubt on claims of negative transference numbers measured in anion blocking cells. In Fig. 3.4, we replicate the plot of ρ_+ versus t_+^0 from Fig. 3.2 as a black trace. The shaded blue region represents the range of t_+^0 values between -0.6 and 0.4 which represents typical values of t_+^0 from the literature. This corresponds to values of $0.02 < \rho_+ < 0.1$ based on the electrolyte properties listed in Fig. 3.2. So, a wide range of t_+^0 values result in a relatively small range of ρ_+ values and it is difficult to conclusively state that a negative transference number has been measured based on the measurement of ρ_+, even if κ and D are measured carefully.

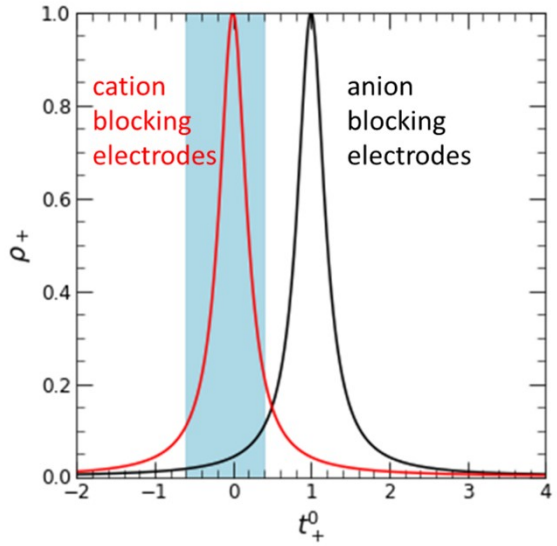

Figure 3.4. Relationship between ρ_+ and t_+^0 for cells with cation blocking electrodes. The red line plots the relationship between ρ_+ and t_+^0 for a hypothetical cell which has electrodes that are blocking to cations but can transport anions across the electrode/electrolyte interface. The black line is reproduced for anion blocking electrodes (*e.g.*, lithium) from Fig. 3.2. All other transport parameters are fixed for both traces. The blue shaded region denotes values of t_+^0 which are typically reported for polymer electrolytes.

If, on the other hand, a symmetric cell is constructed with cation blocking electrodes, the picture becomes drastically different. The same formalism which is used to derive Eqn. 3.6 and 3.7 can be used to derive analogous expressions for a cell with cation blocking electrodes and the '+' in Eqn. 3.6 and 3.7 are replaced with '-'. Using the same fixed values of κ, D, and T_f for an electrolyte with r = 0.08 (c = 1.59 x 10^{-3} mol cm^{-3}), we plot the relationship between ρ_+ and t_+^0 based on a cell with cation blocking electrodes as a red curve. In this case, ρ_+ is a much stronger function of t_+^0 in the range -0.6 < t_+^0 < 0.4. Importantly, ρ_+ equals 1 when t_+^0 = 0 (i.e. t_-^0 = 1) if cation blocking electrodes are used. In addition, based on our arguments around Fig. 3.3, we expect a change in sign of $\frac{dc}{dx}$ from negative to positive when going from negative to positive t_+^0.

In Fig. 3.3b, we showed that a negative t_+^0 would result in a net velocity of cations in the direction opposite the electric field. If this could be experimentally observed, one would conclusively prove a negative transference number. This is challenging but there are ongoing efforts to do this using electrophoretic NMR. Another approach would be to measure the sign of $\frac{dc}{dx}$ in a constant polarization experiment using cation blocking electrodes. If $\frac{dc}{dx}$ is found to be negative (using a spectroscopic technique described previously, for example), it can unambiguously be concluded that t_+^0 < 0.

3.5 Hypothetical cell to prove negative transference numbers

The proposed experiment requires a reliable cation-blocking electrode which can facilitate dc current through an electrolyte that is suspected of having a negative cation transference number.

It seems plausible that perovskites[89] or layered aromatic amines[90] may be able to function as anion-intercalation electrodes. Another possibility is to use anion-exchange membranes (AEM) in conjunction with either lithium or sodium electrodes. Craig, et al demonstrated the use of a Lithium/PEO/AEM/PEO/Lithium cell to measure T_f for PEO/LiTFSI electrolytes.[91] The AEM used in that work was polydiallyldimethylammonium bis(trifluoromethanesulfonyl)imide (polyDADMAT). We propose a similar cell configuration to measure the sign of $\frac{dc}{dx}$ in a constant polarization experiment. The cell is shown schematically in Fig. 3.5. To alleviate the need for a cation blocking electrode, we propose a cell with a two AEMs sandwiched around a PEO/LiTFSI electrolyte. Because the AEM does not store anions (the number of anions in the membrane is fixed, but anions can pass through in either direction while cations are blocked) it cannot function as the electrode. To circumvent this, two additional PEO/LiTFSI electrolytes are placed next to the AEMs with two lithium electrodes sandwiching the entire cell.

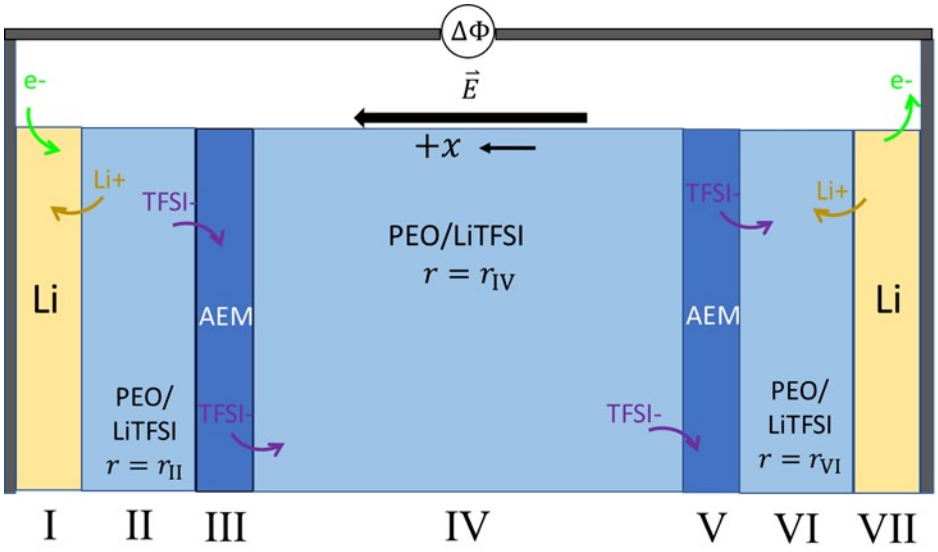

Figure 3.5. Schematic of a cell which could be used to prove negative transference numbers in PEO/LiTFSI electrolytes. Anion exchange membranes (AEM) are used to allow anions but block cations from passing to and from phase IV. From left to right the phases are: I – lithium metal, II – PEO/LiTFSI with $r = r_{II}$, III – AEM, IV – PEO/LiTFSI with $r = r_{IV}$, V – AEM, VI – PEO/LiTFSI with $r = r_{VI}$, VII – lithium metal, where r is the molar ratio of LiTFSI to ethylene oxide moieties. The pathway for current to flow through the cell is indicated by arrows. Green arrows represent electrons, gold arrows represent lithium cations, and purple arrows represent TFSI anions.

The phases in Fig. 3.5 are labeled with Roman numerals from left to right: I – lithium metal, II – PEO/LiTFSI with $r = r_{II}$, III – AEM, IV – PEO/LiTFSI with $r = r_{IV}$, V – AEM, VI – PEO/LiTFSI with $r = r_{VI}$, VII – lithium metal. The pathway for ionic current is shown with arrows. In general, lithium cations are transported across the Li/PEO interfaces, and TFSI anions are transported across the AEM/PEO interfaces. It is suggested to make the length of phase IV much larger than phase II and VI. This reduces the Ohmic drop across the two external PEO/LiTFSI phases. A consequence of the cell configuration is that the salt concentration in phase II decreases as current flows through the cell and increases in phase VI (salt concentration will not

change in phase IV). The salt concentrations should be chosen such that $r_{II} > r_{VI}$ to allow for long polarizations without depleting salt in phase II or over saturating with salt in phase VI. We are interested in measuring the sign of $\frac{dc}{dx}$ in phase IV, so r_{IV} is a salt concentration for which a negative t_+^0 is expected. Based on ref [81], $r = 0.14$ is a good candidate. Finally, a spectroscopic technique such as Raman or XAS is used to measure the salt concentration as a function of position in phase IV while current flows through the cell. If $\frac{dc}{dx} < 0$, then we can conclusively say that t_+^0 is negative.

The cell proposed in Fig. 3.5 is admittedly complicated and extracting accurate measurements of ρ_+ based on cation blocking interfaces may be difficult or impossible. However, the sign of the salt concentration gradient in phase IV should be measurable with no ambiguity, and the result indicates if t_+^0 is positive or negative. The experiment may be more effective if electrodes which intercalate TFSI anions can be used, however to my knowledge, such a symmetric cell has not been implemented and there may be experimental challenges incorporating a polymer electrolyte. The cell in Fig. 3.5 comprises components which are well studied and known to be compatible.

3.6 Conclusions

In this chapter, we have demonstrated the mechanism by which salt concentration gradients form in battery electrolytes when $t_+^0, \rho_+ \neq 1$. We make the point that, for a given measurement of ρ_+, there are two possible values of t_+^0 which can yield the same ρ_+ (one value that is less than unity and one that is greater than unity). To distinguish between the two possibilities, the sign of the concentration gradient must be measured. In practice, there is little evidence to suggest that typical battery electrolytes exhibit a $t_+^0 > 1$. However, $t_+^0 < 0$ have been routinely measured for polymer electrolytes, particularly PEO/LiTFSI. There is some skepticism in the community as to whether these reports are valid or simply due to imprecise measurements. ρ_+ is readily measured in an anion blocking symmetric cell, however there is no distinct signature of an electrolyte with negative t_+^0. We propose a hypothetical cell based on anion exchange membranes which could be used to definitively prove that PEO/LiTFSI electrolyte exhibit negative values of t_+^0 by measuring the sign of the salt concentration gradient.

3.7 Acknowledgement

The ideas described in this chapter are the result of many stimulating conversations with Dr. Jacqueline Maslyn, Dr. Deep Shah, Eric McShane, Prof. Hans-Georg Steinrück, and my advisor, Prof. Nitash Balsara. I am grateful to have benefited from their wisdom.

3.8 Supporting Information

3.8.1 Supporting Figures

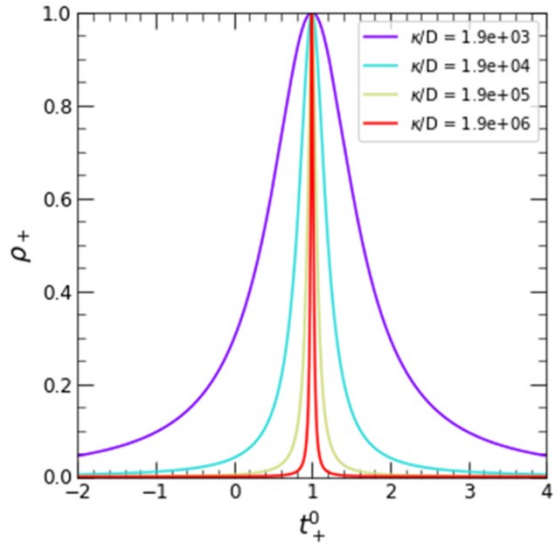

Figure 3.6. Relationship between ρ_+ and t_+^0 for different ratios of κ/D. The values of κ/D in the legend are reported in S cm s^{-1}. Smaller values of κ/D result in larger values of ρ_+.

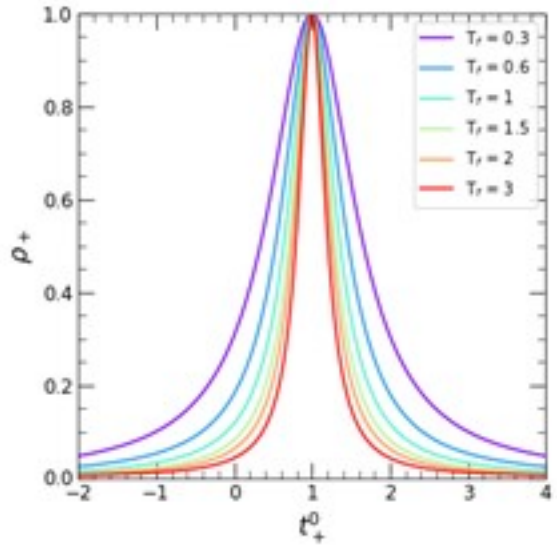

Figure 3.7. Relationship between ρ_+ and t_+^0 for different ratios of the thermodynamic factor, T_f. Lower values of T_f result in larger values of ρ_+. For PEO/LiTFSI, T_f is approximately equal to three over a wide range of salt concentrations.

3.9 Nomenclature

Table 2.4 List of symbols and abbreviations

Symbol	Meaning
AEM	anion exchange membrane
$\boldsymbol{c}$	salt concentration (mol cm^{-3})
$\boldsymbol{c_T}$	total electrolyte concentration (mol cm^{-3})

$\boldsymbol{D}$	restricted diffusion coefficient of the salt ($cm^2\ s^{-1}$)
$\boldsymbol{\mathcal{D}_{0+}}$	Stefan-Maxwell diffusion coefficient describing the interactions between the solvent and cation ($cm^2\ s^{-1}$)
$\boldsymbol{\mathcal{D}_{0-}}$	Stefan-Maxwell diffusion coefficient describing the interactions between the solvent and anion ($cm^2\ s^{-1}$)
$\boldsymbol{\mathcal{D}_{+-}}$	Stefan-Maxwell diffusion coefficient describing the interactions between the cation and anion ($cm^2\ s^{-1}$)
$\boldsymbol{F}$	Faraday constant (96485 C mol^{-1})
$\boldsymbol{i}$	current density (mA cm^{-2})
$\boldsymbol{i_0}$	initial current density measured after polarization at ΔV (mA cm^{-2})
$\boldsymbol{i_{ss}}$	current density measured at steady-state in response to ΔV (mA cm^{-2})
LiTFSI	lithium bis(trifluoromethanesulfonyl)imide
$\boldsymbol{m}$	salt molality (mol kg^{-1})
$\boldsymbol{N_i}$	Flux of species *i* (mol $cm^{-2}\ s^{-1}$)
PEO	poly(ethylene oxide)
polyDADMAT	polydiallyldimethylammonium bis(trifluoromethanesulfonyl)imide
$\boldsymbol{R}$	universal gas constant (8.314 J $mol^{-1}\ K^{-1}$)
$\boldsymbol{r}$	molar ratio of lithium cations to oxygens in the electrolyte
$\boldsymbol{T}$	temperature (K)
$\boldsymbol{T_f}$	thermodynamic factor
$\boldsymbol{t}$	time (s)
$\boldsymbol{t_+}$	Transference number of the cation with respect to the electrode reference frame
$\boldsymbol{t_+^0}$	transference number of the cation with respect to the velocity of the solvent
$\boldsymbol{U}$	battery open circuit potential (V)
$\boldsymbol{v_i}$	velocity of species *i*, (cm s^{-1})
$\boldsymbol{x}$	axis perpendicular to the electrodes
$\boldsymbol{z_+}$	charge number of cation
$\boldsymbol{z_-}$	charge number of anion

Table 2.5 List of symbols (Greek)

Symbol	Meaning
$\boldsymbol{\gamma_\pm}$	mean molal activity coefficient of the electrolyte
$\boldsymbol{\Delta\Phi}$	dc potential drop across an electrolyte, (V)
$\boldsymbol{\eta}$	overpotential (V)
$\boldsymbol{\kappa}$	ionic conductivity (S cm^{-1})
$\boldsymbol{\mu_i}$	electrochemical potential of species *i* (J mol^{-1})
$\boldsymbol{\rho_+}$	current ratio obtained using i_Ω

4. Measurement of Three Transport Coefficients and the Thermodynamic Factor in Block Copolymer Electrolytes with Different Morphologies[†]

ABSTRACT

The design and engineering of composite materials is one strategy to satisfy the materials needs of systems with multiple orthogonal property requirements. In the case of rechargeable batteries with lithium metal anodes, the system requires a separator with fast lithium ion transport and good mechanical strength. In this work, we focus on the system polystyrene-block-poly(ethylene oxide) (SEO) with bis(trifluoromethane)sulfonimide lithium salt (LiTFSI). Ion transport occurs in the salt-containing poly(ethylene oxide)-rich domains. Mechanical rigidity arises due to the glassy nature of polystyrene (PS). If we assume that the salt does not interact with the PS-rich domains, we can describe ion transport in the electrolyte by three transport parameters (ionic conductivity, κ, salt diffusion coefficient, D, and cation transference number, t_+^0) and a thermodynamic factor, T_f. By systematically varying the volume fraction of the conducting phase, ϕ_c between 0.29 and 1.0, and chain length, N between 80 and 8000, we elucidate the role of morphology on ion transport. We find that κ is the strongest function of morphology, varying by three full orders of magnitude, while D is a weaker function of morphology. To calculate t_+^0 and T_f, we measure the current fraction, ρ_+, and the open circuit potential, U, of concentration cells. We find that ρ_+ and U follow universal trends as a function of salt concentration, regardless of chain length, morphology, or ϕ_c, allowing us to calculate t_+^0 for any SEO/LiTFSI or PEO/LiTFSI mixture when κ and D are known. The framework developed in this paper enables predicting the performance of any block copolymer electrolyte in a rechargeable battery.

4.1 Introduction

Polymer membranes that selectively transport small molecules are used in a variety of applications including gas separations[92,93], water purification[94,95], fuel cells[96–98], and battery electrolytes[17,20,22,99–101]. Beyond tuning the chemistry, branching, or size of the polymer, heterogeneous materials with novel properties can be created by adding components such as a second polymer block[102–104]or nanoparticles.[105,106] Understanding how the additional phase (or phases) impacts the material properties is important for designing nanostructured materials with improved transport capabilities. Nanophase-separated block copolymer electrolytes have been applied to enable secondary batteries with lithium metal anodes.[107] Recharging a battery with a lithium metal anode often results in the formation of dendrites that are detrimental to battery

[†] Adapted (with permission) from Galluzzo, M. D.; Loo, W. S.; Wang, A. A.; Walton, A.; Maslyn, J. A.; Balsara, N. P. Measurement of Three Transport Coefficients and the Thermodynamic Factor in Block Copolymer Electrolytes with Different Morphologies. *J. Phys. Chem. B* **2020**. *124* (5), 921-935.

performance and safety.[7,9] Nanostructured block copolymer electrolytes are capable of transporting ions and suppressing lithium dendrites simultaneously in lithium metal batteries.[32,100] These systems comprise mechanically rigid domains composed of a polymer such as polystyrene (PS) and soft domains capable of transporting lithium ions such as polyethylene oxide (PEO) mixed with bis(trifluoromethane)sulfonimide lithium salt (LiTFSI). Sax and Ottino developed simple expressions for quantifying the effect of nanostructure on gas diffusion using an effective medium theory.[108] These expressions serve as a starting point for quantifying ionic conductivity in block copolymer electrolytes.

It is well understood that the diffusion of molecules through nanostructured materials depends strongly on morphology.[109–111] In Fig. 4.1, we present schematics of the experimentally observed morphologies of a polystyrene-*block*-poly(ethylene oxide) (SEO) electrolyte as a function of composition.[23,24,112] We use the volume fraction of the conducting domain (*i.e.* salt dissolved in PEO), ϕ_c, to quantify composition. For $\phi_c = 0$ or $\phi_c = 1$, the system is a homopolymer of the non-conducting (PS) or conducting phase (PEO), respectively. As ϕ_c is increased from 0 to 1, we observe the following sequence of morphologies: PEO-rich spheres on a body centered cubic lattice (BCC), PEO-rich cylinders on a hexagonal lattice (HEX), double gyroid comprising a PEO-rich network in a PS-rich matrix (GYR), alternating PS- and PEO-rich lamellae (LAM), double gyroid comprising a PS-rich network in a PEO-rich matrix (GYR'), PS-rich cylinders on a hexagonal lattice (HEX'), and PS-rich spheres on a body centered cubic lattice (BCC'). (The prime in our notation denotes that PEO/LiTFSI is the majority component.) A BCC morphology is not expected to conduct ions because the salt-containing domains are isolated. Similarly, a membrane with BCC' morphology will not be mechanically robust because the rigid PS-rich domains are not interconnected. Thus, neither BCC nor BCC' morphologies are particularly interesting for battery applications, and much research attention has been focused on morphologies where ϕ_c is close to 0.5 (i.e. GYR, LAM, and GYR'). Recent computational studies by Shen, Brown, and Hall have shown that the lamellar morphology is optimal for ion diffusion.[33] The purpose of this paper is to experimentally characterize ion transport through different morphologies.

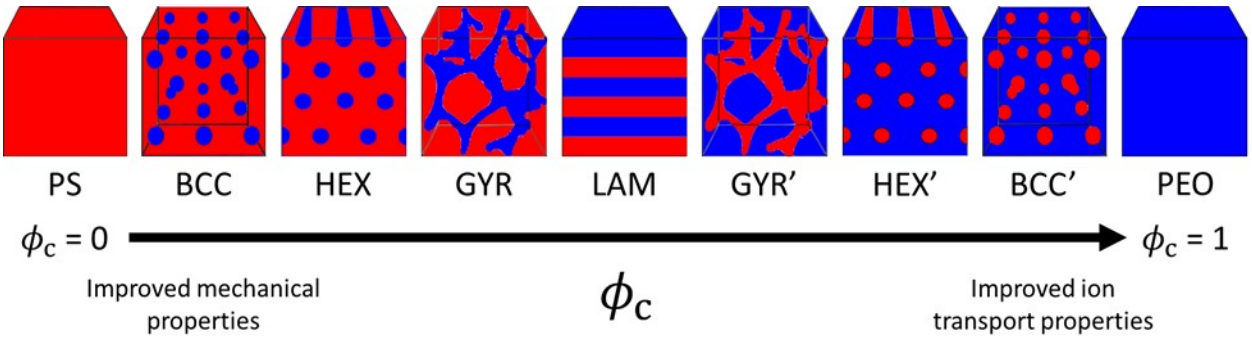

Figure 4.1. SEO morphologies as a function of conducting phase volume fraction , ϕ_c, with polystyrene (PS) depicted in red and poly(ethylene oxide) (PEO) with LiTFSI depicted in blue. As ϕ_c increases from $\phi_c = 0$ (PS homopolymer) to $\phi_c = 1$ (PEO homopolymer), the observed morphologies are: BCC – body centered cubic spheres of PEO in a PS matrix, HEX – hexagonally packed cylinders of PEO in a PS matrix, GYR – minority gyroid of PEO in a matrix of PS, LAM – alternating lamellae of PS and PEO, GYR' – minority gyroid of PS in a matrix of PEO, HEX' – hexagonally packed cylinders of PS in a matrix of PEO,

BCC' – body centered cubic spheres of PS in a matrix of PEO. At low ϕ_c, the electrolytes are rigid due to the continuous PS matrix but poor ionic conductors. At high ϕ_c, the electrolytes are highly conductive due to the continuous PEO matrix but not very rigid.

Complete electrochemical characterization of ion transport enables prediction of time-dependent salt concentration and potential gradients across a battery electrolyte during dc polarization.[42,61] A desirable electrolyte will have small salt concentration and potential gradients within the electrolyte at large current densities. Predicting the magnitude of these gradients in a homogeneous (single phase) electrolyte requires knowledge of three transport coefficients: ionic conductivity (κ), salt diffusion coefficient (D), and the cation transference number with respect to the solvent velocity (t_+^0). It also requires a thermodynamic factor defined as $T_f = 1 + \frac{d \ln \gamma_{+-}}{d \ln m}$, where γ_{+-} is the mean molal activity coefficient of the salt and m is the salt molality in mol kg^{-1}.[42,51] Fully characterizing transport in a nanostructured electrolyte will, in principle, require measuring many more transport and thermodynamic factors. The presence of polystyrene makes SEO/LiTFSI a four-component system (PS, PEO, Li^+, $TFSI^-$). The presence of nanophase separated domains adds additional complexity. In this paper, we make the simplifying assumption that knowledge of three transport coefficients and the T_f is adequate to describe ion transport in block copolymer electrolytes. We examine the effect of morphology and ϕ_c on each transport coefficient and T_f. We find that T_f exhibits a surprisingly complex dependence on morphology. This dependence is outside the scope of simple effective medium theories. Our approach uses concentrated solution theory[42] to develop a complete picture of ion transport based on our assumptions. The theory may be used to make testable predictions[46,113] and, in turn, validate or invalidate our assumptions. We address this in Chapter 7. In principle, similar approaches may be applied to other problems associated with simultaneous diffusion of small molecules through nanostructured media.

4.2 Experimental Section

4.2.1 Polymer Synthesis and Characterization

All electrochemical and morphological characterization was carried out at 90 °C. The SEO copolymers in this study were synthesized, purified, and characterized using methods described in refs [24,114]. The polymers are referred to as SEO(*x*-*y*) for block copolymers and PEO(*y*) for PEO homopolymers, where *x* and *y* are the number-averaged molecular weights of PS, M_{PS}, and PEO, M_{PEO}, in kg mol^{-1}, respectively. The volume fractions of each block of the copolymers are calculated by:

$$\phi_{EO} = \frac{v_{EO}}{v_{EO} + \frac{M_{PS}M_{EO}}{M_S M_{PEO}} v_S} \tag{4.1}$$

where v_{EO} and v_S are the volumes of ethylene oxide (0.0682 nm^3) and styrene monomers (0.167 nm^3) and M_{EO} and M_S are the molar masses of ethylene oxide (44.05 g mol^{-1}) and styrene (104.1 g mol^{-1}). Monomer volumes were calculated by $v_i = \frac{M_i}{\rho_i N_A}$, where N_A is Avogadro's number. The

densities of the PEO and PS blocks at 90 °C are ρ_{PEO} = 1.07 g cm^{-3} and ρ_{PS} = 1.03 g cm^{-3}, respectively.[115] The overall degree of polymerization, N, was calculated by $N = N_{\mathrm{PS}} + N_{\mathrm{PEO}}$ where

$$N_i = \frac{M_{\mathrm{i}}}{\rho_{\mathrm{i}} N_{\mathrm{A}} v_{\mathrm{ref}}} \tag{4.2}$$

and v_{ref} was fixed at 0.1 nm^3. The neat copolymers are completely transparent and colorless.

4.2.2 Electrolyte Preparation

The block copolymer and salt mixtures were prepared by freeze-drying using methods described in ref [116], except for SEO(240-260) and SEO(200-222) which were prepared by solvent casting[55]. All electrolyte and cell preparation was performed in an argon-filled glovebox maintained with water and oxygen concentrations below 1 ppm each. The molar ratio of lithium ions to ethylene oxide (EO) moieties, $r = [\mathrm{Li}]/[\mathrm{EO}]$, is used in this study to quantify salt concentration. r is related to the salt molality, m, by Eqn. 4.3,

$$m = \frac{r}{M_{EO}}. \tag{4.3}$$

Note that m is the molality of the PEO domains in our nanostructured electrolyte (i.e. moles of salt per kg of PEO) and it is calculated assuming that all of the salt resides in the PEO domains.[35,36,117] We determine the volume fraction of the salty PEO domain, ϕ_{c}, using

$$\phi_c = \frac{v_c}{v_c + \left(\frac{M_{PS} M_{EO}}{M_S M_{PEO}}\right) v_S}, \tag{4.4}$$

where v_{c} is the volume of the conducting phase per EO monomer and is given by $v_{\mathrm{c}} = \frac{M_{\mathrm{PEO}}}{\rho_{\mathrm{c}} N_{\mathrm{A}}}$ where ρ_{c} is the density of the conducting domain at a specific salt concentration. ρ_{c} as a function of r was taken from ref [58] and we assume that the density of the conducting domain does not depend on ϕ_{c} for the SEO electrolytes. In general, ϕ_{c} increases with increasing salt concentration.

The electrolytes used in this study are listed in Table 4.1. For each polymer we list M_{PS}, M_{PEO} and N. For each electrolyte we list r, ϕ_{c}, and the morphology at 90 °C. Information about morphology is generally based on small angle X-ray scattering (SAXS) experiments. We include the neat polymers for completeness. The morphologies of SEO(4-22.4), SEO(5.1-12.8), SEO(3.8-8.2), and SEO(9.4-4) are given in ref [23]. We have taken electrochemical and morphological data from previous studies on PEO(5) and a variety of other SEO/LiTFSI systems listed in Table 4.1, and we list the relevant references next to the polymer name. Most of the electrolytes studied in this work exhibit the ordered morphologies presented in Fig. 4.1. Many of the short-chained (*i.e.* low-N) polymers are disordered (DIS) in the neat state and at low salt concentrations. The disordered morphology is characterized by fluctuating PEO-rich and PS-rich domains but with no long-range order.[118] These fluctuations give rise to a characteristic broad scattering peak. The disordered systems listed in Table 4.1 give way to ordered morphologies with the addition of salt. All of the electrolytes are ordered when $r > 0.05$. The effect of added salt on the morphology and thermodynamics of block copolymer electrolytes is an active research topic[23,24,119–121], but is not

the focus of this study. In most cases, a single morphology is present at each salt concentration. In SEO(4.0-22.4), we observe coexisting ordered morphologies as indicated in Table 4.1.

Table 4.1. List of electrolytes used in this study. The polymer name, molecular weight of polystyrene block (M_{PS}) in kg mol^{-1}, molecular weight of poly(ethylene oxide) block (M_{PEO}) in kg mol^{-1}, number of repeat units (N) calculated from Eqn. 4.2, salt concentration (r), conducting phase volume fraction (ϕ_{c}) calculated from Eqn. 4.4, and morphology are listed. Some electrochemical data was taken from other works, and we report the reference for those electrolytes next to the polymer name. An (') indicates that PEO is the majority phase and an (*) indicates that the morphology for that salt concentration was not determined experimentally but assumed based on ϕ_{c}.

Polymer	M_{PS}	M_{PEO}	N	r	ϕ_c	Morph.	Polymer	M_{PS}	M_{PEO}	N	r	ϕ_c	Morph.
PEO(5)[55,58]	0	5.0	77	neat	1	-	SEO(3.8-8.2)	3.8	8.2	188	0.250	0.78	HEX'
				0.005	1	-					0.300	0.80	HEX'
				0.010	1	-	SEO(74-98)[122]	74	98	2707	neat	0.56	LAM
				0.020	1	-					0.085	0.61	LAM
				0.040	1	-	SEO(6.0-7.0)[36]	6.0	7.0	205	neat	0.53	LAM
				0.060	1	-					0.085	0.58	LAM
				0.080	1	-	SEO(200-222)	20	222	6653	neat*	0.52	LAM
				0.100	1	-					0.085*	0.57	LAM
				0.120	1	-	SEO(240-260)[55]	24	260	7885	neat	0.51	LAM
				0.140	1	-					0.020*	0.52	LAM
				0.160	1	-					0.035*	0.53	LAM
				0.180	1	-					0.050*	0.54	LAM
				0.210	1	-					0.085*	0.57	LAM
				0.240	1	-					0.100*	0.57	LAM
				0.270	1	-					0.120*	0.58	LAM
				0.300	1	-					0.150*	0.60	LAM
SEO(4.0-22.4)	4.0	22.4	411	neat	0.84	DIS					0.200*	0.62	LAM
				0.005	0.85	DIS					0.250*	0.64	LAM
				0.010	0.85	DIS					0.300*	0.66	LAM
				0.025	0.85	HEX'	SEO(16-16)[123,124]	16	16	505	neat	0.49	LAM
				0.050	0.86	HEX'					0.030	0.51	LAM
				0.075	0.87	HEX'/					0.060	0.53	LAM
				0.100	0.87	HEX'/					0.080	0.54	LAM
				0.150	0.89	BCC'					0.110	0.56	LAM
				0.200	0.90	BCC'					0.150	0.58	LAM
				0.250	0.90	BCC'					0.180	0.59	LAM
				0.300	0.91	BCC'					0.210	0.61	LAM
SEO(5.1-12.8)	5.1	12.8	280	neat	0.71	DIS					0.240	0.62	LAM
				0.005	0.71	DIS					0.270	0.63	LAM
				0.010	0.71	DIS					0.300	0.64	LAM
				0.025	0.72	GYR'	SEO(352-166)[125]	35	166	8232	neat	0.31	HEX
				0.050	0.74	HEX'					0.085	0.36	HEX
				0.065*	0.74	HEX'	SEO(247-116)[125]	24	116	5769	neat	0.31	HEX
				0.075	0.75	HEX'					0.085	0.36	HEX
				0.100	0.76	HEX'	SEO(54-23)[125]	54	23	1225	neat	0.29	HEX
				0.150	0.78	HEX'					0.085	0.34	HEX
				0.200	0.79	HEX'	SEO(9.4-4.0)	9.4	4.0	213	neat	0.29	DIS
				0.250	0.81	HEX'					0.010	0.29	HEX
				0.300	0.82	HEX'					0.025	0.30	HEX
				0.350*	0.83	HEX'					0.040*	0.31	HEX
SEO(3.8-8.2)	3.8	8.2	188	neat	0.67	DIS					0.050	0.32	HEX
				0.005	0.68	DIS					0.065*	0.33	HEX
				0.010	0.68	DIS					0.075	0.33	HEX
				0.025	0.69	DIS					0.100	0.34	HEX
				0.050	0.70	GYR'					0.150	0.37	HEX
				0.075	0.72	HEX'					0.200	0.39	HEX
				0.100	0.73	HEX'					0.250	0.41	HEX
				0.150	0.75	HEX'					0.300	0.43	HEX
				0.200	0.77	HEX'					0.350*	0.45	HEX

4.2.3 Electrochemical Characterization

SEO samples for electrochemical measurements were prepared by placing electrolytes in annular silicone spacers with inner diameters of 3.18 mm and hand-pressing them into pellets. Samples were hot-pressed at 90 ºC to create a uniform, non-porous films. The polymer sample was sandwiched between stainless steel or lithium electrodes of known thickness. The total cell thickness was measured using a micrometer before attaching nickel current collectors and sealing the cell in polypropylene-lined aluminum pouch material. At this point the cells were removed from the glovebox for testing. The inner diameter of the spacer and the thickness measurements allow for determination of the cell constants A and L, the electrochemically active area and distance between electrodes, respectively.

Ionic conductivity of samples with blocking electrodes (stainless steel), κ, was measured by ac impedance spectroscopy at 90 ºC using a BioLogic VMP3 potentiostat with an amplitude of 80 mV and frequency range of 1 MHz to 100 mHz. The bulk resistance, R_{b}, was determined by fitting an equivalent circuit and used to calculate κ from Eqn. 4.5,

$$\kappa = \frac{L}{R_b A} \,. \tag{4.5}$$

Prior to measurement, cells were annealed at 120 ºC for at least 12 hours on a custom-built temperature-controlled heating stage.

Cells with lithium electrodes were used to measure the current fraction, ρ_+, as described in refs [58] and Chapter 2. Our methods follow those pioneered by Bruce and Vincent.[47,49] Lithium cells were annealed for at least four hours at 90 °C followed by at least four conditioning cycles. Conditioning cycles allowed the interfacial resistance to reach a stable value that did not change with time or as current was passed. The bulk resistance (*i.e.* conductivity) remained within the reported experimental error bars throughout the conditioning cycles. Each cycle consisted of passing current at +20 μA cm^{-2} for 4 h followed by -20 μA cm^{-2} for 4 h. ρ_+ is measured in an experiment where a constant voltage, ΔV, is applied across the cell to obtain the ratio of the current measured at steady state, i_{ss}, to the initial current given by Ohm's law, i_Ω, corrected for the change in potential drop across the electrolyte due to the change in current over the experiment. The equation used to calculate ρ_+ is given by:

$$\rho_+ = \frac{i_{ss}}{i_\Omega} \frac{(\Delta V - i_\Omega R_{i,0} A)}{(\Delta V - i_{ss} R_{i,ss} A)} \,, \tag{4.6}$$

where $R_{\mathrm{i},0}$ and $R_{\mathrm{i,ss}}$ are the interfacial resistance measured by ac impedance spectroscopy before the experiment and once steady state is reached, respectively. ρ_+ is equal to the cation transference number for an ideal electrolyte at infinite dilution. Because this is never the case for practical electrolytes, we avoid calling this quantity "the transference number" as is commonly done in the literature and instead refer to it as "the current fraction".[56] We measured the ionic conductivity of the cells with non-blocking (i.e. lithium) electrodes, κ_{nb}, and calculated i_Ω using Eqn. 4.7:

$$i_\Omega = \frac{\Delta V}{L/\kappa_{nb} + R_{i,0} A} \,. \tag{4.7}$$

The same cells were used to measure the diffusion coefficient of the salt, D, in a restricted diffusion experiment following methods described in refs [55,58]. We measure the open circuit potential, U, over time as the salt concentration gradient relaxes and fit the data to Eqn. 4.8 to obtain D:

$$-\frac{d\ ln\ U}{dt} = \frac{\pi^2 D}{L^2}. \tag{4.8}$$

Concentration cells of SEO electrolytes were prepared by placing an annular silicone spacer of 0.5 or 1.0 mm thickness onto a lithium electrode. The electrolyte was then hot pressed into the spacer at 90 °C to create a uniform film. Next, another electrode/spacer assembly was made with an electrolyte of the same SEO polymer but different salt concentration. The two assemblies were then pressed together and aligned in such a way that the two electrolytes were in physical contact. We then measured the open circuit potential, U, of the cells at 90 °C once thermal equilibrium was achieved. The cells were made with one electrolyte fixed at a reference salt concentration of r = 0.065. The salt concentration of the second electrolyte was varied between r = 0.005 and r = 0.35 to obtain the quantity $\frac{\mathrm{d}U}{\mathrm{d}\ln m}$.

4.3 Results and Discussion

This work focuses on the electrochemical properties of nanostructured electrolyte films with thicknesses in the range of 250 to 500 μm. The relationship between conductivity and morphology in confined polymer films (<10 μm thick) has been studied in detail.[126–129] The typical length scale (domain spacing) of the ordered morphologies in block copolymers range from 10 to 100 nm. For all practical purposes, the electrolytes are isotropic comprising many randomly oriented grains. Coherent order is generally restricted to grains with a characteristic length of a few μm.[130] The morphologies depicted in Fig. 4.1 only show the structure within a grain.

In Fig. 4.2a and 4.2b, we present κ as a function of salt concentration for many of the polymers listed in Table 4.1 on a semi-log plot. The SEO electrolytes containing 3D conducting pathways (BCC', HEX', GYR') are shown in Fig. 4.2a. The conductivity of the homopolymer, PEO(5), is shown for comparison. The inset of Fig. 4.2a highlights the conductivity trends at low salt concentration ($r \leq 0.05$). All three SEO copolymers presented in Fig. 4.2a are disordered in the neat state. The addition of salt results in the formation of ordered morphologies. The dominant morphology of each electrolyte is indicated by the schematic in the legend above the plots. For SEO(22.4-4.0), a HEX' phase emerges when salt is added. Additional salt results in the coexistence of HEX' and BCC' phases and further salt added results in a BCC' phase. For SEO(3.8-8.2) and SEO(5.1-12.8), the addition of salt results in a GYR' morphology and further salt addition results in a HEX' morphology. These phase transitions are discussed thoroughly in ref [23]. The dependence of conductivity on salt concentration of all of the copolymers discussed in Fig. 4.2a is remarkably similar. At low salt concentrations, conductivity increases with increasing salt concentration due to the increase in charge carrier concentration. It is well known that the addition of salt slows down segmental relaxation of the PEO chains, and this results in a conductivity maximum in the vicinity of r = 0.10.[131] Qualitatively similar behavior is seen in electrolytes based on PEO homopolymer; the slight dip in conductivity in the vicinity of r = 0.13

in the PEO(5) data in Fig. 4.2a is a peculiarity of 5 kg mol^{-1} PEO homopolymer. The data obtained from different copolymers in Fig. 4.2a is relatively similar despite the differences in morphology discussed above. There is little difference in the conductivity of disordered and ordered block copolymer electrolytes, most apparent at $r = 0.025$ in the inset of Fig. 4.2a. We attribute this to the presence of large concentration fluctuations in the disordered state. It appears as if the salt molecules are localized in the PEO-rich fluctuations in the disordered state and this leads to ion transport that is not very different from that observed in weakly ordered block copolymer electrolytes. In all electrolytes discussed in Fig. 4.2a, ion transport occurs through the matrix phase of the block copolymer. It is evident that the morphology of the dispersed polystyrene domains has relatively little impact on ionic conductivity on SEO electrolytes with 3D conducting pathways.

In Fig. 4.2b, we show conductivity versus salt concentration for SEO electrolytes with 2D (LAM) and 1D conducting pathways (HEX). We first consider the values of κ in the low r-limit. We see the same general trend in Figs 4.2a and 4.2b: κ increases with r at low salt concentrations. At high salt concentration, κ appears to approach a plateau. The conductivity of SEO(16-16) is about an order of magnitude lower than that of PEO(5) while that of SEO(9.4-4.0) is about two orders of magnitude lower than that of PEO(5). These drops correspond to transitions from 3D (homopolymer) to 2D (LAM) to 1D (HEX) conducting pathways. The conductivity of SEO(240-260) lies between SEO(16-16) and PEO(5). This effect has been previously discussed in studies of symmetric block copolymer electrolytes.[20,116,122]

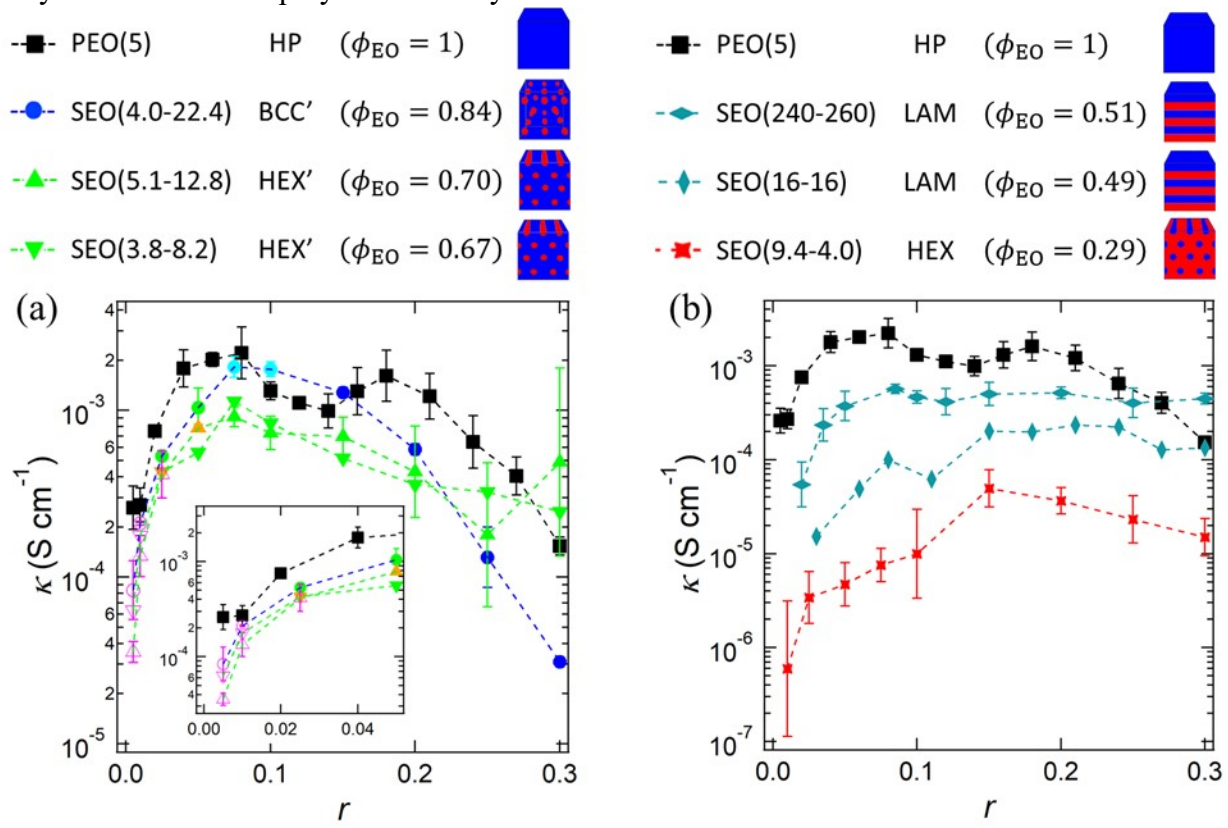

Figure 4.2. Conductivity, κ, of PEO and various SEO electrolytes as a function of salt concentration, r, the molar ratio of lithium ions to ether oxygens. The color of the symbol denotes the morphology:

black/homopolymer, blue/BCC', cyan/coexisting BCC' and HEX', green/HEX', gold/GYR', teal/LAM, red/HEX, purple (open)/DIS. The dominant morphology across the range of salt concentrations is indicated by the schematic in the legend above the plots. The volume fraction of the neat polymer, ϕ_{EO}, is listed in the legend and the conducting phase volume fraction, ϕ_c, of each electrolyte is given in Table 4.1. (a) κ vs r for PEO(5) and SEO electrolytes with 3D conducting morphologies. The inset is a magnified view of the low salt concentration region. (b) κ vs r for PEO(5) and SEO electrolytes with 2D and 1D conducting morphologies.

The conductivity of SEO/LiTFSI electrolytes is a complex function of both chain length, quantified by N, and composition, quantified by ϕ_c. In Fig. 4.3 we focus on the effect of chain length at two fixed compositions: ϕ_c = 0.58 ± 0.03 and ϕ_c = 0.35 ± 0.01 corresponding to LAM and HEX morphologies, respectively. The salt concentration in these electrolytes is held fixed at r = 0.085. For both morphologies, κ increases by nearly an order of magnitude when N increases from 200 to 2000. Ion transport through block copolymer electrolytes is affected by many factors including ϕ_c, the geometry of the conducting phase, the extent to which PS monomers are present in the PEO-rich conducting domains, the width of the interface between the PS-rich and PEO-rich domains[116], and the grain size.[37] The similarity of the data from LAM and HEX phases in Fig. 4.3 suggests a common origin for the observed increase in κ with N. The geometry of the conducting phase and ϕ_c are more or less fixed within the two data sets in Fig. 4.3. The presence of a large interfacial region between PS and PEO-rich domains will slow down the motion of ions that are located in the vicinity of the interface. The width of this interface decreases with increasing segregation strength (which increases with N), resulting in increased conductivity. Increasing N also results in a dramatic decrease in polymer diffusion which is necessary for eliminating defects. We thus expect smaller grains in samples with higher chain length: smaller grains also lead to an increase in conductivity in samples with 2D or 1D conducting pathways.[37,125] Defects are not expected to play an important role in electrolytes with 3D conducting pathways.

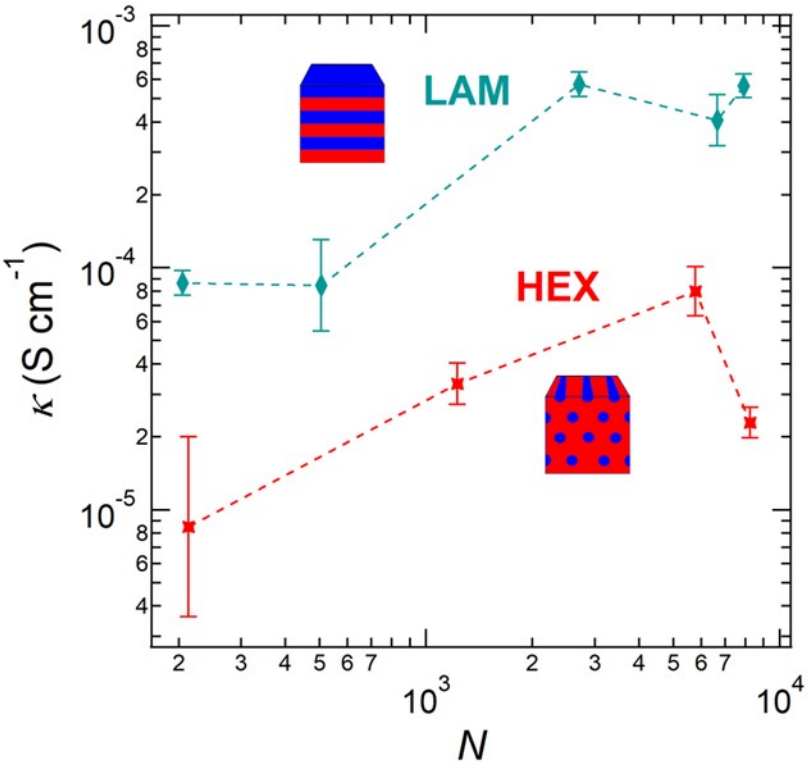

Figure 4.3. Conductivity, κ, of SEO electrolytes with LAM morphologies and HEX morphologies as a function of chain length, N. The salt concentration is fixed at $r = 0.085$ for all samples. The conducting phase volume fraction, ϕ_c, is 0.58 ± 0.03 for the LAM electrolytes and 0.35 ± 0.01 for the HEX electrolytes. For both LAM and HEX morphologies, conductivity increases by nearly an order of magnitude from $N = 200$ to $N = 2000$.

The Nernst-Einstein relationship is often invoked to relate conductivity and the self-diffusion coefficient of the ions.[42] This relationship is only applicable to ideal electrolytes in the dilute limit. (In ideal electrolytes, the salt dissociates completely to yield non-interacting ions and the salt activity coefficient of ideal electrolytes is unity.) It is well understood that polymer electrolytes do not behave ideally, even at very low salt concentrations.[43,55,58] In addition, the salt diffusion coefficient relevant to ion transport in electrolytes is a mutual diffusion coefficient, D. There may thus be little correlation between κ and D. In Fig. 4.4a we present D as a function of r for the polymers with 3D conducting domains listed in Table 4.1, with PEO(5) included for comparison. To a good approximation, D of block copolymer electrolytes with BCC', HEX', GYR' morphologies is independent of salt concentration and not very different from that of PEO(5). In Fig. 4.4b, we present D as a function of r for 2D and 1D conducting morphologies. For the LAM morphologies, we again see that D is not a strong function of r. Similar to the trend observed for κ, we find that there is a significant increase in D for SEO(240-260) compared to SEO(16-16). There is a four-fold increase in D of SEO(9.4-4.0) when r increases from 0.06 to 0.1. We see a similar step change in conductivity in this copolymer around the salt concentration $r = 0.1$. We do not have a definitive explanation for these observations in low ϕ_c electrolytes; SAXS data across this concentration range shows no discernable change in morphology.

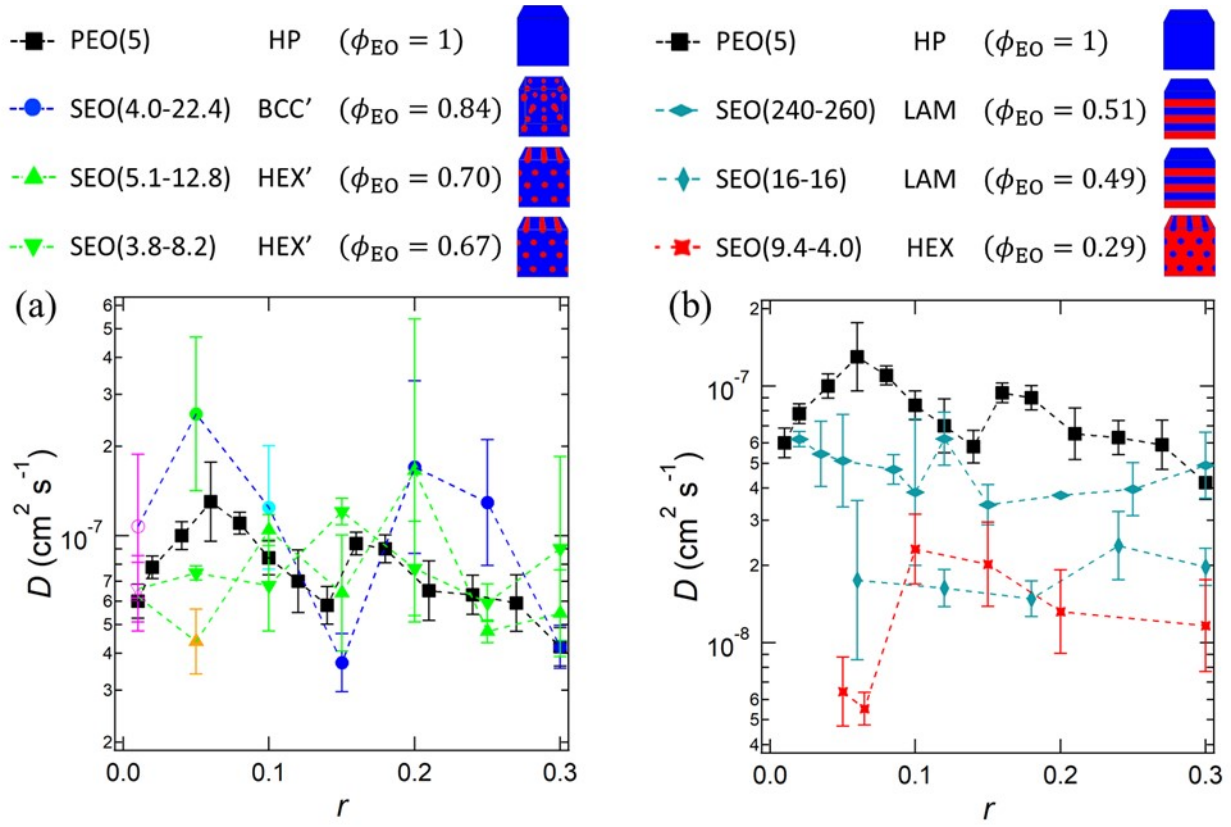

Figure 4.4. Salt diffusion coefficient, D, of PEO and various SEO electrolytes as a function of r, the molar ratio of lithium ions to ether oxygens for the polymers listed in the figure. The color of the symbol denotes the morphology: black/homopolymer, blue/BCC', cyan/coexisting BCC' and HEX', green/HEX', gold/GYR', teal/LAM, red/HEX, purple (open)/DIS. The dominant morphology across the range of salt concentrations is indicated by the schematic in the legend above the plots, which is identical to the legend in Fig. 4.2. The volume fraction of the neat polymer, ϕ_{EO}, is listed in the legend and the conducting phase volume fraction, ϕ_c, of each electrolyte is given in Table 4.1. (a) D vs r for PEO(5) and SEO electrolytes with 3D conducting morphologies. The inset is a magnified view of the low salt concentration region. (b) D vs r for PEO(5) and SEO electrolytes with 2D and 1D conducting morphologies.

It is useful to define κ and D for model nanostructured electrolytes and use these definitions to normalize our data.[20,104,132] We define a model nanostructured electrolyte as one where salt does not interact with the polystyrene chains and the PEO-rich nanodomains can be approximated as homopolymer electrolytes. In addition, model electrolytes comprise randomly oriented grains with negligible inter-grain resistance. We use the term "model" instead of "ideal" to avoid implying that the electrolytes are thermodynamically ideal. The thermodynamic interactions between the salt and EO monomer unit in a model nanostructured electrolyte are identical to those in PEO homopolymer, which do not behave ideally at any salt concentration. To calculate κ or D in a model morphology, we must consider how ions move within a grain and geometric factors that affect inter-grain transport of a given morphology. The baseline for our analysis is a homogeneous electrolyte sandwiched between parallel electrodes which are used to apply an electric field across the electrolyte. In a model nanostructured electrolyte, the ion moves in a tortuous path because it can only reside in a conducting domain. For 3D conducting morphologies (i.e. GYR', HEX',

BCC'), the hinderance to ion motion is quantified by a tortuosity factor, τ. The values of τ for these morphologies taken from the literature are given in Table 4.2. LAM and HEX phases do not have tortuous paths within a grain and $\tau = 1$. Morphology influences ion transport in these systems because the effectiveness of each grain depends on the orientation of the grain relative to direction of the electric field. We use the morphology factor, *f*, to quantify this effect. Sax and Ottino pioneered the use of effective medium theory to calculate f in the context of diffusion of small molecules in nanostructured media.[108] Their results have frequently been applied to block copolymer electrolytes in the literature.[20,33,122,123] The values of f for LAM and HEX phases taken from ref [133] are listed in Table 4.2. When transport occurs through the matrix phase (i.e. BCC', HEX', GYR'), we assume that $f = 1$. The numerical values of f and τ reported in Table 4.2 are taken from refs [33,134].

Table 4.2. Morphology factor, f, and tortuosity, τ, for the morphologies of interest.

Morphology	f	τ
BCC'	1	(3-ϕ_c)/2
HEX'	1	2-ϕ_c
GYR'	1	5/4
LAM	2/3	1
HEX	1/3	1

We define the conductivity, κ_{m}, and salt diffusion coefficient, D_{m}, of model nanostructured electrolytes in Eqns. 4.9 and 4.10:

$$\kappa_m(r) = \frac{f}{\tau}\phi_c\kappa_{PEO}(r), \tag{4.9}$$

$$D_m(r) = \frac{f}{\tau}D_{PEO}(r), \tag{4.10}$$

where $\kappa_{\mathrm{PEO}}(r)$ and $D_{\mathrm{PEO}}(r)$ are transport coefficients of the PEO homopolymer at a specific salt concentration where it is assumed that the molecular weight of the PEO homopolymer is large enough so that ion transport properties are independent of molecular weight.[19,135] Physical justification for the inclusion of ϕ_{c} in Eqn. 4.9 but not Eqn. 4.10 can be found in ref [132]. Next, we define normalized transport coefficients, denoted by a subscript n, in Eqns. 4.11 and 4.12:

$$\kappa_n(r) = \frac{\kappa}{\phi_c\kappa_{PEO}(r)}, \tag{4.11}$$

$$D_n(r) = \frac{D}{D_{PEO}(r)}. \tag{4.12}$$

Both κ_{n} and D_{n} equal $f\tau^{-1}$ for a model morphology. In Fig. 4.5a and 4.5b we present κ_{n} and D_{n}, respectively, as a function of volume fraction with r = 0.05, 0.15 and 0.30. We include the homopolymer for completeness where $\phi_{\mathrm{c}} = \kappa_{\mathrm{n}} = D_{\mathrm{n}} = 1$ by definition. The vertical lines separate different morphologies observed within a volume fraction range, and the solid black line represents the value of $f\tau^{-1}$.

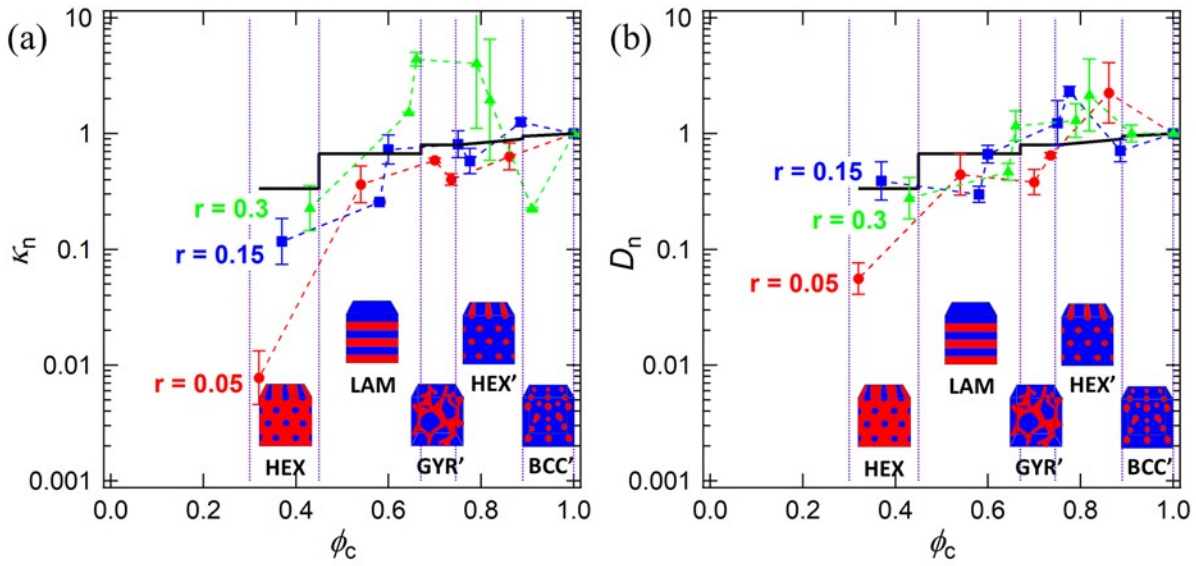

Figure 4.5. Normalized conductivity and diffusion coefficient as a function of conducting phase volume fraction. (a) Normalized conductivity, κ_n, and (b) normalized salt diffusion coefficient, D_n, as a function of conducting phase volume fraction, ϕ_c, for r = 0.05 (red circles), r = 0.15 (blue squares), and r = 0.30 (green triangles). The vertical lines and illustrations indicate the volume fraction range where each morphology is observed. For a model morphology, $\kappa_n = D_n = f\tau^{-1}$. We plot $f\tau^{-1}$ as a black line based on the values of f and τ given in Table 4.2.

We discuss the data in Fig. 4.5a starting with the low salt concentration data set, r = 0.05. In this salt concentration regime, the normalized conductivity spans three orders of magnitude. At low ϕ_c values (i.e. the HEX morphology), κ_n is a factor of 40 below $f\tau^{-1}$. However, more reasonable agreement between κ_n and $f\tau^{-1}$ is observed once ϕ_c exceeds 0.4. Qualitatively similar behavior is seen at an intermediate salt concentration, r = 0.15; however, at low values of ϕ_c (ϕ_c < 0.45), κ_n is still a factor of 3 below $f\tau^{-1}$. At a high salt concentration, r = 0.30, we see reasonable agreement between κ_n and $f\tau^{-1}$ even at the lowest value of ϕ_c. It is evident that conductivity through block copolymers with low values of ϕ_c depends strongly on salt concentration. The measured conductivity approaches that expected for a model nanostructured electrolyte as salt concentration is increased. This observation appears to suggest that grain connectivity increases with increasing salt concentration.[37] An interesting observation is that κ_n is significantly larger than unity (i.e. κ_n = 4) for ϕ_c values of 0.67 and 0.79. This implies that the intrinsic conductivity of PEO-rich domains in the block copolymer is higher than that of PEO homopolymer electrolytes. Molecular dynamics studies have shown evidence for large ion clusters consisting of >100 ions in concentrated PEO/LiTFSI electrolytes.[88] It is not unreasonable to hypothesize that the PS domains impact the size and nature of the salt aggregates, resulting in increased conductivity. Recent coarse-grained simulations of ion transport through block copolymer electrolytes by Seo et al. suggest similar effects.[136]

In Fig. 4.5b, we see that D_n has similar behavior to κ_n, except that the decay in D_n versus ϕ_c compared to that of κ_n is slightly less severe, especially for the HEX morphology at r = 0.05. In general, D_n tends to be close to the value of $f\tau^{-1}$ at high values of r and high values of ϕ_c. The

value of D_n does not vary much with salt concentration compared to κ_n. This is because D is a much weaker function of salt concentration than κ (compare Fig. 4.2 and 4.4).

The current ratio, ρ_+, is an important electrolyte property as the product of $\kappa\rho_+$ dictates the performance of an electrolyte in the limit of small applied potentials.[47,49,50,60] In Fig. 4.6, we present ρ_+ for all of the polymers listed in Table 4.1. Regardless of composition and chain length, all systems in this study show the same general trend of ρ_+ with salt concentration: ρ_+ decreases with increasing salt concentration until r is approximately 0.15 and then increases until r = 0.30. We fit a universal curve which can be used to predict the current ratio for any SEO or PEO/LiTFSI electrolyte as a function of salt concentration. The fit is shown by the black curve in Fig. 4.6 and is given by Eqn. 4.13,

$$\rho_+ = (0.18 \pm 0.01) - (1.7 \pm 0.1)r + (6.3 \pm 0.5)r^2. \quad (4.13)$$

Equation 4.13 was determined by a least-squares fit through the data in Fig. 4.6 and the coefficients are given with one standard deviation. Equation 4.13 can be used to predict the current fraction for any SEO or PEO/LiTFSI electrolyte and is valid in the salt concentration range $0.01 < r < 0.30$.

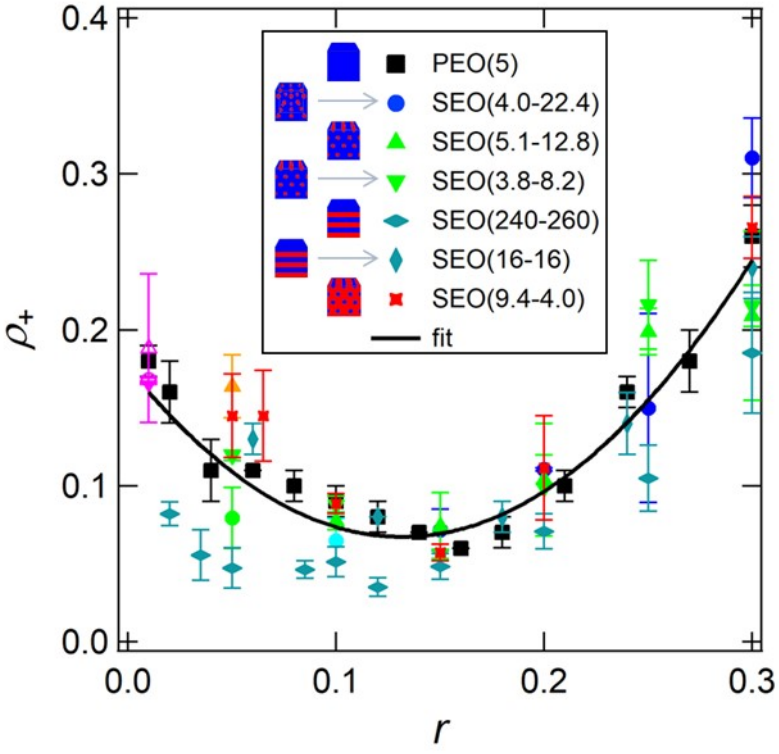

Figure 4.6. Current fraction, ρ_+, for PEO(5) and various SEO electrolytes as a function of r , the molar ratio of lithium ions to ether oxygens. The color of the symbol denotes the morphology: black/homopolymer, blue/BCC', cyan/coexisting BCC' and HEX', green/HEX', gold/GYR', teal/LAM, red/HEX, purple (open)/DIS. The dominant morphology across the range of salt concentrations is indicated by the schematic in the legend. Presence of the non-conducting phase does not have a significant impact on the value of ρ_+ and we are able to fit a universal curve through the data (black line). The solid curve is given by $\rho_+ = 0.18 - 1.7r + 6.3r^2$.

The current fraction is often equated to the cation transference number with respect to the solvent velocity, t_+^0. Much work, however, suggests that there is little correspondence between ρ_+ and t_+^0, especially in polymer electrolytes which exhibit behavior of non-ideal solutions even at low salt concentrations.[43,55,58,79] To calculate t_+^0, we use Eqn. 4.14,

$$t_+^0 = 1 + \left(\frac{1}{\rho_+} - 1\right)\frac{(z_+\nu_+)FDc\phi_c}{\kappa_{nb}}\left(\frac{dU}{d\,ln\,m}\right)^{-1}, \tag{4.14}$$

where z_+ is the charge on the cation and ν_+ is the number of cations in the dissociated salt, F is Faraday's constant (96,485 C mol^{-1}), and c is the molar salt concentration in the conducting domain.[42,51,55] In Eqn. 4.14 we assume that $t_+^0 < 1$ (see Chapter 3). The quantity $c\phi_c$ is equivalent to the moles of salt per unit of total volume (*i.e.* both the conducting and non-conducting domain). c is calculated by Eqn. 4.15,

$$c = \frac{\rho_{PEO}r}{M_{EO} + rM_{LiTFSI}}, \tag{4.15}$$

where M_{LiTFSI} is the molar mass of LiTFSI (287.08 g mol^{-1}).

Ion transport in a block copolymer electrolyte is governed by numerous transport coefficients as discussed in the Introduction. Equation 4.14 is strictly applicable to model nanostructured electrolytes. The limitations of this approach are evident in Fig. 4.5 where deviations from model behavior are seen especially in the low ϕ_c and low r limit.

Calculating t_+^0 from Eqn. 4.14 requires measurement of κ, D, ρ_+, and $\left(\frac{dU}{d\ln m}\right)^{-1}$. In principle, κ is an intrinsic property of the electrolyte and does not depend on the electrodes used to measure it by ac impedance spectroscopy. In practice, we find some differences in the conductivity measured with blocking electrodes, κ, compared to that measured with non-blocking electrodes, κ_{nb}, at some salt concentrations. We compare these values in Fig. 4.7 for (a) SEO(4.0-22.4), (b) SEO(5.1-12.8), (c) SEO(3.8-8.2), and (d) SEO(9.4-4.0). The general trends discussed above in the context of Fig. 4.2 apply to the data in Fig. 4.7. The largest difference between κ and κ_{nb} is seen in SEO(9.4-4.0) at r = 0.10. However even for this electrolyte, κ and κ_{nb} are within experimental error for $r \geq 0.15$. Differences between κ and κ_{nb} may arise for block copolymer electrolytes due to differences in the morphology of the block copolymer at the electrode-electrolyte interface or differences in thermal history (see Section 4.2.2.). We note in passing that discrepancies between κ and κ_{nb} are found in many instances throughout the literature but without discussion.[63,66,67] For consistency, we use κ_{nb} for the conductivity in Eqn. 4.14 for calculating t_+^0 in SEO(4.0-22.4), SEO(5.1-12.8), SEO(3.8-8.2), and SEO(9.4-4.0) because measurement of D, ρ_+, and $\left(\frac{dU}{d\ln m}\right)^{-1}$ must be done in a cell with lithium electrodes.

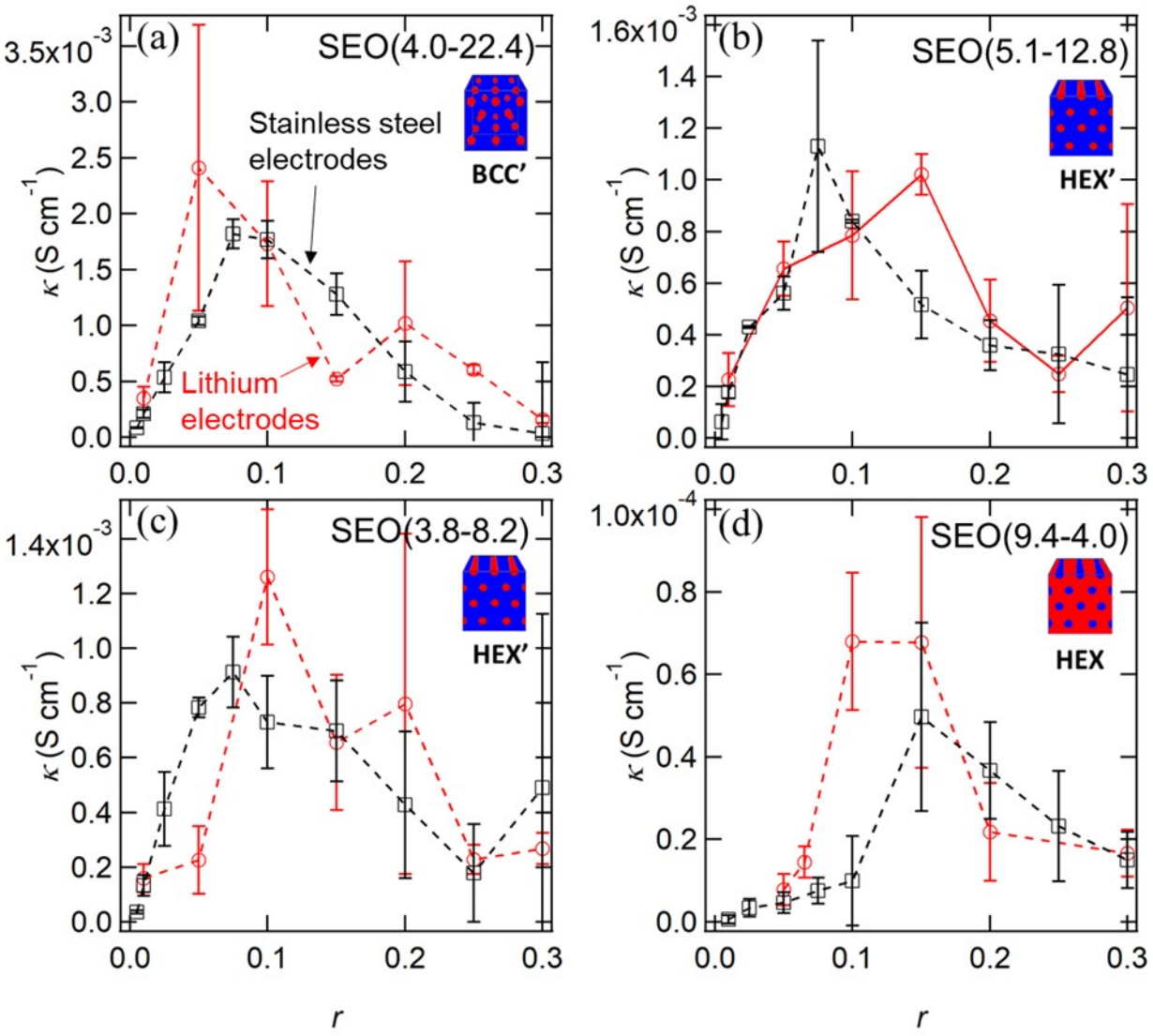

Figure 4.7. Comparison of ionic conductivity measured with blocking versus non-blocking electrodes. Conductivity, κ, measured by ac impedance spectroscopy for (a) SEO(4.0-22.4) which exhibits a BCC' morphology over most salt concentrations, (b) SEO(5.1-12.8) which exhibits a HEX' morphology over most salt concentrations, (c) SEO(3.8-8.2) which exhibits a HEX' morphology over most salt concentrations, and (d) SEO(9.4-4.0) which exhibits a HEX morphology over most salt concentrations. We compare data obtained using lithium/polymer/lithium cells (non-blocking electrodes, red circles) and stainless steel/polymer/stainless steel cells (blocking electrodes, black squares) for each system.

In Fig. 4.8, we present U as a function of the logarithm of the salt molality, $\ln m$, measured in concentration cells for SEO(9.4-4) and SEO(5.1-12.8) using a reference electrolyte salt molality, m_r, of 1.47 mol kg^{-1} (r = 0.065). The slope of U at a given value of $\ln m$ is independent of the reference salt concentration. Choosing a different reference salt concentration results in a vertical shift of U.[91] Therefore, we can include data from previous studies by plotting $U(\ln m)$ with a vertical offset, U', such that $U'(\ln m) = U(\ln m) + C$. We solve for the constant, C, by setting $U'(\ln m) = 0$ at m = 1.47 mol kg^{-1} where $U(\ln m)$ is given by a polynomial fit through the data.

For SEO(16-16), $U(\ln m)$ was reported in ref [124] with m_r = 0.681 (r = 0.030) and we obtained C = 43.0 mV. For SEO(240-260), $U(\ln m)$ was reported in ref [55] with m_r = 1.93 (r= 0.085), and we obtained C = -17.5 mV. For PEO(5), $U(\ln m)$ was reported in ref [58] with m_r = 1.36 (r = 0.060), and we obtained C = 14.6 mV.

We find that U is remarkably consistent across all five systems with ϕ_c varying from 0.3 to 1 and N varying from 80 to 8000. This suggests that the presence of polystyrene does not affect the potential of the concentration cell, and a universal relationship can be used to determine $\frac{dU}{d\ln m}$ for any SEO or PEO/LiTFSI mixture, regardless of morphology, ϕ_c, or N. We fit a single curve through the data in Fig. 4.8 to obtain the function:

$$U = (25 \pm 5) - (74 \pm 7)(\ln m) - (33 \pm 2)(\ln m)^2 - (4.6 \pm 2)(\ln m)^3. \quad (4.16)$$

Equation 4.16 was determined by a least-squares fit through the data in Fig. 4.8 and the coefficients are given with one standard deviation. The coefficients are given with one standard deviation. Equation 4.16 is used to calculate $\frac{dU}{d\ln m}$, which is the last piece of information needed to calculate t_+^0 according to Eqn. 4.14. Uncertainty in using Eqn. 4.16 to calculate $\frac{dU}{d\ln m}$ is greater near the bounds of the data set, especially at the lower bound, so we limit use of Eqn. 4.16 to the range $-0.80 < \ln m < 1.9$ (*i.e.,* $0.02 \leq r \leq 0.3$).

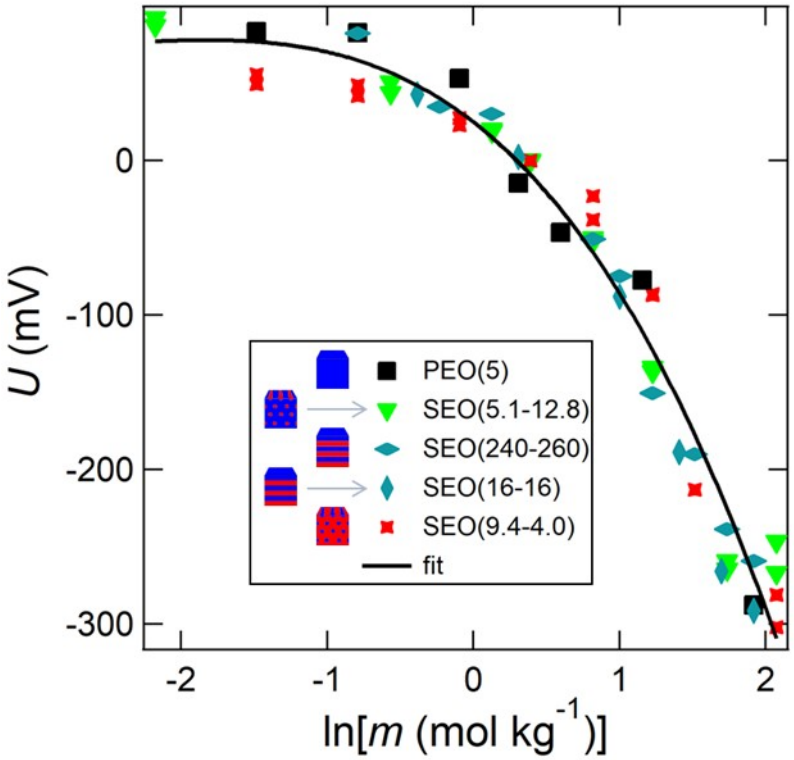

Figure 4.8. Open circuit potential, U, of concentration cells plotted against the natural log of the salt molality, $\ln m$, where m is in mol kg^{-1}. Each data set is vertically offset by a constant such that U = 0 at $\ln m$ = 0.39 (*i.e.* r = 0.065). We fit a universal curve through the data (black line), given by Eqn. 4.16: $U = 25 - 74(\ln m) - 33(\ln m)^2 - 4.6(\ln m)^3$.

We next consider the effect of morphology and ϕ_c on t_+^0 at salt concentrations ranging from r = 0.05 to r = 0.30 in Fig. 4.9a. We calculate t_+^0 from Eqn. 4.14 for SEO(4-22.4), SEO(5.1-12.8), SEO(3.8-8.2) and SEO(9.4-4) electrolytes using κ_{nb} reported in Fig. 4.7, D reported in Fig. 4.3, ρ_+ given by Eqn. 4.13, c given by Eqn. 4.15, and $\frac{d\,U}{d\ln m}$ given by taking the derivative of Eqn. 4.16. t_+^0 has been reported elsewhere for PEO(5), SEO(16-16), and SEO(240-260) electrolytes; however, we recalculate it using the universal relationships presented in this work for ρ_+ and U. We use κ presented in Fig. 4.2 for these systems because measurements of κ_{nb} were not available. We plot t_+^0 as a function of ϕ_c in Fig. 4.9a at various salt concentrations. At low values of ϕ_c, t_+^0 is negative. Increasing ϕ_c results in a maximum around ϕ_c = 0.6 for all salt concentrations. At low salt concentrations (*e.g.* r = 0.05), t_+^0 is a weakly decreasing function of ϕ_c above ϕ_c = 0.6, and the maximum is relatively shallow. At intermediate salt concentrations (*e.g.* r = 0.20), t_+^0 decreases rapidly above ϕ_c = 0.6, reaching a minimum in the vicinity of ϕ_c = 0.8. At high salt concentrations (*e.g.* r = 0.30), the behavior is similar to that seen at low salt concentrations. If the SEO electrolytes behaved as model nanostructured electrolytes, then t_+^0 would be independent of ϕ_c and equal to that of homopolymer electrolytes, represented in Fig. 4.9a by the values at ϕ_c = 1. The horizontal dashed lines in Fig. 4.9a show the behavior expected for model electrolytes at each salt concentration.

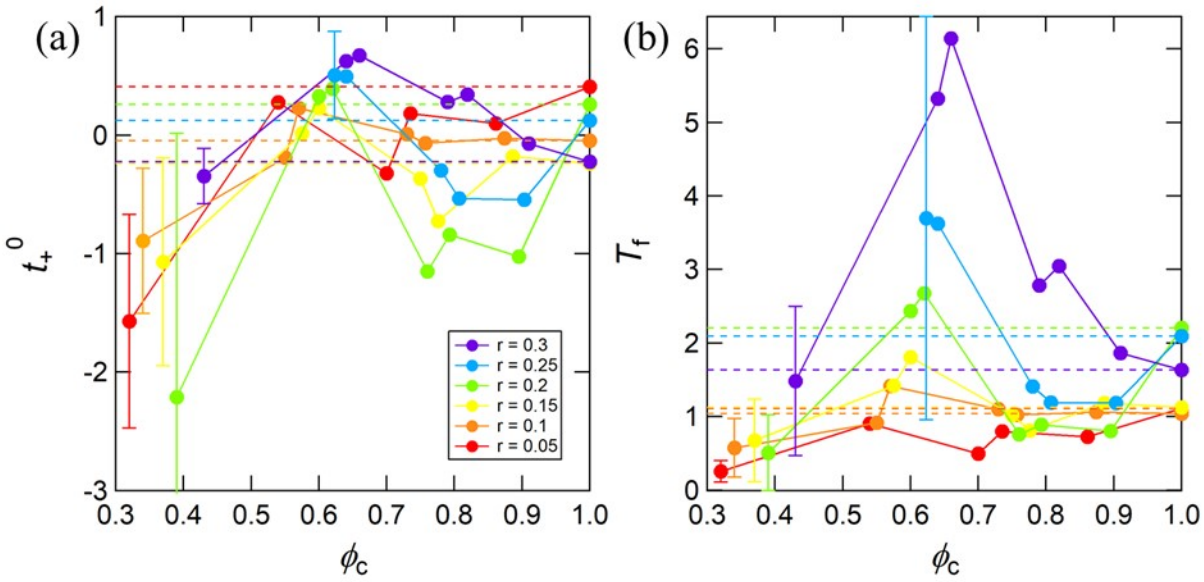

Figure 4.9. Cation transference number and thermodynamic factor as a function of conducting phase volume fraction for SEO/LiTFSI electrolytes with different morphologies. (a) Cation transference number, t_+^0, and (b) thermodynamic factor, T_f, of various SEO morphologies as a function of conducting phase volume fraction, ϕ_c, at salt concentrations ranging from r = 0.05 to r = 0.30. t_+^0 and T_f are calculated based on Eqn. 4.14 and 4.17, respectively. Error bars on the first data point of each data series represent the average percent error for the entire data set. The horizontal dashed lines represent the value of t_+^0 and T_f predicted for model nanostructured electrolytes.

A negative transference number implies the presence of negatively charged ion clusters (containing both Li^+ and $TFSI^-$ ions) which are more mobile than free cations. Molinari et al.

showed that large ion clusters with a net negative charge appeared more frequently in PEO/LiTFSI electrolytes than ion clusters with a net positive charge,[88] providing computational evidence for this hypothesis. t_+^0 is negative and significantly lower than other morphologies for the hexagonally packed PEO cylinders (SEO(9.4-4)) across all salt concentrations (see the range $0.32 < \phi_c < 0.43$ in Fig. 9a), indicating that negatively charged ion clusters especially dominate in this system (see Chapter 3 for further discussion). Electrolytes with values of t_+^0 in the vicinity of unity are expected to operate with minimal salt concentration gradients.

We calculate the thermodynamic factor, $T_f = 1 + \frac{d \ln \gamma_{+-}}{d \ln m}$, for these systems from Eqn. 4.17:

$$T_f = -\frac{z_+ \nu_+}{(\nu_+ + \nu_-)} \frac{F}{2RT(1 - t_+^0)} \left(\frac{d\ U}{d\ ln\, m} \right), \tag{4.17}$$

where R is the ideal gas constant and ν_- is the number of anions in the dissociated salt. As with Eqn. 4.14, Eqn. 4.17 only applies to model nanostructured electrolytes. We plot T_f as a function of ϕ_c in Fig. 4.9b. Here we see a clear trend with increasing salt concentration. At low salt concentrations, T_f is a weak function of ϕ_c. At high salt concentrations, T_f exhibits a pronounced maximum in the lamellar region (ϕ_c between 0.55 and 0.65). The amplitude of the maximum increases systematically with increasing salt concentration. For a thermodynamically ideal electrolyte (nanostructured or homopolymer), T_f = 1. It is clear that the SEO electrolytes are far from thermodynamic ideality, especially at high salt concentrations. In theory, T_f of model nanostructured electrolytes should be independent of ϕ_c and equal to that of the homopolymer PEO electrolyte at the same salt concentration. The dashed horizontal lines represent the theoretical value for model nanostructured electrolytes. These horizontal lines emanate from the data points at ϕ_c = 1 in Fig. 4.9b.

The error bars on the first data point in each series in Fig. 4.9 represent the average percent error for that particular data set. The uncertainty is propagated from the measurements of κ, ρ_+, D, and U, where the error for ρ_+ and U is obtained from the standard deviations of the fit coefficients from the fits in Figs. 4.6 and 4.8. Note that we have used a single function to describe the dependence of ρ_+ and U on salt concentration irrespective of the electrolyte. While the percent errors of t_+^0 and T_f are relatively large, the general trends that we have noted above are consistent across all of the salt concentrations and block copolymer compositions covered in this work.

The thermodynamic factor plays an important role in ion transport as it relates the salt concentration gradient, ∇c, to the electrochemical potential gradient of the electrolyte, $\nabla \mu_e$. This can be seen by combining Eqns. 12.12 and 12.13 of ref [42] to obtain the expression:

$$c \nabla \mu_e = \left[(\nu_+ + \nu_-) RT \left(1 - \frac{d\ ln\, c_0}{d\ ln\, c} \right) \nabla c \right] T_f, \tag{4.18}$$

where $\mu_e = \nu_+ \mu_+ + \nu_- \mu_-$ is the electrochemical potential of the electrolyte, μ_+ and μ_- are the electrochemical potentials of the cation and anion, respectively, and c_0 is the solvent concentration. The product of the salt concentration and the gradient of the electrochemical potential of the electrolyte, $c\nabla\mu_e$, is the driving force per unit volume for transport of the salt. It is evident from

Eqn. 18 that, for a fixed concentration gradient (∇c), an electrolyte with a large value of T_f will have a relatively strong driving force to relieve the concentration gradient.

We conclude this section by reviewing the literature on ion transport in nanostructured block copolymer electrolytes. Irwin et al. examined the relationship between morphology and κ by blending different amounts of PS and PEO homopolymer with a symmetric SEO block copolymer doped with LiTFSI to obtain LAM, HEX, bicontinuous microemulsion, and disordered phases.[109] Their results suggest that reducing long range order and thus resistance across grain boundaries results in increased conductivity, which is consistent with the trend of normalized conductivity with salt concentration in Fig. 4.5a. Morris, Gartner, and Epps have used tapered block copolymer electrolytes to demonstrate the relationship between conductivity and the glass transition temperature.[137] Park and coworkers have demonstrated that introducing strongly interacting end groups to block copolymers can be used as a tool to tune morphology while holding N and ϕ_c constant.[27] The resulting LAM and GYR morphologies show similar conductivities, in agreement with Fig. 4.5a and previous work.[138] Interestingly, end-group functionalization has a substantial impact on ρ_+.[139] In an early study, Cho and coworkers used amphiphilic dendrons containing linear PEO doped with lithium triflate salt which exhibit thermally accessible phase transitions to probe the structure-conductivity relationship.[110] Conductivity increases by a factor of six across the 1D HEX to 3D GYR transition in this system, which is a two times larger increase than predicted by effective medium theory. Osuji and coworkers have demonstrated that a magnetic field can be used to align the conducting domains of a PEO-based liquid crystalline diblock copolymer electrolyte, and they compared the conductivity of aligned systems relative to systems with randomly oriented grains. They find a ten-fold increase in conductivity for the HEX morphology[111] and two-fold increase for the LAM morphology,[140] suggesting that deviations from model nanostructured electrolyte behavior are far more prominent in the HEX morphology with randomly oriented grains. These results are consistent with our observation of unexpectedly low conductivity for the HEX morphology in SEO (see Fig. 4.5a).

4.4 Conclusions

The nature of small molecule transport through polymer membranes is complicated when the membrane consists of two (or more) distinct phases. For the simplest case where the small molecule is insoluble in the second phase, we can perhaps make the simplification that the inert phase only serves to divert the paths of the small molecules. For a block copolymer electrolyte doped with a lithium salt, this simplification allows us to assume a three component system (solvent, cation, and anion) wherein ion transport is governed by the ionic conductivity, κ, salt diffusion coefficient, D, cation transference number with respect to the solvent velocity, t_+^0, and thermodynamic factor, T_f and the role of the insulating phase is quantified by the tortuosity, τ, and morphology factor, f. Such a system is termed a model nanostructured electrolyte. We use this framework to fully characterize ion transport in a library of SEO/LiTFSI electrolytes (summarized in Table 4.1) with different conducting phase volume fractions, ϕ_c, and chain lengths, N. By systematically varying ϕ_c and N to obtain electrolytes with different morphologies and measuring the transport properties, we can begin to elucidate the role of the insulating (PS) phase.

Our results show that κ and D are strong functions of morphology while the current fraction, ρ_+, and $\frac{\mathrm{d}U}{\mathrm{d}\ln m}$ from concentration cells do not depend on morphology. The quantities ρ_+ and $\frac{\mathrm{d}U}{\mathrm{d}\ln m}$ are required to calculate t_+^0 and T_f. We fit universal curves through data from PEO/LiTFSI and multiple SEO/LiTFSI systems for these parameters. These fits should apply to any SEO/LiTFSI or PEO/LiTFSI mixture. Measurements of κ and D from SEO block copolymer electrolytes with different morphologies can be presented on the same plot using a normalization scheme presented in Eqns. 4.11 and 4.12. We compare experimental measurements of the normalized quantities κ_n and D_n to predictions based on values of τ and f for model nanostructured electrolytes in Table 4.2 (see Fig. 4.5). Experimental data for t_+^0 and T_f based on the assumption of model electrolytes are given in Fig. 4.9. Deviations from model behavior are most evident at low salt concentrations in κ_n (see Fig 4.5a). Conversely, the largest deviations from model behavior are seen at high salt concentration for T_f (see Fig 4.9b). This suggests that, at low salt concentration, the structure of the block copolymer (including morphology, grain boundaries, defects, etc.) results in ion transport through the conducting domain that is fundamentally different than that which occurs in PEO homopolymer with the same salt concentration. Conversely, at high salt concentrations, the presence of the PS domains result in thermodynamic interactions of the salt which are fundamentally different than that which occurs in PEO homopolymer at the same salt concentration.

The framework developed in this paper enables predicting the performance of any block copolymer electrolyte in a rechargeable battery. Further work[46,113] is required to test these predictions, which we address in Chapter 7.

4.5 Acknowledgement

This work was supported by the Assistant Secretary for Energy Efficiency and Renewable Energy, Office of Vehicle Technologies of the U.S. Department of Energy under Contract DE-AC02-05CH11231 under the Battery Materials Research Program.

4.6 Nomenclature

Table 4.3 List of symbols and abbreviations

Symbol	Meaning
A	electrochemical active area of a cell (cm^2)
BCC	body centered cubic morphology with PEO-rich spheres
BCC'	body centered cubic morphology with PS-rich spheres
c	salt concentration in the conducting phase (mol cm^{-3})
c_0	solvent concentration in the conducting phase (mol cm^{-3})
C	constant offset applied to U versus $\ln m$ data (mV)
D	salt diffusion coefficient (cm^2 s^{-1})
D_m	salt diffusion coefficient of a model nanostructured electrolyte (cm^2 s^{-1})
D_n	normalized salt diffusion coefficient

DIS	disordered morphology
f	morphology factor
F	faraday's constant (96,485 C mol^{-1})
GYR	double gyroid morphology with a minority PEO phase
GYR'	double gyroid morphology with a minority PS phase
HEX	hexagonally packed cylinders morphology with PEO-rich cylinders
HEX'	hexagonally packed cylinders morphology with PS-rich cylinders
i_Ω	initial current density calculated using Ohm's law (mA cm^{-2})
i_{ss}	current density measured at steady-state during dc polarization (mA cm^{-2})
L	electrolyte thickness (cm)
LAM	lamellar morphology with alternating PS- and PEO-rich domains
LiTFSI	bis(trifluoromethane)sulfonimide lithium salt
m	molality of the conducting domain (mol kg^{-1})
m_r	molality of the conducting domain of the reference electrolyte in a concentration cell (mol kg^{-1})
M_{EO}	molar mass of an ethylene oxide monomer (44.05 g mol^{-1})
M_{LiTFSI}	molar mass of LiTFSI (287.08 g mol^{-1})
M_{PEO}	number averaged molecular weight of PEO (kg mol^{-1})
M_{PS}	number averaged molecular weight of PS (kg mol^{-1})
M_S	molar mass of a styrene monomer (104.1 g mol^{-1})
N	number of repeat units in a polymer or block copolymer chain
N_A	Avogadro's number (6.022×10^{23} mol^{-1})
N_i	number of repeat units of component *i* in a block copolymer chain
PEO	poly(ethylene oxide)
PS	polystyrene
r	molar ratio of lithium ions to ethylene oxide moieties, $r = [Li]/[EO]$
R	ideal gas constant (8.314 J mol^{-1} K^{-1})
R_b	bulk resistance of the electrolyte measured by ac impedance spectroscopy (Ω)
$R_{i,0}$	interfacial resistance measured by ac impedance spectroscopy before dc polarization (Ω)
$R_{i,ss}$	interfacial resistance measured by ac impedance spectroscopy at steady-state during dc polarization (Ω)
SAXS	small angle X-ray scattering
SEO	polystyrene-*block*-polyethylene
SEO(*x*-*y*)	SEO with M_{PS} = *x* kg mol^{-1} and M_{PEO} = *y* kg mol^{-1}
t	time (s)
t_+^0	transference number of the cation with respect to the velocity of the solvent
T	temperature (K)
T_f	thermodynamic factor
U	open circuit potential of a concentration cell (mV)

U'	open circuit potential of a concentration cell offset by a constant, C (mV)
ΔV	dc potential drop applied across a symmetric cell (mV)
v_{c}	volume of the conducting phase per ethylene oxide monomer (nm^3)
v_{EO}	volume of the ethylene oxide monomer at 90 °C (0.0682 nm^3)
v_{S}	volume of the styrene monomer at 90 °C (0.167 nm^3)
z_+	charge number of the cation

Table 4.3 List of symbols (Greek)

Symbol	Meaning
γ_{+-}	mean molal activity coefficient of the electrolyte
κ	ionic conductivity of an electrolyte (S cm^{-1})
κ_{m}	ionic conductivity of a model nanostructured electrolyte (S cm^{-1})
κ_{n}	normalized ionic conductivity
κ_{nb}	ionic conductivity of an electrolyte measured in a cell with non-blocking electrodes (S cm^{-1})
μ_+, μ_-	electrochemical potential of the cation and anion, respectively (J mol^{-1})
μ_{e}	electrochemical potential of the electrolyte (J mol^{-1})
ν_+, ν_-	number of cation and anions, respectively, in the dissociated salt
ρ_+	current fraction
ρ_{c}	density of the conducting phase (g cm^{-3})
ρ_{PEO}	density of PEO at 90 °C (1.07 g cm^{-3})
ρ_{PS}	density of PS at 90 °C (1.03 g cm^{-3})
τ	tortuosity factor
ϕ_{c}	volume fraction of the conducting phase in a salty block copolymer
ϕ_{EO}	volume fraction of PEO in a neat block copolymer

5. Dissolution of Lithium Metal in Poly(ethylene oxide)[‡]

ABSTRACT

We demonstrate that lithium metal is sparingly soluble in poly(ethylene oxide) (PEO). ^{7}Li NMR shows that when a PEO sample is placed in contact with lithium metal at elevated temperatures, a lithium species dissolves and diffuses into the bulk polymer. A lithium/PEO/lithium electrochemical cell, containing no lithium salts, shows increasing conductivity over time when annealed at 120 °C. Chronoamperometry shows that the annealed cell obeys Ohm's law, implying that conduction occurs without the development of concentration gradients. To explain the results, it is proposed that atomic lithium dissolves into PEO, where it exists as a lithium cation and free electron. The dissolution of lithium also affects the phase behavior of block copolymer electrolytes. These observations explain the strong adhesion between lithium metal and PEO and have important implications for lithium metal battery systems that contain PEO-based electrolytes.

5.1 Introduction

Rechargeable batteries containing a lithium metal anode will provide the next step towards more efficient energy storage compared to today's lithium ion batteries.[8] While lithium metal batteries were once produced commercially, several issues resulted in their retraction from the market place. Organic liquid electrolytes currently used in lithium-ion batteries cannot be used in cells with lithium metal anodes due to dendrite formation, irreversible parasitic reactions at the lithium-electrolyte interface, and the increased likelihood that a short circuit will ignite the flammable electrolyte.[141,142] Solid electrolytes provide an attractive option to enable lithium metal anodes.[101]

Salt-doped poly(ethylene oxide) (PEO) has been studied extensively due to its potential to enable rechargeable batteries with lithium metal anodes.[17,19,58,143] Mixtures of PEO and salt exhibit reasonable conductivities at temperatures above the melting point of PEO. PEO-based solid electrolytes can be prepared by adding salts to a block copolymer comprising a PEO block and a mechanically rigid block such as polystyrene (PS). A remarkable property of the interface between PEO-based electrolytes (both homopolymers and block copolymers) and lithium metal is the observation that good mechanical and electrical contact are maintained even when tens of micrometers of lithium are displaced during cycling.[31,144] Rigid, inorganic solid electrolytes (ceramics and glasses) have also been used to stabilize the lithium metal anode but are limited by high interfacial resistance and require large applied pressures.[13] In contrast, cells with polymer electrolytes and lithium metal anodes cycle with no applied pressure.[145] In spite of extensive studies,[146,147] the nature of the PEO-lithium interface is not well understood.

[‡] Adapted (with permission) from Galluzzo, M. D.; Halat, D. M.; Loo, W. S.; Mullin, S. A.; Reimer, J. A.; Balsara, N. P. Dissolution of Lithium Metal in Poly(ethylene oxide). *ACS Energy Lett.* **2019**. *4* (4), 903-907.

We report herein a simple observation that provides fresh insight into the nature of the PEO-lithium interface: lithium metal is sparingly soluble in PEO. Primary evidence comes from ^{7}Li nuclear magnetic resonance (NMR) spectroscopy. In addition, we present the signatures of lithium dissolution in electrochemical cells as well as changes in the thermodynamic properties of a PEO-containing block copolymer electrolyte. To our knowledge, this is the first report of metal solubility in a polymer.

5.2 Experimental Section

5.2.1 Materials

All hydroxy terminated poly(ethylene oxide) (PEO) was purchased from Polymer Source. 2 kg mol^{-1} PEO terminated with dimethyl ether was purchased from Sigma Aldrich. Before use, polymers were dried under vacuum at 130°C for at least 24 hours. The polystyrene-*block*-poly(ethylene oxide) (SEO) block copolymers used in this study were synthesized, purified, and characterized using methods described by Teran et al.[24] and Hadjichristidis et al.[114] The block copolymer electrolyte used in Fig. 5.4 of Section 5.3 (PS molecular weight of 1.7 and PEO molecular weight of 1.4 kg mol^{-1}) was prepared following the methods of Yuan et al.[116] to produce an SEO/LiTFSI mixture with a molality of 1.70 mol kg^{-1}. Lithium metal was purchased from MTI and scraped with a nylon brush prior to use to expose a fresh lithium surface.

5.2.2 Sample Preparation

All sample preparation was performed in an argon filled glove box (VAC) with oxygen and water concentrations maintained below 3 and 1 ppm respectively. Electrochemical and small angle X-ray scattering (SAXS) samples were assembled by placing polymer inside a silicone rubber spacer sandwiched by two lithium, stainless steel, or aluminum electrodes/windows and gently pressed on a hot plate at 90 °C. For electrochemical cells, nickel current collectors were attached. Electrochemical and small angle X-ray scattering (SAXS) samples were sealed in aluminum laminated pouch material purchased from MTI.

5.2.3 Nuclear Magnetic Resonance (NMR) Spectroscopy

NMR measurements were performed at 14.1 T using a 600 MHz Bruker Avance III spectrometer with a 5 mm PABBO direct detection broad-band probe (BB-1H/D Z-GRD) and a variable temperature unit. All measurements were performed at 90 °C. The temperature was calibrated prior to the experiment using the known temperature dependence of the 1H chemical shift of ethylene glycol.[148] Measurements were performed on ^{7}Li at a resonance (Larmor) frequency of 233.23 MHz with a 90° pulse time of 12 μs at a power level of -1 dB, acquisition time of 0.1 s, and relaxation (recycle) delay of 1 s. Samples were placed in coaxial borosilicate NMR tubes (5.0 mm outer tube diameter and 3.3 mm inner tube diameter) purchased from Wilmad and sealed with custom built air-free caps. The PEO sample was placed in the inner tube and a standard solution of LiTFSI in tetraglyme was placed in the outer tube. The mass of both the PEO

and standard were recorded (approximately 50 mg each). Because the volume of the sample was small (taking up less than 1 cm of the NMR tube), we assume that the entire sample contributed to the signal observed, and the signal can be normalized to the mass of the sample. Each individual spectrum was the result of 1600 scans to enhance signal to noise.

5.2.4 Electrochemical Measurements

All electrochemical measurements were made using a Biologic VMP3 potentiostat. Cells were maintained at 120 °C using a custom-built heating stage. Ac impedance measurements were made in a frequency range from 1 MHz to 100 mHz with an amplitude of 80 mV.

5.2.5 Small Angle X-ray Scattering (SAXS)

Lithium symmetric cells were assembled shortly before the SAXS experiments and maintained at room temperature prior to the experiment. Sample temperature was maintained using a custom-built heating stage calibrated with a separate polyethylene standard. Silver behenate was used to determine the beam center and sample-to-detector distance. Two-dimensional scattering patterns were integrated azimuthally using the Nika program for IGOR Pro to produce one-dimensional scatter profiles[149]. The stage temperature was ramped at roughly 10 °C per minute. $t = 0$ for the SAXS experiments was set as the time that the heating stage reached 120 °C.

5.2.6 Gel Permeation Chromatography (GPC)

Measurements were made on an Agilent 1260 Infinity series GPC with Waters Styragel HR 3 and 4 columns. The eluent was n-methyl-2-pyrrolidone (NMP) with 0.05 M LiBr at 70 °C. The GPC was calibrated using a set of PEO standards (Fluka).

5.2.7 Fourier Transform Infrared (FTIR) Spectroscopy

Measurements were taken on a Thermo Fisher FTIR spectrometer using an air-free attenuated total reflectance attachment at room temperature.

5.3 Results and Discussion

A cell comprising two lithium foils sandwiched around a 2 mm thick PEO sample was sealed in an aluminum laminated pouch and placed in an oven at 130 °C. After 12 days, the sample was removed from the oven, cooled to room temperature, and brought into the glovebox to remove the lithium foils. Lithium metal adheres strongly to PEO. A razor blade was used to extract a slice of the polymer from the middle of the cell (taking care to exclude the lithium foils). We performed this experiment on three PEO samples with molecular weights 5, 35, and 275 kg mol^{-1}.

The PEO sample was placed in a 3.3 mm NMR tube and inserted into a 5 mm tube designed for a coaxial sample configuration. The outer compartment was then filled with a solution of bis(trifluoromethylsulfonyl)amine lithium salt (LiTFSI) in tetraglyme with known salt

concentration. The mass of the PEO sample and the LiTFSI/tetraglyme solution was roughly 50 mg each. The entire coaxial sample was sealed with a hermetic cap and removed from the glovebox. Variable temperature ^{7}Li NMR was performed at 90 °C using a Bruker Avance III 600 MHz spectrometer. (For the purpose of the NMR experiment, it is only important that the sample temperature be above the melting temperature of PEO.) The ^{7}Li NMR spectra are plotted as open circles for 5, 35, and 275 kg mol^{-1} in Figs. 5.1a through 5.1c.

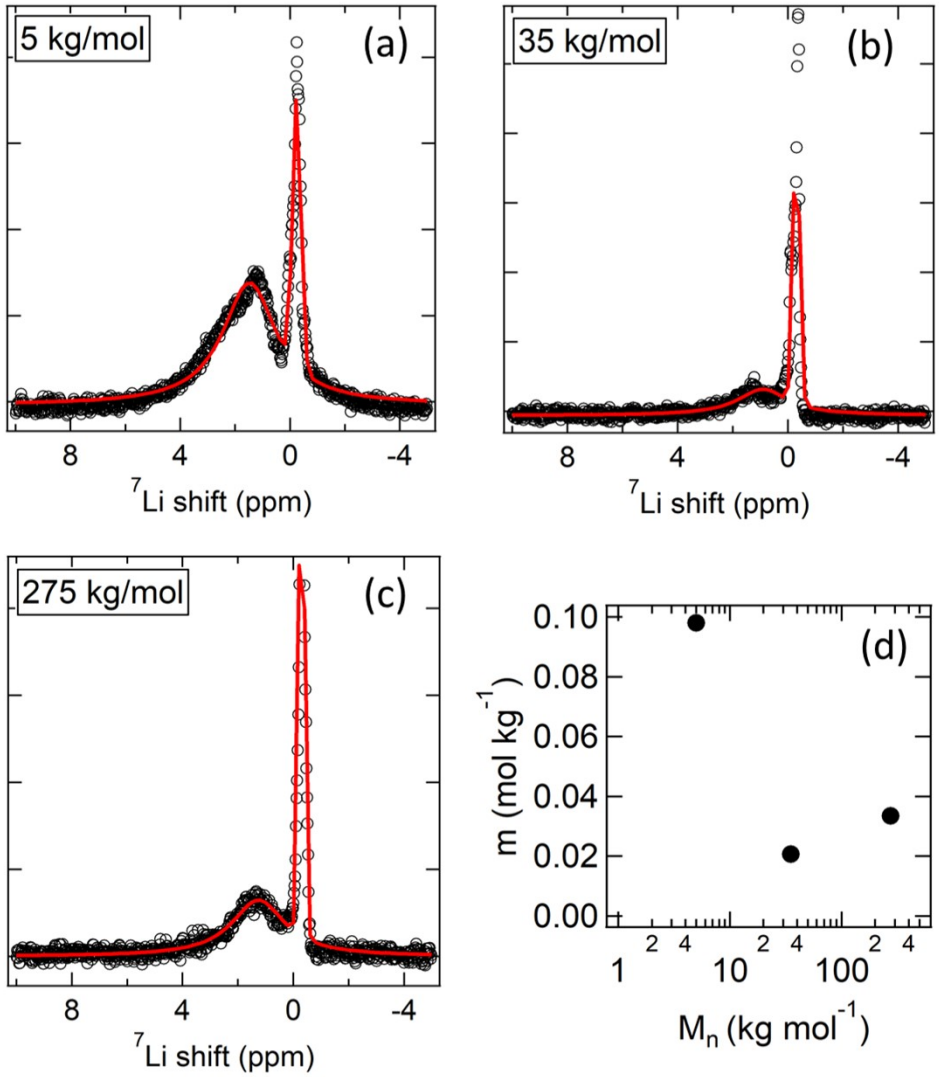

Figure 5.1. Evidence of lithium dissolution from nuclear magnetic resonance spectroscopy (NMR). ^{7}Li NMR spectra (open circles) of (a) 5 kg mol^{-1} (b) 35 kg mol^{-1} and (c) 275 kg mol^{-1} PEO annealed against lithium metal for 12 days at 130 °C in a coaxial NMR tube with a reference solution in the outer compartment. Red lines are fits to the experimental data. (d) Lithium molality as a function of PEO molecular weight calculated by comparing peak integrations from the lithium in the PEO sample to the reference.

In Fig. 5.1a (5 kg mol^{-1} PEO), we see two peaks in the spectrum; a broad peak at approximately 1.5 ppm and a sharper peak at -0.2 ppm. NMR spectra from samples without the

reference solution only showed a broad peak at 1.5 ppm (see Fig. 5.5a). The sharp peak is attributed to the LiTFSI in tetraglyme. We note in passing that the NMR signature of lithium metal is a peak at 260 ppm.[150] In order to deconvolute the integrated intensity of the two peaks in Fig. 5.1a, we fit the broad peak to a Lorentzian function and the sharp peak to a Gaussian function. The combined fit is shown as a red line in Fig. 5.1a. We then obtained the integrated intensity for each peak and compare them to solve for the lithium concentration (in molality, m) in the PEO sample (see details of calculation in Section 5.6.1). Qualitatively similar results are obtained for 35 and 275 kg mol^{-1} PEO in Fig. 5.1b and 5.1c annealed at 130 °C. While the dependence on the dissolution process with annealing temperature remains to be determined, we have observed qualitatively similar results (i.e. NMR signatures of a solvated lithium species) in samples annealed for a variety of annealing times and at annealing temperatures ranging from 90 °C to 140 °C.

Figure 5.1d shows the lithium concentration in molality as a function of PEO molecular weight. In 5 kg mol^{-1} PEO, the molality of lithium is 0.1 mol kg^{-1}. We note that a typical PEO/LiTFSI electrolyte will have an LiTFSI molality between 1.0 and 2.0 mol kg^{-1}. When the molecular weight is increased to 35 kg mol^{-1}, we observe a decrease in the lithium concentration by a factor of about 5. The lithium concentration in the 275 kg mol^{-1} sample is similar to that in the 35 kg mol^{-1} sample. If the dissolution mechanism was facilitated by a reaction with the hydroxy end groups, we would expect the lithium concentration to be proportional to the molecular weight. This suggests that the lithium dissolution occurs due to an interaction with the ether backbone of the polymer chain. Gel permeation chromatography (GPC) and Fourier transform infrared spectroscopy (FTIR) experiments on the PEO/Li mixtures (presented in Fig. 5.6 and 5.7 of Section 5.6.3, respectively) indicate that the PEO chains are not degraded by the dissolution process.

To further characterize the solvated lithium species, we assembled lithium/PEO/lithium cells and performed electrochemical impedance spectroscopy while annealing them at 120 °C. The thickness of the PEO layer (L) was 275 μm. Figure 5.2a shows representative Nyquist plots for the 35 kg mol^{-1} PEO sample over the course of 7 days at 120 °C. The diameter of the semicircle presented in the Nyquist plot is a measure of the overall resistance of the PEO layer. Pure PEO conducts neither electrons nor ions, and at early times (less than 1 day), the Nyquist plot indicates a resistance of 100 kΩ cm^2. We attribute this to the presence of ionic impurities with the PEO. The diameter of the Nyquist semicircle decreases significantly after two days of annealing, and it reaches a plateau after seven days. The data in Fig. 5.2a can be used to calculate conductivity, κ, as a function of time (see details in Section 5.6.2). The results are shown in Fig. 5.2b. Over the timescale of seven days, κ increases by a factor of 16. We attribute this increase to the dissolution of lithium species in PEO. We also performed a control experiment wherein PEO was sandwiched between stainless steel electrodes at 120 °C. The result of this experiment is shown in Fig. 5.2b. In the control experiment, κ is more-or-less independent of time in the window between 2 hours and 7 days. The finite conductivity measured in the control experiment is attributed to impurities. It is clear that contacting PEO with lithium metal results in the dissolution of lithium species that contribute to conductivity.

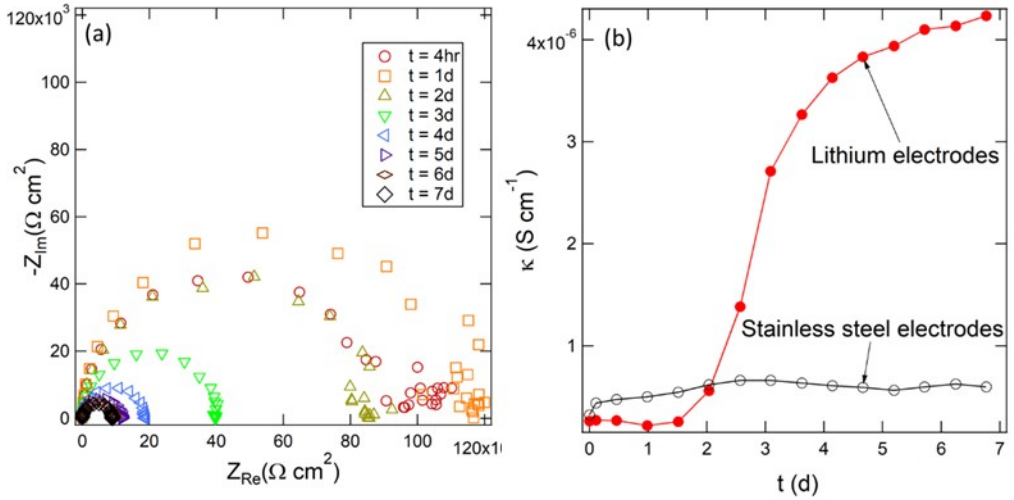

Figure 5.2. Evidence of lithium dissolution in PEO from ac impedance spectroscopy. (a) Representative series of Nyquist plots obtained from a lithium/35 kg mol^{-1} PEO/lithium cell annealed at 120 °C over the course of 7 days. (B) Conductivity, κ, of a lithium/35 kg mol^{-1} PEO/lithium (closed symbols) and stainless steel/35 kg mol^{-1} PEO/stainless steel cell (open symbols) as a function of time at 120 °C.

Figure 5.3 presents the results of a dc polarization experiment on a lithium/PEO/lithium cell (L = 500 μm). The cell, containing 35 kg mol^{-1} PEO, was annealed at 120 °C for 10 days and the resulting Nyquist plot is shown in Fig. 5.3a. The resistance of the PEO with dissolved lithium species is 5.7 kΩ cm^2 at this point. A constant potential, Φ, of 19 mV was applied to the cell and the resulting current density, i, as a function of time is shown in Fig. 5.3b. When lithium salts are dissolved in PEO, a gradual decrease in i is typically observed due to the development of salt concentration gradients.[47,53] In contrast, i is independent of time in Fig. 5.3b. This is the characteristic of conduction in samples without concentration gradients, *e.g.,* a single-ion conductor.[151,152] In the absence of concentration gradients, i can be calculated using Ohm's law (see Section 2.2). The calculated i, 3.3 μA cm^{-2}, is similar to the measured value of 3.4 μA cm^{-2}. After imposing Φ = 19 mV across the cell for 66 min, the current was set to zero and the resulting Φ (i.e. the open circuit potential) was monitored as a function of time. The result is shown in Fig. 5.3c where we see that the open circuit potential drops instantaneously to zero. This is also a property of conductors without concentration gradients. The dissolved lithium species thus enable conduction in PEO without the introduction of concentration gradients.

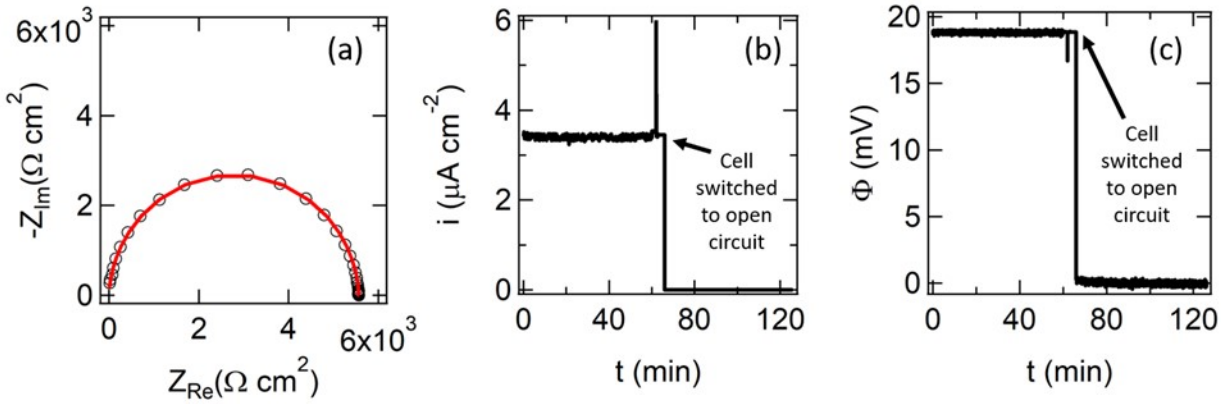

Figure 5.3. Electrochemical signatures of lithium dissolution in PEO. Electrochemical data from a chronoamperometry experiment preformed on a Li/35 kg mol^{-1} PEO/Li cell after being annealed at 120 °C for 10 days. (a) Nyquist plot (open circles) from ac impedance spectroscopy performed before polarization. The cell resistance is obtained by fitting to an equivalent circuit (red line). (b) Current density, i, measured in response to a 19 mV polarization. i is set to zero at t = 66 min. (c) Cell potential, Φ, monitored over the course of the experiment. At t = 66 min, the cell is set to open circuit (i.e. i = 0). The applied potential was momentarily interrupted at t = 60 min, resulting in the spike observed in (b) and (c).

We posit that the dissolved lithium species in PEO comprise a lithium cation and free electron. It is well known that alkali metals are soluble in polar solvents such as ammonia and cyclic ethers; indeed the solubility of lithium metal in ammonia has been known for over a century.[153] These mixtures are highly reactive electron conductors. While there are many reports of dissolving sodium and potassium in cyclic ethers,[154–157] the possibility of dissolving lithium in ethers has, to our knowledge, not been reported. Additional work is required to establish the properties of lithium metal dissolved in PEO. Recent work has shown that electrical conductivity can be obtained in a radical-containing polymer.[158] The observed conduction in PEO with dissolved lithium could be due to the mobility of lithium cations, free electrons, or both.

Block copolymers exhibit a reversible order-to-disorder transition, and dissolving salts is known to stabilize the ordered phase.[159–161] In particular, the addition of LiTFSI to polystyrene-*block*-polyethylene oxide (SEO) results in an increase in the order-to-disorder transition temperature (T_{ODT}).[38] Figure 5.4a presents a phase diagram of an SEO block copolymer with a PS molecular weight of 1.7 kg mol^{-1} and PEO molecular weight of 1.4 kg mol^{-1} reproduced from ref [38]. (The molecule is terminated by a sec butyl group and a hydroxy group on the PS and PEO ends, respectively.) The system exhibits a disordered phase at low salt concentrations and an ordered lamellar phase at high salt concentrations. The T_{ODT} of SEO/LiTFSI mixtures is plotted as a function of salt molality, m, in Fig. 5.4a.

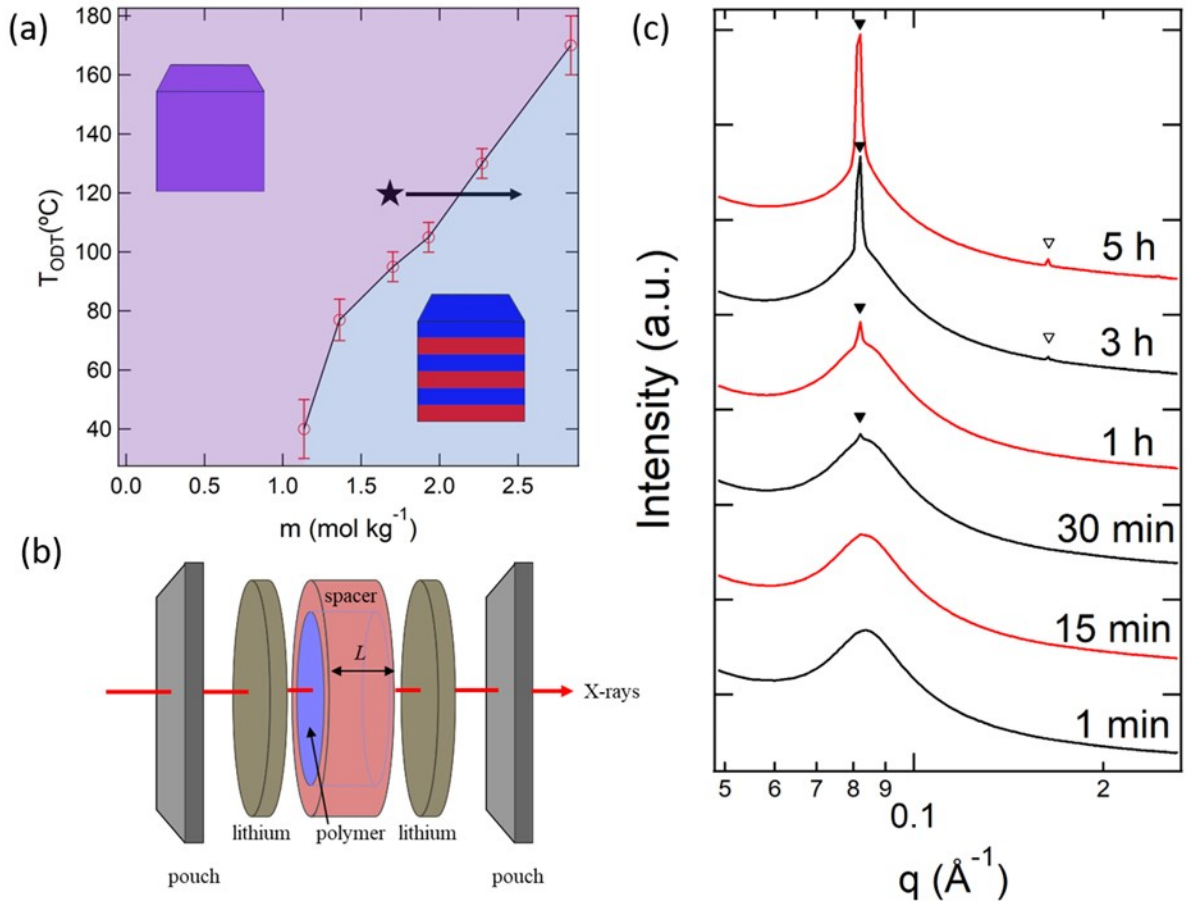

Figure 5.4. Signatures of lithium dissolution into a PEO-containing block copolymer from small angle X-ray scattering. (a) Order-to-disorder transition temperature (T_{ODT}) of the SEO/LiTFSI mixture as a function of LiTFSI molality, m, denoted by open circles[38]. (b) Sample configuration for the SAXS experiments, indicating the orientation of the X-ray beam. (c) SAXS profiles of the SEO/LiTFSI mixture as a function of time. Filled and open triangles indicated the appearance of a primary and secondary scattering peak at q^* and $2q^*$, respectively.

We sandwiched an SEO/LiTFSI mixture with m = 1.70 mol kg^{-1} and L = 380 μm between two lithium windows and studied the morphology of this mixture as a function of time at 120 °C using small angle X-ray scattering (SAXS). At equilibrium (i.e. with inert windows), this sample is disordered and the filled star in Fig. 5.4a indicates the position of this sample on the phase diagram. All SAXS measurements were performed at beamline 7.3.3. of the Advanced Light Source (ALS) at Lawrence Berkeley National Laboratory[162] and data was reduced using the Nika program for IGOR Pro.[149] The sample geometry is shown schematically in Fig. 5.4b. X-rays are passed perpendicular to the lithium windows. The time dependent SAXS profiles thus obtained are shown in Fig. 5.4c.

At early times, the SAXS profile contains a broad scattering peak which is a standard signature of disordered concentration fluctuations.[163] This is not surprising, as the mixture is 25 °C above the T_{ODT}. However, the emergence of a sharp scattering peak superimposed on the broad peak after 15-30 minutes indicates the presence of an ordered phase. As time proceeds, the sharp

peak grows at the expense of the disordered peak. After 5 hours, the sample is nearly completely ordered as indicated by a sharp primary peak at $q = q^*$. The second order peak at $q = 2q^*$ confirms that the ordered phase is lamellar. A control experiment was performed using aluminum windows. The resulting SAXS profiles were independent of time with a scattering profile characteristic of a disordered morphology (see Fig. 5.8b in Section 5.6.3). Qualitatively similar results are shown for a higher molecular weight SEO polymer with no lithium salts added. A disorder-to-order transition occurs at a temperature greater than 40 °C above the T_{ODT} when placed in contact with lithium metal (see Fig. 5.8a in Section 5.6.3). The SAXS data in Fig. 5.4c and 5.8a indicate that the lithium species that dissolves into the SEO copolymer (with or without LiTFSI present) stabilizes the ordered phase. The arrow in Fig. 5.4a qualitatively depicts this phenomenon. This result is consistent with the phenomena observed when neat PEO is placed against lithium metal and confirms that the lithium dissolution process occurs in both homopolymer and block copolymers.

5.4 Conclusions

In summary, we have shown that when PEO-containing polymers are placed against lithium metal, lithium ions along with the associated electrons dissolve into the polymer. This dissolved species is shown to affect the conductivity of the polymer as well as the thermodynamics of block copolymer systems. These results have important implications for battery systems containing lithium metal and any PEO-based material. On one hand, the dissolution of lithium metal may be problematic and lead to decreased coulombic efficiency. On the other hand, it may explain why PEO-containing polymers exhibit strong adhesion to lithium metal, even in the case of block copolymers with high elastic moduli. Future work should be directed at characterizing the chemical environment of the solvated lithium, determining the solubility limit, and studying the dissolution process when a lithium salt is present.

5.5 Acknowledgement

This work was supported by the Assistant Secretary for Energy Efficiency and Renewable Energy, Office of Vehicle Technologies of the U.S. Department of Energy under Contract DE-AC02-05CH11231 under the Battery Materials Research Program. This research used beamline 7.3.3 of the Advanced Light Source, which is a DOE Office of Science User Facility under contract no. DE-AC02-05CH11231. We thank the UC Berkeley College of Chemistry NMR Facility, and especially Hasan Celik for help with instrumentation. We are thankful to Dr. David Prendergast (Lawrence Berkeley National Laboratory) for helpful scientific discussions.

5.6 Supporting Information

5.6.1 Fitting of NMR Data

All processing of NMR spectra was performed using TopSpin software package from Bruker. The NMR spectra in Fig. 5.1a through 5.1c were fitted to two peaks in order to deconvolute the peak integrations with a linear the offset. The function used to fit the data is given by:

$$I(\delta) = I_0 + G(\delta) + L(\delta), \tag{5.1}$$

where $I(\delta)$ is the intensity at ^{7}Li chemical shift δ in ppm, I_0 is a constant offset, $G(\delta)$ is a Gaussian function given by Eqn. 5.2 and $L(\delta)$ is a Lorentzian function given by Eqn. 5.3.

$$G(\delta) = a\, exp\left[\frac{-(\delta - b)^2}{2c^2}\right] \tag{5.2}$$

$$L(\delta) = \frac{d}{(\delta - e)^2 + f} \tag{5.3}$$

In Eqn. 5.2 and 5.3 *a*, *b*, *c*, *d*, *e* and *f* are fitting parameters.

The resulting fits allowed integration of $G(\delta)$ and $L(\delta)$ to obtain the peak integration for the broad peak, A_{PEO}, at 1.5 ppm (corresponding to lithium dissolved in the PEO sample) and the sharp peak, A_{std} at -0.2 ppm (corresponding to LiTFSI in tetraglyme), respectively:

$$A_{PEO} = \int_{-\infty}^{\infty} G(\delta)\, d\delta \tag{5.4}$$

$$A_{std} = \int_{-\infty}^{\infty} L(\delta)\, d\delta. \tag{5.5}$$

We assume that each lithium atom contributes equal intensity. We can then calculate the mass fraction of lithium in the PEO sample, x_{Li}, by:

$$x_{Li} = x_{Li,std} \frac{m_{std}}{m_{PEO}} \frac{A_{PEO}}{A_{std}}, \tag{5.6}$$

where m_{std} and m_{PEO} are the total mass of the LiTFSI in tetraglyme standard solution and PEO sample, respectively, and $x_{Li,std}$ is the mass fraction of lithium atoms in the standard (note: this value differs from the mass fraction of LiTFSI in the standard solution by a factor equal to the ratio of the molar mass of lithium to the molecular weight of LiTFSI). For all three experiments, $x_{Li,std}$ = 0.000102. Because there is a small amount of lithium (μgs of lithium compared to mgs of PEO), we can assume that the mass of the sample is approximately equal to the mass of the PEO. We can then convert x_{Li} to molality by:

$$m = \frac{x_{Li}}{M_{Li}} \tag{5.7}$$

where M_{Li} is the molar mass of lithium in (6.941×10^{-3} kg mol^{-1}).

5.6.2 Conductivity Measurements

Ac impedance spectroscopy was used to measure the conductivity of the, initially neat, 35 kg mol^{-1} PEO samples annealed against lithium electrodes at 120 °C. The resistance of the cell

was obtained by fitting the Nyquist plot to an equivalent circuit consisting of a resistor and constant phase element in series. The choice of equivalent circuit is justified by the single semi-circle observed in the Nyquist plot. From the fit, the cell resistance, R, was obtained. Conductivity, κ, was calculated using Eqn. 5.8.

$$\kappa = \frac{L}{AR} \tag{5.8}$$

L is the distance between electrodes and A is the interfacial contact area between the electrode and PEO.

5.6.3 Supporting Figures

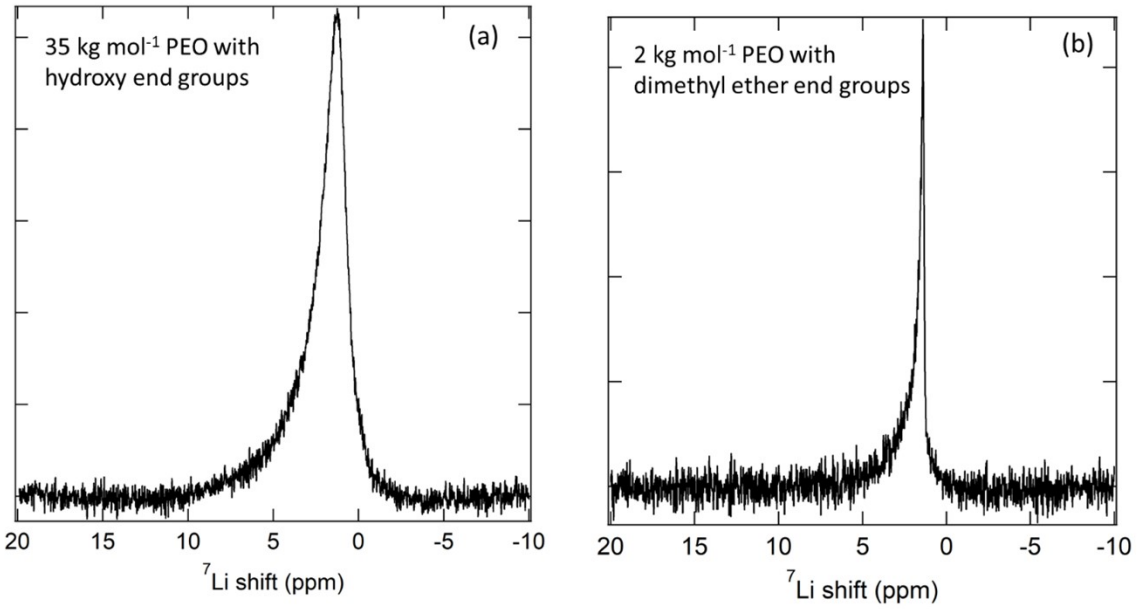

Figure 5.5. Control experiment showing lithium dissolution in PEO with different end groups. (a) ^{7}Li NMR spectrum taken at 90 °C of 35 kg mol^{-1} PEO annealed against lithium in a Li/PEO/Li cell configuration at 90 °C for 12 days. The lithium foils were removed inside the glove box prior to placing the sample in a 5 mm borosilicate NMR tube for characterization. Qualitatively similar spectra were obtained for PEO annealed against lithium at a range of temperatures between 90 and 140 °C and a variety of annealing times from 6 to 20 days. (b) ^{7}Li NMR taken at 90 °C of a 2 kg mol^{-1} PEO sample terminated with dimethyl ether end groups (Sigma Aldrich) annealed against lithium metal for 6 days at 90 °C. Because this sample has a low viscosity at this temperature which makes it difficult to contain in a symmetric cell configuration, the PEO was placed in a glass vial with small pieces of lithium foil placed on top. The sample was then stirred at 90 °C for 6 days before approximately 50 mg of the PEO was removed with a pipette and placed in a 5 mm borosilicate NMR tube for analysis. The peak location for this sample with DME end groups is identical to that shown in (a) for 35 kg mol^{-1} PEO with hydroxy end groups. We attribute the width of the peak in (b) being narrower than in (a) to faster diffusion in 2 kg mol^{-1} PEO. These results indicate that the lithium dissolution process is not limited to PEO molecules terminated with hydroxy end groups, and the nature of the dissolved lithium species is independent of the end group.

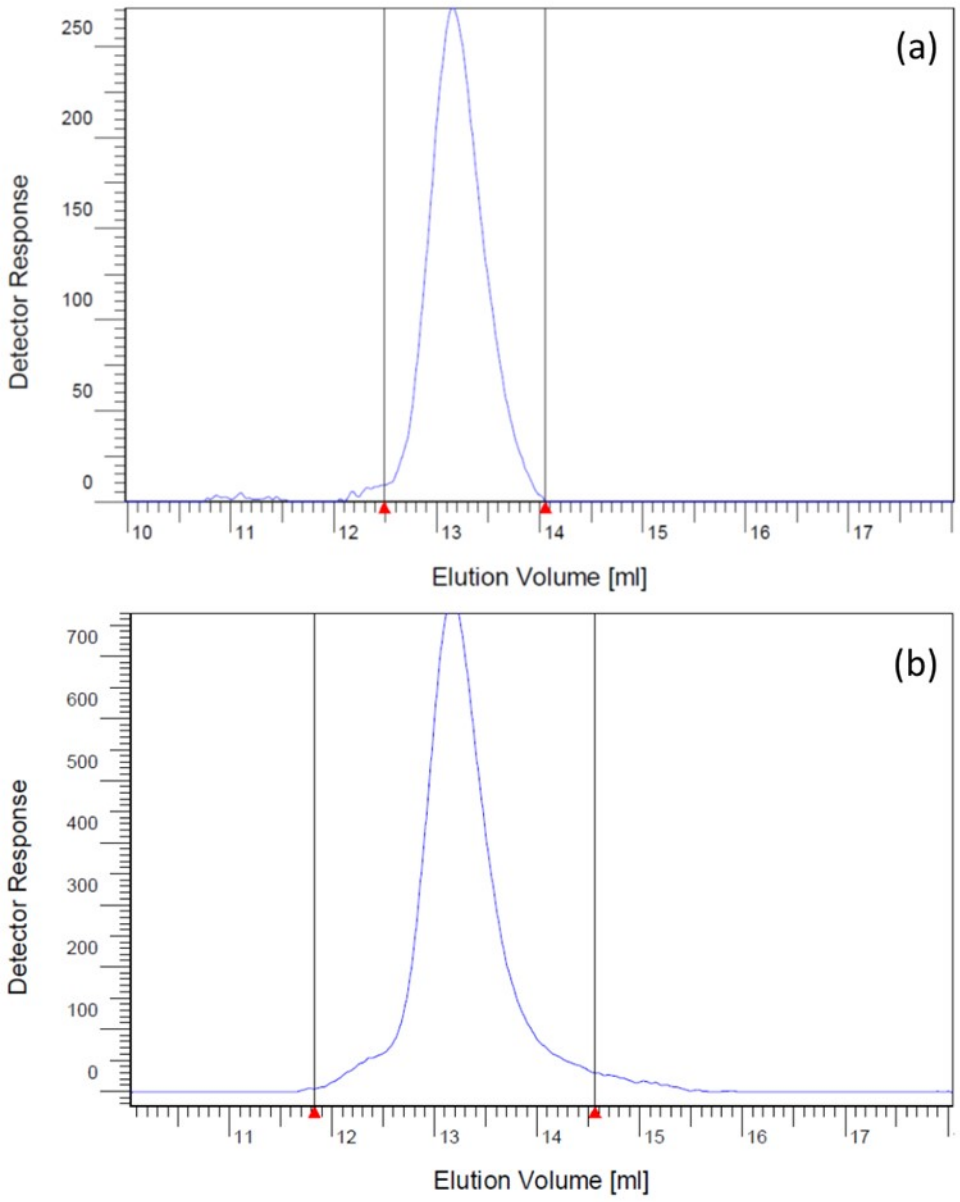

Figure 5.6. GPC results before and after annealing PEO against lithium metal. Gel permeation chromatography (GPC) results for 35 kg mol^{-1} PEO (a) annealed against lithium metal at 120 °C for 6 days and (b) annealed under the same conditions with no lithium metal present. There are no significant differences in the GPC traces between (a) and (b), indicating that the molecular weight distribution of the PEO chains does not change due to annealing against lithium metal. For reasons that are unclear, the GPC peak is narrower after exposure to lithium metal.

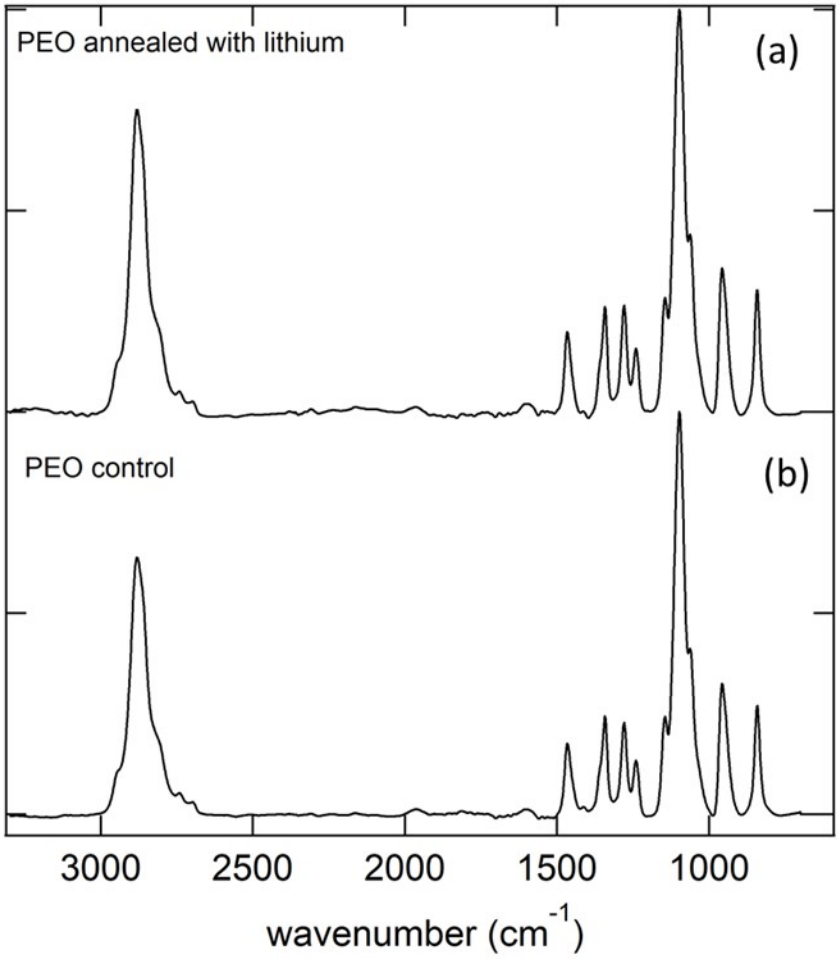

Figure 5.7. FTIR results before and after annealing PEO against lithium metal. Results of Fourier transform infrared (FTIR) spectroscopy on 35 kg mol^{-1} PEO (a) annealed against lithium metal at 120 °C for 6 days and (b) annealed under the same conditions with no lithium metal present. The spectra for the lithium annealed sample and control are identical, indicating that the chemical bonds in the PEO chains are not impacted by the dissolved lithium metal.

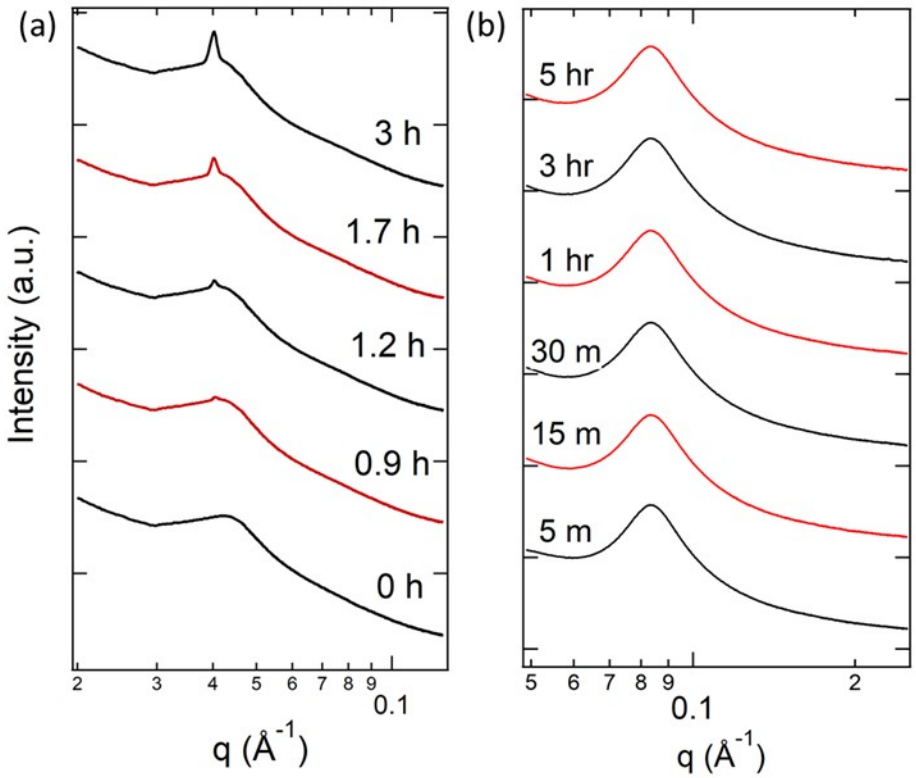

Figure 5.8 Signatures of lithium dissolution in a neat block copolymer and SAXS control experiment. (a) Time dependent SAXS profiles of a neat SEO block copolymer (L = 0.5 mm) against lithium windows at 120 °C. Lithium dissolution stabilizes an ordered phase without the presence of salt. For this polymer, the PS and PEO molecular weights were 6.4 and 7.3 kg mol^{-1} respectively and it exhibits an order-to-disorder transition at 78 °C.[164] (b) Time dependent SAXS profiles of a 0.5 mm thick SEO/LiTFSI mixture (with 1.7 and 1.4 kg mol^{-1} PS and PEO molecular weight) against aluminum windows at 120 °C.

5.7 Nomenclature

Table 5.1 List of symbols and abbreviations

Symbol	Meaning
A	Integrated area under an NMR peak
DME	Dimethyl ether
FTIR	Fourier transform infrared spectroscopy
GPC	Gel permeation chromatography
$G(\delta)$	Gaussian function
i	Current density (μA cm^{-2})
I	Intensity
$L(\delta)$	Lorentzian function
L	Distance between lithium electrodes (μm)
LiTFSI	bis(trifluoromethane)sulfonimide lithium salt
M_n	Molar mass of species n (g mol^{-1})

m	Molality (mol kg^{-1})
NMR	Nuclear magnetic resonance spectroscopy
PEO	Poly(ethylene oxide)
PS	Polystyrene
q	Scattering vector ($Å^{-1}$)
q^*	Scattering vector at the primary scattering peak ($Å^{-1}$)
SAXS	Small angle X-ray scattering
SEO	Polystyrene-block-poly(ethylene oxide)
t	Time (h or min)
T_{ODT}	Order to disorder transition temperature
x	Mass fraction
Z_{Im}	Imaginary component of impedance
Z_{Re}	Real component of impedance

Table 5.2 List of symbols (Greek)

Symbol	Meaning
δ	Chemical shift (ppm)
κ	Ionic conductivity (S cm^{-1})
ϕ	Potential (mV)

6. Dynamic Structure and Phase Behavior of a Block Copolymer Electrolyte Under Dc Polarization[§]

ABSTRACT

An important consideration when designing lithium battery electrolytes for advanced applications is how the electrolyte facilitates ion transport at fast charge and discharge rates. Large current densities are accompanied by large salt concentration gradients across the electrolyte. Nanostructured composite electrolytes have been proposed to enable the use of high energy density lithium metal anodes, but many questions about the interplay between the electrolyte morphology and the salt concentration gradient that forms under dc polarization remain unanswered. To address these questions, we use an *in situ* small angle X-ray scattering technique to examine the nanostructure of a polystyrene-*block*-poly(ethylene oxide) copolymer electrolyte under dc polarization with spatial and temporal resolution. In the quiescent state, the electrolyte exhibits a lamellar morphology. The passage of ionic current in a lithium symmetric cell leads to the formation of concurrent phases: a disordered morphology near the negative electrode, lamellae in the center of the cell, and coexisting lamellae and gyroid near the positive electrode. The most surprising result of this study was obtained after the applied electric field was turned off: a current-induced gyroid phase grows in volume for six hours in spite of the absence of an obvious driving force. We show that this reflects the formation of localized pockets of salt-dense electrolyte, termed concentration hotspots, under dc polarization. Our methods may be applied to understand the dynamic structure of composite electrolytes at appreciable current densities.

6.1 Introduction

There are many challenges associated with designing rechargeable batteries that offer increased performance over the current state of the art in lithium-ion technology. From the perspective of the electrolyte, one must address two critical design goals: 1) ensure compatibility with high energy density electrode materials,[9,142] and 2) enable ion transport at rates required by the application.[165] There is considerable interest in developing new composite electrolytes to meet these goals. Multiple phases with different material properties are leveraged to obtain an electrolyte with orthogonal properties (*e.g.* compatibility with lithium metal anodes and high ionic conductivity). Examples include ceramic nanoparticles dispersed in an ion conducting matrix,[166] block copolymers with co-continuous ion conducting and rigid domains,[22] and crosslinked polymer gels swollen with an electrolyte solution.[167] In homogeneous electrolyte systems (*i.e.*, a mixture of a salt in a single solvent), the second law of thermodynamics requires that passing ionic

[§] Adapted (with permission) from Galluzzo, M. D.; Loo, W. S.; Schaible, E.; Zhu, C; Balsara, N. P. Dynamic Structure and Phase Behavior of a Block Copolymer Electrolyte under Dc Polarization. *ACS Appl. Mater. Interfaces* **2020**. *12* (51) 57421–57430.

current result in a monotonic salt concentration profile between the electrodes when the electrolyte is initially uniform in concentration. There are, however, many unanswered questions about the interplay between morphology and concentration gradients in multiphase systems wherein ion transport is fundamentally different in the two phases. Passing current through these electrolytes can lead to rearrangement of phases or the formation of new structures that are not present in the quiescent state.[38] In principle, composite electrolytes can exhibit salt concentration hotspots, *i.e.,* pockets where the local salt concentration exceeds the nominal value due to transport bottlenecks. Our understanding of these phenomena is limited.

The rearrangement of phases in a composite electrolyte is a natural consequence of dc polarization because the structure of composite electrolytes often varies with salt concentration.[23,24,168,169] Concentration gradients emerge across the electrolyte when the mobility of the anion is non-zero (see Chapter 3).[42] At early times, the gradients are localized near the electrodes and the salt concentration in the middle of the cell remains more or less unchanged. With time, the gradients propagate toward the middle of the cell until a time-invariant concentration profile is achieved. Consequently, the rearrangement of phases will depend on both distance from the electrode and time. Additional complexities may arise due to concentration hotspots. We note that these phenomena are also relevant for standard lithium-ion battery components which inherently consist of multiple phases: the electrodes are comprised of active particles mixed with electrolyte, and ion transport between the electrodes occurs within the pores of an inert separator wetted with electrolyte.

The composite electrolyte system studied in this work is a polystyrene-*block*-poly(ethylene oxide) (SEO) with bis(trifluoromethylsulfonyl)amine lithium salt (LiTFSI) where glassy polystyrene (PS) provides mechanical rigidity and poly(ethylene oxide) (PEO) solvates the lithium salt and enables ion conduction. The development of concentration gradients in SEO/LiTFSI mixtures can be predicted using concentrated solution theory because ionic conductivity, salt diffusion coefficient, cation transference number with respect to the solvent velocity, and thermodynamic factor have been measured as a function salt concentration (see Chapter 4).[55] However, concentrated solution theory does not account for the rearrangement of phases or phase transitions. Our purpose is to study the effect of applied current on the morphology and phase behavior of an SEO/LiTFSI electrolyte. We track the rearrangement of phases and phase transitions that occur in this electrolyte during polarization by *in situ* small angle X-ray scattering (SAXS) experiments. These experiments enable determination of the local structure of the electrolyte as a function of time and distance from the electrodes. The equilibrium lamellar phase gives way to a disordered phase near the negative electrode and small pockets of a gyroid phase near the positive electrode. The most surprising result of this study was obtained after the applied field was turned off: the current-induced gyroid phase grows in volume for six hours in spite of the absence of an obvious driving force.

6.2 Experimental Section

6.2.1 Materials

The polystyrene-*block*-poly(ethylene oxide) (SEO) block copolymer used in this study was synthesized, purified, and characterized using methods described by Teran et al.[24] and Hadjichristidis et al[114]. The block copolymer electrolyte (polystyrene (PS) molecular weight of 1.7 and poly(ethylene oxide) (PEO) molecular weight of 1.4 kg mol^{-1}) was prepared following the methods of Yuan et al.[116] to produce an SEO/LiTFSI mixture with r_{avg} = 0.07. Lithium metal with nominal thickness of 0.75 mm was purchased from MTI and scraped with a nylon brush to expose a fresh lithium surface. The lithium was then cut into a 3.18 mm diameter disk and pressed at 500 psi, resulting in disk approximately 1 cm in diameter and 0.1 mm thick. The lithium was then pressed against a stainless-steel block and the excess trimmed away from the edges to form the electrodes.

6.2.2 Electrochemical Cell for In Situ SAXS Experiments

We designed a custom electrochemical cell (shown schematically in Fig. 6.1a of Section 6.3.1) to enable structural characterization of the electrolyte during polarization via SAXS measurements. The cell was held in a 2 mm thick polyether ether ketone (PEEK) component with a rectangular channel cut through. Lithium metal was pressed on one face of two stainless-steel blocks that served as current collectors and were then inserted into the channel resulting in a 1.23 mm gap between the two lithium electrodes. The active face of the stainless-steel block/lithium metal assembly had dimensions of 1.95 mm by 3.95 mm and the lithium was approximately 100 μm thick. The polymer electrolyte was then hot pressed into the resulting gap with Kapton windows affixed over the exposed faces. Cell assembly was performed in an argon-filled glove box with less than 1 ppm O_2 and H_2O levels. The entire cell was sealed in an aluminum laminated pouch with nickel tabs secured to the stainless-steel blocks protruding out to allow electrical connections. The cell was then removed from the glove box and affixed to a custom-built heat stage for testing. The nickel tabs were attached to a Biologic VMP3 potentiostat for electrochemical measurements. A picture of the assembled cell before pouch sealing is shown in Fig. 6.5 of Section 6.6.6. The orientation of the cell was such that the X-ray beam passed parallel to the electrodes, passing through the cell components in the following order: pouch, Kapton, 1.95 mm of electrolyte, Kapton, and pouch. All SAXS data was obtained at beamline 7.3.3. of the Advanced Light Source (ALS) at Lawrence Berkeley National Laboratory.[162] The size of the beam was approximately 700 μm x 300 μm. We oriented the cell such that the 700 μm dimension was parallel to the electrode and the 300 μm dimension was perpendicular. The X-ray beam was then scanned between the two electrodes with the optimal spatial resolution considering the electrolyte thickness, L = 1.23 mm, and beam dimensions. Previous studies have been conducted with the X-ray beam oriented perpendicular to the electrodes, resulting in scattering data averaged over the entire length of the electrolyte.[38,170] To our knowledge, this is the first report of an X-ray scattering experiment performed on a block copolymer electrolyte under dc polarization with spatial and temporal resolution.

6.2.3 Thermal History

Prior to polarization, the sample was heated from room temperature to 120 °C to remove any effects of thermal history. Based on the phase diagram in Fig. 6.1b of Section 6.3.1, the sample should be disordered at this temperature and salt concentration. However, in Chapter 5 we demonstrated that the dissolution of lithium metal from the electrodes into the electrolyte at elevated temperatures can stabilize the ordered phase. To minimize the impact of this phenomena on the experiment, we limited the annealing step at 120 °C to 20 min. Time and temperature dependent SAXS data for the annealing step is presented in Fig. 6.6 of Section 6.6.6 which show signatures of lithium dissolution. The coordinates of Region I, II, and III were mapped out after cooling the cell back to 90 °C, so the two regions shown in Fig. 6.6 do not correspond exactly to any of the three regions discussed in the main text. After cooling to 90 °C, the sample was equilibrated for approximately one hour before beginning the polarization experiment. The sample temperature was maintained at 90 °C for the duration of the experiment.

6.2.4 Small Angle X-ray Scattering (SAXS)

All SAXS data was obtained at beamline 7.3.3. of the Advanced Light Source (ALS) at Lawrence Berkeley National Laboratory. Preliminary work was conducted at beamline 1-5 at the Stanford Synchrotron Radiation Light Source.

Silver behenate was used to determine the beam center and sample-to-detector distance. Two dimensional scattering patterns were collected with a Pilatus3 2M detector (Dectris Ltd) and integrated azimuthally using the Nika program for IGOR Pro to produce one-dimensional scatter profiles[149]. A custom-built sample heating stage was used for the measurements and temperature was ramped at roughly 10 °C per minute. The beam size is fixed at 700 μm (horizontal direction, y) by 300 μm (vertical direction, x) by the scatter slits which are positioned downstream of the multilayer monochromator and toroidal focusing mirror. The sample is aligned such that the x-coordinate (where $x/L = 0$ is defined as the anode/electrolyte interface and $x/L = 1$ is the cathode/electrolyte interface) is along the vertical direction. Based on the cell geometry, we expect the sample to be uniform in structure and r along the y-coordinate. The y-position of the beam was consistent across all three sampled regions. The X-ray energy was 10 keV and the exposure time at each position was either 2 or 5 s. When comparing scattered intensity, $I(q)$, or the scattering invariant (Q), data was normalized by the exposure time. At each time point, Region I, II, and III were sampled in succession with each line scan taking less than 15 s. The *x*- and *y*- coordinates on the cell were mapped out by scanning the beam around the sample and measuring the beam-stop diode intensity. The intensity reading from the diode was zero when the beam was positioned on the stainless-steel current collector and non-zero when passing through the lithium metal, polymer electrolyte, or PEEK. The center of the cell was found by scanning the beam in 50 μm increments along the x-coordinate and taking the middle point between the stainless-steel current collectors, identified by where the beam-stop diode intensity went to zero. This was performed just before the beginning of the polarization experiment after the sample had equilibrated at 90 °C.

6.2.5 Electrochemical Measurements

All electrochemical measurements were made using a Biologic VMP3 potentiostat. Ac impedance measurements were made in a frequency range from 1 MHz to 100 mHz with an amplitude of 80 mV about a constant bias equal to the controlled voltage (623 mV for $0 < t < 8.3$ h) or the last recorded open circuit voltage prior to initiating the impedance measurement.

6.3 Results and Discussion

6.3.1. Phase Behavior of the Electrolyte in the Quiescent State

The electrolyte was comprised of a linear SEO diblock copolymer with a 1.7 kg mol^{-1} PS block and 1.4 kg mol^{-1} PEO block mixed with LiTFSI. The molar ratio of LiTFSI molecules to ether oxygens, $r_{avg} = \frac{[\text{LiTFSI}]}{[\text{EO}]}$, was 0.07. We use the subscript '*avg*' to denote that this is the average salt concentration for the entire electrolyte, which must be conserved throughout the experiment. When a dc potential is applied across the cell, salt accumulates at the positive electrode (where the anodic reaction, $Li^0 \rightarrow Li^+ + e^-$, occurs) and is depleted at the negative electrode (where the cathodic reaction, $Li^+ + e^- \rightarrow Li^0$, occurs), which results in a gradient in the local salt concentration, $r(x,t)$. We define the x-coordinate such that $x = 0$ at the anode (positive electrode) and $x = L$ at the cathode (negative electrode). Salt concentration gradients have been measured experimentally in homogeneous electrolytes.[85,86,171] For a nanostructured (*i.e.* inhomogeneous) block copolymer electrolyte, there is the additional complication that morphology will depend on the local salt concentration.

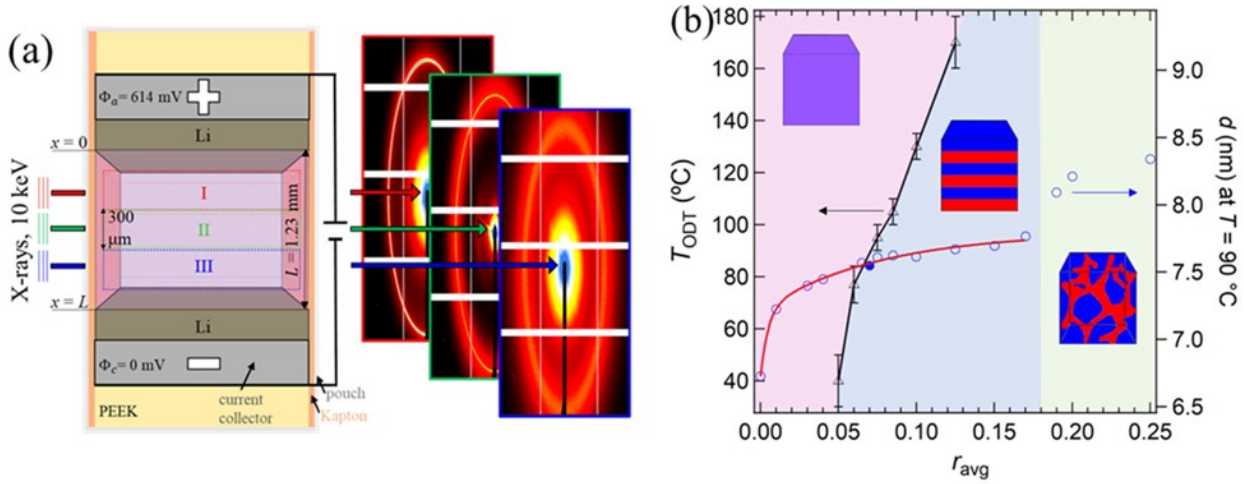

Figure 6.1. Experimental configuration and phase diagram. (a) Schematic representation of the experimental set up. 10 keV X-rays pass perpendicular to the direction of ion motion (parallel to the lithium electrodes), sampling three distinct regions of the electrolyte (pink shaded region) which are directly adjacent to each other. Region I, II, and III are centered at $xL^{-1} = 0.24$, 0.50, and 0.74, as shown by the dashed boxes and the beam dimension in the x-direction is 300 μm. Based on the cell polarity, the salt concentration of Region I increases and Region III decreases during polarization. Representative 2D SAXS patterns are shown for each region (corresponding to $t = 7$ h). (b) Phase diagram of the polymer electrolyte SEO(1.7-1.4)/LiTFSI used in this study. The order-to-disorder transition temperature (T_{ODT}) versus salt concentration, r_{avg}, is plotted with triangle markers on the left axis; r_{avg} = [LiTFSI]/[EO]. Shaded regions

indicate the phases observed at each temperature and r_{avg}, where pink, blue, and green correspond to the disordered, lamellar, and gyroid morphologies, respectively. The domain spacing, d, versus r_{avg} at 90°C is plotted on the right axis as open circle markers. The filled circle represents the sample used for this study (r_{avg} = 0.07) which exhibits a lamellar morphology but is near the disordered/lamellar phase boundary. Data points with open markers were taken from refs [24,38]. The red line is a fit given by Eqn. 6.1.

We present the phase behavior of the SEO copolymer as a function of r_{avg} in Fig. 6.1b. The addition of salt to a block copolymer affects the morphology, conducting phase volume fraction (f_c), and domain spacing, relative to the neat state.[23,24,36,117] The phase behavior of the SEO copolymer doped with different amounts of salt was characterized by conventional SAXS experiments in inert sample holders. At low salt concentrations, *i.e.* r_{avg}< 0.05, the sample is disordered (DIS) at all temperatures (T > 40°C). Increasing salt concentration results in a phase transition to an ordered lamellar (LAM) phase. The order-to-disorder transition temperature (T_{ODT}) increases with r_{avg}. We plot T_{ODT} as a function of r_{avg} on the left axis of Fig. 6.1b as open triangles. When r_{avg} exceeds 0.17, the lamellar phase gives way to a gyroid (GYR) morphology, regardless of temperature. The disordered-to-lamellar-to-gyroid transitions are driven by changes in polymer/salt interactions[120] and changes in f_{c}. As r_{avg} is increased from 0 to 0.25, f_c increases from 0.44 to 0.58. The shaded regions and cartoon schematics in Fig. 6.1b represent the morphology in the designated temperature and salt concentration windows. SAXS data from this system contains a primary SAXS peak at $q = q^*$, where q is the magnitude of the scattering vector. On the right axis in Fig. 6.1b, we plot the domain spacing, d, as a function of salt concentration at 90°C as circles ($d = \frac{2\pi}{q^*}$). Data plotted with open symbols (circles and triangles) in Fig. 6.1b was taken from Refs [24,38]. The closed symbol represents the sample used in this study. The disordered state (DIS) is characterized by fluctuations in the local density of styrene and ethylene oxide monomer units with a characteristic spacing between fluctuations, d_{DIS}, but no long-range order. The lamellar morphology (LAM) is characterized by alternating 2D PS- and PEO-rich domains where the characteristic distance, d_{LAM}, is the distance between the center of two lamella of the same component. The gyroid morphology (GYR) is characterized by 3D network of a minority component (PS) dispersed in a matrix of the majority component (PEO) with a characteristic spacing, d_{GYR}. From the neat state (*i.e.*, r_{avg} = 0) to r_{avg} = 0.04, d_{DIS} increases rapidly from 6.73 nm to 7.45 nm. Above r_{avg} = 0.04, d increases slowly and smoothly across the disordered to lamellar transition with d_{LAM} = 7.78 nm at r_{avg} = 0.17. The domain spacing for the disordered and lamellar morphologies is well-described by a double exponential function:

$$d = 7.80 - 0.585\, exp\left[-13.3 r_{avg}\right] - 0.486\, exp[-210 r_{avg}] \qquad (6.1)$$

shown as a red curve in Fig. 6.1b and applies for $0 \leq r_{\mathrm{avg}} \leq 0.15$. For r_{avg} > 0.17, the transition from lamellar to gyroid is accompanied by a discontinuous change in the dependence of domain spacing on salt concentration, with d_{GYR} = 8.09 nm at r_{avg} = 0.19 and reaching 8.34 nm at r_{avg} = 0.25.

6.3.2 Phase Behavior of the Electrolyte under Dc Polarization

The electrolyte was loaded into the cell shown in Fig. 6.1a and subjected to a constant potential of 500 mV mm^{-1} beginning at time t = 0 h. Based on the thickness of cell (L = 1.23 mm), the applied potential translates to an anodic potential, Φ_a = 614 mV; the cathodic potential, Φ_c, is defined to be zero. In a practical battery electrolyte, L is on the order of 10 μm, which corresponds to a potential drop of 5 mV across the electrolyte. While the cell thickness is much larger than a practical battery electrolyte, the behavior we observe will be analogous in thinner membranes at the same $\Delta\Phi/L$ or iL, where $\Delta\Phi$ is the potential drop across the electrolyte and i is the current density.

The SEO electrolyte with r_{avg} = 0.07 used in this experiment is represented by a filled blue circle in Fig. 6.1b; it has a lamellar morphology but is near the DIS-LAM phase boundary. To monitor the structure of the polymer in response to the applied field, we sample three regions of the cell. Region I, II, and III are centered at xL^{-1} = 0.26, 0.50, and 0.74, respectively, and spaced by 300 μm, as shown in Fig. 6.1a. We use the notation r_{I}, r_{II}, and r_{III} to denote the average salt concentration in each region. Before polarization, the sample was heated to 120 °C to access the disordered state and erase any thermal history before cooling to 90°C to run the experiment. We have established that lithium is prone to dissolve from the electrode at elevated temperatures (>90 °C)[24], so we limited the annealing step to 20 min at 120 °C. In Fig. 6.2a through 6.2c, we present the azimuthally averaged 1D SAXS intensity as a function of q for the three regions. The black curve in each plot (t = -0.1 h) represents the structure after cooling to 90 °C and before polarization. The sharp scattering peak at q^* = 0.83 nm^{-1} and higher order scattering peak at $2q^*$ = 1.6 nm^{-1} is indicative of the lamellar morphology. The red curves represent data taken during polarization at 500 mV mm^{-1}, and the blue curves represent the data taken after the cell was switched to open circuit at t = 8.3 h. The time stamp on the curves in Fig. 6.2c apply to Fig. 6.2a through 6.2c. A total of 86 measurements were made for each region over the course of the experiment, and the selected curves in Fig. 6.2a through 6.2c highlight the observed phase transitions.

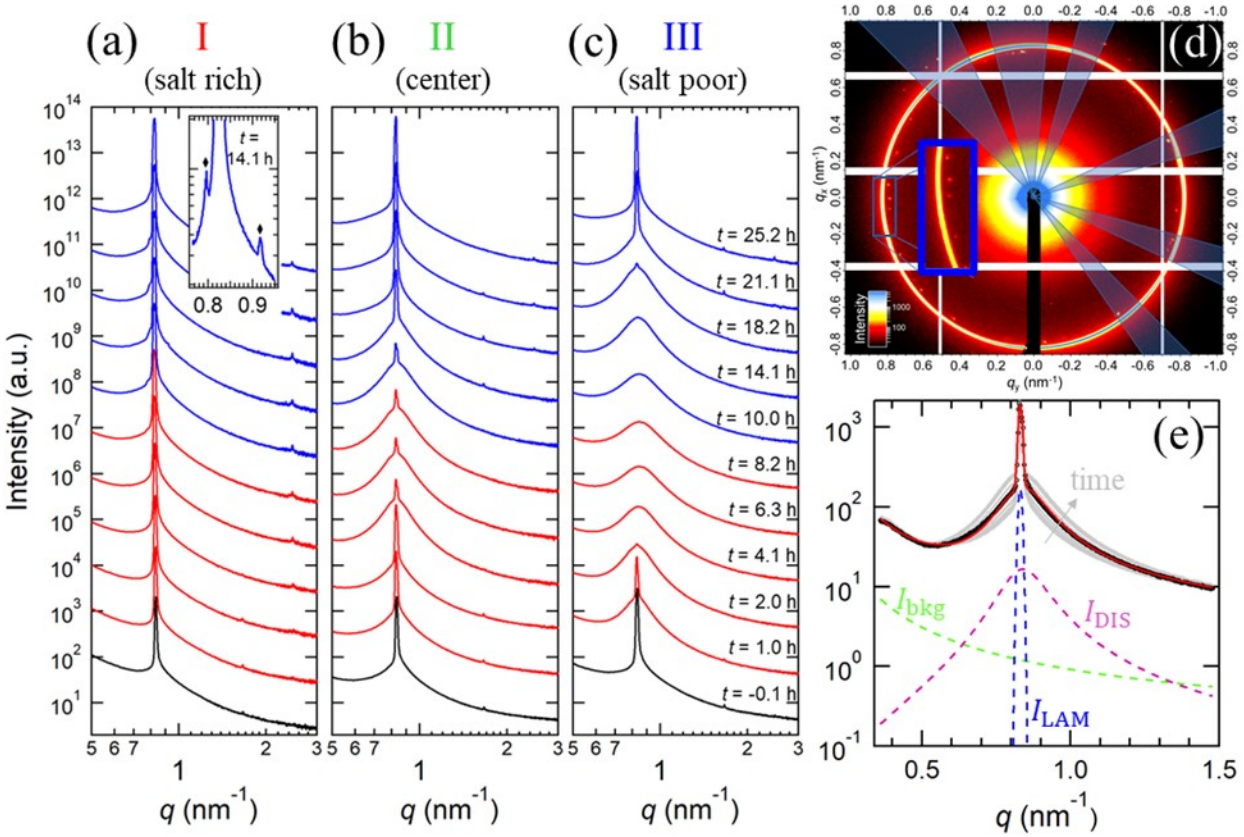

Figure 6.2. Results from *in situ* SAXS experiment on an SEO/LiTFSI electrolyte. Azimuthally averaged SAXS profiles as a function of time for (a) Region I, near the positive (salt rich) electrode, (b) Region II, near the middle of the cell, and (c) Region III, near the negative (salt poor) electrode. Black curves represent the initial morphology taken before polarization. Red curves indicate the morphology during polarization at 500 mV/mm. Blue curves indicate the morphology after the cell is switched to open circuit at t = 8.3 h. The inset in (a) highlights the emergent peak corresponding to the gyroid morphology with Bragg reflections at q^*_{GYR} and $\sqrt{4/3}\ q^*_{GYR}$ (diamond markers). (d) 2D SAXS pattern of Region I at t = 14.1 h. The ring corresponds to the primary scattering peak of the lamellar phase. The scattered spots directly inside of the ring correspond to q^*_{GYR} (magnified in the inset) and the spots outside of the ring correspond to the $\sqrt{4/3}\ q^*_{GYR}$ reflection. The highlighted sectors were selectively averaged to characterize scattering from the gyroid phase. (e) 1D plots of $I(q)$ for Region II from t = 0.8 h to t = 4.8 h (gray curves). $I(q)$ at t = 2.6 h is plotted with black open circles and the red curve is a fit of Eqn. 6.2 to the data. The fit is deconvoluted into three parts and offset by a decade for clarity: background (green dashed line), broad disordered peak (purple dashed line), and sharp ordered peak (blue dashed line).

Near the negative electrode (Region III, Fig. 6.2c), the sharp scattering peak seen at t = -0.1 h and t = 1.0 h is replaced by a broad scattering peak characteristic of a disordered phase that persists through the polarization step (up to t = 8.2 h). It is evident that the block copolymer electrolyte in Region III undergoes an order-to-disorder transition. After the field is turned off at t = 8.3 h, the sharp scattering peak characteristic of the lamellar phase is recovered. Near the center of the cell (Region II, Fig. 6.2b), a similar trend is observed, however at t = 8.2 h, the scattering profile contains signatures of both ordered and disordered domains. As was the case in Region III,

the lamellar phase is recovered after the cell is switched to open circuit. Near the positive electrode (Region I, Fig. 6.2a), the ordered lamellar phase persists throughout polarization ($0 < t$ (h) < 8.3). At t = 8.2 h (near the end of the 500 mV mm^{-1} polarization step), a small peak emerges on the low-q side of the primary peak. As time progresses, an additional peak emerges on the high-q side. The diamond markers in the inset of Fig. 6.2a denote these two peaks at q = 0.796 and 0.918 nm^{-1}, respectively.

The 2D SAXS pattern from Region I at t = 14.1 h is presented in Fig. 6.2d. The primary scattering peak corresponding to the lamellar phase in the 1D plot is represented by the narrow, continuous ring of high intensity. The small peaks on either side of the primary lamellar peak in the 1D plot correspond to the spots of high intensity inside and outside of the bright ring in the 2D image. These spots are highlighted in the inset of Fig. 6.2d. The azimuthal angles of the spots do not change during the course of the experiment. While the spots are clear in the 2D image, they are not well resolved when the 2D scattering intensity profile is azimuthally averaged. To achieve better resolution, we averaged selected sectors of the 2D scattering profiles which are indicated by the shaded regions in Fig. 6.2d. An example of the resulting 1D profile is shown as an inset in Fig. 6.2a. In addition to the scattering peak corresponding to the lamellar phase, we observe peaks at q^*_{GYR}= 0.796 nm^{-1} and $\sqrt{4/3}\ q^*_{GYR}$ = 0.918 nm^{-1}. These peaks are standard signatures of the gyroid morphology in block copolymers[26,38,172] and this morphology coexists with the lamellar morphology in Region I.

To track the phase transitions observed in Fig. 6.2a through 6.2c, we fit the scattering data, $I(q)$ for $0.36 < q$ (nm^{-1}) < 1.48 to Eqn. 6.2:[161]

$$I(q) = I_{DIS}(q) + I_{LAM}(q) + I_{bkg}(q), \qquad (6.2)$$

where $I_{\mathrm{DIS}}(q)$, $I_{\mathrm{LAM}}(q)$, and $I_{\mathrm{bkg}}(q)$ account for the scattering from the disordered phase, lamellar phase, and background, respectively. (The scattered intensity from the gyroid phase in Region I is much smaller than the lamellar phase, so we neglect it in the fit.) I_{DIS} is given by the Liebler structure factor,[163] I_{LAM} is a Gaussian function, and I_{bkg} is a decaying exponential. The details of the fit are discussed in Section 6.6.1. The gray curves in Fig. 6.2e represent the raw data from Region II from t = 0.8 h to t = 4.8 h and the raw data at t = 2.6 h is plotted as black data points. We use the t = 2.6 h scattering profile to describe our fitting procedure. The solid red line in Fig. 6.2e represents the fit of Eqn. 6.2 and three contributions to $I(q)$, I_{DIS} (purple), I_{LAM} (blue), and I_{bkg} (green) are shown by dashed curves that are offset by a decade for clarity. These fits were repeated for all of the scattering profiles obtained from Region I, II, and III. When the sample is completely disordered (*e.g.* t = 6.3 h in Fig. 6.2c), we set I_{LAM} = 0. For the scattering from the SEO/LiTFSI electrolyte in the quiescent state (*i.e.*, t = -0.1 h in Fig. 6.2c), our fitting procedure results in a finite I_{DIS} contribution. In other words, the sharp Gaussian function presented in Fig. 6.2e does not account for all scattering seen from the nominally ordered sample. Our sample is in the weak segregation limit and, with the presence of salt, the Gibbs phase rule requires a coexistence window between the lamellar and disordered phase.[173] In other words, there must be a range of salt concentrations where the equilibrium morphology of the SEO/LiTFSI electrolyte consists of coexisting lamellae and disordered grains. The coexistence in this sample was predicted from theory in Ref [174] and confirmed experimentally in Ref [161]. Given the proximity of our sample

(with r_{avg} = 0.07) to the order-disorder phase boundary, we interpret the diffuse scattering at the base of the primary peak to indicate coexistence of a disordered phase with the ordered lamellar phase. We certainly expect ordered and disordered phases to exist simultaneously as the sample undergoes an order-to-disorder transition due to salt depletion near the negative electrode. The scattering signatures of the disordered phase emerge smoothly from the diffuse scattering at the base of the primary peak when the cell is polarized (see gray curves in Fig. 6.2e). With increasing time (in the range $0.8 < t$ (h) < 4.8), the I_{DIS} contribution to $I(q)$ increases in Region II.

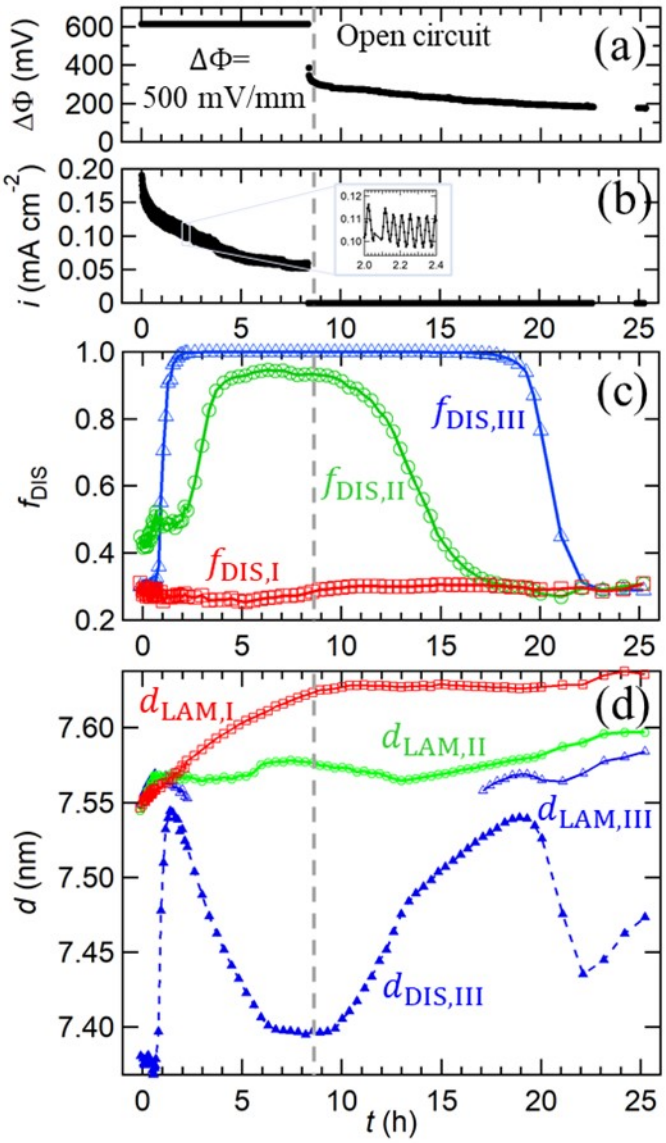

Figure 6.3. Disordered phase volume fraction and domain spacing from SAXS. (a) Cell potential drop, $\Delta\Phi$, versus time, t. (b) Current density, i, versus t. From t = 0 to t = 8.3 h, a constant potential of 614 mV (500 mV mm^{-1}) is applied across the cell and the current is measured. At t = 8.3 h (represented by a vertical dashed line), the current is set to zero and the potential is measured. The noise in the voltage and current data is due to interference from the heating stage, shown in the inset of (b). (c) Volume fraction of the disordered phase, f_{DIS}, versus t for Regions I (red squares), II (green circles), and III (blue triangles). (d)

Domain spacing of the lamellar phase, d_{LAM}, (open symbols) for Regions I, II, and III and domain spacing of the disordered phase for Region III, d_{DIS} (filled symbols) as a function of time.

The time dependence of cell potential drop, $\Delta\Phi = \Phi_a - \Phi_c$, and current density, i, are presented in Fig. 6.3a and 6.3b, respectively. A constant potential, $\Delta\Phi$ = 623 mV (500 mV mm^{-1}), was applied across the cell for $0 < t$ (h) < 8.33 during which time the current density, i, was measured. At t = 8.3 h, the cell was switched to open circuit ($i = 0$ mA cm^{-2} for $8.3 < t$ (h) < 25.2) and the open circuit potential was recorded. The bulk and interfacial resistance of the cell was measured at intervals spaced by 0.5 h. Similar values were obtained at the beginning and end of the experiment (see Fig. 6.7 of Section 6.6.6). The noise in the current and voltage data (inset of Fig. 6.3b highlights an example) is due to interference from the power cycle of the heating stage and could not be avoided. The gray dashed line in Fig. 6.3a through 6.3d represents the switch from chronoamperometry to open circuit. In order to quantify the extent of the salt concentration-induced order-to-disorder and disorder-to-order transitions, we calculated the scattering invariants (see Section 6.6.4. for details) of the disordered and lamellar phases (Q_{DIS} and Q_{LAM}, respectively) from the fits described in the preceding paragraph.[40,161] We then calculated the disordered phase volume fraction, f_{DIS}, for Region I, II, and III as a function of time by:

$$f_{DIS} = \frac{Q_{DIS}}{Q_{DIS} + \alpha Q_{LAM}}\ , \qquad (6.3)$$

where α is a correction factor that accounts for the anisotropic scattering of lamellar grains and the presence of LiTFSI. While all of the scattering from the isotropic disordered phase reaches the detector, lamellar grains with normal orientation along the path of the X-ray beam do not contribute to the scattering signal. During a phase transition, the local salt concentration in the ordered domain will not be equal to that in the disordered domain,[161] instead it is the chemical potential of the salt that is equilibrated between the two phases. In principle, α will be a function of both the salt concentration in the ordered domain and disordered domain, both of which change with time in our system. We make the simplification that α does not depend on r and estimate α = 2.4, which we use for all calculations of f_{DIS}. Our methodology for estimating α is given in Section 6.6.5.

We present f_{DIS} as a function of time for Region I (red squares), Region II (green circles), and Region III (blue triangles) in Fig. 6.3c. In Region I, $f_{\mathrm{DIS,I}}$ remains fixed at about 0.30, the lowest value seen in our experiment, for the duration of the experiment. Near the positive electrode (Region I), we expect polarization to result in an increase in salt concentration, *i.e.* $r_{\mathrm{I}} > r_{\mathrm{avg}}$. Since the sample is ordered in the quiescent state at $r = r_{\mathrm{avg}}$ and because the addition of salt stabilizes the ordered phase (Fig. 6.1b), we expect this region to remain ordered during polarization. In Region III, $f_{\mathrm{DIS,III}}$ = 0.30 until t = 0.6 h when f_{DIS} begins to increase sharply. At t = 1.8 h, $f_{\mathrm{DIS,III}}$ = 0.98 and the region is almost completely disordered. Near the negative electrode, we expect polarization to result in a decrease in salt concentration, i.e. $r_{\mathrm{III}} < r_{\mathrm{avg}}$, resulting in the disordering of Region III based on the phase diagram presented in Fig. 6.1b. Near the center of the cell (Region II), we expect $r_{\mathrm{II}} \approx r_{\mathrm{avg}}$ due to the constraint that the average salt concentration in the electrolyte must be constant throughout the experiment. Unlike Region I and III, $f_{\mathrm{DIS,II}}$ = 0.45 at t = -0.1 h. Prior to polarization, we expect no difference in the morphology of Regions I, II, and III. We

attribute this to subtle differences in the ordered morphology across a 1.23 mm wide sample due to effects such as non-uniformity of sample temperature or an inhomogeneous stress distribution from the electrodes and sample holder. In Region II, $f_{\mathrm{DIS,II}}$ increases in two steps. It first increases from 0.45 to 0.49 over the first hour and approaches a short plateau. The second step occurs at t = 2.1 h: $f_{\mathrm{DIS,II}}$ begins to increase sharply and reaches 0.92 at t = 4.5 h, reaching a plateau value of 0.94 that persists throughout polarization ($5.6 < t$ (h) < 8.3). The second step commences shortly after Region III is fully disordered, suggesting that the disordered phase propagates from the negative electrode towards the center of the cell, and at steady state the boundary between disorder and order resides in Region II. When the cell is switched to open circuit, the salt concentration gradient begins to relax, and the disordered regions give way to the equilibrium lamellar morphology. This disorder-to-order transition starts at the middle of the cell and propagates towards the negative electrode; Region II is completely ordered by t = 18.1 h, at which point Region III begins to transition from disorder to order. By t = 22.1 h the entire sample is ordered with f_{DIS} = 0.30; an indication that the current induced phase transitions are completely reversible. The subtle differences in f_{DIS} in the three regions prior to polarization are not seen at t = 25.2 h.

Measurement of the domain spacing as a function of time and position provides insight into the effect of polarization on molecular length scales; the data in Fig. 6.1b allows us to make inferences about the local salt concentration based on measurements of the local domain spacing. We plot the time dependence of d_{LAM} (open symbols) and d_{DIS} (closed symbols) for the three regions in Fig. 6.3d. Because the beam size is much larger than a single lamella (300 μm versus 8 nm), d_{LAM} represents an average over many lamellar grains. In general, $d_{\mathrm{LAM}} > 7.55$ nm while $d_{\mathrm{DIS}} < 7.55$ nm. This is consistent with the equilibrium properties of the electrolyte: the value of d at the equilibrium order-to-disorder transition is 7.55 nm (see Fig. 6.1b). As the salt concentration in Region I increases, the lamellae near the positive electrode swell in response to an increase in the local salt concentration. $d_{\mathrm{LAM,I}}$ increases from 7.55 nm to 7.63 nm while the cell is polarized and then remains more-or-less constant when the current is turned off. In Regions II and III, d_{LAM} is nearly independent of time. The data for $d_{\mathrm{LAM,III}}$ is absent in Fig. 6.3d between $2.2 < t$ (h) < 17.1 because the sample is completely disordered during this time window.

In Region III, polarization results in a decrease in salt concentration and the order-to-disorder transition as described by Fig. 6.3c. Before polarization, the disordered phase coexists with ordered lamellae. The free energy required to place an LiTFSI molecule into a PEO-rich lamella is lower than that required to place it in a homogeneous PS/PEO mixture. Since the salt partitions to equate its chemical potential between the two phases, the local value of r in the disordered region must be less than that in the PEO-rich lamella, as required by the Gibbs phase rule. This is consistent with our observation that $d_{\mathrm{DIS,III}}$ measured at the beginning of the experiment (7.37 nm) is lower than that of $d_{\mathrm{LAM,III}}$ (7.55 nm) based on the mapping of d to r by Eqn. 6.1. At t = 0.55 h, the local value of r in the PEO-rich lamellae falls below the critical value needed to maintain phase separation and they become disordered, starting first at the bottom of Region III (depicted in Fig. 6.1a) and propagating upward. At t = 0.9 h, $f_{DIS,III}$ = 0.55 and Region III consists of a completely disordered morphology at the bottom (*i.e.*, closer to the negative electrode) and a lamellar phase in coexistence with a disordered phase at the top (*i.e.*, closer to the positive electrode). We refer to the neighboring ordered and disordered phases that are formed due

the presence of ionic flux across the electrolyte as concurrent phases. It is important to distinguish between concurrent phases formed out of equilibrium (*e.g.* t = 0.9 h) and coexisting phases obtained at equilibrium due to the Gibb's phase rule (*e.g.* t = -0.1 h). The sharp increase of $d_{\mathrm{DIS,III}}$ for 0.63 < t (h) < 1.8 is because the PEO-rich lamellae (prior to the order-to-disorder transition) have a higher local r than the coexisting disordered phase, and as the lamellae become disordered (*i.e.* mix the PS-rich domains), the amount of salt per ethylene oxide moiety in the disordered region must increase. At t = 1.8 h, the entirety of Region III is disordered and $d_{\mathrm{DIS,III}}$ = 7.54 nm. With no additional phase transitions occurring, $d_{\mathrm{DIS,III}}$ begins to decrease as the local salt concentration continues to drop and the domain spacing plateaus at $d_{\mathrm{DIS,III}}$ = 7.40 nm by t = 6.0 h. This indicates that the salt concentration gradient has almost fully developed by this time. When the cell is switched to open circuit at t = 8.3 h, $d_{\mathrm{DIS,III}}$ increases as the salt concentration gradient relaxes and the local salt concentration in Region III increases. At t = 18.6 h, we begin to observe the formation of a concurrent lamellar phase. Note that the ionic flux in the cell is not zero at this time even though the cell is at open circuit. With time, $f_{\mathrm{DIS,III}}$ decreases and the equilibrium value of 0.30 is obtained at t = 23.0 h. The decrease in $d_{\mathrm{DIS,III}}$ from t = 18.6 to 23.0 h is attributed to the partitioning of salt away from the disordered phase. For brevity, we do not include the data for $d_{\mathrm{DIS,I}}$ and $d_{\mathrm{DIS,II}}$ here but defer it to Fig. 6.10 of the Section 6.6.6. Assuming the cell was at equilibrium at t = 0, we expect the cell to return to equilibrium at long times when $\Delta\Phi$ = 0 mV. It appears that equilibration of our sample requires longer times; $\Delta\Phi$ is 180 mV at 25.2 h, so it is not surprising that $d_{\mathrm{LAM,I}}$ and $d_{\mathrm{DIS,III}}$ at t = 25.2 h are different from those at t = 0 h.

We may use the measured domain spacing in Fig. 6.3d to infer the local salt concentration as a function of xL^{-1} and t based on the relationship between d and r_{avg} presented in Fig. 6.1b. The mapping between d and r by Eqn. 6.1 (obtained from data in Fig. 6.1b) requires accounting for the presence of both coexisting phases at equilibrium and concurrent phases when ionic flux is present. The value of d reported in Fig. 6.1b based on the location of the primary scattering peak from ordered phases ignores the coexisting disordered phase. We thus rescale f_{DIS} given in Fig. 6.3b to span from 0 to 1 and denote the rescaled volume fraction f'_{DIS} (*i.e.* f'_{DIS} = 0 when f_{DIS} = 0.3 and f'_{DIS} = 1 when f_{DIS} = 1; $f'_{\mathrm{DIS}} = \frac{1}{0.7}(f_{\mathrm{DIS}} - 0.3)$) . We then calculate the local salt concentration, r_i, for each region (i = I, II, or III) by Eqn. 6.4 for each time point:

$$r_i = f'_{DIS,i} r_{DIS,i} + \left(1 - f'_{DIS,i}\right) r_{LAM,i} \qquad (6.4)$$

where $r_{i,j}$ is the solution to Eqn. 6.1 (with r_{avg} replaced with $r_{i,j}$) which yields $d = d_{i,j}$ and j denotes LAM or DIS. In Fig. 6.4a, we present the local salt concentration in Region I (red squares), Region II (green circles), and Region III (blue triangles) as a function of time. Initially, $r_i \approx 0.06$ in all three regions, which is slightly lower than the nominal value of r_{avg}= 0.07. The changes in local salt concentration in Regions I, II, and III during polarization are shown in Fig. 6.4a. As expected, salt concentration increases in Region I with increasing time, remains more or less constant in Region II, and decreases in Region III. The average salt concentrations in the different regions at the end of polarization are r_{I} = 0.090 (xL^{-1} = 0.26), r_{II} = 0.059 (xL^{-1} = 0.50), and r_{III} = 0.028 (xL^{-1} = 0.74). We note that the average salt concentration in Region I cannot be much higher than 0.09 because the salt in Region I must come from Regions II and III and the

average salt concentration throughout the electrolyte is fixed at r_{avg}= 0.07. This analysis relies on the assumption that the electrolyte morphology under applied electric fields at a given local salt concentration is identical to that obtained at equilibrium in individual electrolytes cast at the same salt concentration.

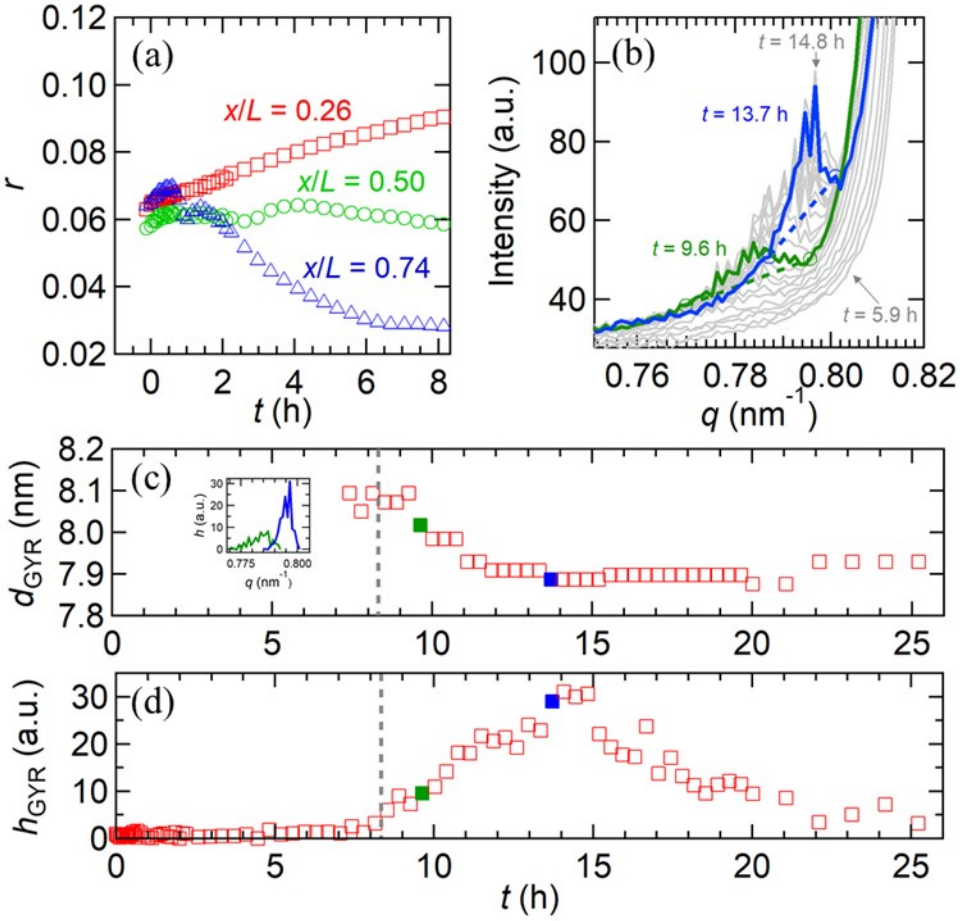

Figure 6.4. Salt concentration versus position and characteristics of the emergent gyroid phase. (a) Estimated local salt concentration in Region I (red squares), Region II (green circles), and Region III (blue triangles) versus time, t, based on Eqn. 6.4. (b) 1D scattering profiles obtained from Region I at t = 9.6 h (green curve) and t = 13.7 h (blue curve). The dashed lines represent a linear baseline. Gray curves represent the scattering data from t = 5.9 (when no gyroid peak is present) to t = 14.8 h (when the height of the peak is maximum). (c) Domain spacing of the gyroid phase, d_{GYR}, versus t. The inset shows the scattering data from t = 9.6 h (green curve) and t = 13.7 h (blue curve) after subtracting the linear baseline shown in Figure 4b. The maximum value for each curve was taken to be h_{GYR}, and the position of the maximum was used to calculate d_{GYR}. (d) Height of the gyroid peak, h_{GYR} versus t. The green and blue filled symbols in (c) and (d) correspond to the data at t = 9.6 and 13.7 h, respectively.

6.3.3 Emergence of the Gyroid Phase

We now discuss the formation of a gyroid phase which gives rise to the spots of high scattering intensity seen in Fig. 6.2b on either side of the primary scattering ring. In Fig. 6.4b, the gray curves represent the 1D scattering profiles obtained from selectively averaging the sectors of

the 2D scattering imaging highlighted in Fig. 6.2b for data obtained from Region I between t = 5.9 and t = 14.8 h for 0.75 < q (nm^{-1}) < 0.82. At early times, there is no feature corresponding to the gyroid phase; *i.e.*, the t = 5.9 h data set has no noticeable peak. As the experiment proceeds, a peak begins to emerge at q = 0.77 nm^{-1} which grows with time and shifts to higher q. The green (t = 9.6 h) and blue (t = 13.7 h) data sets in Fig. 6.4b show two examples of scattering data with noticeable gyroid peaks. The location and intensity of the peak provide information on the nature of the current-induced gyroid phase. The measured scattering curves are corrected for scattering from the lamellar phase by subtracting linear baselines shown as dashed lines for the two examples in Fig. 6.4b. We define the height of the peak, h_{GYR}, as the maximum intensity of the baseline corrected data and q^*_{GYR} to be the location of h_{GYR} on the q-axis. We calculate the periodic length scale of the gyroid phase, $d_{\mathrm{GYR}} = \frac{2\pi}{q^*_{\mathrm{GYR}}}$. The time dependence of d_{GYR} and h_{GYR} are presented in Fig. 6.4c and 6.4d, respectively. Examples of background subtracted intensity profiles are shown in the inset of Figure 4c for the t = 9.6 h (green curve) and t = 13.7 h (blue curve) data sets. The dashed gray line in Fig. 6.4c and 6.4d represent t = 8.3 h when the cell was switched to open circuit. The gyroid phase emerges near the end of the polarization step.

The gyroid phase is the thermodynamically favored morphology for the SEO copolymer electrolyte when $r > 0.17$ (see Fig. 6.1b). The appearance of a gyroid phase in our experiment is surprising because we have estimated the maximum salt concentration in Region I to be r_{I} = 0.09 (see Fig. 6.4a) based on the domain spacing of the lamellar phase. The fact that the gyroid phase is announced by spots rather than rings in the SAXS patterns indicates that the current-induced transformation from lamellae to gyroid occurs in relatively few grains. The current-induced gyroid phase first appears at t = 7.1 h and d_{GYR} = 8.1 nm. This suggests that the salt concentration within the gyroid grains is r = 0.19 based on the characteristic domain spacing of the gyroid morphology under quiescent conditions (Fig. 6.1b). The fraction of Region I occupied by the gyroid phase is extremely small at all times: the integrated intensity of the SAXS peaks associated with this phase amounts to 0.42% or less (see Fig. 6.11 of Section 6.6.6; the value of 0.42% is an upper limit calculated at t = 13.7 h when h_{GYR} in near the maximum). Thus, the presence of a small volume fraction of a salt-dense gyroid phase does not significantly change our calculation of the average salt concentration in Region I presented in Fig. 6.4a.

The mechanism by which the gyroid phase forms in response to ionic current remains an open question, although it has been previously reported in an SEO/LiTFSI electrolyte of the same copolymer.[38] We posit that the gyroid phase nucleates in Region I at defects where PEO-rich lamellae orientated parallel to the electric field terminate in a wall of polystyrene. Ions are driven towards the positive electrode in the PEO-rich channel but cannot penetrate the polystyrene, and salt accumulates in a highly salt-dense pocket, *i.e.*, a salt concentration hotspot. This may result in a steep microscopic salt concentration gradient on the length scale of the grain size (smaller than 1 μm). Such grain boundaries are necessarily rare in an unaligned sample, so we would expect only a few gyroid grains to emerge. When the cell is switched to open circuit (t = 8.3 h), the salt diffuses away from the pocket and d_{GYR} decreases to 7.9 nm by t = 14.1 h, suggesting a decrease in r within the gyroid from 0.19 to 0.17 over the first six hours of open circuit. The relaxation of the microscopic salt concentration gradient results in an increase in the volume of polymer around the pocket where r > 0.17, and a local lamellar to gyroid transition occurs. We thus observe an

increase in h_{GYR} from 6 to 31 in the time window from t = 8.3 to 14.9 h. The decay of h_{GYR} from 31 towards 0 for t > 14.9 h reflects the reconversion of the gyroid grains to the lamellar phase as the local salt concentration falls below the critical value needed to maintain the gyroid (r = 0.17). As expected, d_{GYR} remains constant during this decay. The changes in the 2D SAXS profiles in Region I, particularly the non-monotonic changes in intensity of the gyroid scattering spots, can be clearly seen in the movie file "Region_I.avi" (see Section 6.6.7).

In a previous work, Mullin et al studied the same SEO copolymer with a salt concentration of r_{avg} = 0.085 under applied fields of 2.5 to 15 V mm^{-1}.[38] They described the formation of gyroidal grains with a continuous gradient in domain spacing, which the termed "gradient crystals". In our experiment, we observe gyroid grains with a single, time-dependent domain spacing at a much lower field of 500 mV mm^{-1}. This suggests that steeper microscopic concentration gradients that must form under higher potential gradients result in a gyroid phase with a continuously changing domain spacing.

The effect of grain structure and defect density on ionic conductivity in block copolymer electrolytes has been studied using ac impedance spectroscopy, and it understood that conductivity decreases as grain size increases (*i.e.*, number of defects decreases) in unaligned samples.[63,175] This conclusion is based on ac impedance spectroscopy which is, by definition, carried out without inducing concentration gradients. Our interpretation of how the current-induced gyroid phase is formed in the SEO/LiTFSI electrolyte at 500 mV mm^{-1} suggests that defects and grain boundaries play a more dramatic role when dc potentials are applied. The formation of concentration hotspots and the concomitant steep microscopic concentration gradients is outside the scope of 1D models of ion transport that are currently used to model batteries.[76,176] The development of 2 or 3D models based on Newman's concentrated solution theory[42] that incorporate the nanostructure of the composite electrolyte may be illuminating. A complete understanding of ion transport in composite electrolytes will require consideration of these effects.

6.4 Conclusions

To summarize, we have revealed rich phase behavior in a block copolymer electrolyte near the lamellar order-to-disorder phase boundary during dc polarization and subsequent relaxation. During polarization, three morphologies are present concurrently with characteristic spacings which vary significantly as a function of both position and time: a pure disordered phase near the negative electrode, coexisting lamellar and disordered phases in the middle of the cell, and coexisting lamellar, disordered, and gyroid phases near the positive electrode. The observation of a gyroid phase is especially significant because it implies the presence of concentration hotspots. We hypothesize that steep microscopic concentration gradients can develop in the cell at defect sites where the non-conducting polystyrene phase blocks the flow of ions parallel to the electric field. Such effects are not captured by existing theories that describe ion transport in lithium batteries using 1D models.[42] The relaxation of the current induced gyroid phase under open circuit conditions is non-monotonic due to the presence of microscopic concentration gradients. While ion transport in block copolymer electrolytes (and composite electrolytes in general) has been extensively studied both experimentally[122,177] (see also Chapter 4) and computationally,[33,178] it is usually assumed that the structure remains fixed during polarization. We have shown that this is

not the case for an SEO/LiTFSI electrolyte operating under practical conditions with significant concentration polarization. It seems obvious that the interplay between the dynamic nanostructure and ion transport will depend on parameters such as domain size, geometry, average salt concentration, and current density. The experiment described in this work serves as an example of how these complex relationships could be unraveled.

6.5 Acknowledgement

This work was supported by the Assistant Secretary for Energy Efficiency and Renewable Energy, Vehicle Technologies Office, under the Advanced Battery Materials Research (BMR) Program, of the U.S. Department of Energy under Contract No. DE-AC02-05CH11231. This research used beamline 7.3.3 of the Advanced Light Source, which is a DOE Office of Science User Facility under contract no. DE-AC02-05CH11231. Preliminary work was completed at the Stanford Synchrotron Radiation Light Source, a user facility at SLAC National Accelerator Laboratory, was supported by the U.S. Department of Energy, Office of Science, Office of Basic Energy Sciences under Contract No. DE-AC02-76SF00515.

6.6 Supporting Information

6.6.1 SAXS Data Fitting

The scattering intensity, $I(q)$, data was fit using a Levenberg-Marquardt nonlinear least-squares algorithm. Data was fit by Eqn. 6.2 in the range $0.36 < q < 1.48$ nm^{-1}. A 360° azimuthal average was performed on the 2D scattering profiles to obtain 1D scattering profiles except where explicitly stated in Section 6.3 (*i.e.* inset of Fig. 6.2a and Fig. 6.4b). The scattering from the disordered phase, I_{DIS}, was fit using the Leibler structure factor[163] modified for polydispersity effects[179] and is given by:

$$I_{DIS}(q) = C\left[\frac{S(q)}{W(q)} - 2\chi\right]^{-1} \tag{6.5}$$

with

$$S(q) = S_{AA}(q) + S_{BB}(q) + 2S_{AB}(q) \tag{6.6}$$

$$W(q) = S_{AA}(q)S_{BB}(q) - S_{AB}^2(q) \tag{6.7}$$

$$S_{AA}(q) = Ng(f_A) \tag{6.8}$$

$$S_{BB}(q) = Ng(1 - f_A) \tag{6.9}$$

$$S_{AB}(q) = \frac{N}{2}[g(1) - g(f_A) - g(1 - f_A)] \tag{6.10}$$

and

$$g(f) = 2(1/x^2)\{fx - 1 + [k/(k + fx)]^k\} \tag{6.11}$$

where

$$x = q^2 R_g^2 \tag{6.12}$$

and

$$k = \frac{1}{PDI - 1}\ . \tag{6.13}$$

where C is the scattering contrast, χ is the Flory-Huggins interaction parameter, f_A is the volume fraction of the PEO block ($f_A = 0.44$ for all fits), R_g is the radius of gyration, N is the number of polymer segments per chain (N = 49 for all fits), and PDI is the polydispersity index of the copolymer (PDI = 1.035 for all fits). The primary lamellar scattering peak, I_{LAM}, was fit to a Gaussian function:

$$I_{LAM}(q) = y_0\, exp\left[-\frac{q - q^*_{LAM}}{2w^2}\right], \tag{6.14}$$

where y_0 is the scattering peak height, q^*_{LAM} is the peak position, and w is the peak width. The background scattering, I_{bkg} was fit to a decaying exponential function:

$$I_{bkg}(q) = y_{b0} + y_{b1}\, exp\left(\frac{y_{b2}}{q}\right), \tag{6.15}$$

where y_{b0}, y_{b1}, and y_{b2} are constants. The adjustable parameters are C, χ, R_g, y_0, q^*_{LAM}, w, y_{b0}, y_{b1}, and y_{b2} for fitting Eqn. 6.2 to the experimental data (see Section 6.3.2). An example fit is provided in Fig. 6.2e and the fitting parameters for each data set can be found in Section 6.6.7.

6.6.2. Gyroid Peak Analysis

To analyze the peaks associated with the gyroid phase, the 2D profiles were divided into 36 sectors spanning 10° intervals. 0° is defined as the line from $q_x = 0$, $q_y = 0$ nm^{-1} to $q_x = 0$, $q_y =$ -1.0 nm^{-1} and the angle increases from 0° in the counterclockwise direction. Sectors with relatively intense spots of intensity corresponding to the gyroid phase were included in the average and the rest were excluded. The sectors which were included are highlighted in Fig. 2d and include the following ranges: 15-25°, 65-75°, 85-105°, 115-135°, 305-315°, 335-345°. These selected averages are reported in the inset of Fig. 6.2a and 6.4b.

6.6.3. Domain spacing and h_{GYR} calculations

The disordered phase domain spacing, d_{DIS}, was calculated by:

$$d_{DIS} = \frac{2\pi R_g}{\sqrt{3.6}} \tag{6.16}$$

where the factor of $\sqrt{3.6}$ was determined using the methodology of Teran et al[24] and R_g was taken from the fits of I_{DIS} described in Section 6.6.1. The domain spacing for the lamellar phase, d_{LAM}, and gyroid phase, d_{GYR} was calculated by:

$$d_{ord} = \frac{2\pi}{q^*_{ord}}. \quad (6.17)$$

where the subscript '*ord*' denotes LAM or GYR. q^*_{LAM} was obtained from the fit in Eqn. 6.2.

The peak position of the gyroid was determined from an iterative process. For each data set, a linear baseline was drawn between the data points $I(q = 0.7687\ \mathrm{nm}^{-1})$ and $I(q = 0.8053\ \mathrm{nm}^{-1})$. For each data point in the range $0.7687 < q < 0.8053$ nm^{-1}, the baseline was subtracted from the raw data. We then took the maximum from this dataset and defined the location of the maximum as $q^{*\prime}_{\mathrm{GYR}}$. On the second iteration, the baseline was drawn between the two points located +/- 18 data points from $q^{*\prime}_{\mathrm{GYR}}$ but truncated the data if it fell out of the range $0.7687 < q < 0.8053$ nm^{-1}. The new baseline was then subtracted from the raw data and we took the maximum of this data set to be h_{GYR} and the location of the maximum to be q^*_{GYR}. The results of the second iteration are shown graphically in Fig. 6.4b in Section 6.3.2.

6.6.4. Scattering Invariant and Volume Fraction Calculations

The scattering invariant, Q, represents the total scattering power of the sample and is proportional to the sample volume. For a heterogeneous system with two distinct phases separated by sharp interfaces (e.g. alternating PS and PEO lamella), Q is well defined and depends only on the volume fraction of one of the phases[40]. The invariant for the lamellar phase, Q_{LAM}, is calculated by:

$$Q_{LAM} = \int_0^\infty I_{LAM}(q) q^2\, dq\,. \quad (6.18)$$

Equation. 6.18 cannot be applied directly to the disordered phase. Replacing I_{LAM} with I_{DIS} results in Q_{DIS} which is unbounded. Following the methods of Thelen et al[161], we calculate the scattering invariant of the disordered phase, Q_{DIS}, by:

$$Q_{DIS} = \int_0^\infty \Delta I_{DIS}(q) q^2\, dq\,, \quad (6.19)$$

where

$$\Delta I_{DIS}(q) = I_{DIS}(q) - I_{DIS,\chi=0}(q), \quad (6.20)$$

and $I_{\mathrm{DIS},\chi=0}(q)$ takes the form of $I_{\mathrm{DIS}}(q)$ and uses the same fit parameters but maintains $\chi = 0$. While $I(q)$ was reported with arbitrary units, the dimensions will be an inverse length (L^{-1}). Conversion of $I(q)$ to absolute units is discussed in Ref [39] and data is typically reported in cm^{-1}. We thus represent the units of Q as L^{-1} nm^{-3}.

Because of the high electron density of the LiTFSI salt, Q_{DIS} and Q_{LAM} vary significantly with salt concentration, which changes with both time and position in the cell. In addition, Eqn. 6.18 and 6.19 assume that the scattering from the sample is independent of the orientation of the sample in the X-ray beam. While this should be a good assumption for the disordered phase, this is not true for lamella. Grains oriented with a normal vector parallel to the X-ray beam do not scatter. To account for these factors, we calculate the disordered phase volume fraction, f_{DIS}, from:

$$f_{DIS} = \frac{\frac{Q_{DIS}}{Q^0_{DIS}}}{\frac{Q_{DIS}}{Q^0_{DIS}} + \frac{Q_{LAM}}{Q^0_{LAM}}} \tag{6.21}$$

where the superscript '0' denotes the scattering invariant measured when only that phase is present (i.e. $f_{\mathrm{DIS}} = 1$ for $Q^0_{\mathrm{DIS}}$and $f_{\mathrm{DIS}} = 0$ for Q^0_{LAM}). We then define the correction factor, α, by:

$$\alpha = \frac{Q^0_{DIS}}{Q^0_{LAM}}. \tag{6.22}$$

Equation 6.3 in Section 6.3.2 is obtained by substituting Eqn. 6.22 into Eqn. 6.21. We can calculate α by plotting $Q_{\mathrm{DIS}}/t_{\mathrm{exp}}$ versus $Q_{\mathrm{LAM}}/t_{\mathrm{exp}}$ during a phase transition, where t_{exp} is the X-ray exposure time of each measurement (either 2 or 5 s, as described in the main text). We normalize Q by t_{exp} because it is expected (and experimentally observed) that Q is proportional to the sample exposure time. (We note that the reason t_{exp} does not appear in Eqn 6.21 or 6.22 is because these equations are related to the scattering intensities of the two phases in a single measurement, so the exposure time is the same for each phase and cancel out.) We do this for each of the four relevant phase transitions in Fig. 6.8 in Section 6.6.6. The relationship is linear in all four cases, and the *x*- and *y*-intercepts of the fit correspond to $Q^0_{\mathrm{DIS}}/t_{\mathrm{exp}}$ and $Q^0_{\mathrm{LAM}}/t_{\mathrm{exp}}$, respectively. For the lamellar to disorder transition in Region III and II, we obtain α = 2.7 and 3.3, respectively. For the disorder to lamellar transition in Region III and II, we obtain α = 1.9 and 1.5, respectively. While Q^0_{DIS} and Q^0_{LAM} still depend on salt concentration and are not identical in each of the four measurements, we prefer to use only one value of α for all calculations of f_{DIS} to avoid discontinuities in the data in Fig 6.3c. Therefore, we take an average and use α = 2.4 and note that the data in Fig. 6.3c is not sensitive to the choice of α (see Section 6.3.2).

6.6.5. Quantification of Anisotropy in 2D Scattering Patterns

It is evident from the 2D scattering profiles that the scattered intensity is not uniform azimuthally. For example, the ring of scattering corresponding to the primary lamellar peak in Fig. 6.2d has regions of higher scattering intensity near the top and bottom of the detector. To quantify the anisotropy, we divided the 2D scattering images into 36 sectors and examined the scattering from the disordered and ordered phases in each sector. The sector is identified by the azimuthal angle at the center of the sector (φ). For each 10° sector, the intensity was azimuthally averaged to obtain 1D scattering profiles. We then fit the $I(q)$ data for each sector to Eqn. 6.2 in Section 6.3.2 and calculated the invariant for the lamellar and disorder phases to obtain $Q_{\mathrm{DIS}}(\varphi)$ and $Q_{\mathrm{ORD}}(\varphi)$. We calculate the ratio of the invariant for each sector to the invariant for a full azimuthal average ($Q_{\beta,\mathrm{avg}}$); $Q_{\beta}(\varphi)/Q_{\beta,\mathrm{avg}}$, where β = '*DIS*' or '*LAM'*. The angle φ is defined in Section 6.6.2. We plot this ratio as a function of φ for Region I and III in Fig. 6.9. If $Q_{\beta}(\varphi)/Q_{\beta,\mathrm{avg}}$ = 1 for all φ, it implies the scattering is completely isotropic. We expect $Q_{\mathrm{DIS}}(\varphi)/Q_{\mathrm{DIS,avg}}$ = 1 because the scattering from a disordered phase should be independent of the beam orientation. For the lamellar phase, $Q_{\mathrm{LAM}}(\varphi)/Q_{\mathrm{LAM,avg}}$ = 1 would imply that all grain orientations are present in the

sample with the same prevalence. Scattering from a single lamellar grain will result in two scattering spots with a difference in φ of 180°. Therefore, if one grain orientation is preferred (*e.g.* in an aligned sample), there will be two peaks in $Q_\beta(\varphi)/Q_{\beta,avg}$ separated by 180°.

6.6.6. Supporting Figures

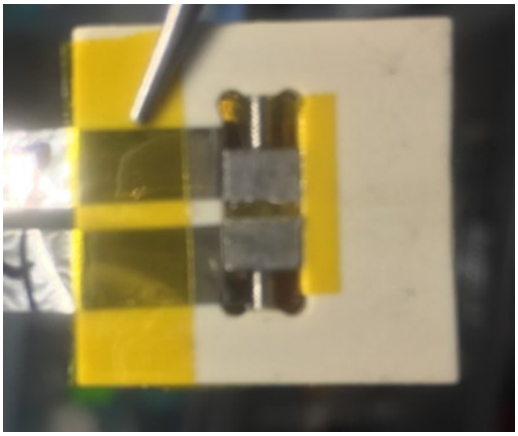

Figure 6.5. Picture of the assembled *in situ* SAXS cell. The picture was taken prior to placing a Kapton window over the cell and sealing inside an aluminum laminated pouch. The two set screws above and below the stainless-steel blocks were adjusted to apply slight pressure on the cell. The nickel tabs (to the left of the stainless-steel blocks) provided electrical contact.

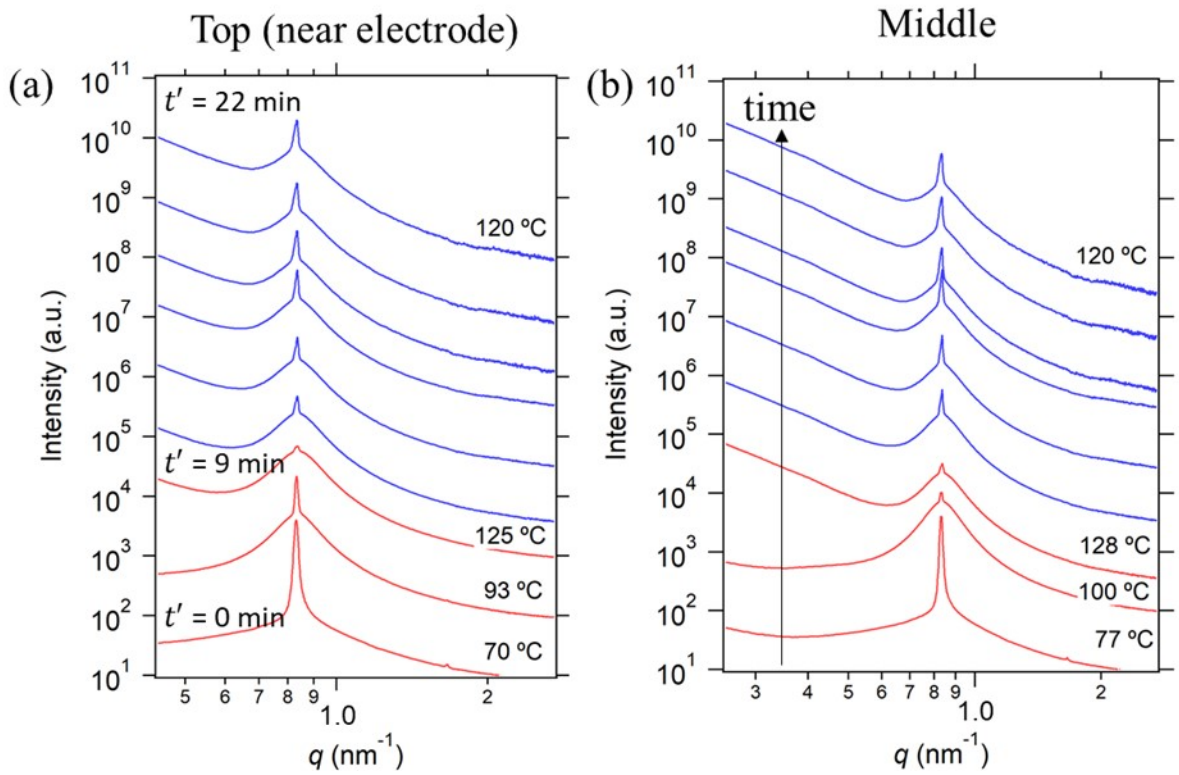

Figure 6.6. Evidence of lithium dissolution prior to *in situ* SAXS experiments. SAXS profiles in two regions of the cell during the initial heating to 120 °C offset by a decade for clarity. The stage temperature was set to 120 °C and the temperature reached a maximum of 128 °C before equilibrating. The background scattering from the pouch material changes significantly during the early times. The time stamps on the left panel give the approximate elapsed time from the point when the temperature set point was changed ($t' = 0$) with time increasing from bottom to top. The temperature labels on the right side of the curves reflect the real-time temperature of each profile. Red curves indicate the morphology during heating, and blue curves indicate the morphology after the maximum temperature was reached and during equilibration at 120 °C. The fact that the sample shows a higher or similar degree of ordering after equilibrating at 120 °C for 22 min (top blue curve in both panels) compared to at 90 to 100 °C during the initial heating (second red curve from the bottom in both panels) indicates that the ordered phase is stabilized at higher temperatures. This phenomenon has been established and is attributed to the dissolution of lithium metal from the electrodes (see Chapter 5).

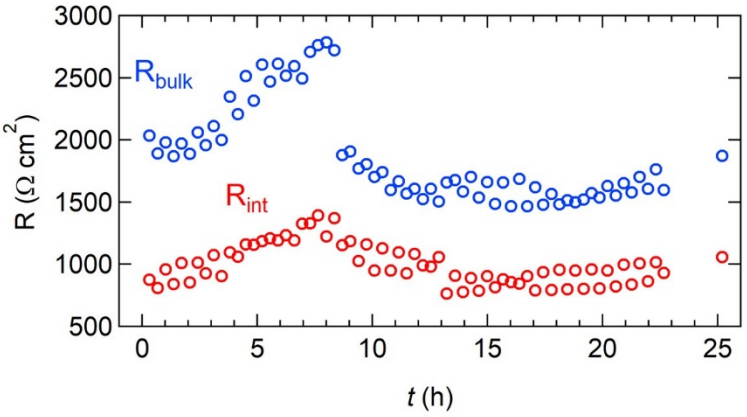

Figure 6.7. Impedance measurements taken during the experiment. The bulk (R_{bulk}) and interfacial (R_{int}) resistance of the cell measured by ac impedance spectroscopy at 30 min intervals throughout the duration of the experiment. The increase in R_{bulk} during polarization is due to the formation of salt concentration gradients in the cell. Similar values of R_{bulk} and R_{int} are obtained at t = -0.11 and 25.2 h.

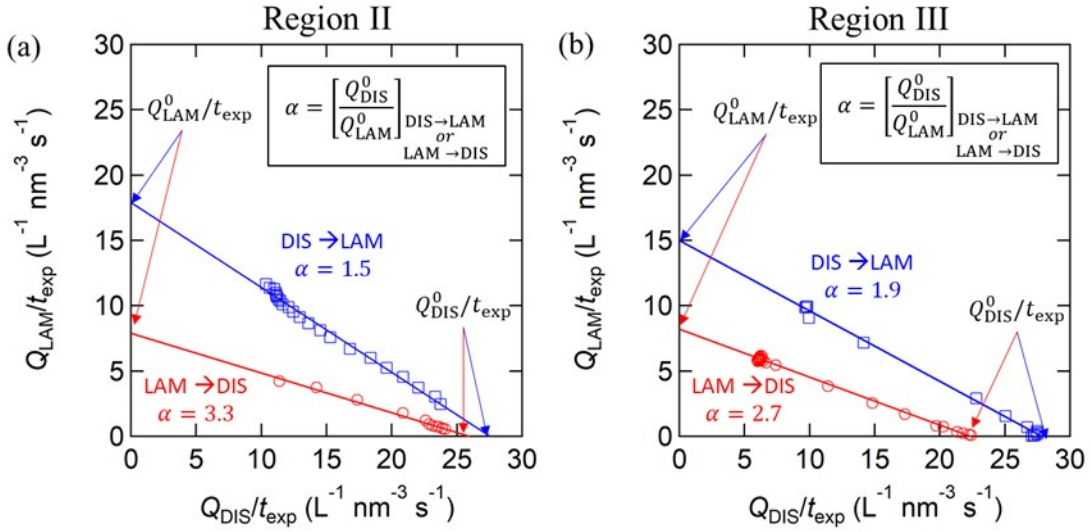

Figure 6.8. Correction factor for calculating the disordered phase volume fraction. Calculation of correction factor, α, used in Eqn. 6.3. We plot $Q_{\mathrm{LAM}}/t_{\mathrm{exp}}$ versus $Q_{\mathrm{DIS}}/t_{\mathrm{exp}}$ for the lamellar (LAM) to disordered (DIS) transition (red circles) and DIS to LAM transition (blue squares) in: (a) Region II and (b) Region III. We obtain α based on the methods discussed in the context of Eqn. S18. We fit a line to each data set and the *x*- and *y*- intercepts give the expected Q^0/t_{exp} for a pure lamellar (f_{DIS} = 0) and pure disordered phase (f_{DIS} = 1), respectively. We then use Eqn. 6.22 to calculate α. The average of all four measurements, $\alpha = 2.4$, is used in Eqn. 6.3 of Section 6.3.2 to calculate f_{DIS}.

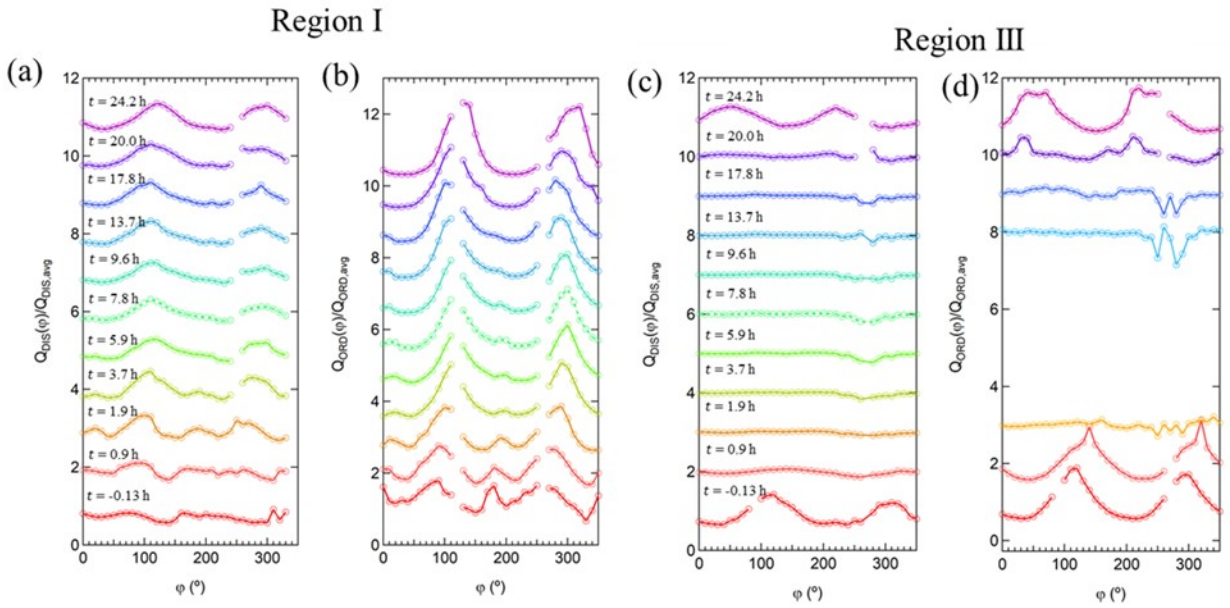

Figure 6.9. Anisotropy of scattering profiles over time. Ratio of the scattering invariant based on a 10° sector centered at azimuthal angle φ to the scattering invariant for the 360° azimuthal average; $Q_{\beta}(\varphi)/Q_{\beta,\mathrm{avg}}$, where β is either '*DIS*' or '*LAM*' for (a) the scattering from the disordered phase in Region I, (b) the scattering from the lamellar phase in Region I, (c) the scattering from the disordered phase in Region III, and (d) the scattering from the lamellar phase in Region III. The curves are offset vertically by

increments of one for clarity, and the time stamps in (a) and (c) also apply to the data sets in (b) and (d). Region I is near the positive electrode and exhibits a lamellar morphology for the entire experiment. In Fig. 6.9b, we observe two peaks in $Q_{\mathrm{LAM}}(\varphi)/Q_{\mathrm{LAM,avg}}$ around 100° and 280°, indicating the preferred grain orientation. In Fig. 6.9a, there are similar peaks for $Q_{\mathrm{DIS}}(\varphi)/Q_{\mathrm{DIS,avg}}$ at the same angles. We would expect that the scattering should be completely isotropic for the disordered phase. This result would thus imply that the diffuse scattering at the base of the lamellar peak is in some way associated with the lamellar phase, and not a completely independent disordered phase. In Region III, the block copolymer is completely disordered during polarization and then reforms the lamellar phase when the cell relaxes during the open circuit step. While the sample is completely disordered ($f_{\mathrm{DIS,III}} = 1$ for $2 < t < 16$ h), $Q_{\mathrm{DIS}}(\varphi)/Q_{\mathrm{DIS,avg}} = 1$ in Fig. 6.9c for all φ, which is the expected result for a completely disordered phase. For the lamellar phase in Region III, we observe peaks in $Q_{\mathrm{LAM}}(\varphi)/Q_{\mathrm{LAM,avg}}$ at $\varphi = 120°$ and 300° at $t = -0.13$ h (prior to polarization), however when the lamellar phase reforms during the open circuit step, the peaks appear at $\varphi = 60°$ and 240° at $t = 24.2$ h, indicating that the preferred grain orientation is different after the sample reforms the lamellar phase. This is an indication that the preferred grain orientation is not tied to some physical aspect of the cell but may be related to the nucleation of the lamellar phase.

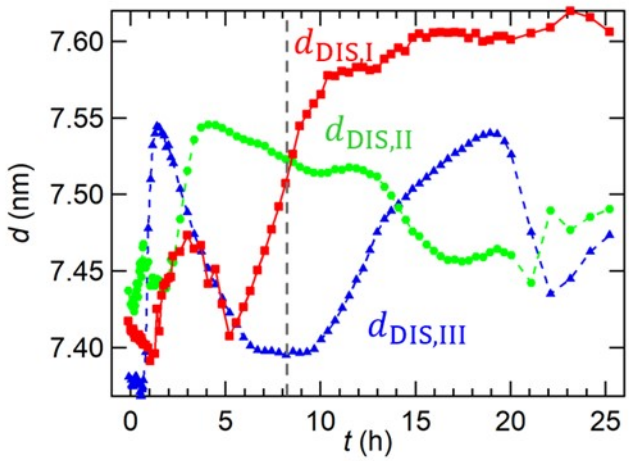

Figure 6.10 Disordered phase domain spacing in Regions I-III versus time. Domain spacing, d, of the disordered phase in Region I (red squares), Region II (green circles), and Region III (blue triangles) as a function of time. The gray dashed line denotes the switch to open circuit. The trends in $d_{\mathrm{DIS,III}}$ are discussed in the main text. The trends in $d_{\mathrm{DIS,II}}$ are qualitatively similar: the increase in $d_{\mathrm{DIS,II}}$ between $t = 2.1$ to 4.5 h is related to the lamellar to disorder transition and the decreases in $d_{\mathrm{DIS,II}}$ between $t = 13.0$ to 17.0 h is related to the reformation of lamellae from the disordered phase. We attribute the increase in $d_{\mathrm{DIS,I}}$ above values observed in the quiescent disordered state after $t = 5$ h to the presence of a high local salt concentration.

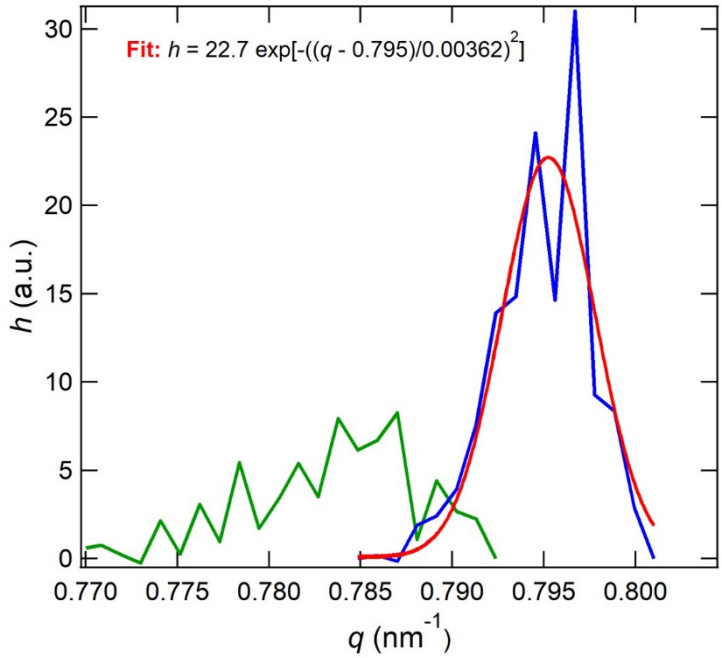

Figure 6.11. Gyroid peak analysis. Primary scattering peak from the gyroid phase at t = 9.6 h (green data set) and t = 13.7 data set (blue curve). The red curve is a fit to the t = 13.7 data set using a gaussian function. The scattering invariant is calculated from Eqn S14 to obtain $Q_{\mathrm{GYR}} = 0.18$ L^{-1} nm^{-3}, where L^{-1} represents the units of arbitrary inverse length. At t = 13.7, Q_{LAM}+ Q_{DIS} = 43.6 L^{-1} nm^{-3} (see Section 6.6.7), and we calculate the gyroid phase volume fraction, $f_{GYR} = \frac{Q_{\mathrm{GYR}}}{Q_{\mathrm{LAM}} + Q_{\mathrm{DIS}} + Q_{\mathrm{GYR}}} = 0.0042$. Here, we neglect the fact that only a fraction of the lamella scatter (*i.e.* Q_{LAM} is underestimated) and that we do not capture all of the scattering from the gyroid phase in our fit because of the selected averaging performed based on Fig. 6.2d in Section 6.3.2 (i.e. Q_{GYR} is underestimated). We expect that former to be more significant than the latter, and thus consider 0.42% to be an upper bound for the gyroid phase volume fraction.

6.6.7. Additional Supporting Information

Additional supporting information can be found at: https://doi.org/10.1021/acsami.0c16209.

The movie file, Region_I.mov, depicts the time evolution of the 2D SAXS profiles corresponding to Region I. The intensity scale bar in Fig. 2d of the main text applies for the images in the movie file. The emergence of the spots of scattered intensity corresponding to the gyroid phase (inside and outside the primary lamellar scatting ring) and the time evolution of their position as described in the main text are clearly visible.

Fit parameters are tabulated, obtained from fitting Eqn. 6.2 in the Section 6.3.2 to the 1D scattering profiles obtained from a 360° azimuthal average of the 2D scattering images and the scattering invariants calculated from $I_{\mathrm{DIS}}(q)$ and $I_{\mathrm{LAM}}(q)$ for the disordered phase and lamellar phase, respectively. The notation L^{-1} is used to denote the arbitrary units of the scattering intensity, which have dimensions of inverse length.

6.7 Nomenclature

Table 6.1 List of symbols and abbreviations

Symbol	Meaning
d	domain spacing, nm
DIS	disordered phase
f	volume fraction
f'	rescaled volume fraction
f_c	conducting phase (*i.e.* PEO/LiTFSI) volume fraction
GYR	gyroid phase
h	peak height, arbitrary units of inverse length
I	X-ray sampling region corresponding to the beam centered at xL^{-1} = 0.24
II	X-ray sampling region corresponding to the beam centered at xL^{-1} = 0.50
III	X-ray sampling region corresponding to the beam centered at xL^{-1} = 0.74
i	current density, mA cm^{-2}
I	scattered intensity, arbitrary units of inverse length
L	distance between the electrodes, mm
LAM	lamellar phase
LiTFSI	bis(trifluoromethylsulfonyl)amine lithium salt
PEO	poly(ethylene oxide)
PS	polystyrene
q	scattering vector, nm^{-1}
q^*	scattering vector at the primary peak, nm^{-1}
Q	scattering invariant, arbitrary units of inverse length per volume
r	salt concentration, molar ratio of LiTFSI molecules to ether oxygens
r_{avg}	average r from xL^{-1} = 0 to 1 in the electrolyte
SAXS	small angle X-ray scattering
SEO	polystyrene-*block*-poly(ethylene oxide)
t	time, h
T	temperature, °C
T_{ODT}	order-to-disorder transition temperature, °C
x	spatial coordinate parallel to the path of ion motion, μm
y	spatial coordinate perpendicular to the path of ion motion, μm

Table 6.2 List of symbols (Greek)

Symbol	Meaning
α	correction factor to obtain volume fraction from scattering invariants
Φ_a	potential at the anode, mV
Φ_c	potential at the cathode, mV
$\Delta\Phi$	cell potential drop, mV

7. Orientation-Dependent Distortion of Lamellae in a Block Copolymer Electrolyte under Dc Polarization**

ABSTRACT

Lithium salt-doped block copolymers have the potential to serve as solid electrolytes in rechargeable batteries with lithium metal anodes. In this work, we use small angle X-ray scattering (SAXS) to study the structure of a polystyrene-block-poly(ethylene oxide) doped with bis-(trifluoromethylsulfonyl)amine lithium salt (LiTFSI) during dc polarization experiments in a lithium symmetric cell. This block copolymer has a total molecular weight of 39 kg mol^{-1} and exhibits a lamellar morphology at all relevant salt concentrations. When ionic current is passed through the electrolyte sandwiched between two lithium electrodes, a salt concentration gradient forms which induces a gradient in the domain spacing, d. The dependence of d on distance from the positive electrode, x, was determined experimentally by scanning the incident X-ray between two lithium electrodes. The SAXS experiments performed as a function of time and position reveal significant asymmetry in d: on average, lamellae near the salt rich electrode swell in volume more than is compensated by the contraction of lamellae near the salt deficient electrode. As the salt concentration gradient becomes steeper (at higher current densities), this effect becomes more pronounced. Our results indicate that this effect limits the maximum current density which can be sustained through the block copolymer below that predicted for a homopolymer electrolyte with the same bulk transport properties. By studying the 2D SAXS patterns as a function of azimuthal scattering angle, we find that at a given location x, lamellae with PS/PEO interfaces oriented parallel to the flow of ionic current ($LAM_{||}$) swell and contract to a greater degree than those with interfaces oriented perpendicular to the current direction ($LAM_{\perp}$). While domains with the $LAM_{\perp}$ do not provide conducting pathways between the electrodes, our analysis suggests they play an important role in facilitating the salt concentration gradient.

7.1 Introduction

Solid-state lithium metal batteries are an attractive alternative to standard lithium-ion batteries as they offer improved energy density on two levels. At the cell level, lithium metal has the highest theoretical specific capacity (3.86 Ah g^{-1}) of any anode material for lithium-based batteries.[9] At the pack and device level, the use of non-flammable solid electrolytes reduces the need for auxiliary (and bulky) systems to mitigate thermal runaway and catastrophic failure, thus

** Adapted (with permission) from Galluzzo, M. D.; Grundy, L. S.; Takacs, C. J.; Cao, C.; Steinrück, H. G.; Fu, S.; Rivas Valadez, M. A..; Toney, M. F.; Balsara, N. P. Orientation-Dependent Distortion of Lamellae in a Block Copolymer Electrolyte under Dc Polarization. *In Preparation.* **2021**.

further increasing the practical energy density of the system while improving safety.[180] Nanostructured block copolymer electrolytes present one approach for enabling solid-state lithium metal batteries.[181] Polymer-based lithium metal batteries have had limited commercial success due to many reasons including: limited electrolyte conductivity, the need to establish new manufacturing protocols, and issues related to the reactive and pyrophoric nature of lithium metal.[182]

The purpose of this paper to shed light on the nature of ion transport in nanostructured block copolymers under dc polarization. Prior to polarization, the salt ions are uniformly distributed in all block copolymer domains. In systems wherein both the cation and anion are mobile, *i.e.*, the cation transference number with respect to the solvent velocity, t_+^0, is less than unity, salt accumulates near the positive electrode where lithium ions enter the electrolyte and is depleted at the negative electrode where lithium ions exit the electrolyte to react with (or intercalate into) the positive electrode. The result is a salt concentration gradient along the direction perpendicular to the current collectors while the total salt concentration within the entire electrolyte is conserved. This process is well understood in the case of homogeneous electrolytes.[42,77] During battery operation, we thus obtain regions of the electrolyte where the salt concentration is higher than the initial salt concentration, and regions where it is lower. If the volume of the electrolyte is fixed, the inescapable conclusion is that the solvent must rearrange to accommodate the salt concentration gradient. For liquid electrolytes, solvent molecules can rearrange easily, and we expect a lower concentration of solvent in regions where there is a high salt concentration and a higher concentration of solvent in regions where there is a lower salt concentration.[183,184] It is not well understood how or if this occurs in solid polymer electrolytes where the "solvent phase" is typically assumed to be immobile on macroscopic length scales. In this work, we show that this process is complex for a block copolymer electrolyte and the lamellar orientation relative to the electrodes plays an important role. Our results indicate that the process of block copolymer rearrangement limits the maximum current that can be sustained by a block copolymer electrolyte. We employ small angle X-ray scattering (SAXS) to study the structure of a block copolymer electrolyte during dc polarization.[38,185] We focus on a system that has been well-characterized in the literature[33,55,186]: polystyrene-block-poly(ethylene oxide) (SEO) block copolymer doped with bis-(trifluoromethylsulfonyl)amine lithium salt (LiTFSI). Polystyrene (PS) provides mechanical rigidity to suppress lithium dendrite growth while poly(ethylene oxide) (PEO) solvates and conducts lithium ions. We previously reported similar experiments on an SEO/LiTFSI electrolyte with PS molecular weight, M_{PS}, of 1.7 kg mol^{-1} and PEO molecular weight, M_{PEO}, of 1.4 kg mol^{-1}, which exhibited phase transitions over the range of salt concentrations studied.[11] In this study, we used an SEO copolymer with M_{PS} = 19 kg mol^{-1} and M_{PEO} = 20 kg mol^{-1} which exhibits a lamellar morphology over all salt concentrations, measured as the molar ratio of LiTFSI to ethylene oxide moieties, $r = [\mathrm{LiTFSI}]/[\mathrm{EO}]$. Since the modulus of the electrolyte increases with molecular weight, a longer chain block copolymer is more practical for battery applications.[20] Our goal is to study the response of a practical nanostructured block copolymer electrolyte subjected to dc polarization and understand the mechanisms which limit performance.

The maximum current that can be sustained through an electrolyte, *i.e.*, the limiting current, i_{lim}, depends on the salt concentration, r, and the distance between electrodes, L.[113,187] In this work, we study electrochemical cells comprising a block copolymer electrolyte sandwiched

between two lithium electrodes (*i.e.*, lithium symmetric cells). We will consider situations where a constant current is passed through the electrolyte in a lithium symmetric cell. As concentration gradients develop, the potential drop across the electrolyte increases. Eventually, the potential drop will either stabilize at some constant value or diverge, depending on whether the applied current density is below or above the limiting current density. The limiting current density is defined as the maximum current density which can be sustained through the electrolyte and typically coincides with the condition that the steady-state salt concentration at the negative electrode approaches zero. Above the limiting current, the potential begins to diverge because, in the absence of lithium ions at the electrode/electrolyte interface, electrons in the negative electrode begin to participate in irreversible parasitic reactions with the electrolyte.[188]

7.2 Experimental Methods

7.2.1 Materials.

The polystyrene-*block*-poly(ethylene oxide) (SEO) block copolymer used in this study was synthesized, purified, and characterized using methods described by Teran et al.[19] and Hadjichristidis et al.[114] The block copolymer electrolyte (polystyrene (PS) molecular weight of 19 and poly(ethylene oxide) (PEO) molecular weight of 20 kg mol^{-1}) was prepared following the methods reported by Yuan et al.[116] to produce an SEO/LiTFSI mixture with r = 0.16. We use the notation SEO(xx-yy) to denote SEO block copolymers with molecular weight of the PS and PEO blocks equal to xx and yy kg mol^{-1}, respectively. Lithium metal with nominal thickness of 0.75 mm was purchased from MTI and scraped with a nylon brush to expose a fresh lithium surface. The lithium was then cut into a 3.18 mm diameter disk and pressed at 500 psi, resulting in a disk approximately 1 cm in diameter and 0.1 mm thick. The lithium was then pressed against a stainless-steel block and the excess trimmed away from the edges to form the electrodes.

7.2.2 Electrochemical characterization of conductivity and limiting current

SEO samples for electrochemical measurements were prepared by placing electrolytes in annular spacers with inner diameters of 3.18 mm and hand-pressing them into pellets. Samples were hot-pressed at 90 ºC to create uniform, non-porous films. The polymer sample was sandwiched between stainless steel or lithium electrodes of known thickness. The total cell thickness was measured using a micrometer before attaching nickel current collectors and sealing the cell in polypropylene-lined aluminum pouch material. At this point the cells were removed from the glovebox for testing. The inner diameter of the spacer and the thickness measurements allow for determination of the cell constants A and L, the electrochemically active area and distance between electrodes, respectively.

Ionic conductivity of samples with blocking electrodes (stainless steel), κ, was measured by ac impedance spectroscopy at 90 ºC. Prior to measurement, cells were annealed at 120 ºC for at least 8 hours and then cooled to 90 °C. The bulk resistance, R_{b}, was determined by fitting an equivalent circuit and used to calculate the ionic conductivity, κ, via $\kappa = \frac{L}{R_{\mathrm{b}} A}$.

The limiting current was measured by assembling cells with lithium electrodes and L = 0.025 cm. All measurements were performed at 90 °C. The cells were polarized at constant current until either a steady state potential was reached or the potential diverged. In some cases, multiple polarizations were made on the same cell. After polarization, the current was set to zero and the potential relaxed until it stabilized around 0 V. For subsequent polarizations, the direction of the current was flipped.

7.2.3 SAXS measurements on samples with inert windows

SAXS characterization was performed on a series of electrolytes with different salt concentrations to obtain the domain spacing, d, as a function of r. We synthesized a series of electrolytes with salt concentrations ranging from r = 0 to 0.36. For each sample, electrolyte was hot pressed into an annular rubber spacer to create uniform, non-porous films with nominal thickness of 0.72 cm. Kapton windows with thickness of 0.025 cm were affixed on either side of the spacer and the sample was sealed in an air-free aluminum sample holder. The samples were then vacuum annealed at 120 °C for 8 h before bringing to the beamline for measurement. SAXS measurements were carried out at 90 °C on a custom built-heating stage. All SAXS experiments on samples with Kapton windows were performed at beamline 7.3.3. of the Advanced Light Source (ALS) at Lawrence Berkeley National Laboratory at an X-ray energy of 10 keV.[162] Silver behenate was used to determine the beam center and sample-to-detector distance. 2D scattering patterns were collected with a Pilatus3 2M detector (Dectris Ltd).

7.2.4 Preparation of electrochemical cells for simultaneous SAXS experiments.

The polymer electrolytes were dried at 120 °C under active evacuation in a glovebox antechamber for 24 h prior to constructing the cells for the simultaneous SAXS and electrochemical experiments. Lithium electrodes were pressed onto stainless steel current collectors and placed in the cell assembly which was machined out of poly(ether ether ketone) (PEEK). Polymer electrolyte was then hot pressed between the electrodes. Set screws were used to press the stainless-steel blocks closer together, until the distance between the two lithium electrodes was approximately 1.5 mm. (The distance between electrodes, L, was measured accurately at the beamline by X-ray transmission measurements, as detailed in the Supporting Information.) Excess polymer was then scraped away, and nickel tabs were affixed to the stainless-steel blocks. A reference channel, isolated from the electrochemical channel, was also filled with electrolyte of the same salt concentration. The PEEK assembly was the screwed shut and sealed in aluminum-laminated pouch material with nickel tabs protruding. A picture of the cell assembly and dimensions is provided in the Section 7.6.2. After assembling the lithium symmetric cells, the samples were vacuum annealed for 120 °C for 8 h. The samples were then cooled to room temperature and brought to the beamline for testing. The samples were affixed to a heating stage custom-built for simultaneous SAXS and electrochemical measurements. The samples were

allowed to thermally equilibrate for 1 h at 90C prior to polarization and then maintained at this temperature for the duration of the experiment.

7.2.5 Simultaneous SAXS and dc polarization experiments.

All simultaneous SAXS and dc polarization experiments were performed at Stanford Synchrotron Radiation Light Source beamline 1−5 at SLAC National Accelerator Laboratory. A custom-built sample heating stage was used for the measurements which allowed for up to three electrochemical cells to be studied simultaneously. The beam size was fixed at 500 μm (y-axis) by 200 μm (x-axis) by slits that are positioned downstream of a multilayer monochromator and toroidal focusing mirror. The sample is aligned such that the x-coordinate (defined as the direction of current flow between the electrodes) is along the vertical direction. The dimensions of the lithium electrodes were 0.195 x 0.395 cm. Thus, the electrolyte formed a rectangular prism where the 0.395 cm x L face was oriented with its normal parallel to the X-ray beam and the X-ray beam passed through 0.195 cm of electrolyte. Based on the cell geometry, we expect the sample to be uniform in structure and r along the y- and z-coordinates. The X-ray energy was 12 keV and the exposure time at each position was 10 s. The x- and y-coordinates of the cell were mapped out by scanning the beam around the sample and measuring the beam-stop diode intensity. The intensity reading from the diode was zero when the beam was positioned on the stainless-steel current collector and non-zero when passing through the lithium metal, polymer electrolyte, or PEEK. Intensity readings were used to calculate L (see Supporting Information). Silver behenate was used to determine the beam center and sample-to-detector distance. 2D scattering patterns were captured on a SX165 CCD detector (Rayonix, LLC). The 2D scattering profiles were reduced to 1D profiles using the PyFAI package for Python.[189]

7.2.6 Electrochemical measurements

All electrochemical measurements were made using a Biologic VMP3 potentiostat. Ac impedance measurements were made in a frequency range from 1 MHz to 100 mHz with an amplitude of 80 mV.

7.3 Results and Discussion

7.3.1 Electrolyte properties as a function of salt concentration.

To understand the transient phase behavior of a block copolymer electrolyte in the presence of a salt concentration gradient between two lithium electrodes, we start by characterizing the electrolyte under quiescent conditions over the range of salt concentrations that may be encountered during polarization. LiTFSI selectively partitions into the PEO domains,[35,36,117] and as a result the volume fraction of the conducting phase (PEO + LiTFSI) increases with salt concentration (see Chapter 4). One consequence is that the domain spacing, d, the distance

between the center of two lamella of the same component, increases as salt is added. Using sample holders with inert Kapton windows, we performed SAXS on a series of SEO(19-20)/LiTFSI electrolytes to extract the domain spacing, d, as a function of salt concentration, r. The domain spacing is related to the position of the primary scattering peak, q^*, by Eqn. 7.1:

$$d = \frac{2\pi}{q^*} \tag{7.1}$$

The results are presented in Fig. 7.1a. The neat block copolymer (r = 0) has a domain spacing of 28.1 nm. The domain spacing increases rapidly with increasing salt concentration until r = 0.04 where d = 35.9 nm. Above r = 0.06, d increases more gradually and shows a linear trend with r up until the highest salt concentration measured, r = 0.36, where d = 52.2 nm. Based on the data in Fig. 7.1a for individual electrolytes cast at different salt concentrations, we have a straightforward analysis to predict the spatial dependence of the domain spacing when a known salt concentration gradient forms across a lithium symmetric cell. This analysis, which relies on a quantitative relationship between d and r, is enabled by empirically fitting the data. The least squares fit using a sum of two exponential functions if given by the curve in Fig. 7.1a and the resulting expression is:

$$d\ (nm) = 149 - 114\,exp[-0.421r] - 7.09\,exp[-46.3r] \tag{7.2}$$

Newman's concentrated solution theory allows us to predict the salt concentration and potential gradient across a lithium symmetric cell during polarization.[42] The steady-state concentration profile, $r(x/L)$, and potential drop, U_{ss}, can be determined using integral relationships when the conductivity, κ, current fraction, ρ_+, and a term related to the thermodynamics of the electrolyte, $\frac{\mathrm{d}\,U}{\mathrm{d}\ln m}$, are known as a function of salt concentration. The details for modeling salt concentration profiles are discussed in refs [46,113,190]. Briefly, the salt concentration gradient at steady state, $r(x/L)$, can be determined from Eqn. 7.3 by an iterative process: 1) guess a salt concentration at x/L = 0, 2) calculate $r(x/L)$ based on the initial guess using Eqn. 7.3, 3) integrate $r(x/L)$ from 0 to 1 to determine the average salt concentration, 4) iterate the initial guess until the calculated average salt concentration matches the desired value (in our case, r = 0.16). Equation 7.3 is given by:

$$\int_{r(x/L=0)}^{r(x/L=1)} J_1(r)dr = -\frac{iL}{F}\left(\frac{x}{L}\right) \tag{7.3}$$

where F is Faraday's constant and

$$J_1(r) = \kappa\left(\frac{d\,U}{d\,ln\,m}\right)\left[r\left(1-\frac{1}{\rho_+}\right)z_+\nu_+F\phi_c\right]^{-1}. \tag{7.4}$$

Here, z_+ is the charge number of the cation, ν_+ is the number of cations the salt dissociates into, and ϕ_c is the volume fraction of the conducting phase. Once $r(x/L)$ is known, the steady state potential drop, U_{ss}, across the electrolyte can then be calculated by solving:

$$U_{ss}(x) = Fz_{-}\nu_{-}\int_{r(x/L=1)}^{r(x/L=0)} J_2(r)dr \tag{7.5}$$

where z_- is the charge number of the anion and ν_- is the number of anions the salt dissociates into and

$$J_2(r) = \left(\frac{d\,U}{d\,ln\,m}\right)\left[r\left(1-\frac{1}{\rho_+}\right)z_+\nu_+F\phi_c\right]^{-1} \tag{7.6}$$

Derivations for Eqn. 7.6 through 7.9 are provided in ref [46]. The equations presented here are rearranged by substituting expressions for the anion transference number with respect for the solvent velocity, t_-^0, which is given by:

$$t_-^0 = 1 - t_+^0 = -\left(\frac{1}{\rho_+}-1\right)\frac{z_+\nu_+FDc\phi_c}{\kappa}\left(\frac{d\,U}{d\,ln\,m}\right) \tag{7.7}$$

In previous work, we demonstrated that ρ_+ and $\frac{\mathrm{d}\,U}{\mathrm{d}\ln m}$ in SEO/LiTFSI electrolytes follow universal trends regardless of chain length and conducting phase volume fraction, given by Eqn. 7.8 and 7.9 (see Chapter 4):

$$\rho_+ = 0.18 - 1.7r + 6.3r^2 \tag{7.8}$$

$$\frac{dU}{d\,ln\,m}(mV) = -74 - 66\,ln\,m - 13.8(ln\,m)^2 \tag{7.9}$$

The dependence of ϕ_c on r is given by:

$$\phi_c = \frac{v_c}{v_c + \frac{M_{PS}M_{EO}}{M_S M_{PEO}}v_S} \tag{7.10}$$

where M_{PS} and M_{PEO} are the molecular weight of the PS and PEO blocks (19,000 and 20,000 g mol^{-1}, respectively), M_s and M_{EO} are the molar mass of the styrene and ethylene oxide monomers (104.2 and 44.05 g mol^{-1}, respectively), and v_c is the molar volume of the conducting phase (PEO + LiTFSI), given by $v_c = \frac{M_{EO}}{\rho_c(r)}$. The density of the conducting phase, $\rho_c(r)$, was taken from ref [58]. The implication of Eqn. 7.3 through 7.9 is that, for any SEO/LiTFSI electrolyte, we need only measure the ionic conductivity, κ, as a function of r to predict $r(x/L)$ at steady state and U_{ss} for a given current density. We present κ as a function of r for SEO(19-20)/LiTFSI in Fig. 1b based on ac impedance spectroscopy preformed on cells with blocking (*i.e.*, stainless steel) electrodes. The data presented in Fig. 1b was obtained at 90 °C after annealing at 120 °C for 8 h. The conductivity of block copolymer electrolytes is a function of the grain size which can change depending on the thermal history of the sample. To avoid this, we kept the thermal history identical for all samples. The conductivity of SEO(19-20) increases with salt concentration from the dilute limit until r = 0.1 and then plateaus at higher salt concentrations. The results are consistent with measurements on other block copolymer electrolytes which have been reported on in the literature and we defer discussion of the relationship between κ and r to those references[37,116,123,186] and Chapter 3. We fit the conductivity following the functional form presented in ref [131] and obtain:

$$\kappa\ (S\ cm^{-1}) = 0.00237r\ exp\left[-\frac{r}{0.170}\right] \tag{7.11}$$

We can thus calculate $J_1(r)$ and $J_2(r)$ for SEO(19-20)/LiTFSI electrolytes using Eqn. 7.8 through 7.11 and the results are presented in the Section 6.6.2.

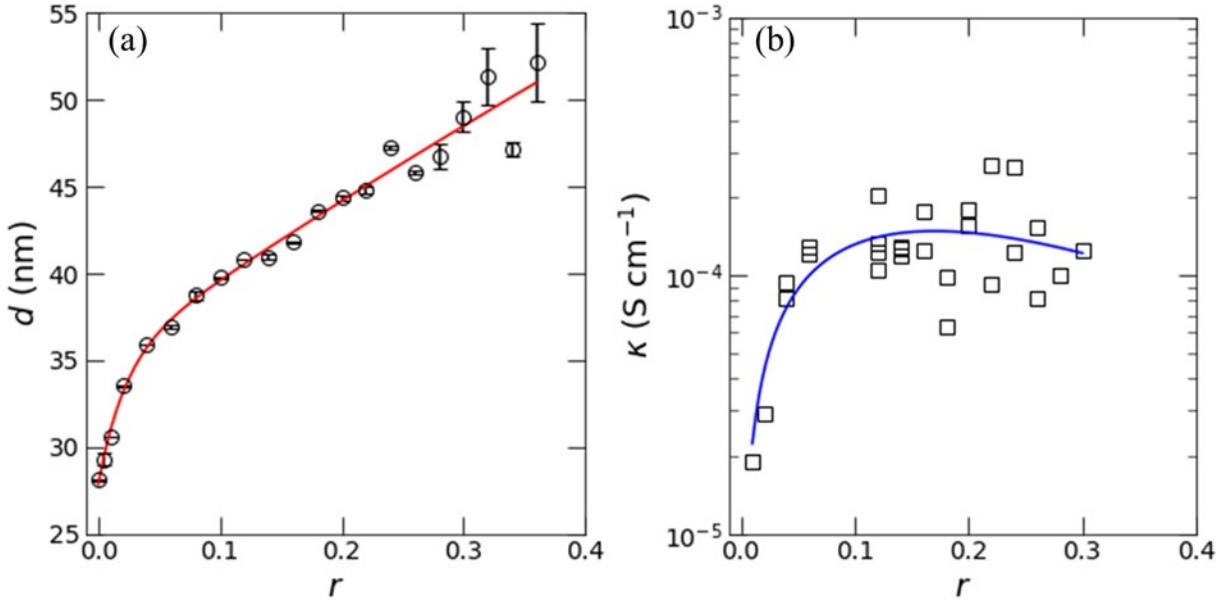

Figure 7.1. Domain spacing and conductivity versus salt concentration. (a) Domain spacing, d, versus molar salt concentration, r, for a series of SEO(19-20)/LiTFSI electrolytes at 90°C. The electrolyte exhibits a lamellar morphology at all salt concentrations. The red line is a double exponential fit to the data given by Equation 2. (b) Conductivity, κ, versus r measured from ac impedance spectroscopy in cells with blocking electrodes at 90°C. Each data point represents a measurement from a unique cell. We performed measurements on 1-4 cells for each salt concentration. The black curve is a fit to the data given by Eqn. 7.3. In both (a) and (b), the samples were annealed at 120 °C for 12 h and then cooled to 90 °C prior to the measurement.

In this paper, we will predict salt concentration profiles at steady state and U_{ss} for various current densities. We test the predictions of concentrated solution theory by experimentally measuring the voltage versus time behavior (at constant polarization current) of our electrolyte with initially uniform salt concentration of r = 0.16. Lithium symmetric cells were constructed with L = 0.025 cm. The cells were polarized at constant current density, i, and the potential was measured. If iL is below $i_{\lim}L$, it is expected that the potential will plateau and reach a steady-state value, $U_{\rm ss}$, indicating that a time-independent concentration profile is achieved. The timescale on which the cell reaches steady state is proportional to L^2. (For the simultaneous polarization and SAXS experiments, which we discuss in the next section, $L \sim 0.15$ cm and the timescales are expected to be about 36 times longer relative to the cells with L = 0.025 cm.) If iL is above $i_{\lim}L$, then the potential will diverge instead of reaching a plateau. In Fig. 7.2a, we plot the potential response for a series of applied current densities: $iL = 0.025$ (red trace), 0.10 (orange trace), 0.40 (yellow trace), 0.60 (green trace), 1.6 (blue trace), 3.2 (purple trace), and 6.4 μA cm^{-1} (black trace).

The cell potential, U, is the potential drop across the electrolyte. Experimentally, we measure the potential drop across the current collectors, ΔV, which includes a significant contribution from the resistance at the lithium electrode/electrolyte interfaces. We calculate the interfacial potential drop, ΔV_{int}, by multiplying the interfacial resistance measured from ac impedance spectroscopy and the current ($\Delta V_{\text{int}} = R_{\text{int}} iA$) (see Chapter 2). The interfacial resistance was approximately constant throughout each polarization experiment, so ΔV_{int} is assumed to be independent of time. The data in Fig. 7.2a and 7.2b have been corrected by subtracting ΔV_{int} from the measured voltage ($U = \Delta V - \Delta V_{\text{int}}$). In Fig. 7.2b, we plot U_{ss} versus iL with red star makers. We see excellent agreement between theory and experiment up to iL = 3.2 μA cm^{-1}. At iL = 6.4 μA cm^{-1}, the potential diverges after about 5 h in Fig. 7.2a. In Fig. 7.2b, we denote this experimental observation by the red dashed line which extends towards infinity above iL = 3.2 μA cm^{-1}. We estimate i_{lim} as the average between the largest sustained current density and the lowest value measured which resulted in a divergence of the potential. Thus, the limiting current measured experimentally is estimated to be 4.8 ± 1.6 μA cm^{-1}.

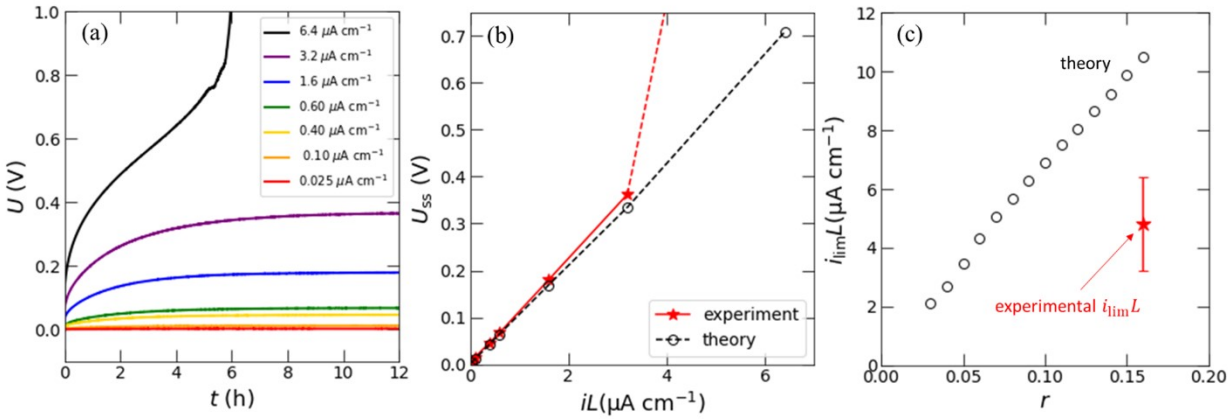

Figure 7.2. Comparison of an experimental limiting current measurement to theory. (a) Experimental measurement of the limiting current. The potential drop across the electrolyte, U, is plotted versus time, t, for increasing current densities from iL = 0.025 to 6.4 μA cm^{-1} with L = 0.025 cm. A steady-state potential, U_{ss} is obtained for all currents except iL = 6.4 μA cm^{-1} where U diverges after 5 h. We take the experimental limiting current to be the average of the lowest unsustainable current density (6.4 μA cm^{-1}) and the highest sustainable current density (3.2 μA cm^{-1}). The error bars in (c) depict the fact that the true value of $i_{\text{lim}}L$ may lie anywhere between these two values. (b) U_{ss} versus iL from experiment (red stars) and theory (black open circles). The dashed red line indicates that the steady state potential diverges to infinity at iL = 6.4 μA cm^{-1}. (c) Normalized limiting current, $i_{\text{lim}}L$, versus molar salt concentration, r. Black open circles represent the predicted $i_{\text{lim}}L$ from concentrated solution theory. The data point marked by a red star indicates the value of $i_{\text{lim}}L$ measured experimentally.

Using Eqn. 7.3 through 7.11, we can predict i_{lim} by extrapolating to the case where the salt concentration reaches zero at the plating electrode (see Fig. 7.11 in Section 7.6.2).[46,113,190] In Fig. 7.2c, we plot theoretically predicted limiting current for SEO(19-20)/LiTFSI electrolytes with r ranging from 0.02 to 0.16 as open black circles. The limiting current normalized by the distance between electrodes, $i_{\text{lim}}L$, is plotted versus r; we choose this format because results obtained using

symmetric cells with other values of L can be compared directly with the data presented here. We note that these predictions are made using no adjustable parameters. We see the expected behavior that $i_{\lim}L$ increases monotonically with salt concentration from 2.12 μA cm^{-1} at r = 0.03 to 10.5 μA cm^{-1} at r = 0.16. The red star in Fig. 7.2c represents the experimentally measured limiting current. The experimental value is approximately a factor of two lower than that predicted by concentrated solution theory. One of the motivations for the simultaneous SAXS and polarization experiments described in the next section is to investigate the reason for this discrepancy.

7.3.2 Gradients in domains spacing as a function of current density

To monitor the structure of the SEO(19-20) with r = 0.16 electrolyte during polarization, we built a custom electrochemical cell to allow simultaneous SAXS measurements. This cell is shown schematically in Fig. 7.3a. The lithium electrodes are in the y-z plane such that the nominal direction of ionic current is parallel to the x-axis. In Fig. 7.3b, we show an example of a SAXS pattern obtained from SEO(19-20) where the incident beam is oriented in the z-direction. Our sample, which is made by pressing the freeze-dried electrolyte into the sample holder, consists of lamellar grains oriented in different directions. The information in a 2D SAXS pattern from a collection of lamellar grains is dominated by lamellae which have normal vectors in the plane parallel to the detector (the x-y plane, in our case); the normal vector is defined to be perpendicular to the nominal interfaces between adjacent lamellae.[191] By scanning the beam along the x-axis, the 2D scattering patterns contain information about the structure of lamellae with normal vectors in the x-y plane along the axis which the salt concentration gradient forms in a dc polarization experiment. We define the azimuthal angle, χ, in Fig. 7.3b and denote χ = 0° along the y-axis, pointing upwards and increasing counterclockwise. The SAXS pattern is divided into 18 sectors as shown in Fig. 7.3b and the cartoons in each sector indicate the orientation of lamellar grains which give rise to scattering in that sector. By analyzing data at χ = 0 and 180° (as defined in Fig. 7.3b) we obtain information about grains with lamellar planes parallel to the flow of ionic current (we call these lamellae $LAM_{||}$, and note that their normal vectors are parallel to the y-axis). For χ = 90 and 270°, we obtain information about grains with lamellar planes perpendicular to the flow of ionic current (we call these lamellae $LAM_{\perp}$, and note that their normal vectors are perpendicular to the y-axis).

From an electrochemical perspective, the component of the normal vector which lies along the direction of current (x-axis) dictates the role of that grain in ion transport. For example, the normal vector for $LAM_{||}$ is along the y-axis, so no component of the normal vector is along the x-axis. Electrochemically, $LAM_{||}$ are identical to lamellar grains with normal vectors along the z-axis (or any vector in the y-z plane, for that matter). Based on the scattering geometry, however, the SAXS patterns contain no direct information about grains with normal vectors along the z-axis. The subset of grain orientations with normal vectors in the y-z plane correspond to grains with lamellar planes parallel to the current (although we reserve the term $LAM_{||}$ to those with normal vectors along the y-axis). This subset of grains provides conducting pathways directly between the electrodes and contribute more than any other orientation to the ionic conductivity.[108] Although scattering data in the χ = 0 and 180° sectors result from the $LAM_{||}$ orientation, we can

extrapolate results to be representative of all grain orientations with normal vectors in the y-z plane. This parity emerges because the y- and z- directions are identical: we do not expect variations in salt concentration or structure in either direction. The grain orientations depicted in the 18 sectors of Fig. 7.3b have fractions of their normal vectors lying along the x-axis spanning from 0 ($LAM_{||}$) to 1 ($LAM_{\perp}$) and thus cover all grain orientations for which we expect distinct electrochemical behavior. The argument which led us to extrapolate results for $LAM_{||}$ to any grain with normal vector in the y-z plane can be made for each orientation shown in Fig. 7.3b: each subset of grain orientations is generated by rotating the normal vector about the x-axis, and grains in a single subset are expected to behave identically. Therefore, the information contained in the 2D scattering patterns is representative of all possible grain orientations in our sample.

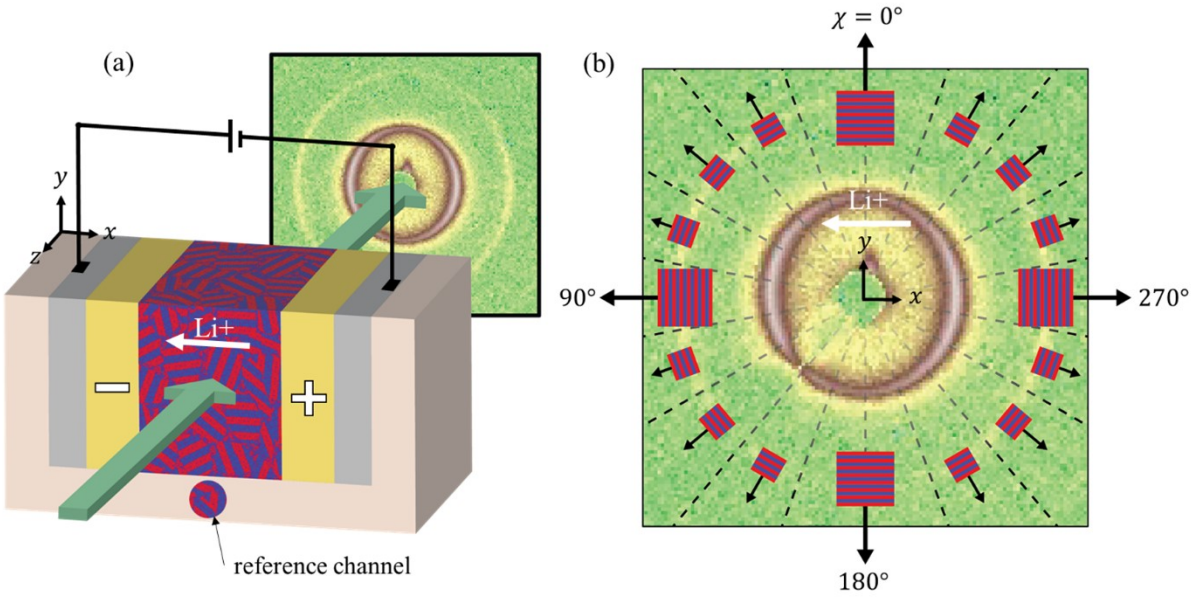

Figure 7.3. Simultaneous SAXS and polarization experimental set up. (a) Schematic representation of the simultaneous polarization and SAXS experiment. An SEO/LiTFSI electrolyte with randomly oriented grains is sandwiched between two lithium electrodes with current passing parallel to the x-axis. X-rays pass parallel to the z-axis, perpendicular to the current. Scanning the beam along the x-axis allows for spatial resolution between the electrodes. A reference channel filled with electrolyte was placed next to the electrochemical cell. (b) Characteristic 2D SAXS pattern obtained from experiments. The pattern is divided into 18 sectors defined by the azimuthal angle, χ. Scattering data in each sector corresponds to lamellae oriented with the angle between the vector normal to the PEO/PS interfaces and the positive y-axis equal to χ. The cartoons in each sector show the lamellar orientation with normal vectors drawn. The white arrows indicate the direction of current flow.

Using the experimental geometry shown schematically in Fig. 7.3, we studied three lithium symmetric cells comprising an SEO(19-20)/LiTFSI electrolyte with r = 0.16 at three current densities. The beam was aligned so that the 200 μm beam dimension was along the x-axis of the cell (i.e., the axis perpendicular to the planar electrodes, which is the direction of ionic current flow). The 500 μm dimension was along the y-axis of the cell and in the center of the channel

along the y-axis. The sample was scanned in 100 μm increments along the x-axis, beginning and ending over the stainless-steel current collectors. When the beam was aligned over the stainless-steel, the beam was completely attenuated, and the transmitted and scattered intensity were both zero. We used the transmitted intensity to define the coordinates and measure L for each cell, as described in the Section 7.6.2. We define the initial time, $t = 0$, as the first moment of polarization. Throughout this work, we discuss the current in terms of iL which is the current, I (μA), divided by the electrode surface area, 0.077 cm^2 for all three cells, multiplied by the distance between electrodes, L (cm).

We begin by analyzing SAXS data for cells polarized at iL = 0.946 μA cm^{-1} (Fig. 7.4a), 2.13 μA cm^{-1} (Fig. 7.4b), and 3.82 μA cm^{-1} (Fig. 7.4c). An example of a 2D SAXS pattern obtained from these experiments is presented in Figure 7.3b. A 360° azimuthal average of the data was performed to obtain 1D SAXS profiles of the scattered intensity, I, as a function of the scattering vector, q. We obtain the domain spacing by fitting the primary scattering peak to a pseudo-Voight function as described in the Supporting Information to obtain q^* and calculating d from Eqn. 7.1. In Fig. 7.4, we plot d as a function of normalized position between the electrodes, x/L. Lithium stripping occurs at the positive electrode where $x/L = 0$ and lithium plating occurs at the negative electrode where $x/L = 1$. The top panel in each figure (Fig. 7.4a-c) shows the potential, U, response of the cell as a function of time. The black dashed line represents U_{ss} predicted from theory. In all cases, the measured potential stays below the predicted value and does not reach a clear plateau before the experiment was halted at t = 48 h, mainly due to limited access to the SAXS instrument. The rainbow color scheme in the top panel and main figure are coordinated such that the color of the data points on the U vs t plot correspond to the time which the data set of the d versus x/L was obtained. Purple data sets were obtained near the beginning of the polarization step (t = 0 h) and red data sets were obtained near the end (t = 47 h). To account for drift of the sample stage, and thus changes in the sample-to-detector distance and interpreted *d*-values, we included a reference sample of electrolyte in a cylindrical channel directly next to, but isolated from, the electrochemical channel. The domain spacing of the reference, d_{ref}, was measured after each scan of the cell and varied by about 0.5 nm over the course of the experiment. We thus corrected the raw measurement of the domain spacing, d_{raw}, by a correction factor given by Eqn. 7.12:

$$d(t) = d_{raw}\left(\frac{d_{ref}(t=0)}{d_{ref}(t=t)}\right) \tag{7.12}$$

Plots of $d_{\mathrm{ref}}(t)$ are presented in the Fig. 7.12 in Section 7.2 for each cell with additional discussion.

In Fig. 7.4a, a constant current density of 6.34 μA cm^{-2} was applied across a cell with L = 0.143 cm (iL = 0.946 μA cm^{-1}). At t = 0 h, the average domain spacing across all positions is 42.4 nm. The domain spacing is not completely uniform initially; d = 42.3 nm near the center of the cell and d = 42.6 nm near the electrodes. We suspect this difference (less than 1% of the domain spacing) is due to uneven pressure distribution on the lamella during sample preparation. This trend is also seen in Fig. 7.4b and 7.4c. In Fig. 7.4b, a current density of 13.5 μA cm^{-2} was applied across a cell with L = 0.158 cm (iL = 2.13 μA cm^{-1}), and in Fig. 7.4c, a current density of 27.3 μA cm^{-2} was applied across a cell with L = 0.140 cm (iL = 3.82 μA cm^{-1}). For each cell, d increases near the positive electrode where local salt concentration increases and decreases near the negative electrode where local salt concentration decreases. The gradient in d develops near the electrodes

first, then propagates towards the center of the cell and becomes more linear with time. To highlight this, we drew lines through the d versus x/L data sets corresponding to t = 4.7 and 19.6 h along with the first (t = 0 h) and last data (t = 46.6 h) set. The vertical dashed lines in the top figure correspond to the data sets with lines drawn through in the bottom figure. The qualitative observation that the domain spacing changes first near the electrodes before propagating into the center of the cell is consistent with predictions of time-dependent concentration profiles from concentrated solution theory.[176]

As the current increases from Fig. 7.4a to 7.4c, the magnitude of the domain spacing gradient increases. For the lowest current density, the difference in d between the positive and negative electrodes at t = 46.6 h is 1.63 nm, for the middle current density, it is 3.84 nm, and for the highest current density, it is 9.08 nm. A larger salt concentration gradient is expected for higher current densities as the flux of the anion due to migration is larger and thus a larger diffusive flux is required to match it and achieve steady state. Interestingly, the domain spacing gradients are not symmetric; the increase in domain spacing at the positive electrode is larger than the magnitude of the decrease in domain spacing at the negative electrode. This effect is most prominent for the largest current density in Fig. 7.4c. We will discuss this observation in more detail in the context of Fig. 7.5 and 7.6. For all three current densities, the point where d shifts from increasing to decreasing is at a position x/L = 0.6. We next turn to Eqn. 7.2 to convert the measured domain spacings into local salt concentrations as they can be directly compared with theoretical predictions.

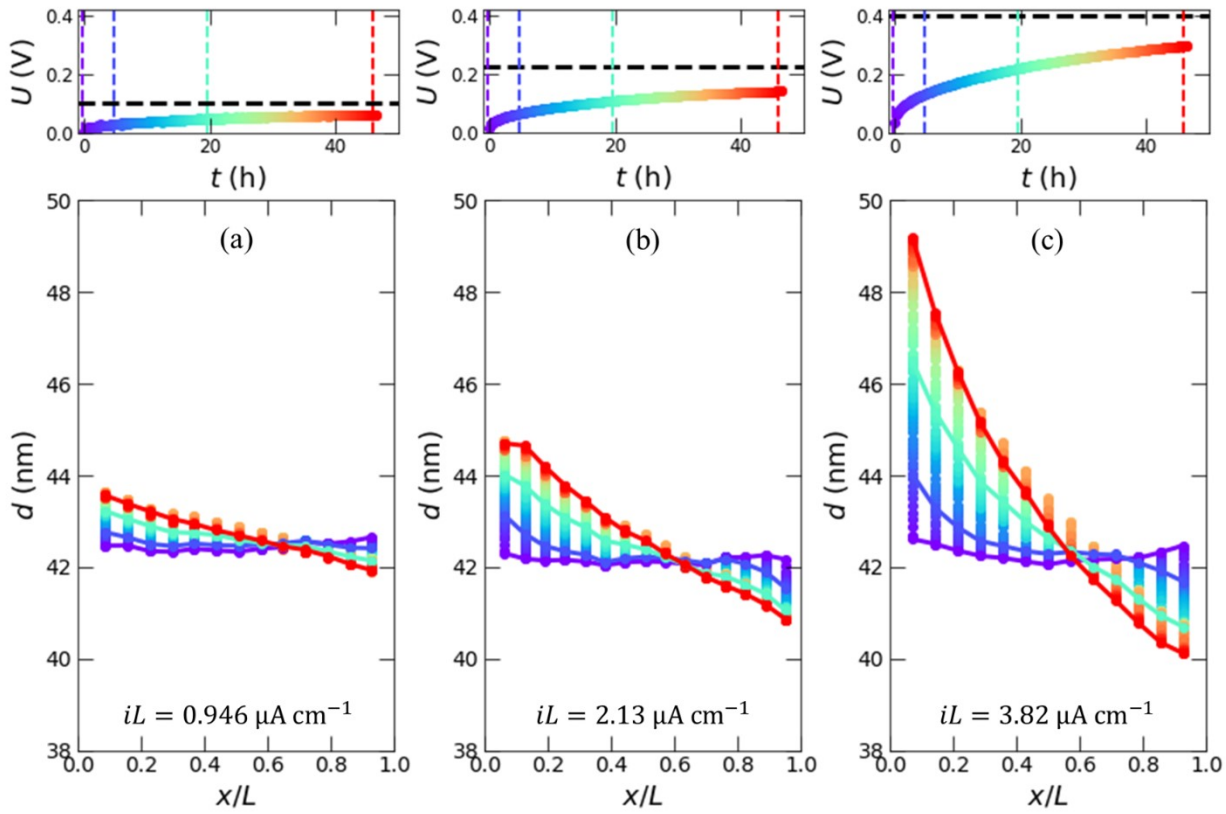

Figure 7.4. Results from simultaneous polarization and SAXS experiments at three current densities. (a) The potential drop across the electrolyte, U, versus time, t, is plotted in the top panel of each figure. The dashed line represents the steady state potential (U_{ss}) predicted from concentrated solution theory. In the main panel, the domain spacing, d, is plotted versus normalized cell position, x/L. The color of each data set corresponds with the U versus t plot in the top panel. Purple data sets were obtained at the beginning of polarization (t = 0 h) and red data sets were obtained at the end of polarization (t = 46.6 h).

7.3.3 Domain spacing as a proxy for salt concentration.

For each data point in Fig. 7.4a through 7.4c, we calculate a local salt concentration from Eqn. 7.2 to obtain $r(x/L, t)$ for each cell, and the results are plotted as data points in Fig. 7.5, following the same color scheme as Fig. 7.4. The black dashed lines represent the nominal initial salt concentration (r = 0.16) of the cell, and the solid black lines represent the steady state salt concentration gradient predicted from theory. Based on Fig. 7.2a, we calculate the ratio of the current density to the limiting current, i/i_{lim}. Because the predicted limiting current differs significantly from the measured limiting current, we report the ratio of the applied current to both the experimental and theoretical limiting currents, $i_{\mathrm{lim,expt}}$ and $i_{\mathrm{lim,theory}}$. The applied current density is 20%, 44%, and 80% of $i_{\mathrm{lim,expt}}$ and 9.0%, 20%, and 36% of $i_{\mathrm{lim,theory}}$ for Fig. 7.5a, 7.5b, and 7.5c, respectively. In Fig. 7.5a and 7.5b, we see good agreement between the experiment and the theory; the magnitude of the salt concentration near the end of the polarization experiment

matches the predicted salt concentration gradient. Conversely, the agreement with $r(x/L)$ is poor in Fig. 7.5c at iL = 3.82 μA cm^{-1}.

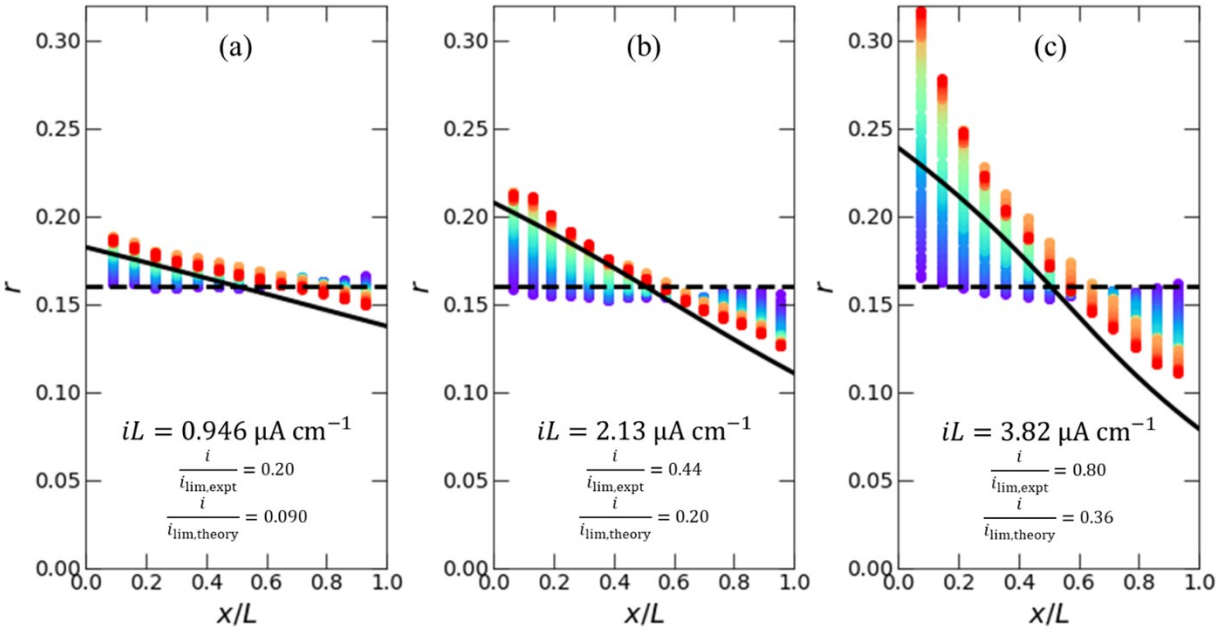

Figure 7.5. Molar salt concentration, r, versus normalized cell position, x/L, based on converting the domain spacing, d, presented in Fig. 7.4 to r with Eqn. 7.2. We report the ratio of the applied current to the experimental limiting current, $i_{\text{lim,expt}}$ and the theoretical limiting current, $i_{\text{lim,theory}}$. (a) Data obtained with iL = 0.946 μA cm^{-1}. (b) Data obtained with iL = 2.13 μA cm^{-1}. (c) Data obtained with iL = 3.82 μA cm^{-1}. The color scheme for each data set matches that presented in Fig. 7.4a through 7.4c. The dashed black line represents the nominal initial salt concentration, r = 0.16. The solid black line represents the predicted salt concentration gradient from theory.

In Fig. 7.5c, using the domain spacing as a proxy for salt concentration results in local values of r which are significantly greater than the theory across the entire cell. The salt concentration averaged across all positions calculated from Eqn. 7.2 in Fig. 7.5c is r = 0.157 at t = 0 h and r = 0.186 at t = 46.6 h, an increase of 18%. This is an unphysical result: the average salt concentration must be conserved throughout the experiment. We thus conclude that the assumed relationship between r and d, which was based on measurements on samples at equilibrium, is not valid when ionic current flows through the sample. Nevertheless, we obtain considerable insight into the origin of the observed gradients in d under applied electric fields by combining equilibrium measurements of domain spacing with concentrated solution theory. Agreement between theory and experiment is reasonable for $i/i_{\text{lim,expt}} < 0.5$ where we see good agreement between theoretical and experimental U_{ss} versus iL data in Fig. 7.2b.

7.3.4 Swelling and contracting lamellae at high current density.

To gain deeper insight into the swelling and contrition of the lamellae at high current density, we performed the following experiments. After polarizing the cell in Fig. 7.4a at 0.946 μA cm^{-1} for 46.6 h, we increased the current by a factor of 12 to 11.3 μA cm^{-1} (*i.e.*, $i/i_{\mathrm{lim,expt}}$ = 2.4 and $i/i_{\mathrm{lim,theory}}$ = 1.07). The potential of the cell is plotted as a function of time in Fig. 7.6a beginning at t = 46.6 h when the current was abruptly increased in a blue to green color scheme. At that time, the potential jumps from 0.08 V to 0.2 V and then steadily increases. At t = 58 h, there is an inflection point and the potential diverges. A cutoff voltage was set at 1.0 V, and the cell was switched to open circuit (i = 0 μA cm^{-2}) at t = 61.1 h. The potential then begins to decay, plotted in a blue to pink color scheme, as the concentration gradient relaxes.

Throughout the experiment, we measured $d(x)$ as a function of time. We define the change in domain spacing, Δd, by Eqn. 7.13:

$$\Delta d(x/L,t) = d(x/L,t) - d(x/L,t=0) \tag{7.13}$$

Recall that $t = 0$ is at the beginning of the first polarization step at 0.946 μA cm^{-1}, so the quantity $\Delta d(x/L,t)$ reflects the change in domain spacing from the quiescent, r = 0.16 electrolyte. In Fig. 7.6b, we plot Δd as a function of normalized position in the cell from t = 0 to 61.1 h. Data sets plotted with black markers represent Δd during the first 0.946 μA cm^{-1}. The magnitude of Δd is less than 2 nm during this time (see Fig. 7.4a). Data for 46.6 < t (h) < 61.1 is plotted in a blue-to-green color scheme where the color corresponds to the U versus t data in Fig. 7.6a. The right axis of Fig. 7.6b represents the percent change of the domain spacing from the nominal initial value of 42.4 nm (averaged over all x/L at t = 0 h). At x/L = 0.088 (near the lithium stripping electrode), Δd reaches 10.8 nm at t = 61.1 h, an increase of 25.4 % from the quiescent state. At x/L = 0.93 (near the lithium plating electrode), we measure Δd of -4.4 nm at t = 61.1 h, a decrease of 10.4 % from the quiescent state. This difference between Δd at x/L = 0.088 and 0.93 highlights the point that the swelling of the salt rich lamellae is not compensated by the contracting of the salt deficient lamellae. We take this analysis a step further by fitting the data set at t = 61.1 h to a 5$^{\mathrm{th}}$ order polynomial plotted as a red in line in Fig. 7.6b and given by:

$$\Delta d = -272(x/L)^5 + 816(x/L)^4 - 955(x/L)^3 + 542(x/L)^2 - 158(x/L) + 21.0) \tag{7.14}$$

Because the cell operates above limiting current, the shape of d vs x/L when the potential diverges (green data set) is non-linear: the gradient in d is most severe near the electrodes. The area under the curve (calculated by integrating Eqn. 7.14 from x/L = 0 to 1) is an average of 1.6 nm; if the lamellar volume were conserved, we would expect this value to be 0. This implies that the average increase in d is 1.6 nm, or 3.8% from the quiescent state. Based on these significant changes in the domain spacing, it is instructive to analyze the scattering profiles more closely.

In Fig. 7.6c and 7.6d, we present the 1D SAXS profiles during polarization (t = 46 to 61 h) for the x/L = 0.088 (highlighted by the dashed gold box in Fig. 7.6b) and x/L = 0.93 (highlighted by the dashed purple box in Fig. 7.6b) positions, respectively. We plot the scattered intensity from the sample $I_s(q)$ divided by a reference intensity, I_{ref}. I_{ref} is the maximum intensity of the primary scattering peak of the reference sample (as described in Section 7.2.5). The scattering from the reference sample was measured once for each data set in Fig. 7.6b. We use the same color scheme in Fig. 7.6c and 7.6d to denote the time of each data set. Our main interest is to investigate if there are any signatures of the lamellar structure being disrupted near the electrodes during the extreme

polarization conditions. Overall, we see a shift of the primary scattering peak to lower q (higher domain spacing) in Fig. 7.6c, but the character of the peak remains consistent throughout the experiment. The same is true in Fig. 7.6d for as the peak shifts to higher q (lower domain spacing). In Fig. 7.6e and 7.6f, we show the 1D SAXS patterns obtained during the open circuit relaxation step (t = 61 to 80 h) at x/L = 0.088 and 0.93, respectively. Again, the character of the primary scattering peak is maintained as the peak position shifts towards the initial peak position prior to polarization.

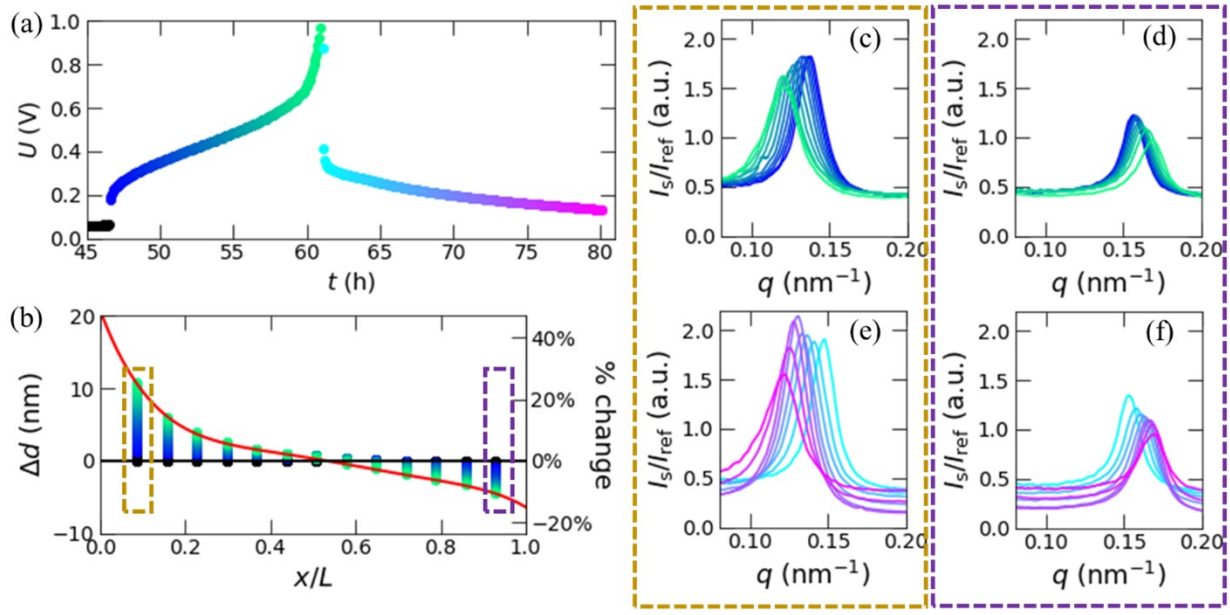

Figure 7.6. Results from simultaneous polarization and SAXS experiments performed above the limiting current, iL = 11.3 μA cm^{-1}. The current was increased from 0.946 μA cm^{-1} at t = 46.6 h (data for t < 46.6 h is presented in Fig. 7.4a and 7.5a at the lower current density). (a) Potential drop across the electrolyte, U, versus t. For 46.6 < t (h) < 61.1, a constant current of iL = 11.3 μA cm^{-1} was applied and U is plotted in a blue to green color scheme. At t = 61.1 h, the cell switched to open circuit (iL = 0) and the open circuit cell potential is plotted in a blue to pink color scheme. (b) Change in domain spacing, Δd, defined by Eqn. 7.7 versus t for the constant current polarization for 46.6 < t (h) < 61.1. Data sets plotted with black symbols were obtained during the 0.946 μA cm^{-1} polarization for t < 46.6 h. The blue to green color scheme of the remaining data set corresponds with the U versus t plot in (a). The red trace is a polynomial fit to the final data set at t = 61.1 h (green data points). 360° azimuthal averages of selected 2D SAXS patterns are presented in (c) through (e) with colors corresponding to the U versus t data in (a). (c) $I(q)$ plots for 46.6 < t (h) < 61.1 during the 11.3 μA cm^{-1} polarization at x/L = 0.088 and (d) x/L = 0.93. (e) $I(q)$ plots for t > 61.1 h when the cell is at open circuit measured at x/L = 0.088 and (f) x/L = 0.93. The gold and purple dashed boxes in (b) through (f) highlight data obtained at x/L = 0.088 and 0.93, respectively.

7.3.5. Lamellar orientation parameter

To further investigate the extent to which the lamella may rearrange due to polarization, we calculated an orientation parameter for the electrolyte as a function of position and time. For

each scan, the scattering pattern was divided into 18 sectors as shown in Fig. 7.3b and averaged to obtain $I(q)$ for each sector. The $I(q)$ data was fit as described previously, and the scattering invariant, Q, was calculated by integrating $q^2 I(q)$ over the fitted primary scattering peak. The result is $Q(\chi)$ for each scan. The orientation parameter, f, was calculated according to Eqn. 7.15:

$$f = \frac{3\langle cos^2\,\chi\rangle - 1}{2} \tag{7.15}$$

using Eqn. 7.16,

$$\langle cos^2\,\chi\rangle = \frac{\int_0^{90} Q(\chi)\, cos^2(\chi)\, sin(\chi)\, d\chi}{\int_0^{90} Q(\chi)\, sin(\chi)\, d\chi} \tag{7.16}$$

where 0° is defined such that it corresponds to lamellae with normal vectors perpendicular to the direction of current flow, as shown in Fig. 7.3b.[192–194] An orientation parameter f = 1 describes a lamellar sample where all grains are oriented with lamellar interfaces perpendiuclar to the direction of curent flow. For a sample with all lamellar interfaces oriented parallel to the direction of curent flow, f = -0.5. Randomly oriented lamellae correspond to f = 0.

The $Q(\chi)$ data ranges from χ = 0 to 360°, while Eqn. 7.16 only includes data from 0 to 90°. We expect the same information to be reflected in all four quadrants of the 2D SAXS patterns because a single lamellar grain generates identical scattering along two azimuths separated by 180°. To minimize noise in the data, we averaged the four quadrants of our data by first adding $Q(\chi)$ from 180 to 360° to the $Q(\chi)$ from 0 to 180°. Next, we folded the resulting data, which ranges from 0 to 180°, around χ = 90°, thus resulting in $Q(\chi)$ that includes data from all four quadrants with χ ranging from 0 to 90°. This data set of $Q(0 < \chi < 90°)$ was numerically integrated to obtain $\langle \cos^2 \chi \rangle$ according to Eqn 7.16.

The resulting orientation parameter, $f(t)$ is presented in Fig.7. 7 for each postion in the cell with iL 2.13 μA cm^{-1}. Similar plots for the other two cells can be found in the Section 7.6.2, and are qualitatively similar. At all positions, f is approximately 0.25, with little change over time. This indicates that before any current is applied, the lamellar grains have a slight preference for orientations such that their normal vectors are parallel to the direction of current flow. This orientation was likely introduced by the mechanical force necessary to deform the electrolyte and fill the cell. Electrochemcial polarization does not affect the distribution of grain orientations. If lamellar grains were to break up and re-form during electrochemical polarization, one would expect newly formed lamellae either to be randomly oriented, corresponding to f = 0, or to form with a new prefential orientation due to current flow. In either case, we would expect to observe f which varies with time. The observation that f is time-invariant suggests that the grain structure remains relatively constant throughout the experiment.

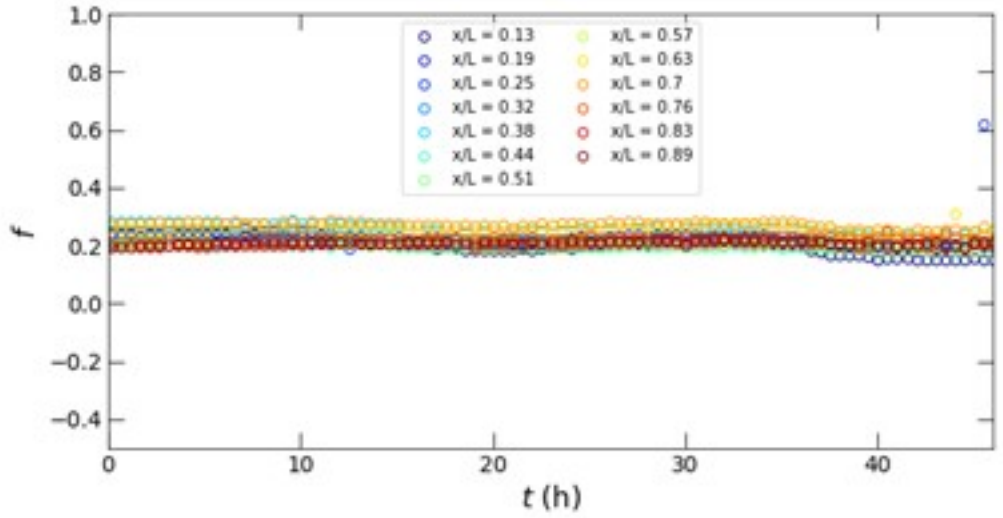

Figure 7.7. Orientation parameter, f, versus time, t, for the cell polarized at iL = 2.13 μA cm^{-1} for positions ranging from x/L = 0.13 to 0.89. f is approximately constant with time across all positions, indicating that polarization does not induce grain alignment or dealignment.

Our analysis of Fig. 7.4 through 7.7 has led us to the conclusion that the lamellae which constitute the block copolymer electrolyte do not break apart and reform to accommodate the salt concentration gradient. We hypothesize two alternative explanations for the observation of a 3.4% net increase in d across the entire sample: 1) individual polymer chains diffuse from one lamella to another, preserving the grain structure but resulting in a total decrease in the number of lamellae in each grain, or 2) there is a net increase in lamellar volume which may be accommodated by annihilation of defects, expansion of the cell walls, or compression of the lithium electrode. Both processes come with large energetic penalties, which may explain the discrepancy between the experimental and theoretical limiting current in Fig. 7.2c. With increasing current density, the domain spacing gradient must increase to accommodate the increasing salt concentration gradient, and eventually the energetic penalty to do so becomes too large, and the potential diverges.

7.3.6 Orientation dependence of lamellar distortion

We next analyze how different orientations of lamella swell and contract in response to the salt concentration gradient. We focus our attention on data from a single positional scan taken at t = 34.6 h in the cell polarized at 2.13 μA cm^{-1}. The qualitative results are representative of all cells studied at times significantly after the onset of polarization. We again divided the 2D scattering pattern into 18 sectors as shown in Fig. 7.3b to obtain $I(q,\chi)$. Here, χ represents the angle at the center of the sector. For example, if χ = 90°, then we are averaging the scattering data between χ = 80 and 100°. Based on the sector averaged data, we follow the same peak fitting procedure as discussed previously to obtain $d(\chi)$ for each 2D scattering plot. Before polarization, we found that $d(\chi)$ was not constant. To account for this, we redefine the quantity Δd for a fixed position x/L in Eqn. 7.17:

$$\Delta d(\chi,t) = d(\chi,t) - d(\chi,t=0) \tag{7.17}$$

In Fig. 7.8a, we plot Δd as a function of χ for each position in the cell for the data set obtained at t = 34.6 h. From top to bottom, x/L increases from 0.13 to 0.89. Near the positive electrode, Δd > 0 for all χ and there are local maxima at χ = 90° and 270°. Near the center of the cell, Δd is approximately equal zero for all values of χ. Near the negative electrode, Δd < 0 for all χ and there are local minima at χ = 90° and 270°. The results presented in Fig. 7.8a suggest that grains with lamellar planes perpendicular to the flow of ionic current ($\mathrm{LAM}_{\perp}$) undergo greater expansion (near the positive electrode) or contraction (near the negative electrode) when compared to those with lamellar planes parallel to the flow of ionic current ($\mathrm{LAM}_{||}$). To highlight this point, we plot the difference in domain spacing between $\mathrm{LAM}_{\perp}$ and $\mathrm{LAM}_{||}$, $d_{\mathrm{LAM}_{\perp}} - d_{\mathrm{LAM}_{||}}$, in Fig. 7.8b. The color of each data point in Fig. 7.8b corresponds to the data set of the same color in Fig. 7.8a and 7.8c. At t = 34.6 h, the $\mathrm{LAM}_{\perp}$ near the positive electrode are swollen 1 nm larger than $\mathrm{LAM}_{||}$. Near the negative electrode, the $\mathrm{LAM}_{\perp}$ are about 1 nm smaller than the $\mathrm{LAM}_{||}$. Near the end of polarization, this difference increases to about 1.6 nm (see Fig. 7.16 in Section 7.6.2).

The orientation-dependent distortion of lamellae shown in Fig. 7.8a and 7.8b indicates that the salt which is preferentially depleted from $\mathrm{LAM}_{\perp}$ at the negative electrode accumulates preferentially in $\mathrm{LAM}_{\perp}$ near the positive electrode. In a randomly oriented lamellar sample, one would conclude that grains in the $\mathrm{LAM}_{||}$ orientation contribute the most to dc conductivity relative to any other orientation, while those in the $\mathrm{LAM}_{\perp}$ do not contribute to the dc conductivity.[108] Our analysis shows that $\mathrm{LAM}_{\perp}$ also play a critical, but more subtle, role in ion transport. The swelling and contracting of the lamellae are required to allow the formation of a salt concentration gradient and thus sustain the applied current, and a larger portion of this volume change is accommodated by those lamellae in the $\mathrm{LAM}_{\perp}$ orientation. While a lamellar sample with only the $\mathrm{LAM}_{\perp}$ orientation would not be desirable as there would be no path for ionic current to pass between the electrodes, one with only the $\mathrm{LAM}_{||}$ orientation may also be undesirable because the resistance to volume change would reduce the limiting current. Therefore, we may conclude that a collection of lamellar grains with a distribution of orientations is likely to lead to the largest limiting current due to the need to accommodate both large ionic currents and to accommodate large salt concentration gradients.

We may take our analysis a step further by using Eqn. 7.2 to estimate the local salt concentration in the lamellar grains as a function of χ. The results are shown in Fig. 7.8c. The shape of the curves in Fig. 7.8c are like those in Fig. 7.8a because of the linear relationship between d and r in the range of salt concentrations from r = 0.1 to 0.2. Although we have discussed that the conversion from d to r fails at high current densities, we do expect that for two grains at the same x/L but different with different d, the grain with higher d will have higher local r. Thus, by calculating r versus χ for each position, we approximate sense of how the salt concentration varies in grains with different orientations. Based on Fig. 7.7b, r is about 0.015 higher in $\mathrm{LAM}_{\perp}$ compared to $\mathrm{LAM}_{||}$ near the salt rich electrode, and about 0.008 lower near the salt deficient electrode. These results suggest that salt concentration gradients can form along all three axes (x, y, and z), not just the axis along ion transport (x). For the y- and z- axis, the concentration gradients which form are on the length scale of the grain size, while along the x-axis, the concentration gradient is on the length scale of L. In Chapter 6, we identified the formation of concentration hotspots in SEO(1.7-

1.4). This new insight suggest that the nucleation of these hotspots likely emerges from grains in the $LAM_{\perp}$ orientation where salt accumulates more heavily.

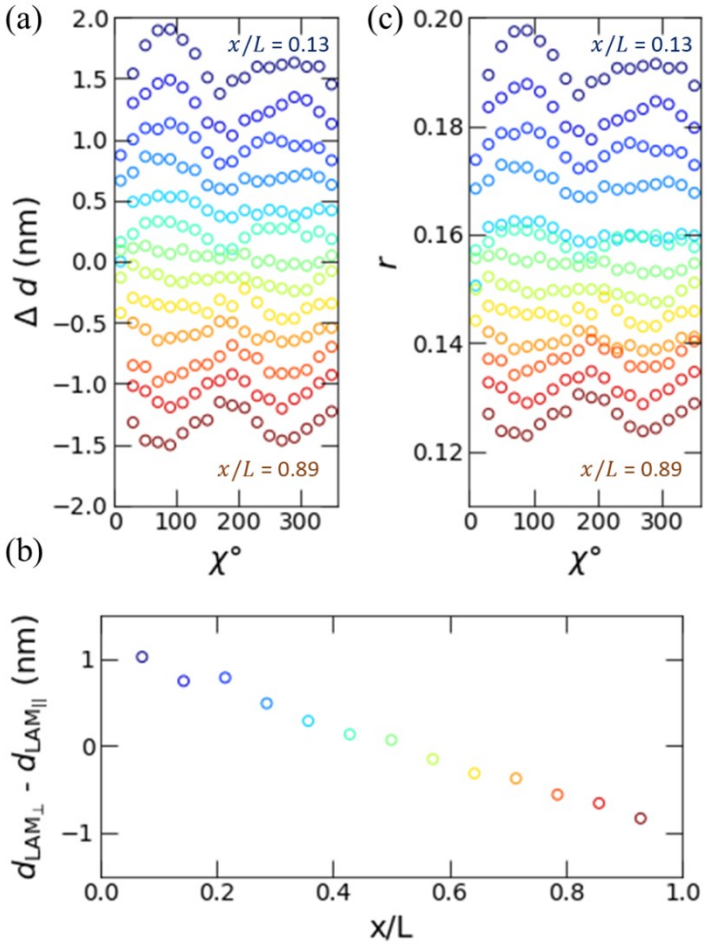

Figure 7.8. Orientation dependence of lamellar distortion for the cell polarized at iL = 2.13 μA cm^{-1} at t = 34.6 h. (a) Change in domain spacing, Δd, defined by Eqn. 7.10 as a function of azimuthal angle, χ. (b) Difference in domain spacing between $LAM_{\perp}$ and $LAM_{||}$ as a function of normalized position, x/L. (c) Local salt concentration, r, versus χ based on the data in (a). r was calculated from $d(\chi)$ using Eqn. 7.2. Data sets of the same color were obtained at the same position in the cell (x/L) which is reported on the bottom axis of (b).

The local salt concentration within a single lamellar grain and domain spacing are intimately related. If salt preferentially accumulates into one grain over another, that grain must swell more to accommodate the higher local salt concentration. Alternatively, if mechanical forces preferentially stretch one grain over another, the density of EO monomers in the PEO phase of that grain will be lower, so salt will preferentially go into the lamella to equalize the density between neighboring grains. We hypothesize that the later situation is what drives the orientation dependence of d and, subsequently, r in Fig. 7.8. Thermodynamically, there is no reason why salt would prefer to reside in one grain over another based strictly on the orientation relative to the

current direction. The salt concentration gradient forms along the x-axis, which is independent of the block copolymer structure (salt concentration gradients also develop along the x-axis in homopolymer electrolytes). Thus, there is force driving the solvent to expand in the x-direction for regions near the positive electrode where $r > r_{avg}$ and a force driving the solvent to contract in the x-direction for regions near the negative electrode where $r < r_{avg}$. This mechanical force preferentially distorts lamellae which have PEO-PS interfaces oriented perpendicular to the x-axis ($\mathrm{LAM}_{\perp}$), as the interfaces are drawn apart near the positive electrode and driven closer together near the negative electrode. For lamellae with interfaces oriented parallel to the x-axis ($\mathrm{LAM}_{||}$), this mechanical force acts parallel to the PEO-PS interfaces, and therefore does not result in additional distortion.

7.4 Conclusions

Concentrated solution theory provides a framework to predict the development of salt concentration gradients and the associated potential drop across the electrolyte when current is passed through a cell. This can be extended to predict the maximum current density which can be sustained through the electrolyte (*i.e.,* the limiting current, i_{lim}). The prediction is based on the condition that the salt concentration reaches zero at the negative electrode where lithium plating occurs. Experimentally, we find that the limiting current in SEO(19-20)/LiTFSI is approximately a factor of two lower than what is predicted from concentrated solution theory. Small angle X-ray scattering performed on the electrolyte during dc polarization provided several key insights into this observation. We found that there was a net increase in the domain spacing of the polymer as the salt concentration gradient developed. At large current densities, the rearrangement of the polymer chains comes at a large energetic penalty, which results in divergence of the cell potential at currents below the predicted limiting current (see the black curve in Fig. 7.2a). Additionally, we observed that grains with lamellar planes perpendicular to the flow of ionic current ($\mathrm{LAM}_{\perp}$) swell and contract to a greater extent compared to those with lamellar planes parallel to the flow of ionic current ($\mathrm{LAM}_{||}$). Because the formation of a salt concentration gradient relies on the ability of the lamellae to swell and contract, this observation indicates that lamellae that do not provide a straight path between electrodes still play a critical role in the functionality of the block copolymer electrolyte.

7.5 Acknowledgement

This work was supported by the Assistant Secretary for Energy Efficiency and Renewable Energy, Vehicle Technologies Office, under the Advanced Battery Materials Research (BMR) Program, of the U.S. Department of Energy under Contract No. DE-AC02-05CH11231. C.J.T., C.C., H.G.S., and M.F.T. were supported by the Joint Center for Energy Storage Research (JCESR), an Energy Innovation Hub funded by the U.S. Department of Energy, Office of Science, Basic Energy Sciences. This research was completed at the Stanford Synchrotron Radiation Light Source, a user facility at SLAC National Accelerator Laboratory, was supported by the U.S. Department of Energy, Office of Science, Office of Basic Energy Sciences under Contract No.

DE-AC02-76SF00515. Preliminary work used beamline 7.3.3 of the Advanced Light Source, which is a DOE Office of Science User Facility under contract no. DE-AC02-05CH11231.

7.6 Supporting Information

7.6.1 Data Fitting

The scattering intensity as a function of the scattering vector, $I(q)$, data was fit using a Levenberg-Marquardt nonlinear least-squares algorithm. Data was reduced to $I(q)$ based on either a 360° azimuthal average or by sector averages, as described in the main text. In all cases, the fitting procedure was the same regardless of whether the $I(q)$ data represented a 360° azimuthal average or a 20° sector average. The $I(q)$ data was fit to the sum of a pseudo-Voigt function and a background function given by Eqn. 7.17 in the range $0.05 < q$ (nm^{-1}) < 0.3:

$$I(q) = I_{pV}(q) + I_{bkg}(q) \tag{7.17}$$

$I_{\mathrm{pV}}(q)$ is a pseudo-Voigt function given by:

$$I_{pV}(q) = A[\eta G(q) + (1-\eta)L(q)], \tag{7.18}$$

where A is the area under the curve, η is the Gaussian fraction. $G(q)$ is the Gaussian component of the fit given by Eqn. 7.19 and $L(q)$ is the Lorentzian component of the fit given by Eqn. 7.20:

$$G(q) = \frac{2}{w}\left(\frac{ln\,2}{\pi}\right)^{0.5} exp\left[\frac{-4\,ln\,2\,(q-q^*)^2}{w^2}\right] \tag{7.19}$$

$$L(q) = \frac{\frac{w}{2\pi}}{(q-q^*)^2 + \left(\frac{w}{2}\right)^2} \tag{7.20}$$

where w is the peak width (*i.e.*, full width at half maximum) and q^* is the position of the primary scattering peak. For fitting the background, we used:

$$I_{bkg}(q) = y_{b0} + y_{b1}\,exp\left[\frac{y_{b2}}{q}\right]. \tag{7.21}$$

In Eqn. S1, the fitted parameters are: η, w, q^*, y_{b0}, y_{b1}, and y_{b2}. The value of η must lie between 0 and 1. The value of q^* was used to calculate the domain spacing, d, by Eqn. 7.1 in the main text.

7.6.2 Supporting Figures

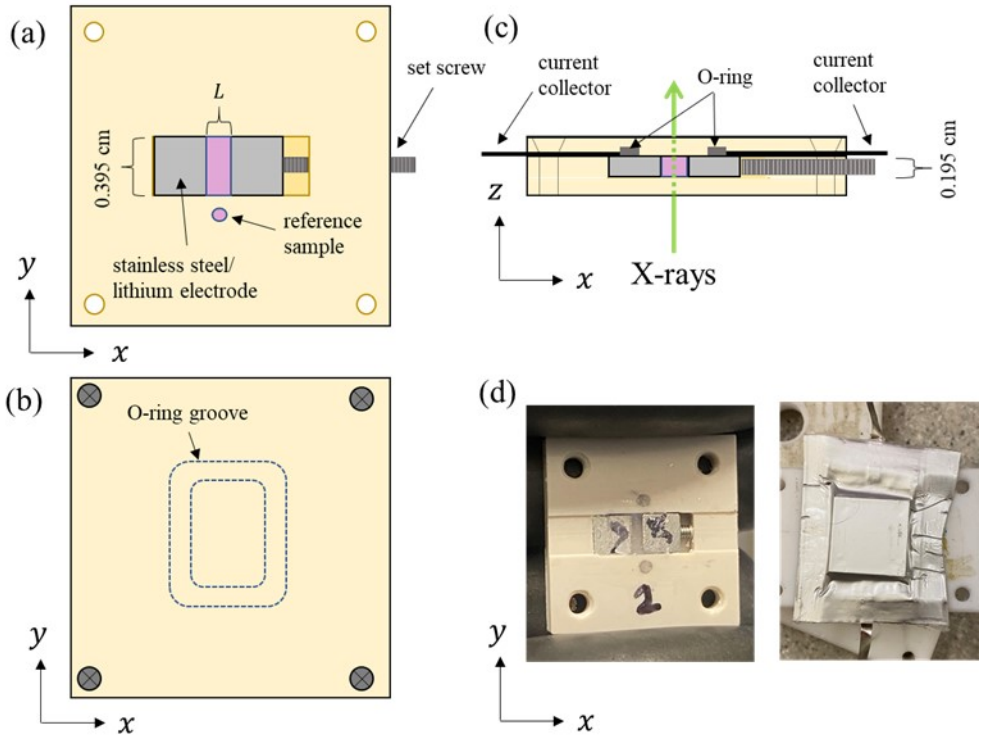

Figure 7.9. Schematic of the cell designed for simultaneous SAXS polarization experiments. (a) Schematic representation of the bottom plate in the two-part PEEK sample holder. Two stainless steel blocks sit in a channel cut into the PEEK. The blocks have lithium metal pressed on the inside face to serve as electrodes. Polymer electrolyte (pink) is hot-pressed between the blocks, and a set screw is used to adjust the distance between the blocks and create an air free sample. The length of the polymer channel along the y-axis is 0.395 cm and the distance between electrodes (width of the polymer channel) was measured in Figure S4 for each sample. The thickness of the polymer channel is 0.195 cm (as shown in part c). The reference sample is isolated from the electrochemical channel and consists of a cylindrical channel cut into the PEEK, also with thickness of 0.195 cm. In this view, the X-rays would pass into the page along the z-axis. The holes near the four corners of the sample holder are tapped to allow the top plate to attach with tapered screws. (b) Top plate of the two-part PEEK sample holder. The top plate screws into the bottom plate and secures the tabs to the stainless-steel blocks which are used to make electrical connections. The dashed lines show the hidden O-ring groove which is cut into the side of the plate which contacts the bottom plate. A Viton O-ring is used to seal the cell around the polymer channel. (c) View of the cell in the x-z plane of a slice taken through the center of the cell. The thickness of the polymer channel is 0.195 cm. The dimensions of the lithium electrodes are 0.395 x 0.195 cm. Dashed lines indicate the location of the tapered screws. Current collectors (nickel foil) are secured to the stainless-steel blocks by a Viton O-ring which also serves to seal the area around the polymer channel. The green arrow indicates the direction which X-rays pass during the experiment. (d) Left panel: picture of the bottom plate (shown schematically in part a) loaded with polymer electrolyte in both the reference channel and electrochemical channel. This cell had two reference channels but only one was used for measurements during the experiment. Right panel: picture of an assembled cell sealed in aluminum laminated pouch material. The nickel tabs protrude out of the pouch and connect to the potentiostat.

$$J_1 = \kappa\left(\frac{d\,U}{d\ln m}\right)\left[r\left(1-\frac{1}{\rho_+}\right)F\phi_c\right]^{-1} \qquad J_2 = -\left(\frac{d\,U}{d\ln m}\right)[r(1-\rho_+)F\phi_c]^{-1}$$

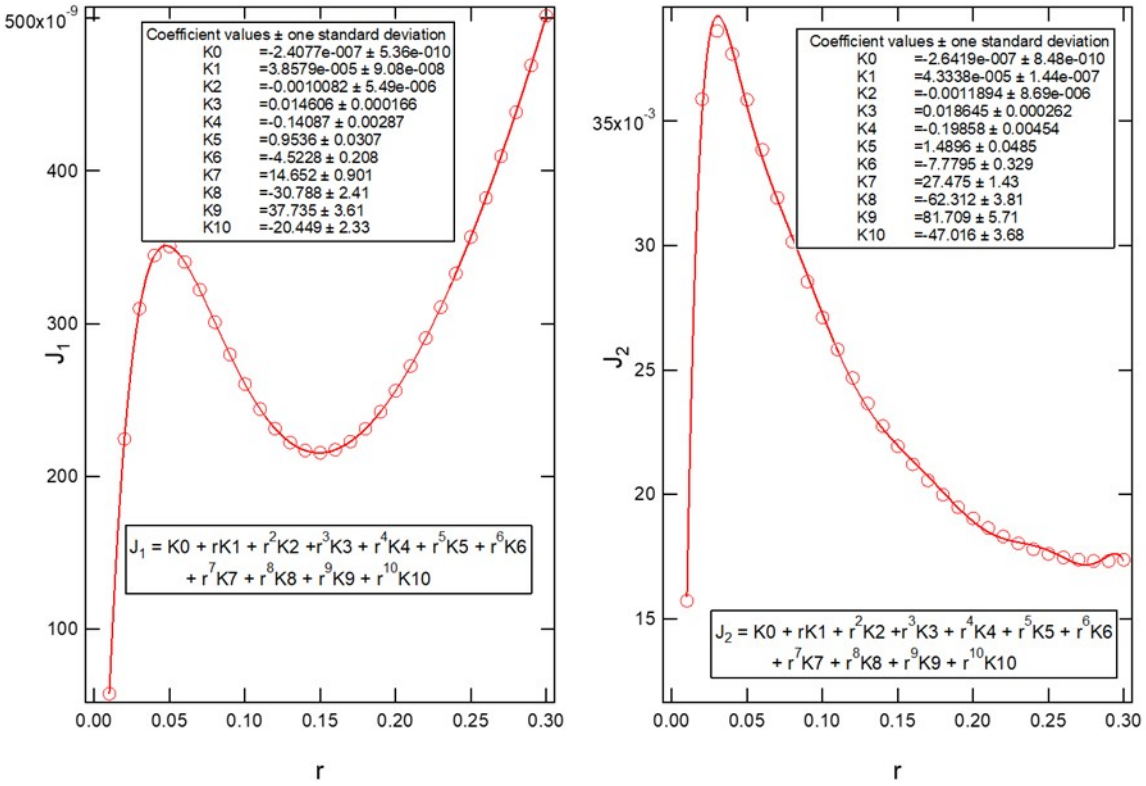

Figure 7.10. Integral parameters used for calculating salt concentration and potential gradients from concentrated solution theory using the methodology discussed in the Section 7.3.1. (a) Calculated values for J_1 as a function of r plotted with open circles. Eqn. 7.4 is reproduced above the plot. The red line is a fit to the data given by the 10th order polynomial and the fit equation and resulting coefficient values are provided. (b) Calculated values for J_2 as a function of r plotted with open circles. Eqn. 7.6 is reproduced above the plot. The red line is a fit to the data given by the 10th order polynomial and the fit equation and resulting coefficient values are provided. There is no physical meaning to the fit equation, it is simply used to obtain the area under the curve. A numerical approach could have also been used.

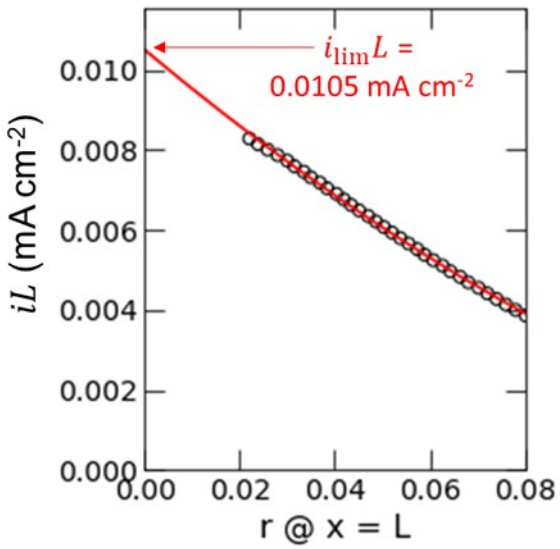

Figure 7.11. Example calculation of the limiting current based on an average salt concentration of r = 0.16. Salt concentration gradients are predicted for increasingly large currents until the salt concentration at x/L = 1 reaches the lower bound of the model. The bottom axis is the value of r at x/L = 1 for the current density (iL) plotted on the left axis. The red curve is a polynomial fit and is extrapolated to r = 0 at x/L = 1. The current at the y-intercept is the limiting current. This calculation was repeated for each salt concentration in Fig. 7.2c.

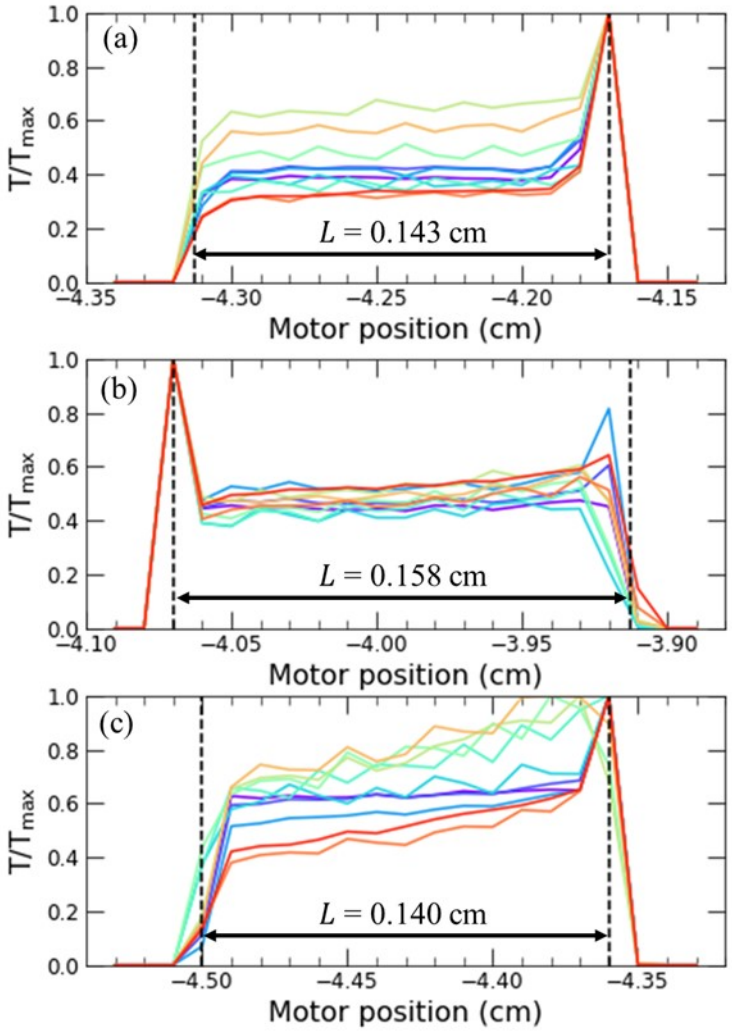

Figure 7.12. Transmission versus motor position for cell (a), (b), and (c), which corresponds to the cells in Figure 4a, 4b, and 4c, respectively. The transmission is given by the intensity recorded from the ion counter at the beam stop divided by the intensity from the ion counter upstream of the sample. We normalize the transmission by the maximum transmission for each data set. The color of each data set corresponds to the data in Figure 4 of the main text. Where $T/T_{\max} = 0$, the beam is centered over the stainless steel electrode. Where $T/T_{\max} > 0$, the beam is passing through polymer and/or lithium metal. The dashed lines represent the motor position for $x/L = 0$ (left most dashed line) and $x/L = 1$ (right-most dashed line). The distance between electrodes, L, is calculated as the distance between the two dashed lines and is reported in the figure for each cell.

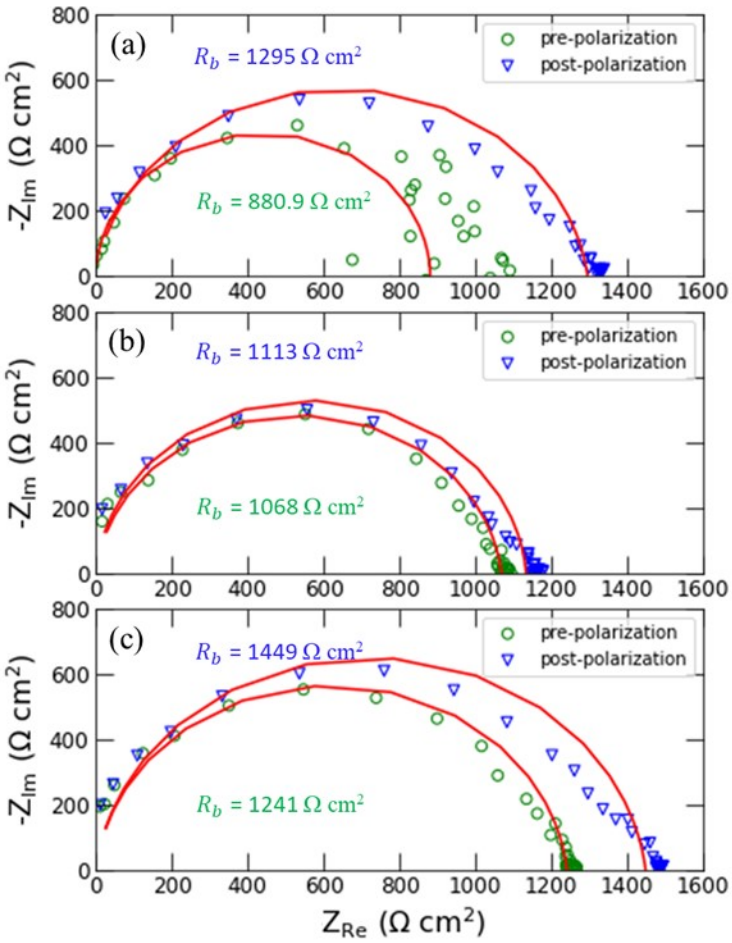

Figure 7.13. Nyquist plots obtained from ac impedance spectroscopy performed on cells (a), (b), and (c) which correspond to the data in Fig. 7.4a, 7.4b, and 7.4c, respectively. Green circles represent data points obtained prior to polarization ($t < 0$ h). Blue triangles represent data points obtained after polarization and subsequent open circuit relaxation ($t > 80$ h). Red lines are fits to the data using a resistor and constant phase element in parallel as the equivalent circuit. In all cases, we only observe one semi-circle. The fitted resistance is reported in the figure. Prior to polarization, the conductivity calculated from the resistance is 1.62 x 10^{-3} S cm^{-1} for cell (a), 1.48 x 10^{-3} S cm^{-1} for cell (b), and 1.13 x 10^{-3} S cm^{-1} for cell (c). These values are in good agreement with the conductivity measured from cells with blocking electrodes (Fig. 7.1b in the main text). The conductivity of SEO(19-20)/LiTFSI as a function of r is given by Eqn. 7.11 in the main text: at $r = 0.16$, $\kappa =$ 1.48 x 10^{-3} S cm^{-1}. Therefore, we can assume that the contribution of the interface to the total resistance of the cell is relatively small and explains why we cannot deconvolute it from the Nyquist plots. We thus assume that $\Delta V_{\text{int}} = 0$ for the cells designed for simultaneous polarization/SAXS experiments. The increase in resistance at the end of the experiment may be due to an increase in the interfacial resistance or due to the lingering presence of a salt concentration gradient (in general, the measured resistance decreases as the salt concentration gradient relaxes).

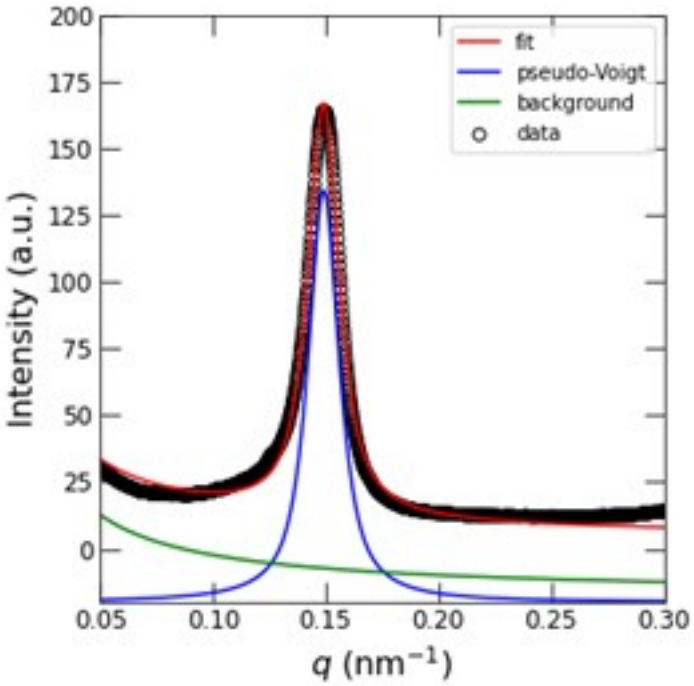

Figure 7.14. Example fit of a 1D SAXS profile obtained from a 360° azimuthal average of the 2D SAXS profile. The data set corresponds to the cell polarized at 2.13 μA cm^{-1} at t = 34.6 h and x/L = 0.51. The black open circles represent the raw data, and the red curve is the total fit given by Eqn. 7.17. The pseudo-Voigt fit is shown in blue (given by Eqn. 7.18) and the background (given by Eqn. 7.19) is shown in green, both offset by -20 a.u. for clarity.

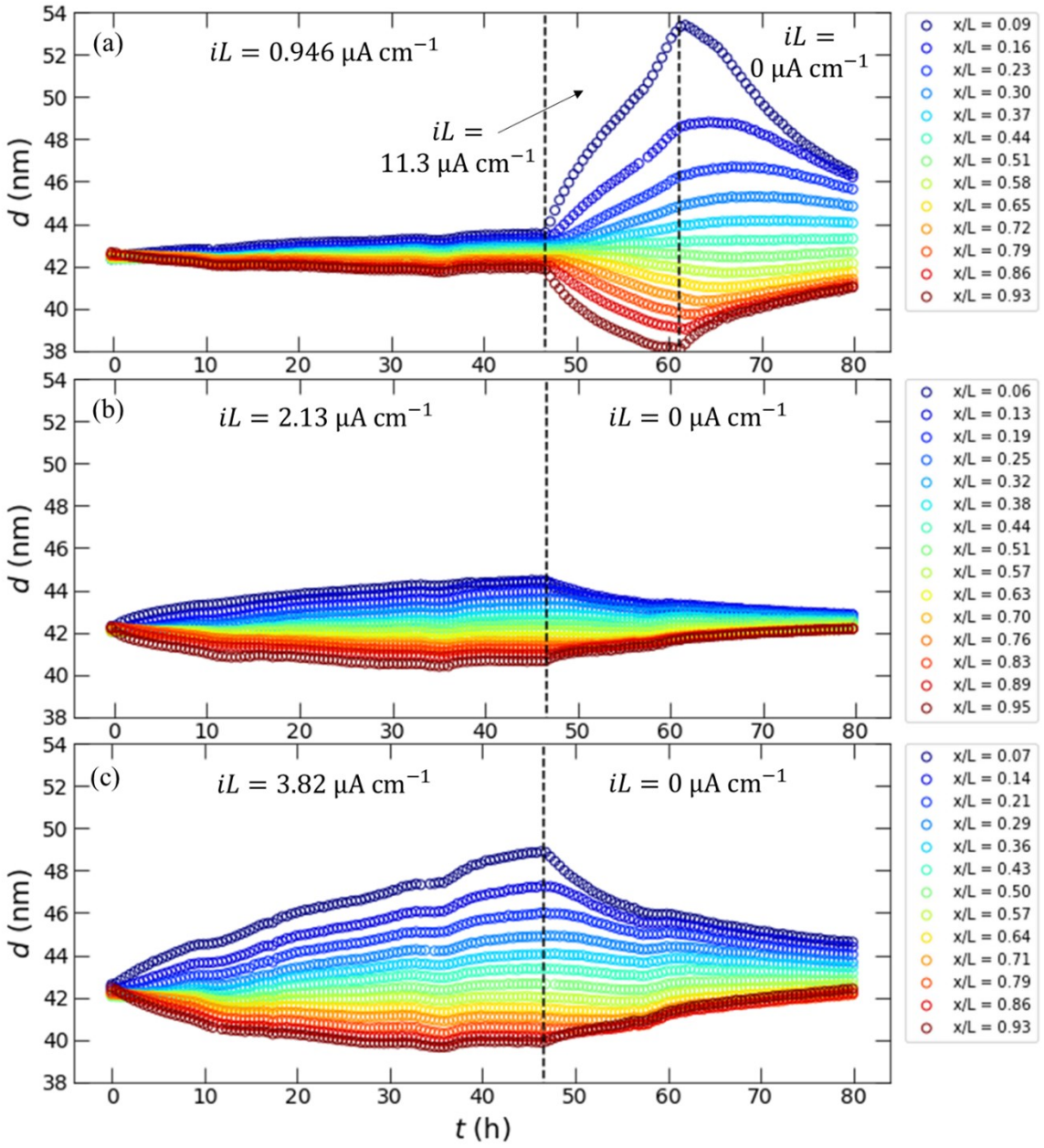

Figure 7.15. Domain spacing, d, as a function of time, t. The vertical dashed lines divide the plots into sections and indicate changes in the electrochemical conditions. The color of each data set corresponds to the position of the cell given in the legend on the right side of the plot. (a) Left section: iL = 0.946 μA cm^{-1}, middle section: iL = 11.3 μA cm^{-1}, right section iL = 0 μA cm^{-1} (*i.e.,* open circuit) (b) Left section: iL = 2.13 μA cm^{-1}, right section: iL = 0 μA cm^{-1} (*i.e.,* open circuit) (c) Left section: iL = 3.82 μA cm^{-1}, right section: iL = 0 μA cm^{-1} (*i.e.,* open circuit). The left section of each plot was reported as d vs x/L plots in Fig. 7.4. The middle section of part (a) was the basis of Fig. 7.6b. The change in d during open circuit was not discussed in the main text. In general, d converges towards the original d at t = 0. In all cases, there is still a spatial gradient in d at t = 80 h, which indicates that we do not reach equilibrium on the time scale of the experiment, but we would expect d to eventually become independent of position at longer times.

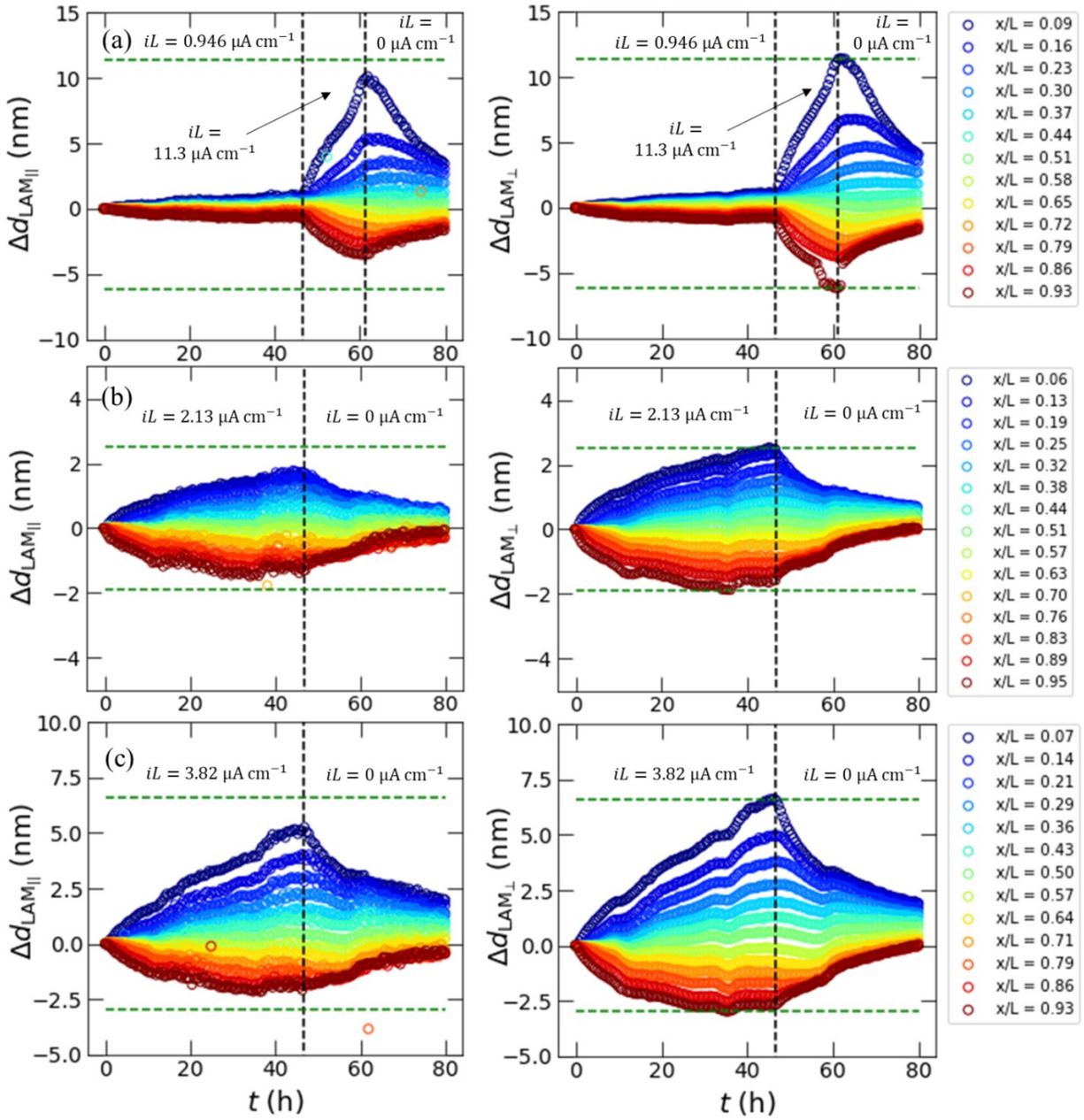

Figure 7.16. Orientation dependence of domain spacing. Change in domain spacing, Δd, for $LAM_{||}$ (left panels) and $LAM_{\perp}$ (right panels) as a function of time, t. Δd is defined by Eqn. 7.17, where $\chi = 0$ and 180° corresponds to $LAM_{||}$ and $\chi = 90$ and 270° corresponds to $LAM_{\perp}$. The vertical dashed lines divide the plots into sections and indicate changes in the electrochemical conditions. The color of each data set corresponds to the position of the cell given in the legend on the right side of the plot. (a) Left section: iL = 0.946 μA cm^{-1}, middle section: iL = 11.3 μA cm^{-1}, right section iL = 0 μA cm^{-1} (*i.e.,* open circuit) (b) Left section: iL = 2.13 μA cm^{-1}, right section: iL = 0 μA cm^{-1} (*i.e.,* open circuit) (c) Left section: iL = 3.82 μA cm^{-1}, right section: iL = 0 μA cm^{-1} (*i.e.,* open circuit). The green dashed lines represent the maximum and minimum $\Delta d_{LAM_{\perp}}$ based on the data in the right plots. We draw the green lines at the same value of Δd on the left plot to highlight the point that $LAM_{\perp}$ are distorted more than $LAM_{||}$.

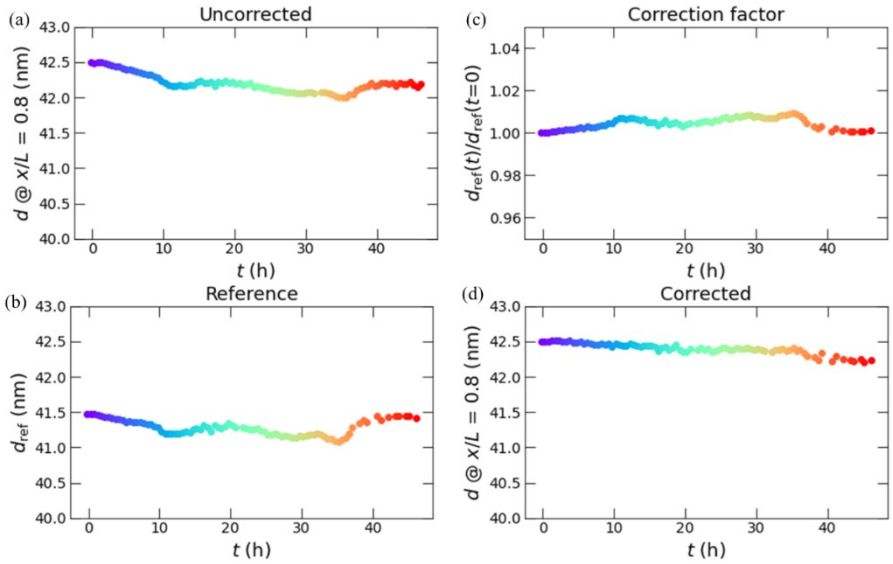

Figure 7.17. Correction of domain spacing data for the cell corresponding to Fig. 7.4a (polarized at iL = 0.946 μA cm^{-1}). (a) Uncorrected domain spacing, d, versus time, t, for a single cell position at x/L = 0.8. (b) d versus t of the reference sample. The reference sample was isolated from the electrochemical polymer channel, so we expect d_{ref} to be independent of time. (Note: each cell was constructed with a reference channel, so the data in Fig. 7.17, 7.18, and 7.19 are corrected using data from the reference channel in that cell.) We suspect that changes in d_{ref} are due to slight changes in the sample-to-detector distance (+/- 3.5 mm) which occurred during the experiment, most likely due to the sample stage drifting. (c) Correction factor, $\frac{d_{\mathrm{ref}}(t=0)}{d_{\mathrm{ref}}(t=t)}$, versus t. (d) Corrected domain spacing, d, versus t using the correction factor in part (c) and Eqn. 7.12. For the cell polarized at iL = 0.946 μA cm^{-1}, the correction produces a smooth curve in d versus t in part (d).

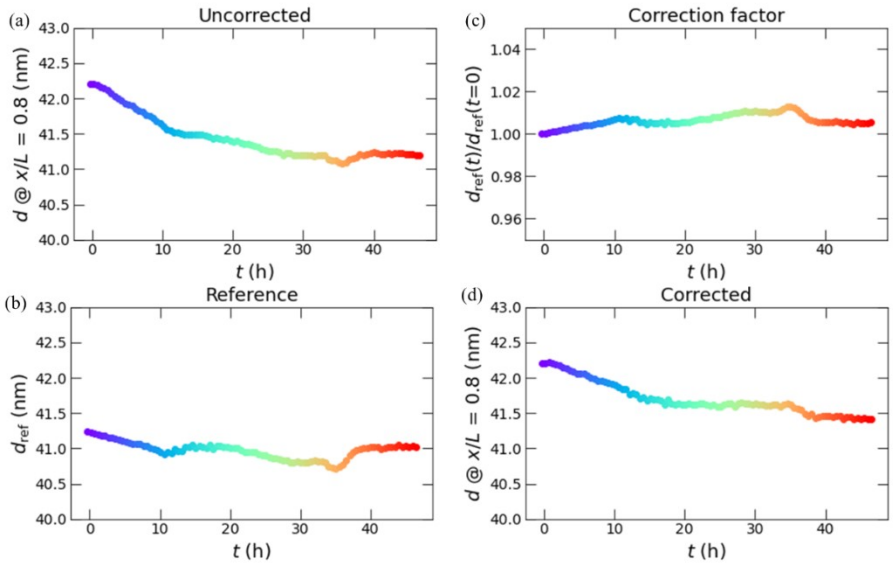

Figure 7.18. Correction of domain spacing data for the cell corresponding to Fig. 7.4b (polarized at iL = 2.13 μA cm^{-1}). (a) Uncorrected domain spacing, d, versus time, t, for a single cell position at x/L = 0.8. (b) d versus t of the reference sample. (c) Correction factor, $\frac{d_{\mathrm{ref}}(t=0)}{d_{\mathrm{ref}}(t=t)}$, versus t. (d) Corrected domain

spacing, d, versus t using the correction factor in part (c) and Eqn. 12. See caption of Fig. 7.17 for additional discussion. For the cell polarized at iL = 2.13 μA cm^{-1}, the correction produces a smooth curve in d versus t in part (d), however there still appears to be an artifact around t = 35 h.

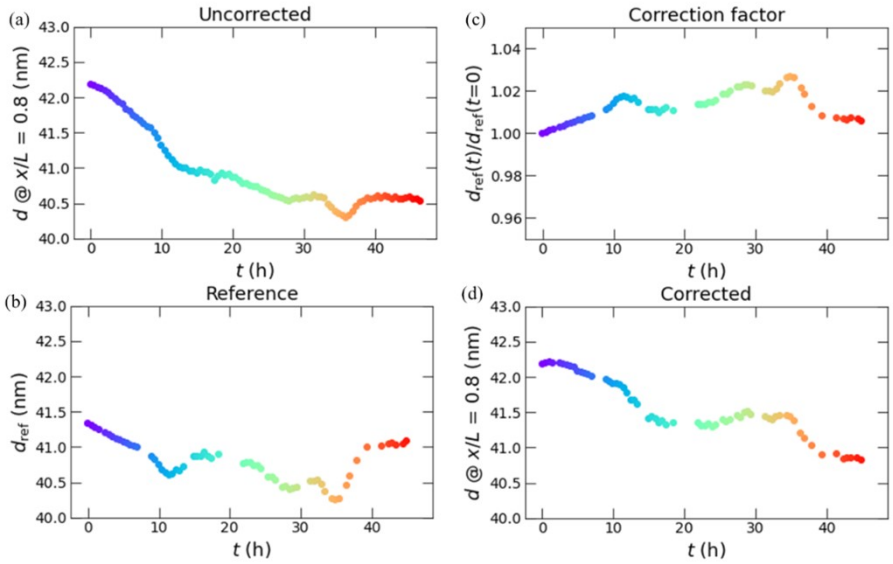

Figure 7.19. Correction of domain spacing data for the cell corresponding to Fig. 7.4c (polarized at iL = 3.82 μA cm^{-1}). (a) Uncorrected domain spacing, d, versus time, t, for a single cell position at x/L = 0.8. (b) d versus t of the reference sample. (c) Correction factor, $\frac{d_{\mathrm{ref}}(t=0)}{d_{\mathrm{ref}}(t=t)}$, versus t. (d) Corrected domain spacing, d, versus t using the correction factor in part (c) and Eqn. 12. See caption of Fig. 7.17 for additional discussion. For the cell polarized at iL = 3.82 μA cm^{-1}, the correction produces a some additional artifacts in the data in part (d). The artifacts in (a) and (b) are similar, but the correction factor overcorrects in some places (e.g. around t = 34 h). We could improve the correction by artificially scaling the correction factor, however there is no physical justification for doing this. In general, the correction is good in Fig. 7.17, but is less satisfactory for Fig. 7.18 and 7.19. Because the drift of the sample stage results in subtle changes in d (*i.e.*, +/- 0.5 nm), it does not significantly impact the analysis in the main text where we are concerned with changes in domain spacing on the order of 3-10 nm.

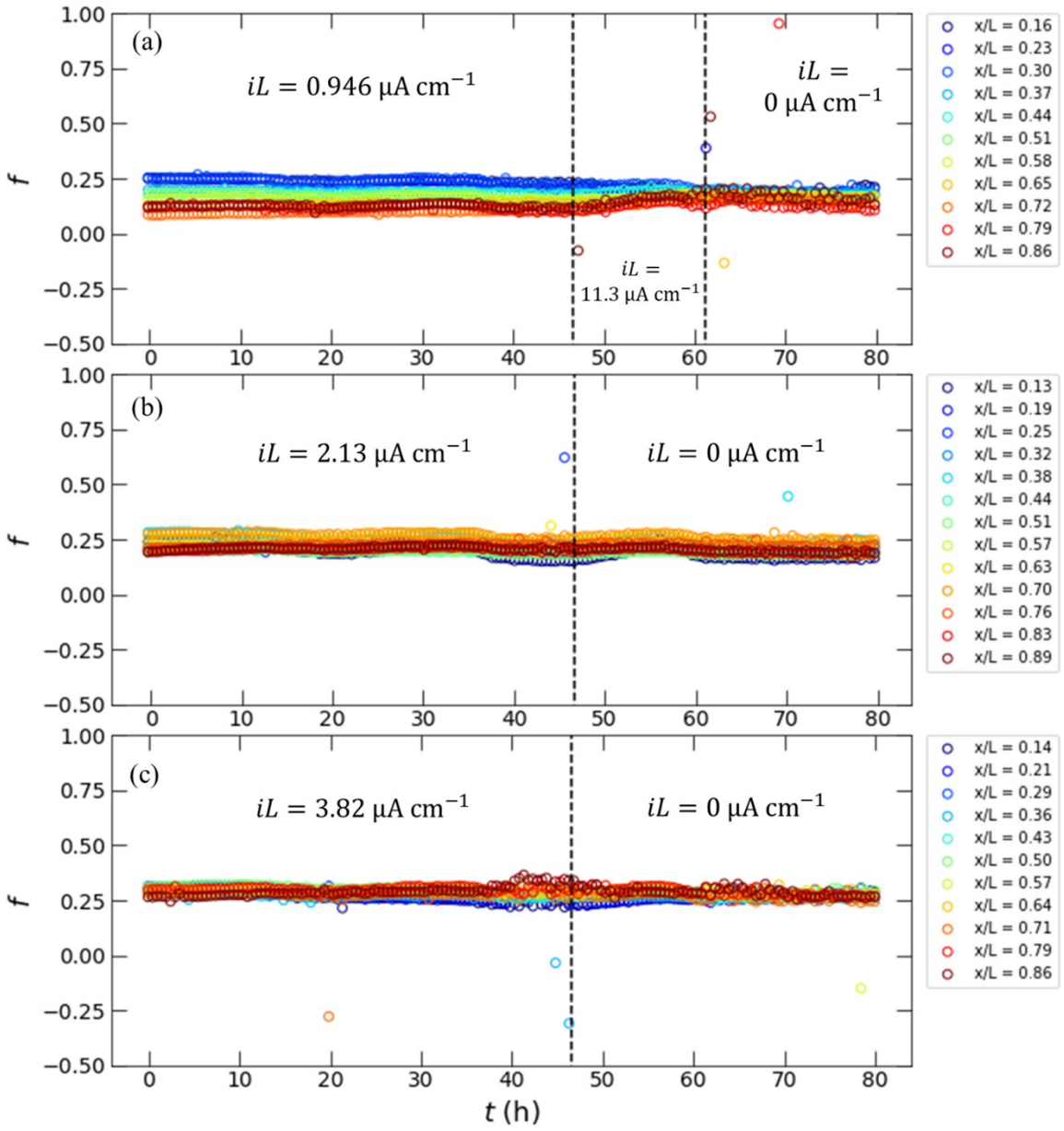

Figure 7.20. Orientation parameter, f, versus time, t for all three cells. f is defined by Eqn. 7.15 and 7.16. The vertical dashed lines divide the plots into sections and indicate changes in the electrochemical conditions. (a) Left section: iL = 0.946 μA cm^{-1}, middle section: iL = 11.3 μA cm^{-1}, right section iL = 0 μA cm^{-1} (*i.e.,* open circuit). (b) Left section: iL = 2.13 μA cm^{-1}, right section: iL = 0 μA cm^{-1} (*i.e.,* open circuit). The left section of part (b) was reported in Fig. 7.7 of the main text. (c) Left section: iL = 3.82 μA cm^{-1}, right section: iL = 0 μA cm^{-1} (*i.e.,* open circuit). f is approximately constant with time across all positions, indicating that polarization does not induce grain alignment or dealignment in any of the samples, even at very high polarizations (middle section of part (a)). We exclude data very close to the electrodes (*i.e.*, x/L = 0.07 and x/L = 0.93) because the beam partially passes through the lithium electrode at these positions, and some sectors of the 2D scattering patterns contain artifacts, resulting in noisy data. However, because the beam spans 200 μm along the x-axis, most of the sample is accounted for by the positions listed in the legends of part (a) through (c).

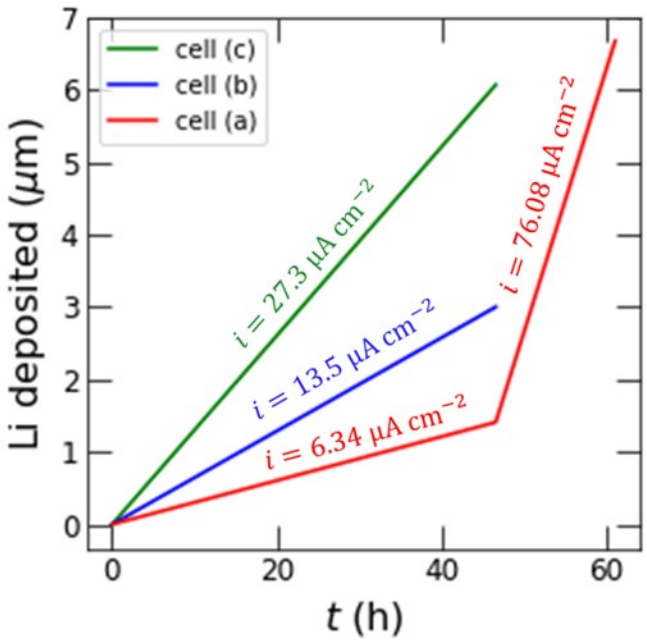

Figure 7.21. Calculation of the thickness of lithium deposited during polarization. The cell in Fig. 7.4a and Fig. 7.6 of the main text is shown in red at the two different current densities used in the experiments. The cells in Fig. 7.4b and 7.4c of the is shown in blue and green, respectively. The amount of lithium deposited is less that 7 μm for all three cells. The cell thicknesses are on the order of 1400 μm and the beam samples a 200 μm region along the x-coordinate of the cell. Therefore, the shifting of the cell positions due to the stripping and plating of the lithium is relatively small and we do not account for it in our definitions of the cell positions.

8. Conclusions and Outlook

Ion transportation through a battery electrolyte is a complicated process. Cations are driven in the direction of the applied electric field while anions are driven in the opposite direction. The principle of electroneutrality ensures that the concentration of cations and anions is equal on length scales larger than a few nanometers. The electrodes allow cations to travel across the electrolyte/electrode interface while anions are blocked. These phenomena result in salt concentration gradient along the axis perpendicular to the electrodes, which introduces a diffusive flux of cations and anions down the salt concentration gradient. Newman's concentrated solution theory provides a framework to describe these processes, but applying the equations to a nanostructured electrolyte is not straightforward. In this dissertation, we take a small step towards understanding ion transport through block copolymer electrolytes.

We have studied a variety of SEO/LiTFSI electrolytes with different morphologies and chain lengths. After introducing the system and characterization techniques in Chapters 1 through 3, we treated the block copolymer structure as a black box in measuring the transport properties in Chapter 4. Instead of accounting for the insulating polystyrene phase directly in our equations, we treated the system as a three-component system (anion, cation, and solvent) and then used geometric arguments to rationalize the results. These approximations were validated in Chapter 7 when we found reasonable agreement between theoretical predictions and experiment by using the domain spacing as a proxy for salt concentration at low to moderate current densities. At higher current densities studied in Chapters 6 and 7, we found that the polymer rearranged in interesting ways to accommodate the salt concentration gradient. The formation of salt-dense gyroid pockets in Chapter 6 indicated that salt can accumulate at pinch points in the structure. In Chapter 7, we found that there was an orientation-dependence to the lamellar distortion in response to the salt concentration gradient. Our conclusion was that a lamellar sample with a distribution of grain orientations may be preferable to one with well oriented grains, even though some of the orientations do not provide pathways for ions to travel between the electrodes. When designing polymer electrolytes, one must also consider the interactions between the polymer in the electrode. In Chapter 5, we showed that, in the case of PEO-containing polymers, lithium is sparingly soluble and the dissolution results in spectroscopic and electrochemical signatures.

It is quite evident that complete understanding of ion transport through composite electrolytes for lithium batteries will require a combination of electrochemical and structural characterization. In our analysis, we have deferred discussion of rheological properties of the electrolytes to other studies. However, to gain more complete insight, rheological measurements should be coupled with the electrochemical and structural characterization to understand how the block copolymer responds to the effects such as volume change of the electrodes and non-uniform lithium deposition. Our structural characterization was limited to length scales ranging from 5 to 50 nm, which excludes information on the dynamics of individual chains. Ongoing work is directed at addressing these deficiencies. Nonetheless, we have gained considerable insight into the mechanisms which govern ion transport through block copolymer electrolytes and the relationship to salt concentration gradients. Using the techniques and methodology presented in this dissertation, further insight may be gained by more carefully exploring the effect of chain length, morphology, and salt concentration on rearrangement processes.

9. References

[1] Yoshio, M.; Brodd, R. J.; Kozawa, A. *Lithium-Ion Batteries,* 1st; Springer-Verlag, **2009**.

[2] Li, A.; Chun, A.; Yuen, Y.; Wang, W.; Miguel, I.; Cordeiro, D. C.; Wang, C.; Bo, T.; Chen, Y.; Zhang, J.; Chan, Q. N.; Yeoh, G. H. A Review on Lithium-Ion Battery Separators towards Enhanced Safety Performances and Modelling Approaches. *Molecules* **2021,** *26* (2), 478.

[3] Desilvestro, J.; Haas, O. Metal Oxide Cathode Materials for Electrochemical Energy Storage: A Review. *J. Electrochem. Soc.* **1990**, *137* (1), 5C-22C.

[4] Wang, L.; Chen, B.; Ma, J.; Cui, G.; Chen, L. Reviving Lithium Cobalt Oxide-Based Lithium Secondary Batteries-toward a Higher Energy Density. *Chem. Soc. Rev.* **2018**, *47* (17), 6505–6602.

[5] Ecker, M.; Nieto, N.; Käbitz, S.; Schmalstieg, J.; Blanke, H.; Warnecke, A.; Sauer, D. U. Calendar and Cycle Life Study of Li(NiMnCo)O_2-Based 18650 Lithium-Ion Batteries. *J. Power Sources.* **2014**, 248, 839–851.

[6] Parikh, D.; Christensen, T.; Hsieh, C. T.; Li, J. Elucidation of Separator Effect on Energy Density of Li-Ion Batteries. *J. Electrochem. Soc.* **2019**, *166* (14), A3377–A3383.

[7] Frenck, L.; Sethi, G. K.; Maslyn, J. A.; Balsara, N. P. Factors That Control the Formation of Dendrites and Other Morphologies on Lithium Metal Anodes. *Front. Energy Res.* **2019**, 7, 115.

[8] Lin, D.; Liu, Y.; Cui, Y. Reviving the Lithium Metal Anode for High-Energy Batteries. *Nat. Nanotechnol.* **2017**, *12* (3), 194–206.

[9] Cheng, X.-B.; Zhang, R.; Zhao, C.-Z.; Zhang, Q. Toward Safe Lithium Metal Anode in Rechargeable Batteries: A Review. *Chem. Rev.* **2017**, 117 (15), 10403–10473.

[10] Asenbauer, J.; Eisenmann, T.; Kuenzel, M.; Kazzazi, A.; Chen, Z.; Bresser, D. The Success Story of Graphite as a Lithium-Ion Anode Material-Fundamentals, Remaining Challenges, and Recent Developments Including Silicon (Oxide) Composites. *Sustainable Energy and Fuels* **2020**, 4, 5387–5416.

[11] Zhang, S. S. A Review on Electrolyte Additives for Lithium-Ion Batteries. *J. Power Sources* **2006**, *162* (2), 1379-1394.

[12] Kim, K.; Ma, H.; Park, S.; Choi, N. S. Electrolyte-Additive-Driven Interfacial Engineering for High-Capacity Electrodes in Lithium-Ion Batteries: Promise and Challenges. *ACS Energy Lett.* **2020**, *5* (5), 1537–1553.

[13] Gao, Z.; Sun, H.; Fu, L.; Ye, F.; Zhang, Y.; Luo, W.; Huang, Y. Promises, Challenges, and Recent Progress of Inorganic Solid-State Electrolytes for All-Solid-State Lithium Batteries. *Adv. Mater.* **2018**, *30* (17), 1705702.

[14] Monroe, C.; Newman, J. The Impact of Elastic Deformation on Deposition Kinetics at Lithium/Polymer Interfaces. *J. Electrochem. Soc.* **2004**, *152* (2), A396-A404.

[15] Porz, L.; Swamy, T.; Sheldon, B. W.; Rettenwander, D.; Frömling, T.; Thaman, H. L.; Berendts, S.; Uecker, R.; Carter, W. C.; Chiang, Y. M. Mechanism of Lithium Metal Penetration through Inorganic Solid Electrolytes. *Adv. Energy Mater*. **2017**, *7* (20), 1–12.

[16] Manalastas, W.; Rikarte, J.; Chater, R. J.; Brugge, R.; Aguadero, A.; Buannic, L.; Llordés, A.; Aguesse, F.; Kilner, J. Mechanical Failure of Garnet Electrolytes during Li Electrodeposition Observed by In-Operando Microscopy. *J. Power Sources* **2019**, *412*, 287–293.

[17] Fenton, D. E.; Parker, M.; Wright, P. V. Complexes of Alkali Metal Ions with Poly(Ethylene Oxide). *Polymer* **1973**, *14*, 589.

[18] Edman, L. Ion Association and Ion Solvation Effects at the Crystalline-Amorphous Phase Transition in PEO-LiTFSI. *J. Phys. Chem. B* **2000**, *104* (31), 7254-7258.

[19] Teran, A. A.; Tang, M. H.; Mullin, S. A.; Balsara, N. P. Effect of Molecular Weight on Conductivity of Polymer Electrolytes. *Solid State Ionics* **2011**, *203* (1), 18–21.

[20] Singh, M.; Odusanya, O.; Wilmes, G. M.; Eitouni, H. B.; Gomez, E. D.; Patel, A. J.; Chen, V. L.; Park, M. J.; Fragouli, P.; Iatrou, H.; Hadjichristidis, N.; Cookson, D.; Balsara, N. P. Effect of Molecular Weight on the Mechanical and Electrical Properties of Block Copolymer Electrolytes. *Macromolecules* **2007**, *40* (13), 4578-4585.

[21] Bates, F. S.; Fredrickson, G. H. Block Copolymers-Designer Soft Materials. *Phys. Today* **1999**, *52* (2), 32–38.

[22] Soo, P. P.; Huang, B.; Jang, Y. I. I.; Chiang, Y. M.; Sadoway, D. R.; Mayes, A. M. Rubbery Block Copolymer Electrolytes for Solid-State Rechargeable Lithium Batteries. *J. Electrochem. Soc.* **1999**, *146* (1), 32–37.

[23] Loo, W. S.; Galluzzo, M. D.; Li, X.; Maslyn, J. A.; Oh, H. J.; Mongcopa, K. I. S.; Zhu, C.; Wang, A. A.; Wang, X.; Garetz, B. A.; Balsara, N. P. Phase Behavior of Mixtures of Block Copolymers and a Lithium Salt. *J. Phys. Chem. B* **2018**, *122* (33), 8065-8074.

[24] Teran, A. A.; Balsara, N. P. Thermodynamics of Block Copolymers with and without Salt. *J. Phys. Chem. B* **2014**, *118* (1), 4–17.

[25] Sethi, G. K.; Jiang, X.; Chakraborty, R.; Loo, W. S.; Villaluenga, I.; Balsara, N. P. Anomalous Self-Assembly and Ion Transport in Nanostructured Organic–Inorganic Solid Electrolytes. *ACS Macro Lett*. **2018**, *7* (9), 1056–1061.

[26] Vigild, M. E.; Almdal, K.; Mortensen, K.; Hamley, I. W.; Fairclough, J. P. A.; Ryan, A. J. Transformations to and from the Gyroid Phase in a Diblock Copolymer. *Macromolecules* **1998**, *31* (17), 5702–5716.

[27] Jo, G.; Ahn, H.; Park, M. J. Simple Route for Tuning the Morphology and Conductivity of Polymer Electrolytes: One End Functional Group Is Enough. *ACS Macro Lett.* **2013**, *2* (11), 990–995.

[28] Sing, C. E.; Zwanikken, J. W.; Olvera De La Cruz, M. Electrostatic Control of Block Copolymer Morphology. *Nat. Mater.* **2014**, *13* (7), 694–698.

[29] Shah, N. J.; Dadashi-Silab, S.; Galluzzo, M. D.; Chakraborty, S.; Loo, W. S.; Matyjaszewski, K.; Balsara, N. P. Effect of Added Salt on Disordered Poly(Ethylene Oxide)- Block-Poly(Methyl Methacrylate) Copolymer Electrolytes. *Macromolecules* **2021**, *54* (3), 1414-1424.

[30] Devaux, D.; Harry, K. J.; Parkinson, D. Y.; Yuan, R.; Hallinan, D. T.; MacDowell, A. A.; Balsara, N. P. Failure Mode of Lithium Metal Batteries with a Block Copolymer Electrolyte Analyzed by X-Ray Microtomography. *J. Electrochem. Soc.* **2015**, *162* (7), A1301–A1309.

[31] Stone, G. M.; Mullin, S. A.; Teran, A. A.; Hallinan, D. T.; Minor, A. M.; Hexemer, A.; Balsara, N. P. Resolution of the Modulus versus Adhesion Dilemma in Solid Polymer Electrolytes for Rechargeable Lithium Metal Batteries. J. Electrochem. Soc. 2012, 159 (3), A222–A227.

[32] Maslyn, J. A.; Loo, W. S.; McEntush, K. D.; Oh, H. J.; Harry, K. J.; Parkinson, D. Y.; Balsara, N. P. Growth of Lithium Dendrites and Globules through a Solid Block Copolymer Electrolyte as a Function of Current Density. *J. Phys. Chem. C* **2018**, *122* (47), 26797–26804.

[33] Shen, K.-H.; Brown, J. R.; Hall, L. M. Diffusion in Lamellae, Cylinders, and Double Gyroid Block Copolymer Nanostructures. *ACS Macro Lett.* **2018**, *7* (9), 1092–1098.

[34] Wang, X.; Chintapalli, M.; Newstein, M. C.; Balsara, N. P.; Garetz, B. A. Characterization of a Block Copolymer with a Wide Distribution of Grain Sizes. *Macromolecules* **2016**, *49* (21), 8198–8208.

[35] Gilbert, J. B.; Luo, M.; Shelton, C. K.; Rubner, M. F.; Cohen, R. E.; Epps, T. H. Determination of Lithium-Ion Distributions in Nanostructured Block Polymer Electrolyte Thin Films by X-Ray Photoelectron Spectroscopy Depth Profiling. *ACS Nano* **2015**, *9* (1), 512–520.

[36] Gomez, E. D.; Panday, A.; Feng, E. H.; Chen, V.; Stone, G. M.; Minor, A. M.; Kisielowski, C.; Downing, K. H.; Borodin, O.; Smith, G. D.; Balsara, N. P. Effect of Ion Distribution on Conductivity of Block Copolymer Electrolytes. *Nano Lett.* **2009**, *9* (3), 1212–1216.

[37] Chintapalli, M.; Chen, X. C.; Thelen, J. L.; Teran, A. A.; Wang, X.; Garetz, B. A.; Balsara, N. P. Effect of Grain Size on the Ionic Conductivity of a Block Copolymer Electrolyte. *Macromolecules* **2014**, *47* (15), 5424–5431.

[38] Mullin, S. A.; Stone, G. M.; Teran, A. A.; Hallinan, D. T.; Hexemer, A.; Balsara, N. P. Current-Induced Formation of Gradient Crystals in Block Copolymer Electrolytes. *Nano Lett.* **2012**, *12* (1), 464–468.

[39] Thelen, J. L. The Influence of Charged Species on the Phase Behavior, Self-Assembly, and Electrochemical Performance of Block Copolymer Electrolytes; PhD thesis, University of California, Berkeley, **2016**.

[40] Roe, R.J. *Methods of X-Ray and Neutron Scattering in Polymer Science*; Oxford University Press, **2000**.

[41] Pauw, R. B. Everything SAXS: Small-Angle Scattering Pattern Collection and Correction. *J. Phys. Condens. Matter* **2013**, *25,* 383201.

[42] Newman, J.; Balsara, N. P. *Electrochemical Systems*, 4th ed.; Wiley, **2021**.

[43] Ma, Y.; Doyle, M.; Fuller, T. F.; Doeff, M. M.; Jonghe, L. C. De; Newman, J. The Measurement of a Complete Set of Transport Properties for a Concentrated Solid Polymer Electrolyte Solution. *J. Electrochem. Soc.* **1995**, *142* (6), 1859.

[44] Matula, R. A. Electrical Resistivity of Copper, Gold, Palladium, and Silver. *J. Phys. Chem. Ref. Data* **1979**, *8* (4), 1147–1298.

[45] Srinivasan, V.; Newman, J. Discharge Model for the Lithium Iron-Phosphate Electrode. *J. Electrochem. Soc.* **2004**, *151* (10), A1517–A1529.

[46] Pesko, D. M.; Feng, Z.; Sawhney, S.; Newman, J.; Srinivasan, V.; Balsara, N. P. Comparing Cycling Characteristics of Symmetric Lithium-Polymer-Lithium Cells with Theoretical Predictions. *J. Electrochem. Soc.* **2018**, *165* (13), A3186–A3194.

[47] Evans, J.; Vincent, C. A.; Bruce, P. G. Electrochemical Measurement of Transference Numbers in Polymer Electrolytes. *Polymer* **1987**, *28* (13), 2324–2328.

[48] Macdonald, J. R. Theory of Space-Charge Polarization and Electrode-Discharge Effects. *J. Chem. Phys.* **1973**, *58* (11), 4982–5001.

[49] Bruce, P. G.; Vincent, C. A. Steady State Current Flow in Solid Binary Electrolyte Cells. *J. Electroanal. Chem. Interfacial Electrochem.* **1987**, *225* (1–2), 1–17.

[50] Watanabe, M.; Nagano, S.; Sanui, K.; Ogata, N. Estimation of Li^+ Transport Number in Polymer Electrolytes by the Combination of Complex Impedance and Potentiostatic Polarization Measurements. *Solid State Ionics* **1988**, 28–30, 911–917.

[51] Balsara, N. P.; Newman, J. Relationship between Steady-State Current in Symmetric Cells and Transference Number of Electrolytes Comprising Univalent and Multivalent Ions. *J. Electrochem. Soc.* **2015**, *162* (14), A2720–A2722.

[52] Sørensen, P. R.; Jacobsen, T. Conductivity, Charge Transfer and Transport Number - An Ac-Investigation of the Polymer Electrolyte LiSCN-Poly(Ethyleneoxide). *Electrochim. Acta* **1982**, *27* (12), 1671–1675.

[53] Doyle, M.; Newman, J. Analysis of Transference Number Measurements Based on the Potentiostatic Polarization of Solid Polymer Electrolytes. *J. Electrochem. Soc.* **1995**, *142* (10), 3465.

[54] Onsager, L. Theories and Problems of Liquid Diffusion. *Ann. N. Y. Acad. Sci*. **1945**, *46* (5), 241–265.

[55] Villaluenga, I.; Pesko, D. M.; Timachova, K.; Feng, Z.; Newman, J.; Srinivasan, V.; Balsara, N. P. Negative Stefan-Maxwell Diffusion Coefficients and Complete Electrochemical Transport Characterization of Homopolymer and Block Copolymer Electrolytes. *J. Electrochem. Soc.* **2018**, *165* (11), A2766–A2773.

[56] Bruce, P. G.; Gray, F. *Solid State Electrochemistry*; Cambridge University Press, **1995**, 157-158.

[57] Zugmann, S.; Moosbauer, D.; Amereller, M.; Schreiner, C.; Wudy, F.; Schmitz, R.; Schmitz, R.; Isken, P.; Dippel, C.; Müller, R.; Kunze, M.; Lex-Balducci, A.; Winter, M.; Gores, J. Electrochemical Characterization of Electrolytes for Lithium-Ion Batteries Based on Lithium Difluoromono(Oxalato)Borate. *J. Power Sources* **2010**, *196*, 1417–1424.

[58] Pesko, D. M.; Timachova, K.; Bhattacharya, R.; Smith, M. C.; Villaluenga, I.; Newman, J.; Balsara, N. P. Negative Transference Numbers in Poly(Ethylene Oxide)-Based Electrolytes. *J. Electrochem. Soc.* **2017**, *164* (11), E3569–E3575.

[59] Abraham, K. M.; Jiang, Z.; Carroll, B. Highly Conductive PEO-like Polymer Electrolytes. Chem. Mater. **1997**, *9* (9), 1978-1988.

[60] Hiller, M. M.; Joost, M.; Gores, H. J. J.; Passerini, S.; Wiemhöfer, H.-D. The Influence of Interface Polarization on the Determination of Lithium Transference Numbers of Salt in Polyethylene Oxide Electrolytes. *Electrochim. Acta* **2013**, *114* (30), 21–29.

[61] Zheng, Q.; Pesko, D. M.; Savoie, B. M.; Timachova, K.; Hasan, A. L.; Smith, M. C.; Miller, T. F.; Coates, G. W.; Balsara, N. P.; Coates, W.; Balsara, N. P. Optimizing Ion Transport in Polyether-Based Electrolytes for Lithium Batteries. *Macromolecules* **2018**, *51* (8), 2847–2858.

[62] Shah, D. B.; Olson, K. R.; Karny, A.; Mecham, S. J.; Desimone, J. M.; Balsara, N. P. Effect of Anion Size on Conductivity and Transference Number of Perfluoroether Electrolytes with Lithium Salts. *J. Electrochem. Soc.* **2017**, *164* (14), A3511–A3517.

[63] Chintapalli, M.; Timachova, K.; Olson, K. R.; Mecham, S. J.; Devaux, D.; DeSimone, J. M.; Balsara, N. P. Relationship between Conductivity, Ion Diffusion, and Transference Number in Perfluoropolyether Electrolytes. *Macromolecules* **2016**, *49* (9), 3508–3515.

[64] Wang, H.; Matsui, M.; Takeda, Y.; Yamamoto, O.; Im, D.; Lee, D.; Imanishi, N. Interface Properties between Lithium Metal and a Composite Polymer Electrolyte of $PEO_{18}Li(CF_3SO_2)_2$ N-Tetraethylene Glycol Dimethyl Ether. *Membranes* **2013**, *3* (4), 298–310.

[65] Cai, F.; Zuo, X.; Liu, X.-M.; Wang, L.; Zhai, W.; Yang, H. The Study of Novel Gel Polymer Electrolytes Plasticized with Non-Volatile Tris(Methoxypolyethyleneglycol) Aluminate Esters. *Electrochim. Acta* **2013**, *106*, 209–214.

[66] Porcarelli, L.; Gerbaldi, C.; Bella, F.; Nair, J. R. Super Soft All-Ethylene Oxide Polymer Electrolyte for Safe All-Solid Lithium Batteries. *Sci. Rep.* **2016**, *6* (1), 19892.

[67] Piszcz, M.; Garcia-Calvo, O.; Oteo, U.; Lopez del Amo, J. M.; Li, C.; Rodriguez-Martinez, L. M.; Youcef, H. B.; Lago, N.; Thielen, J.; Armand, M. New Single Ion Conducting Blend Based on PEO and PA-LiTFSI. *Electrochim. Acta* **2017**, *255*, 48–54.

[68] Zhang, W.; Nie, J.; Li, F.; Lin, Z.; Sun, C.; Wang, Z. L.; Sun, C. A Durable and Safe Solid-State Lithium Battery with a Hybrid Electrolyte Membrane. *Nano Energy* **2018**, *45*, 413–419.

[69] Yang, G.; Oh, H.; Chanthad, C.; Wang, Q. Dumbbell-Shaped Octasilsesquioxanes Functionalized with Ionic Liquids as Hybrid Electrolytes for Lithium Metal Batteries. *Chem. Mater.* **2017**, *29* (21), 9275–9283.

[70] Lin, Y.; Li, J.; Liu, K.; Liu, Y.; Liu, J.; Wang, X. Unique Starch Polymer Electrolyte for High Capacity All-Solid-State Lithium Sulfur Battery. *Green Chem.* **2016**, *18* (13), 3796–3803.

[71] Colò, F.; Bella, F.; Nair, J. R.; Destro, M.; Gerbaldi, C. Cellulose-Based Novel Hybrid Polymer Electrolytes for Green and Efficient Na-Ion Batteries. *Electrochim. Acta* **2015**, *174*, 185–190.

[72] Makhlooghiazad, F.; Yunis, R.; Mecerreyes, D.; Armand, M.; Howlett, P. C.; Forsyth, M. Comparison of the Physicochemical and Electrochemical Behaviour of Mixed Anion Phosphonium Based OIPCs Electrolytes for Sodium Batteries. *Solid State Ionics* **2017**, *312,* 44–52.

[73] Mulder, M. *Basic Principles of Membrane Technology*, 2nd ed.; Kluwer Academic Publishers, **1996**.

[74] Yampolskii, Y.; Freeman, B. *Membrane Gas Separation*; John Wiley & Sons, **2010**.

[75] Lloyd M. Robeson; Robeson, L. M. Correlation of Separation Factor versus Permeability for Polymeric Membranes. *J. Memb. Sci.* **1991**, *62* (2), 165–185.

[76] Doyle, M.; Fuller, T. F.; Newman, J. Modeling of Galvanostatic Charge and Discharge of the Lithium/Polymer/Insertion Cell. *J. Electrochem. Soc.* **1993**, *140* (6), 1526-1533.

[77] Doyle, M.; Fuller, T. F.; Newman, J. The Importance of the Lithium Ion Transference Number in Lithium/Polymer Cells. *Electrochim. Acta* **1994**, *39* (13), 2073–2081.

[78] Diederichsen, K. M.; McShane, E. J.; McCloskey, B. D. Promising Routes to a High Li^+ Transference Number Electrolyte for Lithium Ion Batteries. *ACS Energy Lett*. **2017**, *2* (11), 2563–2575.

[79] Shah, D. B.; Nguyen, H. Q.; Grundy, L. S.; Olson, K. R.; Mecham, S. J.; DeSimone, J. M.; Balsara, N. P. Difference between Approximate and Rigorously Measured Transference Numbers in Fluorinated Electrolytes. *Phys. Chem. Chem. Phys.* **2019**, *21* (15), 7857–7866.

[80] Valøen, L. O.; Reimers, J. N. Transport Properties of $LiPF_6$-Based Li-Ion Battery Electrolytes. *J. Electrochem. Soc.* **2005**, *152* (5), A882-A891.

[81] Gao, K. W.; Balsara, N. P. Electrochemical Properties of Poly(ethylene oxide) Electrolytes above the Entanglement Threshold. *Solid State Ionics* **2021**, *364,* 115609.

[82] Molinari, N.; Kozinsky, B. Chelation-Induced Reversal of Negative Cation Transference Number in Ionic Liquid Electrolytes. *J. Phys. Chem. B* **2020**, *124* (13), 2676–2684.

[83] Molinari, N.; Mailoa, J. P.; Kozinsky, B. General Trend of a Negative Li Effective Charge in Ionic Liquid Electrolytes. *J. Phys. Chem. Lett.* **2019**, *10* (10), 2313–2319.

[84] Gouverneur, M.; Schmidt, F.; Schönhoff, M. Negative Effective Li Transference Numbers in Li Salt/Ionic Liquid Mixtures: Does Li Drift in the "Wrong" Direction? *Phys. Chem. Chem. Phys.* **2018**, *20* (11), 7470–7478.

[85] Steinrück, H.-G.; Takacs, C. J.; Kim, H.-K.; Mackanic, D. G.; Holladay, B.; Cao, C.; Narayanan, S.; Dufresne, E. M.; Chushkin, Y.; Ruta, B.; Zontone, F.; Will, J.; Borodin, O.; Sinha, S. K.; Srinivasan, V.; Toney, M. F. Concentration and Velocity Profiles in a Polymeric Lithium-Ion Battery Electrolyte. *Energy Environ. Sci.* **2020**, *13*, 4312-4321

[86] Rey, I.; Bruneel, J.; Grondin, J.; Servant, L.; Lassègues, J. Raman Spectroelectrochemistry of a Lithium/Polymer Electrolyte Symmetric Cell. *J. Electrochem. Soc.* **1998**, *145* (9), 3034.

[87] Fawdon, J.; Ihli, J.; Mantia, F. La; Pasta, M. Characterising Lithium-Ion Electrolytes via Operando Raman Microspectroscopy. *ChemRxiv* **2020**, 13–15.

[88] Molinari, N.; Mailoa, J. P.; Kozinsky, B. Effect of Salt Concentration on Ion Clustering and Transport in Polymer Solid Electrolytes: A Molecular Dynamics Study of PEO–LiTFSI. *Chem. Mater.* **2018**, *30* (18), 6298–6306.

[89] Nan, H. -S.; Hu, X. -Y.; Tian, H. -W. Recent Advances in Perovskite Oxides for Anion-Intercalation Supercapacitor: A Review. *Mater. Sci. Semicond. Process.* **2019**, *94*, 35-50.

[90] Deunf, É.; Moreau, P.; Quarez, É.; Guyomard, D.; Dolhem, F.; Poizot, P. Reversible Anion Intercalation in a Layered Aromatic Amine: A High-Voltage Host Structure for Organic Batteries. *J. Mater. Chem. A* **2016**, *4* (16), 6131–6139.

[91] Craig, N.; Mullin, S. A.; Pratt, R.; Crane, G. B. Determination of Transference Number and Thermodynamic Factor by Use of Anion-Exchange Concentration Cells and Concentration Cells. *J. Electrochem. Soc.* **2019**, *166* (13), A2769–A2775.

[92] Galizia, M.; Chi, W. S.; Smith, Z. P.; Merkel, T. C.; Baker, R. W.; Freeman, B. D. Polymers and Mixed Matrix Membranes for Gas and Vapor Separation: A Review and Prospective Opportunities. *Macromolecules* **2017**, *50* (20), 7809–7843.

[93] Robeson, L. M. Polymer Membranes for Gas Separation. *Curr. Opin. Solid State Mater. Sci.* **1999**, *4* (6), 549–552.

[94] Werber, J. R.; Osuji, C. O.; Elimelech, M. Materials for Next-Generation Desalination and Water Purification Membranes. *Nat. Rev. Mater.* **2016**, *1*, 16018.

[95] Ma, H.; Burger, C.; Hsiao, B. S.; Chu, B. Highly Permeable Polymer Membranes Containing Directed Channels for Water Purification. *ACS Macro Lett.* **2012**, *1* (6), 723–726.

[96] Prater, K. The Renaissance of the Solid Polymer Fuel Cell. *J. Power Sources* **1990**, *29* (1–2), 239–250.

[97] Wang, Y.; Ruiz Diaz, D. F.; Chen, K. S.; Wang, Z.; Adroher, X. C. Materials, Technological Status, and Fundamentals of PEM Fuel Cells − A Review. *Mater. Today* 2019, *32*, 178-203.

[98] DeLuca, N. W.; Elabd, Y. A. Polymer Electrolyte Membranes for the Direct Methanol Fuel Cell: A Review. *J. Polym. Sci. Part B Polym. Phys.* **2006**, *44* (16), 2201–2225.

[99] Berthier, C.; Gorecki, W.; Minier, M.; Armand, M. B.; Chabagno, J. M.; Rigaud, P. Microscopic Investigation of Ionic Conductivity in Alkali Metal Salts-Poly(ethylene oxide) Adducts. *Solid State Ionics* **1983**, *11*, 91−95.
[100] Hallinan, D. T.; Mullin, S. A.; Stone, G. M.; Balsara, N. P. Lithium Metal Stability in Batteries with Block Copolymer Electrolytes. *J. Electrochem. Soc.* **2013**, *160* (3), A464–A470.
[101] Long, L.; Wang, S.; Xiao, M.; Meng, Y. Polymer Electrolytes for Lithium Polymer Batteries. *J. Mater. Chem. A* **2016**, *4* (26), 10038–10069.
[102] Arbizzani, C.; Mastragostino, M.; Hamaide, T.; Guyot, A. An All Solid-State Polymer-Polymer Electrolyte-Lithium Rechargeable Battery for Room Temperature Applications. *Electrochim. Acta* **1990**, *35* (11–12), 1781–1785.
[103] Rzayev, J.; Hillmyer, M. A. Nanoporous Polystyrene Containing Hydrophilic Pores from an ABC Triblock Copolymer Precursor. *Macromolecules* **2005**, *38* (1), 3−5.
[104] Young, W.-S.; Kuan, W.-F.; Epps, T. H. Block Copolymer Electrolytes for Rechargeable Lithium Batteries. *J. Polym. Sci. Part B Polym. Phys.* **2014**, *52* (1), 1–16.
[105] Barteau, K. P.; Wolffs, M.; Lynd, N. A.; Fredrickson, G. H.; Kramer, E. J.; Hawker, C. J. Allyl Glycidyl Ether-Based Polymer Electrolytes for Room Temperature Lithium Batteries. *Macromolecules* **2013**, *46* (22), 8988–8994.
[106] Villaluenga, I.; Chen, X. C.; Devaux, D.; Hallinan, D. T.; Balsara, N. P. Nanoparticle-Driven Assembly of Highly Conducting Hybrid Block Copolymer Electrolytes. *Macromolecules* **2015**, *48* (2), 358–364.
[107] Balsara, N. P.; Singh, M.; Eitouni, H. B.; Comex, E. D. High Elastic Modulus Polymer Electrolytes. US Patent Application 12/225, 934, PCT No. PCT/US2007/008435, Oct 22, **2013**.
[108] Sax, J.; Ottino, J. M. Modeling of Transport of Small Molecules in Polymer Blends: Application of Effective Medium Theory. *Polym. Eng. Sci.* **1983**, *23*, 165–176.
[109] Irwin, M. T.; Hickey, R. J.; Xie, S.; So, S.; Bates, F. S.; Lodge, T. P. Structure-Conductivity Relationships in Ordered and Disordered Salt-Doped Diblock Copolymer/Homopolymer Blends. *Macromolecules* **2016**, *49* (18), 6928–6939.
[110] Cho, B. K.; Jain, A.; Gruner, S. M.; Wiesner, U. Mesophase Structure-Mechanical and Ionic Transport Correlations in Extended Amphiphilic Dendrons. *Science* **2004**, *305* (5690), 1598−1601.
[111] Majewski, P. W.; Gopinadhan, M.; Jang, W.-S.; Lutkenhaus, J. L.; Osuji, C. O. Anisotropic Ionic Conductivity in Block Copolymer Membranes by Magnetic Field Alignment. *J. Am. Chem. Soc.* **2010**, *132* (49), 17516–17522.
[112] Bates, F. S.; Fredrickson, G. H. Block Copolymer Thermodynamics: Theory and Experiment. *Annu. Rev. Phys. Chem.* **1990**, *41* (1), 525–557.
[113] Gribble, D. A.; Frenck, L.; Shah, D. B.; Maslyn, J. A.; Loo, W. S.; Mongcopa, K. I. S.; Pesko, D. M.; Balsara, N. P. Comparing Experimental Measurements of Limiting Current in Polymer Electrolytes with Theoretical Predictions. *J. Electrochem. Soc.* **2019**, *166* (14), A3228–A3234.
[114] Hadjichristidis, N.; Iatrou, H.; Pispas, S.; Pitsikalis, M. Anionic Polymerization: High Vacuum Techniques. J. *Polym. Sci. Part A Polym. Chem.* **2000**, *38* (18), 3211–3234.
[115] Mark, J. E. *Physical Properties of Polymers Handbook*, 2nd ed.; Springer, **2007**.
[116] Yuan, R.; Teran, A. A.; Gurevitch, I.; Mullin, S. A.; Wanakule, N. S.; Balsara, N. P. Ionic Conductivity of Low Molecular Weight Block Copolymer Electrolytes. *Macromolecules* **2013**, *46*, 914−921.
[117] Gartner, T. E.; Morris, M. A.; Shelton, C. K.; Dura, J. A.; Epps, T. H. Quantifying Lithium Salt and Polymer Density Distributions in Nanostructured Ion-Conducting Block Polymers. *Macromolecules* **2018**, *51* (5), 1917–1926.
[118] Fredrickson, G. H.; Helfand, E. Fluctuation Effects in the Theory of Microphase Separation in Block Copolymers. *J. Chem. Phys.* **1987**, *87* (1), 697–705.

[119] Qin, J.; de Pablo, J. J. Ordering Transition in Salt-Doped Diblock Copolymers. *Macromolecules* **2016**, *49* (9), 3630–3638.
[120] Nakamura, I.; Wang, Z.-G. G. Salt-Doped Block Copolymers: Ion Distribution, Domain Spacing and Effective χ Parameter. *Soft Matter* **2012**, *8* (36), 9356–9367.
[121] Loo, W. S.; Sethi, G. K.; Teran, A. A.; Galluzzo, M. D.; Maslyn, J. A.; Oh, H. J.; Mongcopa, K. I.; Balsara, N. P. Composition Dependence of the Flory−Huggins Interaction Parameters of Block Copolymer Electrolytes and the Isotaksis Point. *Macromolecules* **2019**, *52* (15), 5590−5601.
[122] Panday, A.; Mullin, S.; Gomez, E. D.; Wanakule, N.; Chen, V. L.; Hexemer, A.; Pople, J.; Balsara, N. P. Effect of Molecular Weight and Salt Concentration on Conductivity of Block Copolymer Electrolytes. *Macromolecules* **2009**, *42*, 4632.
[123] Chintapalli, M.; Le, T. N. P.; Venkatesan, N. R.; Mackay, N. G.; Rojas, A. A.; Thelen, J. L.; Chen, X. C.; Devaux, D.; Balsara, N. P. Structure and Ionic Conductivity of Polystyrene- Block -Poly(Ethylene Oxide) Electrolytes in the High Salt Concentration Limit. *Macromolecules* **2016**, *49* (5), 1770–1780.
[124] Timachova, K.; Villaluenge, I.; Cirrincione, L.; Gobet, M.; Bhattacharya, R.; Jiang, X.; Newman, J.; Madsen, L. A.; Greenbaum, S. G.; Balsara, N. P. Anisotropic Ion Diffusion and Electrochemically Driven Transport in Nanostructured Block Copolymer Electrolytes. *J. Phys. Chem. B* **2018**, *122* (4), 1537.
[125] Mullin, S. A.; Teran, A. A.; Yuan, R.; Balsara, N. P. Effect of Thermal History on the Ionic Conductivity of Block Copolymer Electrolytes. *J. Polym. Sci. Part B Polym. Phys.* **2013**, *51* (12), 927–934.
[126] Arges, C. G.; Kambe, Y.; Dolejsi, M.; Wu, G.-P. P.; Segal-Pertz, T.; Ren, J.; Cao, C.; Craig, G. S. W. W.; Nealey, P. F. Interconnected Ionic Domains Enhance Conductivity in Microphase Separated Block Copolymer Electrolytes. *J. Mater. Chem. A* **2017**, *5* (11), 5619–5629.
[127] Arges, C. G.; Kambe, Y.; Suh, H. S.; Ocola, L. E.; Nealey, P. F. Perpendicularly Aligned, Anion Conducting Nanochannels in Block Copolymer Electrolyte Films. *Chem. Mater.* **2016**, *28* (5), 1377–1389.
[128] Sharon, D.; Bennington, P.; Liu, C.; Kambe, Y.; Dong, B. X.; Burnett, V. F.; Dolejsi, M.; Grocke, G.; Patel, S. N.; Nealey, P. F. Interrogation of Electrochemical Properties of Polymer Electrolyte Thin Films with Interdigitated Electrodes. *J. Electrochem. Soc.* **2018**, *165* (16), H1028–H1039.
[129] Kim, S. H.; Misner, M. J.; Yang, L.; Gang, O.; Ocko, B. M.; Russell, T. P. Salt Complexation in Block Copolymer Thin Films. *Macromolecules* **2006**, *39* (24), 8473–8479.
[130] Balsara, N. P.; Garetz, B. A.; Dai, H. J. Relationship between Birefringence and the Structure of Ordered Block Copolymer Materials. *Macromolecules* **1992**, *25* (22), 6072–6074.
[131] Mongcopa, K. I. S.; Tyagi, M.; Mailoa, J. P.; Samsonidze, G.; Kozinsky, B.; Mullin, S. A.; Gribble, D. A.; Watanabe, H.; Balsara, N. P. Relationship between Segmental Dynamics Measured by Quasi-Elastic Neutron Scattering and Conductivity in Polymer Electrolytes. *ACS Macro Lett.* **2018**, *7* (4), 504–508.
[132] Hallinan, D. T.; Villaluenga, I.; Balsara, N. P. Polymer and Composite Electrolytes. *MRS Bull.* **2018**, *43* (10), 759–767.
[133] Hallinan, D. T.; Balsara, N. P. Polymer Electrolytes. *Annu. Rev. Mater. Res.* **2013**, *43* (1), 503–525.
[134] Desmet, G.; Deridder, S. Effective Medium Theory Expressions for the Effective Diffusion in Chromatographic Beds Filled with Porous, Non-Porous and Porous-Shell Particles and Cylinders. Part I: Theory. *J. Chromatogr. A* **2011**, *1218* (1), 32–45.
[135] Shi, J.; Vincent, C. A. The Effect of Molecular Weight on Cation Mobility in Polymer Electrolytes. *Solid State Ionics* **1993**, *60* (1–3), 11–17.
[136] Seo, Y.; Shen, K.-H.; Brown, J. R.; Hall, L. M. Role of Solvation on Diffusion of Ions in Diblock Copolymers: Understanding the Molecular Weight Effect through Modeling. *J. Am. Chem. Soc.* **2019**, *141*, 18455.

[137] Morris, M. A.; Gartner, T. E.; Epps, T. H. Tuning Block Polymer Structure, Properties, and Processability for the Design of Efficient Nanostructured Materials Systems. *Macromol. Chem. Phys.* **2017**, *218* (5), 1600513.
[138] Wanakule, N. S.; Panday, A.; Mullin, S. A.; Gann, E.; Hexemer, A.; Balsara, N. P. Ionic Conductivity of Block Copolymer Electrolytes in the Vicinity of Order−Disorder and Order−Order Transitions. *Macromolecules* **2009**, *42* (15), 5642–5651.
[139] Jung, H. Y.; Mandal, P.; Jo, G.; Kim, O.; Kim, M.; Kwak, K.; Park, M. J. Modulating Ion Transport and Self-Assembly of Polymer Electrolytes via End-Group Chemistry. *Macromolecules* **2017**, *50* (8), 3224–3233.
[140] Majewski, P. W.; Gopinadhan, M.; Osuji, C. O. The Effects of Magnetic Field Alignment on Lithium Ion Transport in a Polymer Electrolyte Membrane with Lamellar Morphology. *Polymers* **2019**, *11* (5), 887.
[141] Tarascon, J.-M.; Armand, M. Issues and Challenges Facing Rechargeable Lithium Batteries. *Nature* **2001**, *414*, 359−367.
[142] Tikekar, M. D.; Choudhury, S.; Tu, Z.; Archer, L. A. Design Principles for Electrolytes and Interfaces for Stable Lithium-Metal Batteries. *Nat. Energy* **2016**, *1* (9), 16114.
[143] Lascaud, S.; Perrier, M.; Vallee, A.; Besner, S.; Prud'homme, J.; Armand, M. Phase Diagrams and Conductivity Behavior of Poly(Ethylene Oxide)-Molten Salt Rubbery Electrolytes. *Macromolecules* **1994**, *27* (25), 7469–7477.
[144] Zhang, Q.; Liu, K.; Ding, F.; Liu, X. Recent Advances in Solid Polymer Electrolytes for Lithium Batteries. *Nano Res.* **2017**, *10* (12), 4139–4174.
[145] Zeng, H.; Ji, X.; Tsai, F.; Zhang, Q.; Jiang, T.; Li, R. K. Y.; Shi, H.; Luan, S.; Shi, D. Enhanced Cycling Performance for All-Solid-State Lithium Ion Battery with $LiFePO_4$ Composite Cathode Encapsulated by Poly (Ethylene Glycol) (PEG) Based Polymer Electrolyte. *Solid State Ionics* **2018**, *320*, 92–99.
[146] Fauteux, D. Lithium Electrode/PEO-Based Polymer Electrolyte Interface Behavior Between 60 and 120C. *J. Electrochem. Soc*. **1988**, *135* (9), 2231−2237.
[147] Bouchet, R.; Lascaud, S.; Rosso, M. An EIS Study of the Anode Li/PEO-LiTFSI of a Li Polymer Battery. *J. Electrochem. Soc.* **2003**, *150* (10), A1385.
[148] Ammann, C.; Meier, P.; Merbach, A. A Simple Multinuclear NMR Thermometer. *J. Magn. Reson.* **1982**, *46* (2), 319–321.
[149] Ilavsky, J. Nika : Software for Two-Dimensional Data Reduction. *J. Appl. Crystallogr.* **2012**, *45* (2), 324−328.
[150] Carter, G. C.; Bennett, L. H.; Kahan, D. J. *Metallic Shifts in NMR : A Review of the Theory and Comprehensive Critical Data Compilation of Metallic Materials*; Pergamon Press, **1977**.
[151] Sun, X.-G.; Reeder, C. L.; Kerr, J. B. Synthesis and Characterization of Network Type Single Ion Conductors. *Macromolecules* **2004**, *37* (6), 2219−2227.
[152] Zhang, H.; Li, C.; Piszcz, M.; Coya, E.; Rojo, T.; Rodriguez-Martinez, L. M.; Armand, M.; Zhou, Z. Single Lithium-Ion Conducting Solid Polymer Electrolytes: Advances and Perspectives. *Chem. Soc. Rev.* **2017**, *46* (3), 797–815.
[153] Seely, C. On Ammonium and the Solubility of Metals without Chemical Action. *Chem. News* **1871**, *23* (594), 169−170.
[154] Cafasso, F.; Sundheim, B. R. Solutions of Alkali Metals in Polyethers. I. *J. Chem. Phys.* **1959**, *31* (3), 809–813.
[155] Panayotov, I. M.; Tsvetanov, C. B.; Berlinova, I. V.; Velichkova, R. S. Alkali Metal Solutions in Organic Solvents Obtained in the Presence of Polyethylene Oxide. *Makromol. Chem.* **1970**, *134* (1), 313−316.
[156] Jedlinski, Z.; Sokol, M. Solubility of Alkali Metals in Non-Aqueous Supramolecular Systems. *Pure Appl. Chem.* **1995**, *67* (4), 587–592.
[157] Dye, J. L. The Alkali Metals: 200 Years of Surprises. *Philos. Trans. R. Soc., A* **2015**, *373* (2037), 20140174.

[158] Joo, Y.; Agarkar, V.; Sung, S. H.; Savoie, B. M.; Boudouris, B. W. A Nonconjugated Radical Polymer Glass with High Electrical Conductivity. *Science* **2018**, *359* (6382), 1391−1395.
[159] Ruzette, A.-V. G.; Soo, P. P.; Sadoway, D. R.; Mayes, A. M. Melt-Formable Block Copolymer Electrolytes for Lithium Rechargeable Batteries. *J. Electrochem. Soc.* **2001**, *148* (6), A537.
[160] Young, W.-S.; Epps, T. H. Salt Doping in PEO-Containing Block Copolymers: Counterion and Concentration Effects. *Macromolecules* **2009**, *42* (7), 2672–2678.
[161] Thelen, J. L.; Teran, A. A.; Wang, X.; Garetz, B. A.; Nakamura, I.; Wang, Z. G.; Balsara, N. P. Phase Behavior of a Block Copolymer/Salt Mixture through the Order-to-Disorder Transition. *Macromolecules* **2014**, *47*, 2666.
[162] Hexemer, A.; Bras, W.; Glossinger, J.; Schaible, E.; Gann, E.; Kirian, R.; MacDowell, A.; Church, M.; Rude, B.; Padmore, H. A SAXS/WAXS/GISAXS Beamline with Multilayer Monochromator. *J. Phys. Conf. Ser*. **2010**, *247* (1), 012007.
[163] Leibler, L. Theory of Microphase Separation in Block Copolymers. *Macromolecules* **1980**, *13* (6), 1602–1617.
[164] Wang, X.; Li, X.; Loo, W.; Newstein, M. C.; Balsara, N. P.; Garetz, B. A. Depolarized Scattering from Block Copolymer Grains Using Circularly Polarized Light. *Macromolecules* **2017**, *50* (13), 5122–5131.
[165] Howell, D.; Boyd, S.; Cunningham, B.; Gillard, S.; Slezak, L.; Ahmed, S.; Bloom, I.; Burnham, A.; Hardy, K.; Jansen, A. N.; Nelson, P. A.; Robertson, D. C.; Stephens, T.; Vijayagopal, R.; Carlson, R. B.; Dias, F.; Dufek, E. J.; Michelbacher, C. J.; Mohanpurkar, M.; Scoffield, D.; Shirk, M.; Tanim, T.; Keyser, M.; Kreuzer, C.; Li, O.; Markel, A.; Meintz, A.; Pesaran, A.; Santhanagopalan, S.; Smith, K.; Wood, E.; Zhang, J. *Enabling Fast Charging: A Technology Gap Assessment*; U.S. Department of Energy, **2017**.
[166] Pandian, A. S.; Chen, X. C.; Chen, J.; Lokitz, B. S.; Ruther, R. E.; Yang, G.; Lou, K.; Nanda, J.; Delnick, F. M.; Dudney, N. J. Facile and Scalable Fabrication of Polymer-Ceramic Composite Electrolyte with High Ceramic Loadings. *J. Power Sources* **2018**, *390*, 153–164.
[167] He, R.; Kyu, T. Effect of Plasticization on Ionic Conductivity Enhancement in Relation to Glass Transition Temperature of Crosslinked Polymer Electrolyte Membranes. *Macromolecules* **2016**, *49* (15), 5637–5648.
[168] Gunkel, I.; Thurn-Albrecht, T. Thermodynamic and Structural Changes in Ion-Containing Symmetric Diblock Copolymers: A Small-Angle X-Ray Scattering Study. *Macromolecules* **2012**, *45* (1), 283–291.
[169] Epps, T. H.; Bailey, T. S.; Waletzko, R.; Bates, F. S. Phase Behavior and Block Sequence Effects in Lithium Perchlorate-Doped Poly(Isoprene-b-Styrene-b-Ethylene Oxide) and Poly(Styrene-b-Isoprene-b-Ethylene Oxide) Triblock Copolymers. *Macromolecules* **2003**, *36* (8), 2873–2881.
[170] Teran, A. A.; Mullin, S. A.; Hallinan, D. T.; Balsara, N. P. Discontinuous Changes in Ionic Conductivity of a Block Copolymer Electrolyte through an Order–Disorder Transition. *ACS Macro Lett.* **2012**, *1* (2), 305–309.
[171] Krachkovskiy, S. A.; Bazak, J. D.; Werhun, P.; Balcom, B. J.; Halalay, I. C.; Goward, G. R. Visualization of Steady-State Ionic Concentration Profiles Formed in Electrolytes during Li-Ion Battery Operation and Determination of Mass-Transport Properties by in Situ Magnetic Resonance Imaging. *J. Am. Chem. Soc.* **2016**, *138* (25), 7992–7999.
[172] Förster, S.; Khandpur, A. K.; Zhao, J.; Bates, F. S.; Hamley, I. W.; Ryan, A. J.; Bras, W. Complex Phase Behavior of Polyisoprene-Polystyrene Diblock Copolymers Near the Order-Disorder Transition. *Macromolecules* **1994**, *27* (23), 6922–6935.
[173] Gibbs, J. W. On the Equilibrium of Heterogeneous Substances. *Trans. Conn. Acad. Arts Sci.* **1876**, *3*, 108−524.
[174] Nakamura, I.; Balsara, N. P.; Wang, Z. G. First-Order Disordered-to-Lamellar Phase Transition in Lithium Salt-Doped Block Copolymers. *ACS Macro Lett.* **2013**, *2* (6), 478–481.

[175] Kambe, Y.; Arges, C. G.; Czaplewski, D. A.; Dolejsi, M.; Krishnan, S.; Stoykovich, M. P.; De Pablo, J. J.; Nealey, P. F. Role of Defects in Ion Transport in Block Copolymer Electrolytes. *Nano Lett.* **2019**, *19* (7), 4684–4691.
[176] Kim, H.-K.; Balsara, N. P.; Srinivasan, V. Continuum Description of the Role of Negative Transference Numbers on Ion Motion in Polymer Electrolytes. *J. Electrochem. Soc.* **2020**, *167*, 110559.
[177] Young, W.-S.; Epps, T. H. Ionic Conductivities of Block Copolymer Electrolytes with Various Conducting Pathways: Sample Preparation and Processing Considerations. *Macromolecules* **2012**, *45* (11), 4689–4697.
[178] Shen, K.-H.; Hall, L. M. Ion Conductivity and Correlations in Model Salt-Doped Polymers: Effects of Interaction Strength and Concentration. *Macromolecules* **2020**, *53*, 3655−3668.
[179] Mori, K.; Okawara, A.; Hashimoto, T. Order-Disorder Transition of Polystyrene-Block-Polyisoprene. I. Thermal Concentration Fluctuations in Single-Phase Melts and Solutions and Determination of X as a Function of Molecular Weight and Composition. *J. Chem. Phys.* **1996**, *104* (19), 7765–7777.
[180] Arya, A.; Sharma, A. L. A Glimpse on All-Solid-State Li-Ion Battery (ASSLIB) Performance Based on Novel Solid Polymer Electrolytes: A Topical Review. *J. Mater. Sci.* **2020**, *55* (15), 6242–6304.
[181] Tu, Z.; Nath, P.; Lu, Y.; Tikekar, M. D.; Archer, L. A. Nanostructured Electrolytes for Stable Lithium Electrodeposition in Secondary Batteries. *Acc. Chem. Res.* **2015**, *48* (11), 2947–2956.
[182] Isikli, S.; Ryan, K. M. Recent Advances in Solid-State Polymer Electrolytes and Innovative Ionic Liquids Based Polymer Electrolyte Systems. *Curr. Opin. Electrochem.* **2020**, *21,* 188–191.
[183] Liu, J.; Monroe, C. W. Solute-Volume Effects in Electrolyte Transport. *Electrochim. Acta* **2014**, *135*, 447–460.
[184] Nyman, A.; Behm, M.; Lindbergh, G. Electrochemical Characterisation and Modelling of the Mass Transport Phenomena in $LiPF_6$-EC-EMC Electrolyte. *Electrochim. Acta* **2008**, *53* (22), 6356–6365.
[185] Möhl, G. E.; Metwalli, E.; Müller-Buschbaum, P. In Operando Small-Angle X-Ray Scattering Investigation of Nanostructured Polymer Electrolyte for Lithium-Ion Batteries. *ACS Energy Lett.* **2018**, *3* (7), 1525–1530.
[186] Sharon, D.; Bennington, P.; Webb, M. A.; Deng, C.; De Pablo, J. J.; Patel, S. N.; Nealey, P. F. Molecular Level Differences in Ionic Solvation and Transport Behavior in Ethylene Oxide-Based Homopolymer and Block Copolymer Electrolytes. *J. Am. Chem. Soc*. **2021**, *143*, 3180–3190.
[187] Maslyn, J. A.; Frenck, L.; Veeraraghavan, V. D.; Mu, A.; Ho, A. S.; Marwaha, N.; Loo, W. S.; Parkinson, D. Y.; Minor, A. M.; Balsara, N. P. Limiting Current in Nanostructured Block Copolymer Electrolytes. *Macromolecules* **2021**. DOI: acs.macromol.1c00425.
[188] Chu, K. T.; Bazant, M. Z. Electrochemical Thin Films at and above the Classical Limiting Current. *J. Appl. Math.* **2005**, *65* (5), 1485–1505.
[189] Kieffer, J.; Karkoulis, D. PyFAI, a Versatile Library for Azimuthal Regrouping. J. *Phys. Conf. Ser.* **2013**, 425.
[190] Frenck, L.; Veeraraghavan, V. D.; Maslyn, J. A.; Müller, A.; Ho, A. S.; Loo, W. S.; Minor, A. M.; Balsara, N. P. Effect of Salt Concentration Profiles on Protrusion Growth in Lithium-Polymer-lithium Cells. *Solid State Ionics* **2020**, *358*, 115517.
[191] Wang, H.; Newstein, M. C.; Krishnan, A.; Balsara, N. P.; Garetz, B. A.; Hammouda, B.; Krishnamoorti, R. Ordering Kinetics and Alignment of Block Copolymer Lamellae under Shear Flow. *Macromolecules* **1999**, *32* (11), 3695–3711.
[192] Samuels, R. J. *Structured Polymer Properties*; Wiley, **1974**.
[193] Wilkes, G. L. *Encyclopedia of Polymer Science and Engineering*, 2nd ed.; Wiley, 1988.
[194] White J. L. *Encyclopedia of Polymer Science and Engineering*, 2nd ed; Wiley, 1988.

10. Appendices

10.1 Derivation of an Expression for the Cation Transference Number in Terms of Measurable Quantities

In this section, we derive an expression for the cation transference number with respect to the solvent velocity, t_+^0, in terms of measurable quantities for a binary electrolyte: κ, D, ρ_+, and $\frac{dU}{d\ln m}$. The transport parameters are measured in cells comprising an electrolyte sandwiched between two lithium electrodes. The ionic conductivity, κ, is measured by ac impedance spectroscopy. The salt diffusion coefficient, D, is measured through a restricted diffusion experiment. The current fraction, ρ_+, is measured using the Bruce and Vincent method. The thermodynamic term, $\frac{dU}{d\ln m}$, is measured from concentration cells. The methodology for measuring these quantities is described in Chapters 2 and 4. This derivation is based on the framework developed in Chapter 12 of *Electrochemical Systems,* 4th Ed by John Newman and Nitash Balsara. The purpose of this section is to compile the derivation and include all algebraic steps while providing additional commentary.

10.1.1 Derivation of Cation and Anion Flux Equations from Concentrated Solution Theory

Concentrated solution theory is based on the Stefan-Maxwell diffusion equations originally derived from the kinetic theory of gases. The velocity of species i, $\boldsymbol{v}_i$, with respect to all other species j is related to the gradient in electrochemical potential, $\nabla\mu_i$, by:

$$c_i\nabla\mu_i = \sum_j K_{ij}(\boldsymbol{v}_j - \boldsymbol{v}_i)\,, \tag{10.1}$$

where c_i is the concentration of species i and K_{ij} is a drag coefficient which represents the frictional forces between species i and j which is related to the Stefan Maxwell diffusion coefficient, D_{ij}, by:

$$K_{ij} = \frac{RTc_ic_j}{c_T\mathcal{D}_{ij}}, \tag{10.2}$$

where c_T is the total concentration of the solution ($c_T = \sum_j c_j$). Plugging in Eqn. 10.2 into 10.1 we obtain:

$$c_i\nabla\mu_i = RT\sum_j \frac{c_ic_j}{c_T\mathcal{D}_{ij}}(\boldsymbol{v}_j - \boldsymbol{v}_i)\,. \tag{10.3}$$

The electrochemical potential of the electrolyte, μ_e, is given by the sum of the components:

$$\mu_e = \nu_+\mu_+ + \nu_-\mu_- \tag{10.4}$$

where the subscripts $+$ and $-$ denote the cation and anion, respectively and ν_i is the number of moles of species i that a mole of salt dissociates into. It follows that:

$$\nabla \mu_e = \nu_+ \nabla \mu_+ + \nu_- \nabla \mu_- \tag{10.5}$$

The flux of species i, $\boldsymbol{N}_i$, is the product of the velocity and the concentration:

$$\boldsymbol{N}_+ = c_+ \boldsymbol{v}_+, \tag{10.6}$$

$$\boldsymbol{N}_- = c_- \boldsymbol{v}_-. \tag{10.7}$$

Based on stoichiometry, the salt concentration is related to the concentration of the individual ions by:

$$c = \frac{c_+}{\nu_+} = \frac{c_-}{\nu_-}. \tag{10.8}$$

For simplicity, we will consider univalent salts which implies:

$$\nu_+ = \nu_- = 1, \tag{10.9}$$

and it follows:

$$c = c_+ = c_-. \tag{10.10}$$

The cation transference number with respect to the solvent velocity is given by the ratio:

$$t_+^0 = \frac{\mathcal{D}_{+0}}{\mathcal{D}_{+0} + \mathcal{D}_{-0}}, \tag{10.11}$$

where the subscript '0' denotes the solvent. The cation and anion transference number are related to each other by:

$$t_-^0 + t_+^0 = 1, \tag{10.12}$$

and it follows:

$$t_-^0 = \frac{\mathcal{D}_{-0}}{\mathcal{D}_{+0} + \mathcal{D}_{-0}} \tag{10.13}$$

We also define the diffusion coefficient of the electrolyte based on a thermodynamic driving force, $\mathcal{D}$, by:

$$\mathcal{D} = \frac{2\mathcal{D}_{+0}\mathcal{D}_{-0}}{\mathcal{D}_{+0} + \mathcal{D}_{-0}} \tag{10.14}$$

At any location within the electrolyte, the current density, i, is related to the flux of cations and anions by:

$$\boldsymbol{i} = F(z_+ \nu_+ \boldsymbol{N}_+ - z_- \nu_- \boldsymbol{N}_-) \tag{10.15}$$

where z_i is the charge number of species i. Most salts for lithium-ion battery electrolytes have $z_+ = -z_- = 1$, so we will make this simplification. Our goal is to use Eqn. 10.11 through 10.15 to obtain flux equations of the form:

$$\boldsymbol{N}_i = A \nabla \mu_e + B\boldsymbol{i} + c_i \boldsymbol{v}_0 \tag{10.16}$$

where A and B are constants to be solved for. The first term in Eqn. 10.16 is the flux due to diffusion, the second term is the migratory flux, and the third term is flux due to convection.

We can recapitulate Eqn. 10.3 where species i is the cation for a solution containing solvent, cations and anions:

$$\frac{c_+\nabla\mu_+}{RT} = \frac{c_+c_-}{c_+\mathcal{D}_\pm}(\boldsymbol{v}_- - \boldsymbol{v}_+) + \frac{c_+c_0}{c_T\mathcal{D}_{0+}}(\boldsymbol{v}_0 - \boldsymbol{v}_+) \tag{10.17}$$

Using the relationships given by Eqn. 10.6 and 10.7 and noting Eqn. 10.10 it follows:

$$\frac{c_+\nabla\mu_+}{RT} = \frac{c_+}{c_+\mathcal{D}_{+-}}(\boldsymbol{N}_- - \boldsymbol{N}_+) + \frac{c_0}{c_T\mathcal{D}_{0+}}(c_+\boldsymbol{v}_0 - \boldsymbol{N}_+) \tag{10.18}$$

Similarly, taking species i to be the anion:

$$\frac{c_-\nabla\mu_-}{RT} = \frac{c_-}{c_+\mathcal{D}_{+-}}(\boldsymbol{N}_+ - \boldsymbol{N}_-) + \frac{c_0}{c_T\mathcal{D}_{0+}}(c_-\boldsymbol{v}_0 - \boldsymbol{N}_-) \tag{10.19}$$

Taking the sum of Eqn. 10.18 and 10.19 and applying Eqn. 10.5:

$$\frac{c}{RT}\nabla\mu_e = \frac{c}{c_T\mathcal{D}_{+-}}(\boldsymbol{N}_+ + \boldsymbol{N}_- - \boldsymbol{N}_- - \boldsymbol{N}_+) + \frac{c_0}{c_T}\left(\frac{c\boldsymbol{v}_0}{\mathcal{D}_{+0}} - \frac{N_+}{\mathcal{D}_{+0}} + \frac{c\boldsymbol{v}_0}{\mathcal{D}_{-0}} - \frac{N_-}{\mathcal{D}_{-0}}\right). \tag{10.20}$$

The left term cancels out. We multiply both sides of Eqn. 10.20 by $\left(\mathcal{D}_{+0}\mathcal{D}_{-0}\frac{c_T}{c_0}\right)$ and obtain:

$$\frac{c_T\mathcal{D}_{+0}\mathcal{D}_{-0}}{c_0RT}c\nabla\mu_e = \mathcal{D}_{0-}c\boldsymbol{v}_0 - \boldsymbol{N}_+\mathcal{D}_{-0} + \mathcal{D}_{+0}c\boldsymbol{v}_0 - \boldsymbol{N}_-\mathcal{D}_{+0}, \tag{10.21}$$

which can be rearranged:

$$\frac{c_T\mathcal{D}_{+0}\mathcal{D}_{-0}}{c_0RT}c\nabla\mu_e = c\boldsymbol{v}_0(\mathcal{D}_{-0} + \mathcal{D}_{+0}) - \boldsymbol{N}_+\mathcal{D}_{-0} - \boldsymbol{N}_-\mathcal{D}_{+0}, \tag{10.22}$$

and dividing through by $(\mathcal{D}_{-0} + \mathcal{D}_{+0})$ and applying the definition of $\mathcal{D}$ given by Eqn 10.14:

$$\frac{c_T\mathcal{D}}{2c_0RT}c\nabla\mu_e = -\frac{\boldsymbol{N}_+\mathcal{D}_{-0}}{\mathcal{D}_{0-} + \mathcal{D}_{0+}} - \frac{\boldsymbol{N}_-\mathcal{D}_{+0}}{\mathcal{D}_{0-} + \mathcal{D}_{0+}} + c\boldsymbol{v}_0 \tag{10.23}$$

Using the definitions of t_+^0 and t_-^0 given by Eqn 10.11 and 10.13 we obtain:

$$\frac{c_T\mathcal{D}}{2c_0RT}c\nabla\mu_e = -\boldsymbol{N}_+t_-^0 - \boldsymbol{N}_-t_+^0 + c\boldsymbol{v}_0 \tag{10.24}$$

Using Eqn. 10.12 to eliminate t_-^0:

$$\frac{c_T\mathcal{D}}{2c_0RT}c\nabla\mu_e = -\boldsymbol{N}_+(1 - t_+^0) - \boldsymbol{N}_-t_+^0 + c\boldsymbol{v}_0, \tag{10.25}$$

and rearranging:

$$\frac{c_T\mathcal{D}}{2c_0RT}c\nabla\mu_e = -\boldsymbol{N}_+ + t_+^0(\boldsymbol{N}_+ - \boldsymbol{N}_-) + c\boldsymbol{v}_0. \tag{10.26}$$

We introduce the current density, i, using Eqn. 10.15 with $z_+ = 1$, $z_- = -1$, and $\nu_+ = \nu_- = 1$, and solving for $\boldsymbol{N}_+$:

$$\boldsymbol{N}_+ = -\frac{c_T \mathcal{D}}{2c_0 RT} c\nabla\mu_e + \frac{t_+^0}{F}\boldsymbol{i} + c\boldsymbol{v}_0, \tag{10.27}$$

we arrive at our desired expression for $\boldsymbol{N}_+$ given in the form of Eqn. 10.16. We can arrive at a similar expression for $\boldsymbol{N}_-$ by returning to Eqn. 10.24 and eliminating t_+^0 by Eqn. 10.12:

$$\frac{c_T \mathcal{D}}{2c_0 RT} c\nabla\mu_e = -\boldsymbol{N}_+ t_-^0 - \boldsymbol{N}_-(1 - t_-^0) + c\boldsymbol{v}_0 \tag{10.28}$$

and rearranging:

$$\frac{c_T \mathcal{D}}{2c_0 RT} c\nabla\mu_e = -\boldsymbol{N}_- + t_-^0(\boldsymbol{N}_- - \boldsymbol{N}_+) + c\boldsymbol{v}_0 \tag{10.29}$$

We introduce the current density, $\boldsymbol{i}$, using Eqn. 10.15 with $z_+ = 1$, $z_- = -1$, and $\nu_+ = \nu_- = 1$, and solving for $\boldsymbol{N}_-$:

$$\boldsymbol{N}_- = -\frac{c_T \mathcal{D}}{2c_0 RT} c\nabla\mu_e - \frac{t_-^0}{F}\boldsymbol{i} + c\boldsymbol{v}_0. \tag{10.30}$$

10.1.2 Introduction of the Potential Gradient, $\nabla\Phi$

We are interested in deriving an expression for the transference number based on measurements made in a cell comprising an electrolyte containing a lithium salt sandwiched between two lithium electrodes. Thus, the electrode reaction is given by:

$$Li^+ + e^- \leftrightarrow Li^0. \tag{10.31}$$

At equilibrium, the electrochemical potentials are related by:

$$\mu_{e^-} = \mu_{Li^0} - \mu_{Li^+}, \tag{10.32}$$

and with the simplification that the electrochemical potential of a neutral species is zero:

$$\nabla\mu_{e^-} = -\nabla\mu_+. \tag{10.33}$$

We insert Eqn. 10.5 to obtain:

$$\nabla\mu_{e^-} = -\nabla\mu_e + \nabla\mu_-. \tag{10.34}$$

The gradient of the electrochemical potential of electrons is related to the potential gradient (*i.e.* the electric field) by:

$$\nabla\mu_{e^-} = -nF\nabla\Phi, \tag{10.35}$$

where n is the number of electrons which participate in the electrode reaction ($n = 1$ in our case) and F is Faraday's constant. Combining Eqn. 10.34 and 10.35 we obtain:

$$-F\nabla\Phi = -\nabla\mu_e + \nabla\mu_-. \tag{10.36}$$

In the next section, we will derive an expression for $\nabla\mu_-$.

10.1.3 Derivation of an expression for $\nabla\mu_-$ in terms of κ, t_+^0, $\boldsymbol{i}$, and $\nabla\mu_e$

We begin with Eqn. 10.3 for the anion:

$$c_-\nabla\mu_- = \frac{RTc_-c_+}{c_T\mathcal{D}_{+-}}(\boldsymbol{v}_+ - \boldsymbol{v}_-) + \frac{RTc_-c_0}{c_T\mathcal{D}_{-0}}(\boldsymbol{v}_0 - \boldsymbol{v}_-). \tag{10.37}$$

Dividing through by c_- and applying Eqn. 10.6 and 10.7 noting Eqn. 10.10:

$$\nabla\mu_- = \frac{RT}{c_T\mathcal{D}_{+-}}(\boldsymbol{N}_+ - \boldsymbol{N}_-) + \frac{RTc_0}{c_T\mathcal{D}_{-0}}(\boldsymbol{v}_0 - \boldsymbol{v}_-). \tag{10.38}$$

Inserting Eqn. 10.27 and 10.30 for $\boldsymbol{N}_+$ and $\boldsymbol{N}_-$ and canceling terms:

$$\nabla\mu_- = \frac{RT}{c_T\mathcal{D}_{+-}}\left(\frac{t_+^0}{F}\boldsymbol{i} + \frac{t_-^0}{F}\boldsymbol{i}\right) + \frac{RTc_0}{c_T\mathcal{D}_{-0}}(\boldsymbol{v}_0 - \boldsymbol{v}_-). \tag{10.39}$$

Rearranging, applying Eqn. 10.12 to the first term on the right-hand side and multiplying the last term on the right-hand side by $\frac{c}{c}$ and applying Eqn. 10.30:

$$\nabla\mu_- = \frac{RT}{Fc_T\mathcal{D}_{+-}}\boldsymbol{i} + \frac{RTc_0}{cc_T\mathcal{D}_{-0}}(c\boldsymbol{v}_0 - \boldsymbol{N}_-). \tag{10.40}$$

Inserting Eqn. 10.30 we obtain:

$$\nabla\mu_- = \frac{RT}{Fc_T\mathcal{D}_{+-}}\boldsymbol{i} + \frac{RTc_0}{cc_T\mathcal{D}_{-0}}\left(c\boldsymbol{v_0} + \frac{c_T\mathcal{D}}{2c_0RT}c\nabla\mu_e + \frac{t_-^0}{F}\boldsymbol{i} - c\boldsymbol{v}_0\right). \tag{10.41}$$

Multiplying through the last term on the right-hand side and simplifying, we obtain:

$$\nabla\mu_- = \frac{RT}{Fc_T\mathcal{D}_{+-}}\boldsymbol{i} + \frac{\mathcal{D}}{2\mathcal{D}_{-0}}\mu_e + \frac{RTc_0t_-^0}{cc_T\mathcal{D}_{-0}F}\boldsymbol{i}\,. \tag{10.42}$$

Combining terms:

$$\nabla\mu_- = \frac{RT}{c_TF}\left(\frac{1}{\mathcal{D}_{+-}} + \frac{c_0t_-^0}{cD_{-0}}\right)\boldsymbol{i} + \frac{\mathcal{D}}{2\mathcal{D}_{-0}}\nabla\mu_e, \tag{10.43}$$

and multiplying the first term on the right-hand side by $\frac{F}{F}$ and eliminating $\mathcal{D}$ by Eqn. 10.14:

$$\nabla\mu_- = \frac{RT}{c_TF^2}\left(\frac{1}{\mathcal{D}_{+-}} + \frac{c_0t_-^0}{cD_{-0}}\right)\boldsymbol{i}F + \frac{\mathcal{D}_{0+}}{\mathcal{D}_{+0} + \mathcal{D}_{-0}}\nabla\mu_e. \tag{10.44}$$

The conductivity, κ, is given by:

$$\frac{1}{\kappa} = \left[\frac{RT}{c_TF^2}\left(\frac{1}{\mathcal{D}_{+-}} + \frac{c_0t_-^0}{c\mathcal{D}_{-0}}\right)\right]^{-1}, \tag{10.45}$$

and we substitute Eqn. 10.45 into Eqn. 10.44 and substitue Eqn. 10.13 to the last term in Eqn. 10.44 to obtain the desired expression:

$$\nabla \mu_- = \frac{F}{\kappa} \boldsymbol{i} + t_+^0 \nabla \mu_e. \tag{10.46}$$

10.1.4 Introduction of the current fraction, ρ_+

We can now insert Eqn. 10.46 into Eqn. 10.36:

$$F \nabla \Phi = \nabla \mu_e - \frac{F}{\kappa} \boldsymbol{i} - t_+^0 \nabla \mu_e, \tag{10.47}$$

and apply Eqn. 10.12:

$$F \nabla \Phi = -\frac{F}{\kappa} \boldsymbol{i} + t_-^0 \nabla \mu_e. \tag{10.48}$$

In a constant polarization experiment, the potential is held constant, and the current is measured. At long times, the current reaches a steady state value, i_{ss}, when the net flux of the anion becomes zero. This also implies that the solvent velocity is zero:

$$c \boldsymbol{v}_0 = 0. \tag{10.49}$$

We can thus set Eqn. 10.30 equal to zero and plugging in Eqn. 10.49:

$$N_- = -\frac{c_T \mathcal{D}}{2 c_0 RT} c \nabla \mu_e - \frac{t_-^0}{F} i_{ss} = 0, \tag{10.50}$$

and solving for $\nabla \mu_e$:

$$\nabla \mu_e = -\frac{2 c_0 RT t_-^0}{F c_T \mathcal{D} c} i_{ss}. \tag{10.51}$$

We now eliminate $\nabla \mu_e$ from Eqn. 10.48 by substituting Eqn. 10.51:

$$F \nabla \Phi = -\frac{F}{\kappa} i_{ss} - \frac{2 (t_-^0)^2 c_0 RT}{F c_T \mathcal{D} c} i_{ss}. \tag{10.52}$$

Rearranging and multiplying through by κ:

$$-\kappa \nabla \Phi = \left[\frac{2 (t_-^0)^2 c_0 RT \kappa}{F^2 c_T \mathcal{D} c} + 1 \right] i_{ss} \tag{10.53}$$

In the constant polarization experiment, the current density at the first moment of polarization is given by a statement of Ohm's law:

$$i_0 = -\kappa \nabla \Phi \tag{10.54}$$

which can be substituted into Eqn. 10.53 to obtain:

$$i_0 = \left[\frac{2 (t_-^0)^2 c_0 RT \kappa}{F^2 c_T \mathcal{D} c} + 1 \right] i_{ss} \tag{10.55}$$

Rearranging:

$$\frac{i_{ss}}{i_0} = \frac{1}{1 + \frac{2(t_-^0)^2 c_0 RT\kappa}{F^2 c_T \mathcal{D}c}} = \frac{1}{1 + Ne}, \tag{10.56}$$

Where we define the Newman number, Ne, as:

$$Ne = \frac{2(t_-^0)^2 c_0 RT\kappa}{F^2 c_T \mathcal{D}c} \tag{10.57}$$

The current fraction, ρ_+, is defined as:

$$\rho_+ = \frac{i_{ss}}{i_0} \tag{10.58}$$

Substituting Eqn. A.58 into Eqn. A.56 and rearranging:

$$1 + \frac{2(t_-^0)^2 c_0 RT\kappa}{F^2 c_T \mathcal{D}c} = \frac{1}{\rho_+}. \tag{10.59}$$

Finally, solving for the anion transference number, t_-^0:

$$t_-^0 = \pm\sqrt{\left(\frac{1}{\rho_+} - 1\right)\frac{F^2 \mathcal{D}c_T c}{2\kappa RT c_0}} \tag{10.60}$$

10.1.5 Expression for the salt diffusion coefficient, D

Equation 10.60 contains the diffusion coefficient of the salt based on a thermodynamic driving force, $\mathcal{D}$. This quantity cannot be measured directly. Instead, it is more common to measure the salt diffusion coefficient based on a concentration gradient, D, in a restricted diffusion experiment. We thus need to derive a relationship between $\mathcal{D}$ and D.

In a restricted diffusion experiment, a salt concentration gradient is established across a lithium symmetric cell and the current is set to zero. In the absence of convection, Eqn. A.30 is simplified to:

$$N_+ = -\frac{\mathcal{D}c_T}{2c_0 RT} c\nabla\mu_e. \tag{10.61}$$

Based on electroneutrality and in the absence of migration, $N_+ = N_-$ and the cation flux is related to the salt concentration gradient (in one dimension) by:

$$N_+ = -D\frac{dc}{dx}, \tag{10.62}$$

where x is the direction perpendicular to the electrodes in the lithium symmetric cell. Combining Eqn. 10.61 and 10.62 we obtain:

$$D\frac{dc}{dx} = \frac{\mathcal{D}c_T c}{2c_0 RT}\frac{d\mu_e}{dx} \tag{10.63}$$

The electrochemical potential of the electrolyte is defined by (see Chapter 2 of Ref [Newman]):

$$\mu_e = \mu_e^\theta + 2RT\, ln\, \gamma_\pm m\,, \tag{10.64}$$

where μ_e^θ is the electrochemical potential of a reference state, $\gamma_\pm$ is the mean molal activity coefficient, and m is the salt molality. Taking the derivative of Eqn. 10.64 with respect to x we obtain:

$$\frac{d\mu_e}{dx} = 2RT\left[\left(\frac{d\, ln\, \gamma_\pm}{dx}\right) + \left(\frac{d\, ln\, m}{dx}\right)\right]. \tag{10.65}$$

Plugging in Eqn. 10.65 to Eqn. 10.63 and multiplying both sides by $\frac{dx}{d\ln m}$:

$$D\frac{dc}{dx}\frac{dx}{d\, ln\, m} = \frac{\mathcal{D}c_T c}{c_0}\left[\left(\frac{d\, ln\, \gamma_\pm}{dx}\right) + \left(\frac{d\, ln\, m}{dx}\right)\right]\frac{dx}{d\, ln\, m}\,, \tag{10.66}$$

which simplifies to:

$$D\frac{dc}{d\, ln\, m} = \frac{\mathcal{D}c_T c}{c_0}\left(\frac{d\, ln\, \gamma\, \pm}{d\, ln\, m} + 1\right). \tag{10.67}$$

The molality and salt concentration are related by the solvent density, ρ_0:

$$c = \frac{m}{\rho_0} \tag{10.68}$$

We can show that the left side of Eqn. 10.67 simplifies by:

$$D\frac{dc}{d\, ln\, m} = \frac{D}{\rho_0}\frac{d\, exp(ln\, m)}{d\, ln\, m} = D\frac{m}{\rho_0} = Dc, \tag{10.69}$$

and therefore:

$$D = \frac{\mathcal{D}c_T}{c_0}\left(\frac{d\, ln\, \gamma\, \pm}{d\, ln\, m} + 1\right) \tag{10.70}$$

Finally, we solve for $\mathcal{D}$ to obtain:

$$\mathcal{D} = \frac{Dc_0}{c_T\left(\frac{d\, ln\, \gamma\, \pm}{d\, ln\, m} + 1\right)} \tag{10.71}$$

In Chapter 4, we refer to the thermodynamic factor, T_f, which is given by the term in parenthesis in Eqn. 10.71:

$$T_f = \frac{d\, ln\, \gamma\, \pm}{d\, ln\, m} + 1 \tag{10.72}$$

10.1.6 Expression for t_+^0

We can now eliminate $\mathcal{D}$ from Eqn. 10.60 by substituting Eqn. 10.71 to obtain:

$$t_-^0 = \pm\sqrt{\frac{\frac{F^2 Dc}{2\kappa RT}\left(\frac{1}{\rho_+}-1\right)}{\left(\frac{d\,ln\,\gamma\,\pm}{d\,ln\,m}+1\right)}} \tag{10.73}$$

The thermodynamic factor can be measured in concentration cells. In particular, for a lithium symmetric cell comprising two electrolytes of the same composition but different salt concentrations separated by a transition region, the potential is given by (see Chapter 2.6 and 2.9 of ref [Newman 4th ed]):

$$FU = -2RT\int_{m_1}^{m_2} t_-^0\left(\frac{d\,ln\,\gamma\,\pm}{d\,ln\,m}+1\right)d\,ln\,m\,, \tag{10.74}$$

which we write in differential form and solve for the thermodynamic factor:

$$\left(\frac{d\,ln\,\gamma\,\pm}{d\,ln\,m}+1\right) = -\frac{F}{2RTt_-^0}\left(\frac{dU}{d\,ln\,m}\right) \tag{10.75}$$

The methodology for obtaining the term $\frac{dU}{d\ln m}$ as a function of salt concentration is given in Chapter 4 and refs [pesko, Ma]. Eliminating the thermodynamic factor from Eqn. A.72 using Eqn. A.74 we obtain:

$$t_-^0 = \pm\sqrt{\frac{-FDct_-^0\left(\frac{1}{\rho_+}-1\right)}{\kappa\left(\frac{dU}{d\,ln\,m}\right)}} \tag{10.76}$$

Squaring both sides and solving for t_-^0:

$$t_-^0 = \pm\frac{FDc}{\kappa}\left(\frac{1}{\rho_+}-1\right)\left(\frac{dU}{d\,ln\,m}\right)^{-1} \tag{10.77}$$

Finally, using Eqn. 10.12 we obtain an expression for t_+^0 in terms of measurable quantities:

$$t_+^0 = 1 \pm \frac{FDc}{\kappa}\left(\frac{1}{\rho_+}-1\right)\left(\frac{dU}{d\,ln\,m}\right)^{-1} \tag{10.78}$$

It is important to note that measurement of κ, D, ρ_+, and $\frac{dU}{d\ln m}$ yields two possible values for t_+^0. Distinguishing between the two possibilities requires measurement of the sign of the salt concentration gradient. This is discussed in detail in Chapter 3.

For a block copolymer electrolyte, c is the salt concentration in the conducting phase and $\phi_c c$ the salt concentration based on the entire volume of the electrolyte, where ϕ_c is the conducting phase volume fraction. Thus, for a nanostructured block copolymer electrolyte where salt is excluded from one of the phases, Eqn. 10.78 becomes:

$$t_+^0 = 1 \pm \frac{FD\phi_c c}{\kappa}\left(\frac{1}{\rho_+}-1\right)\left(\frac{dU}{d\,ln\,m}\right)^{-1} \tag{10.79}$$

Eqn. 10.79 is used to solve for t_+^0 in Chapter 4.

10.2 Additional discussion on simultaneous SAXS and dc polarization experiments

Small angle X-ray scattering (SAXS) is a useful technique for characterizing the structure of an electrolyte on the 5 to 100 nm length scale. In Chapter 6 and 7, we described experiments wherein we performed SAXS simultaneously with dc polarization on a block copolymer electrolyte in a lithium symmetric cell. In this section, we discuss some best practices and tips for performing these measurements effectively. There are two experimental geometries that are employed in this thesis that are depicted schematically in Figure 10.1. In Fig. 10.1a, we show a geometry where the X-ray beam passes parallel to the flow of ionic current (i.e. perpendicular to the planar lithium electrodes). This orientation was utilized in Chapter 5. In Figure 10.1b, we show a geometry where the X-ray beam passes perpendicular to the flow of ionic current (i.e. parallel to the planar lithium electrodes). This orientation was utilized in Chapter 6 and 7. There are benefits and challenges associated with each experimental geometry which we discuss in this section.

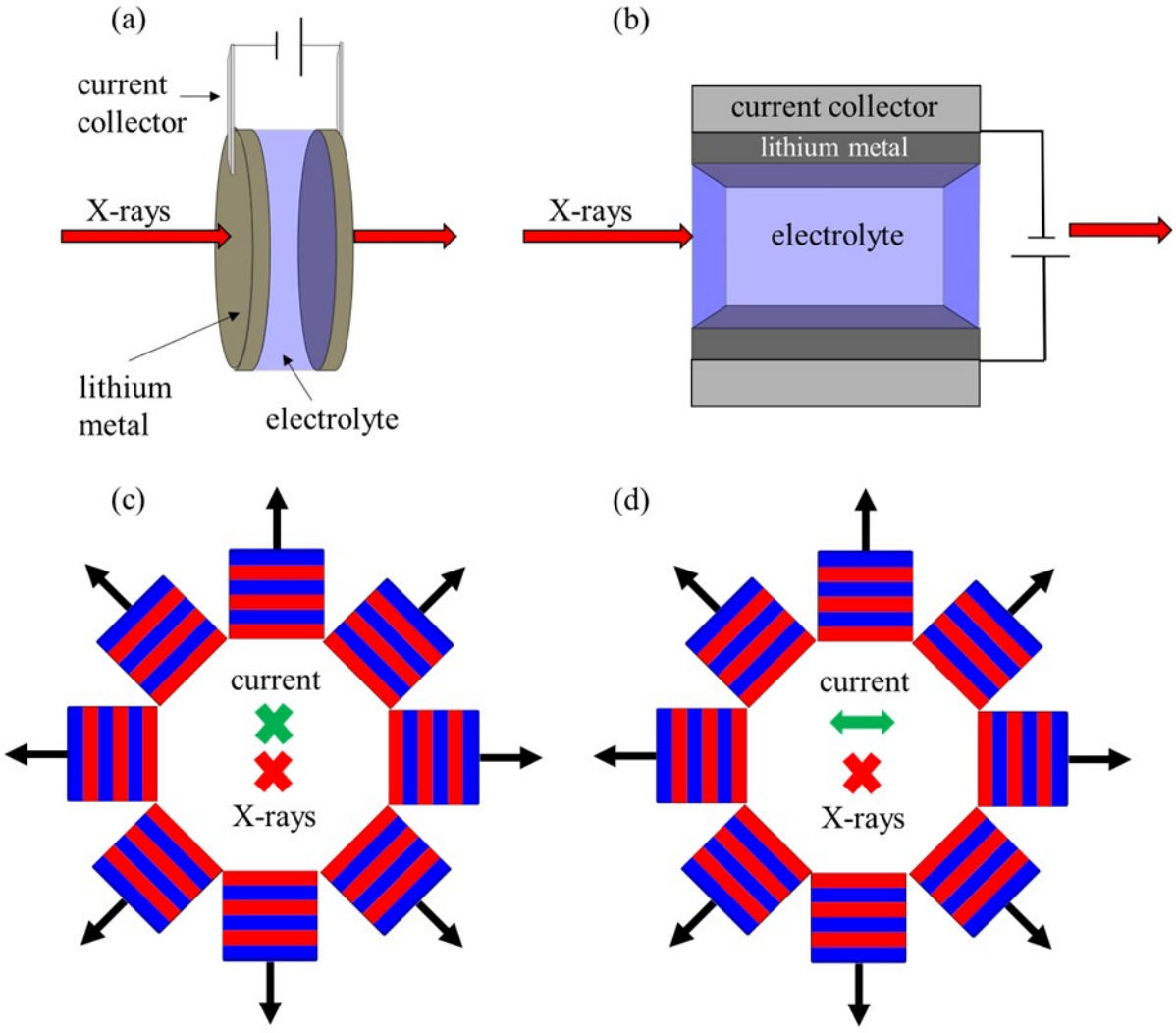

Figure 10.1. Two possible experimental geometries for simultaneous SAXS and polarization experiments. (a) The X-ray beam passes parallel to the flow of ionic current. (b) The X-ray beam passes perpendicular to the flow of ionic current. (c) Grain orientations with current and X-ray directions indicated for the geometry in part (a). (d) Grain orientations with current and X-ray directions indicated for the geometry in part (b). In (c) and (d) and 'x' indicates the direction is in/out of the page.

10.2.1 X-ray beam oriented parallel to the flow of ionic current.

The main advantages associated with the geometry depicted in Fig. 10.1a are related to the simplicity of the cell construction. To assemble the cells, two lithium electrodes are sandwiched around the polymer electrolyte. An annular spacer may be used if the electrolyte does not form a free-standing membrane (typical for block copolymer electrolytes with total molecular weight below about 100 kg mol^{-1}). Nickel current collectors are placed in contact with the lithium metal, but the cell must be constructed such that the current collectors are not in the X-ray beam. Nickel is strongly attenuating, and even thin nickel foils will completely attenuate the X-ray beam. The inner layer of pouch material designed specifically for lithium-ion batteries (in this thesis, the pouch material was purchased from MTI) is compatible with lithium metal, so it is acceptable for the lithium to be in direct contact with the pouch. For any materials that X-rays pass through, the attenuation of that material must be considered. When introducing new materials into the cell design, it is good practice to test compatibility with lithium metal and the attenuation of the X-ray beam. It is important to consider that the attenuation depends on the X-ray energy, which may or may not be an adjustable parameter based on the beamline used.

Advantages:

- Relatively easy cell to assemble, no custom-made parts required.
- A well-defined beam size and shape is not as important.

Disadvantages:

- No spatial resolution, data is an average over the entire distance between electrodes.
- For lamellar samples, all grain orientations sampled have normal vectors which are perpendicular to the X-ray beam (see Section 10.2.3)

10.2.2 X-ray beam oriented perpendicular to the flow of current

SAXS experiments performed in the geometry depicted in Fig. 10.1b offer a variety of advantages over the geometry in Fig. 10.1a. Performing the experiment in this configuration requires a more complicated cell design. In this thesis, custom built cells were made as discussed in the Supporting Information of Chapter 6 and 7. Poly(ether ether ketone) (PEEK) was used for the body of the cell construction. PEEK is a good material to use because the X-ray attenuation is low (in our cells, the X-ray beam passed through 2-3 mm of PEEK). The cells were also sealed with aluminum laminated pouch material to maintain an air-free cell environment.

Advantages:

- By scanning the sample through the X-ray beam, spatial resolution is attainable.

- For lamellar samples, the normal vectors of the grain orientations sampled in the experiment range from 0 to 360° (see Section 10.2.3).

Disadvantages:

- A more complicated cell design is required.
- Beam size and shape is important. As of 2021, the beamline 7.3.3. of the Advanced Light Source did not have the optics necessary to create a well-defined beam size and shape. Out of the two beamlines that we used for these experiments, the best data we obtained for the experiments were obtained at beamline 1-5 of the Stanford Synchrotron Radiation Light Source (SSRL).

10.2.3 Lamellar grain orientations

For a lamellar sample, we define a normal vector which is perpendicular to the planar block copolymer interfaces, as shown in Figure 10.1c. In a scattering experiment, only grain orientations with a normal vector perpendicular to the X-ray beam (within a certain acceptance angle, we estimate 10°) will contribute to the scattering pattern. In Figure 10.1c, we show 6 cartoons of the lamellar morphology with their corresponding normal vectors, representative of the experimental geometry in Fig. 10.1a. In this schematic, both the X-ray beam and current are directed into and out of the page (as indicated by a red and green 'x', respectively). The lamellar cartoons represent the grain orientations which would contribute to the scattering pattern because the normal vectors are perpendicular to the X-ray beam. In this configuration, all grain orientations shown in Fig. 10.1c are identical with respect to the current direction: they each provide direct pathways between the two lithium electrodes. However, in a bulk electrolyte sample there are a distribution of grain orientations. Some grain orientations provide direct conducting pathways between the electrodes, others completely block current. Therefore, the data obtained in this configuration is limited to information about one particular orientation relative to the current direction. In Fig. 10.1d, we present a similar schematic for the experimental geometry presented in Fig. 10.1b. Here, the current passes from left to right. The advantage of this geometry is that we sample the entire distribution of grain orientations relative to the current direction. By analyzing different sectors of the scattering pattern, we obtain information about unique grain orientations relative to the current direction, as discussed in Chapter 7.

10.2.4 Tips for performing simultaneous SAXS and polarization experiments.

Sample preparation:

- Anneal the pouch material prior to bringing the cell to the beamline.
    - There is a scattering signal from the pouch material. We found that this signal changes over time when the sample is heated. However, if the pouch material is annealed above the temperature that the experiment is performed, this effect is significantly reduced.
    - The pouch material can be annealed before sealing the cell inside or after
- Ensure the block copolymer sample is completely transparent and free of air pockets before beginning the experiment.

- Check that the sample does not leak at elevated temperatures prior to bringing it to the beamline.
- Take pictures of the cells before and after the experiment and check the polymer for beam damage.
- Be sure placement of nickel tabs does not enter the intended path of the X-ray beam
- Minimize the thickness of any materials that must be placed in the path of the X-ray beam (e.g., Kapton, PEEK).
- It is prudent to perform the electrochemical experiments that you plan to run at the beamline ahead of time and ensure repeatability.
- Test compatibility of all materials used with lithium metal at the temperatures planned for the experiment.
- Check the attenuation of the cell windows at the X-ray energy and flux planned for the experiment to insure adequate scattered intensity will be obtained.

At the beamline:

- For the experiments, drift of beam intensity and position may significantly impact the results. Take control measurements often. Measuring a reference sample at the same frequency that the electrochemical cell is scanned is a valuable strategy to detect drift in the beamline set up.
- When scanning the sample, scan in regular increments and being and end over the electrode where the beam is completely attenuated. This allows you to determine the cell coordinates independently from each scan (see Supporting Information of Chapter 7) and monitor if there is any drift in the motor positions.
- Consider strategies for mitigating beam damage. It is a good idea to take the minimum number of scans needed to achieve the necessary temporal resolution. In Chapter 7, we did not observe any beam dagame, however we also could have increased the increment of each scan by a factor of two.
    - Depending on the beam size and sample dimensions, it may be possible to scan the cell in different locations at the same distance between electrodes.
- It is a good idea to take multiple scans of the sample prior to beginning any polarization experiments. This will alert you to any variation in the data which is not due to the electrochemistry.
- Bring an empty cell to measure, this will help with analyzing any transmission data.
- Perform impedance spectroscopy throughout the experiment to check for large changes in resistance, which could indicate that the polymer has leaked out of the cell or air has leaked into the cell.

Data analysis:

- Begin data analysis by analyzing the 2D scattering images and note any irregularities. ImageJ is useful software for quickly cycling through stacks of image files.
- PyFAI is a useful tool for reducing data from 2D images to 1D $I(q)$ plots.

- It is beneficial to have code set up to analyze and fit the scattering peaks as the data is obtained. This will aid decision making, and you can avoid stopping an experiment prematurely if a sample is showing interesting behavior.
- Transmission data can be analyzed to give the salt concentration. Several issues arose in the experiments presented in this thesis that prevented us from obtaining clean transmission data, however it should be straightforward. A similar calibration curve of transmission versus salt concentration as was done in Fig. 7.1a to relate the domain spacing to salt concentration. In principle, this should give a more direct indication of the local salt concentration compared to using domain spacing as a proxy.